INSTITUTE

FOR

AEROSPACE STUDIES

UNIVERSITY OF TORONTO

THE APPLICATION OF IMPLOSION WAVE DYNAMICS TO A HYPERVELOCITY LAUNCHER

by

Robert F. Flagg

UTIAS

UTIAS REPORT NO. 125

THE APPLICATION OF IMPLOSION WAVE DYNAMICS TO A HYPERVELOCITY LAUNCHER

by

Robert F. Flagg

SUMMARY

- A detailed theoretical and experimental study of the concept of using spherical implosions as the driving mechanism for producing projectiles with velocities of the order of 50,000 feet per second has been made. Experimental results which include launchings of 0.22 and 0.312 inch diameter, one caliber, magnesium and polyethelene projectiles, up to velocities of 17,000 feet per second verify the validity of the implosion driving concept, although discrepancies still exist in the magnitude of the predicted and measured velocities. The present performance limit is dictated by apparatus limitations and is not representative of the ultimate performance limit for implosion drivers. Theoretically, velocities in the 50,000 to 100,000 feet per second regime are possible provided the projectiles can withstand the acceleration profile. Calculations are included which indicate the feasibility of accelerating 1 inch diameter projectiles, 1 caliber long ($\rho = 1.0$ g/cc) to 50,000 feet per second in a larger launcher having a 30 inch diameter hemispherical chamber and a 1.0 inch liner of explosive.

The theoretical work shows the dynamics of the waves in the chamber is predictable from modified classical implosion theory. A theoretical model of an implosion in a sphere is made with which the conditions inside the sphere can be calculated. A detailed examination of the results of three numerical experiments is made and the properties of the resulting wave phenomena determined. A comparison of the theory, numerical experiments and some actual measurements in a hemispherical chamber show that the theoretical predictions of conditions inside the hemisphere agree reasonably well with the numerical and experimental results.

An approximate model of the dynamics of the flow and the projectile in the barrel is formulated and performance is calculated using a numerical code which takes into account the effects of friction, counter pressure, time variation of the conditions at the origin of the hemisphere. A comparison of the predicted and measured performance shows that most of the effects of the various initial conditions and operating parameters are predicted. However a much more rigorous analysis will be required to obtain more accurate values of projectile velocity.

The instantaneous and uniform ignition of the explosive liner used to drive the implosion is shown to be a crucial part of the implosion driving concept. The results of a study undertaken to determine the explosive materials and conditions that can be used for generating the implosion are presented and show that several explosive materials, including several PETN formulations, lead azide, nitrocellulose and combinations of these have properties that make them amenable to initiation by an impinging gaseous detonation wave. Some of these are rejected for safety reasons. Experiments were made which prove conclusively that symmetric spherical implosions can be produced by using gaseous detonation waves at moderate pressures to initiate safe, secondary, solid explosives.

TABLE OF CONTENTS

NOTATION

a	sound speed
a	acceleration
c_e	elastic wave speed
C	capacitance
c_p	specific heat at constant pressure
c_v	specific heat at constant volume
d	explosive thickness
d	projectile diameter
D	detonation velocity
$D_{f'}$	denominator of f' relation, Eq. (2.70)
e	specific internal energy
E	elastic modulus
E_a	reaction energy
E_{total}	total energy
E_v	energy per unit volume
$E_\square$	energy per unit surface area
f	fraction burned
f	similarity quantity representing pressure
f_s	coefficient of sliding friction
F	similarity quantity representing pressure (Latter's notation)
F	force
g	chemical reaction rate
h	specific static enthalpy
K	factor in artifical viscosity relation, Eq. (2.56)
$K(\gamma)$	constant in implosion time relation, Eq. (2.105)
L	barrel length

m	mass
M_f	flow Mach number
M_s	shock Mach number
n	reaction order
n	ratio of peak pressure to yield stress
N	cycle number
N_f	zeros term of f' relation, Eq. (2.72)
p	pressure
q	artificial viscosity
Q	energy release or addition
r	radius or distance coordinate
$\hat{r}$	normalized radius or distance coordinate
R_o	chamber radius
R	resistance
$\mathcal{R}$	universal gas constant
S	detonation wave velocity - density slope
s	specific entropy
t	time
t	explosive thickness
t	non-dimensionalized implosion time
T	temperature
u	velocity
U_s	shock velocity
v	specific volume
V	similarity parameter from Sedov
W	explosive weight
x	distance coordinate

α	$= \dfrac{\gamma+1}{\gamma-1}$
α	time constant in pressure decay
γ	ratio of specific heats
γ_e	isentropic exponent
δ	deflection
δ	exponent of radial variation of pressure
ϵ	energy per unit volume
ψ	similarity variable representing density
φ	similarity variable representing particle velocity
η	similarity variable representing distance
σ_y	yield stress
θ	decay factor
ω	exponent on spacial variation of density
ϵ	a small quantity
ρ	density
μ	Poisson's ratio
ν	spacial index (= 1, plane coordinates; = 2, cylindrical coordinates; = 3 spherical coordinates)
ν	collision rate
Λ	ratio of internal energy to total energy
$\Phi(\zeta)$	cycle time integral
τ	characteristic time
Φ	ignition delay parameter
Φ_g	gravitational potential
λ_s	characteristic explosion radius
λ	ratio of internal energy to kinetic energy

Subscripts

cyc	cycle
c	singular or critical value
D	detonation state
E	explosion state
exact	exact value
exp	explosion phase
i	initial conditions
i	inner radius
imp	implosion phase
inbound	conditions left by imploding shock
incub	incubation
max	maximum
o	outer radius
orig	conditions at the origin or origin zone
outbound	conditions immediately behind reflected imploding shock
p	projectile
pl	plastic flow
R	reflected shock
S	shock front
z	zero condition
*	conditions at t_* or r_*
o	reference conditions
1	conditions ahead of a moving normal shock
2	conditions immediately behind a moving normal shock
5	conditions behind a reflected normal shock
∞	conditions at asymptote
( )'	represents differentiation with respect to η

1. INTRODUCTION

The hypervelocity launcher, because of its ability to accelerate
a known aerodynamic shape to an accurately known velocity in a variety of
atmospheres and conditions in a ballistics range, has been used successfully
for many years in the investigation of hypersonic phenomena. Data obtained
from ranges has increased our knowledge in the areas of hypersonic aerothermo-
dynamics, vehicle stability, wake structure, radiative and convective heat
transfer and impact phenomena. In some of these areas, the area of applicability
of the ballistics range overlaps those of other aerothermodynamic simulation
devices such as shock tubes and shock tunnels, enabling independent checks
to be made of the various data and phenomena. The ballistics range is uniquely
qualified for hypervelocity impact research and as such has been particularly
useful in dealing with meteorite impact in space flight applications and its
military counterpart in anti-missile defence problems. No small effort has
been expended to increase the velocity capability of these devices. Propellant
driven guns, which were the first to be used, were limited to velocities of the
order of 8,000 to 10,000 feet per second by the low escape speeds of the pro-
pellant gases.[1] Later, they were superseded by the light-gas gun technique of
Crozier and Hume[2] which produced velocities of up to 15,000 to 20,000 feet per
second for projectiles weighing a few grams. At present multiple-stage light-
gas guns, using the "accelerated reservoir" technique of Curtiss[3] can produce
velocities up to about 35,000 feet per second[4,5] for projectiles weighing
45 milligrams. Heavier projectiles can be launched, but at correspondingly lower
velocities. The present state of the art can be described by the mass-velocity
limit shown in Fig. 1, which is taken from a very recent survey by Lukasiewicz[6].

Although numerous schemes and techniques including explosive
driving[7], electrical driving,[8,9,10] electromagnetic driving[11] and augmentation[12]
have been suggested to further increase the projectile velocity, to date (March
1967) 35,000 feet per second for a 0.05 gram projectile is about the upper limit
of present technology.

It should be noted that some laboratories[13] have produced copper
jet sprays of up to 100 kilometers per second (328,000 feet per second) and
Wenzel and Gehring[14] of General Motors have succeeded in accelerating fragments
weighing from 0.08 to 0.31 grams up to from 45,600 to 54,100 feet per second
using shaped charges. In the present work, the discussion will be restricted
to those devices which accelerate predetermined and known aerodynamic shapes
to accurately measured velocities. "Fragment accelerators" will be excluded
from the discussion, as they do not represent "true" guns, using this defini-
tion.

The "performance barrier" is unfortunate since velocities of
interest for many space-research problems extend presently up to 60,000 feet
per second,[15] and the area of interest is expected to increase in the forseeable
future. Indeed for meteorite impact work, velocities of 200,000 feet per second
are currently of importance. While the latter velocity may not be obtained in
the immediate future, it appears that 50,000 to 60,000 feet per second velocity
regime can be reached by using the spherical-implosion technique.

The principle problems of extending the velocity limit are that
the pressures and temperatures that can be produced and contained in a laboratory
apparatus and the accelerations that projectiles can withstand are limited.

In 1959, Prof. I. I. Glass of the Institute for Aerospace Studies suggested a method for overcoming the pressure and temperature limit[16] by using explosive-driven spherical implosion waves instead of the planar waves, which are the basis for most of the existing launchers. Not only are the peak pressures and temperatures considerably higher (infinite at the origin in the ideal case) than the one-dimensional case, but they act over smaller interior regions that have limited contact with the containing walls hence are somewhat easier to contain and control. The high pressures and temperatures of an implosion-driven device are transient by nature and aggravate an already serious projectile integrity problem, but as will be shown subsequently, are of sufficient duration to produce hypervelocities for projectiles of practical interest.

The basic construction and the principle of operation of the implosion driven launcher are shown in Figs. 2 and 3 which are respectively, a diagramatic view of the implosion-driven launcher and a schematic of the various phases in the operating cycle.

The implosion-driven hypervelocity launcher consists essentially of a hemispherical cavity in a massive metal block. A barrel is placed such that the entrance to the barrel is coincident with the origin of the hemisphere. The interior of the hemispherical surface is coated with a thin layer of explosive; a diaphragm and projectile is positioned at the entrance to the barrel; and the remainder of the hemispherical cavity is filled with a combustable mixture of oxygen and hydrogen. The gaseous mixture is ignited at the origin with sufficient violence to generate a detonation wave in the gas (Fig. 3a). The detonation wave propagates outward spherically and reflects from the surface of the explosive igniting it instantaneously and uniformly over the entire surface, generating an explosive-driven, imploding shock wave (Fig. 3b). This shock wave converges on the origin monotonically increasing in strength as it approaches the origin. On reflection (Fig. 3c) it leaves a very high-temperature, high-pressure region which bursts the diaphragm and acts on the base of the projectile, accelerating it along the barrel.

While the concept sounds straight-forward, it has in fact required great effort to bring it to the point of practical reality. In the years since 1959, much background work has had to go into translating this concept into a workable, practical device,[17] especially since it encompasses areas of gas dynamics that have not been the subject of much research. The technical problems of producing a stable, uniform, imploding wave are manifold involving a number of discrete research areas, such as spherical wave dynamics, spherical detonation waves, shock initiation of explosives, wave stability as well as the more mundane problems of the physical strength of the apparatus under shock loading and very high pressures. The key technical problem for the implosion was that of the initiation of the explosive. If an explosive cannot be made to detonate instantaneously and uniformly, then little hope can be held for generating a symmetric implosion. Accordingly, much effort went into solving this particular problem. The results now show that the ignition, by the impingement of gaseous detonation waves, is both possible and practical and that there are several explosive materials which will detonate when gaseous detonation waves of moderate pressures, collide with them.

In the subsequent sections a review and discussion is made of the applicable gasdynamics, wave interactions and the classical self-similar theory for imploding shocks. A model is then developed of the dynamics of an "implosion in a sphere" and coupled to the ballistics problem and the gasdynamics of the gas in the gun barrel. The anticipated performance of the implosion driven gun is then calculated and a comparison with the measured performance made. The model is used further for optimization purposes and an assessment of the feasibility of larger and/or higher velocity guns. In Sec. 4 the results of the one-dimensional, explosive-initiation studies are presented and discussed and the apparatus and operating procedures are detailed. In the remaining sections the launcher facility, the apparatus and operating procedures are enumerated and the present state of the art discussed and recommendations made for future work.

2. THEORETICAL CONSIDERATIONS

In this section the theory on which the implosion-driven hyper-velocity launcher is based is developed. In Sec. 2.1 the salient features of plane one-dimensional waves are reviewed with a view towards the limiting behavior in the strong shock case. The similar solution for exploding shocks made possible by the assumption of strong shocks as given by Taylor and Sedov is discussed in Sec. 2.2. Using this as a basis the classical similar solution for the imploding shock is discussed in Sec. 2.3, and numerical solutions presented for values of ratio of specific heats not previously published. Values of the exponent of the variation of pressure with radius are also given. In Sec. 2.4 a model of an "implosion in a sphere" based on classical implosion theory is made and examined. This is followed in Sec. 2.5 by a detailed examination of the results of a set of three numerical experiments and a comparison of the results with the implosion in a sphere model.

2.1 Review of Planar Nonstationary Waves

Although the important features of the implosion driven launcher are dictated primarily by the spherical waves and their dynamics inside the chamber, a short discussion of planar waves is in order since many of the boundary conditions are given by plane-wave considerations. Furthermore locally, a spherical wave can be treated as a plane phenomena. This is true for both an exploding wave, the reflection of the exploding wave from a wall and for an imploding wave, but not for the reflection of an imploding wave at the origin (see Sec. 2.5.4). However, in this last case there are certain similarities between the reflection of a spherically imploding wave at the origin and the reflection of a plane wave from a plane surface in that they both have an asymptotic behavior for the strong shock case. Since the properties of planar waves will be referred to repeatedly in the derivations and discussions to follow, it was felt advisable to review their most important properties.

Starting with the basic premises of the conservation of mass, momentum, and energy and for the assumption of an ideal (inviscid, non heat-conducting, thermally and calorically perfect) gas with no body forces, the conservation equations for the planar case can be written[18]

$$\text{(mass)} \qquad \frac{\partial \rho}{\partial t} + \frac{\partial}{\partial x}(\rho u) = 0 \qquad\qquad (2.1)$$

3

(momentum) $\quad\quad \dfrac{\partial u}{\partial t} + u\,\dfrac{\partial u}{\partial x} = -\dfrac{1}{\rho}\,\dfrac{\partial p}{\partial x}$ $\quad\quad\quad\quad\quad$ (2.2)

(energy) $\quad\quad\quad \dfrac{\partial s}{\partial t} + u\,\dfrac{\partial s}{\partial x} = 0$ $\quad\quad\quad\quad\quad\quad\quad$ (2.3)

These three fundamental equations can be manipulated into a form which gives the ratios of the conditions across a moving plane shock, in terms of a nondimensional shock velocity, or shock Mach numbers, $M_s = U_s/a_1$

The static pressure ratio p_2/p_1 is given by

$$\frac{p_2}{p_1} = p_{21} = \frac{2\gamma}{\gamma+1}\,M_s^2 - \frac{\gamma-1}{\gamma+1} \;. \quad\quad\quad (2.4)$$

The static temperature ratio T_2/T_1 is

$$\frac{T_2}{T_1} = T_{21} = \left[\left(\frac{\gamma-1}{\gamma+1}\right)\left(M_s^2-1\right) + M_s^2\right]\left[\left(\frac{\gamma-1}{\gamma+1}\right)\left(M_s^2-1\right) + 1\right]\frac{1}{M_s^2} \quad (2.5)$$

The density ratio ρ_2/ρ_1 is

$$\frac{\rho_2}{\rho_1} = \rho_{21} = \frac{\gamma+1}{\gamma-1 + 2/M_s} \quad\quad\quad\quad (2.6)$$

and the particle velocity u_2 is

$$\frac{u_2}{a_1} = \frac{2}{\gamma+1}\left(M_s - \frac{1}{M_s}\right) \quad\quad\quad\quad (2.7)$$

where $\quad \gamma = C_p/C_v$

These equations can also be written in terms other than M_s, for example, in terms of the shock pressure ratio p_{21}, the shock temperature may be written

$$T_{21} = p_{21}\;\frac{1 + \dfrac{\gamma-1}{\gamma+1}\,p_{21}}{\dfrac{\gamma-1}{\gamma+1} + p_{21}} \quad\quad\quad\quad (2.8)$$

Many of these alternate forms can be found in Refs. 19, 20 and 21, to mention a few.

Much of the difficulty and challenge of gasdynamics comes from the non-linear behavior of Eqs. (2.4) through (2.7) with shock wave velocity. However, for $M_s \gg 1$ these relations take on a much simpler form. The shock wave static pressure ratio p_{21}, equation (2.4), reduces to

$$p_{21} \sim \frac{2\gamma}{\gamma+1}\,M_s^2 \quad\quad\quad\quad (2.9)$$

4

The shock static temperature ratio T_{21}, Eq. (2.5) reduces to

$$T_{21} \sim \left(\frac{2\gamma}{\gamma+1}\right)\left(\frac{\gamma-1}{\gamma+1}\right) M_s^2 \quad, \tag{2.10}$$

The density ratio ρ_{21} reduces to a constant which is given by

$$\rho_{21} \sim \frac{\gamma+1}{\gamma-1} \quad, \tag{2.11}$$

the particle velocity behind the shock simplifies to

$$\frac{u_2}{a_1} \sim \frac{2}{\gamma+1} M_s \quad, \tag{2.12}$$

or

$$u_2 \sim \frac{2}{\gamma+1} U_s \quad, \tag{2.13}$$

and the flow Mach number behind the shock becomes

$$M_f \sim \left[\frac{2}{\gamma(\gamma-1)}\right]^{\frac{1}{2}} \tag{2.14}$$

These simpler forms will make possible the similar solutions for the imploding and exploding spherical shocks. Note that the constants in Eqs. (2.9) through (2.14) are a function only of the ratio of specific heats γ.

While $1 \leq \gamma \leq 1.67$ is commonly found in gasdynamics problems ($\gamma \to 1$ for heavy molecules such as SF_6, which has 15 vibrational degrees of freedom), explosive products and gases at very high densities often behave as if $\gamma \sim 3$, corresponding to a single degree of freedom. The behavior of these relations with γ can be seen from Fig. 4. They are tabulated for convenience in Table 1. Note for $\gamma < 2$, the flow immediately behind a strong shock is supersonic. For $\gamma = 2$ it is just sonic and for $\gamma > 2$ it is subsonic.

From the same cited references (19, 20, 21) the properties across a reflected plane shock, in the ideal case, are shown to take the form:
for the reflected shock static pressure ratio p_5/p_2

$$\frac{p_5}{p_2} = p_{52} = \frac{\alpha + 2 - p_{12}}{1 + \alpha \, p_{12}} \quad, \tag{2.15}$$

for the reflected shock static temperature ratio T_5/T_2

$$\frac{T_5}{T_2} = T_{52} = \frac{p_{52}(\alpha + p_{52})}{1 + \alpha \, p_{52}} \quad, \tag{2.16}$$

and for the reflected shock density ratio ρ_5/ρ_2

$$\frac{\rho_5}{\rho_2} = \rho_{52} = \frac{1 + \alpha \, p_{52}}{\alpha + p_{52}} \tag{2.17}$$

5

where

$$\alpha = \frac{\gamma + 1}{\gamma - 1}$$

Again, for the assumption that $M_s \gg 1$ i.e. $p_{21} \gg 1$ or conversely $p_{12} \sim 0$ the non linear behavior disappears and the ratios become constants which depend only on the ratio of specific heats γ, and are independent of any other parameter. For example

$$p_{52} \sim \frac{3\gamma - 1}{\gamma - 1} \tag{2.18}$$

$$\rho_{52} \sim \frac{\gamma}{\gamma - 1} \tag{2.19}$$

$$T_{52} \sim \frac{3\gamma - 1}{\gamma} \tag{2.20}$$

Equations (2.18) through (2.20) are plotted for $1 \le \gamma \le 3$ in Fig. 5 and are tabulated in Table 1.

Combining Eqs. (2.9) through (2.13) with equations (2.18) through (2.20) respectively, the pressure, temperature and density jumps as seen by the reflecting surface are determined to be

$$p_{51} = p_{52} \cdot p_{21} = \frac{2\gamma}{\gamma + 1} \left(\frac{3\gamma - 1}{\gamma - 1} \right) M_s^2 \tag{2.21}$$

$$T_{51} = T_{52} \cdot T_{21} = \frac{2(\gamma - 1)(3\gamma - 1)}{(\gamma + 1)^2} M_s^2 \tag{2.22}$$

$$\rho_{51} = \rho_{52} \cdot \rho_{21} = \frac{\gamma(\gamma + 1)}{(\gamma - 1)^2} \tag{2.23}$$

These limiting relations are plotted in Fig. 6 and tabulated in Table.1. It is of interest to note that for all of the limiting cases

$$\frac{p_i}{p_j} = \frac{\rho_i \, T_i}{\rho_j \, T_j} \tag{2.24}$$

i.e., the perfect gas law is not violated, as must of course be the case.

From the figures, the following behavior can be noted. The reflected shock ratios take on possible values

$$4 \le p_{52} \le \infty$$

$$\frac{3}{2} \le \rho_{52} \le \infty \quad \text{For } 3 \ge \gamma \ge 1. \tag{2.25}$$

$$\frac{8}{3} \ge T_{52} \ge 2$$

The total jumps as seen at the reflecting surface take on

values

6

$$6 \leq \frac{p_{51}}{M_s^2} \leq \infty$$

$$3 \leq \rho_{51} \leq \infty \qquad 3 \leq \gamma \leq 1 \qquad (2.26)$$

$$2 \geq \frac{T_{51}}{M_s^2} \geq 0$$

It should be noted that the variation of the pressure with γ is opposite to the variation of temperature with γ i.e., γ effects which tend to increase the pressure tend to decrease the temperature and vice versa. In launchers as in shock tubes both high temperatures and high pressures are required for high performance hence generally an optimum can be found for a given set of initial conditions.

All of the above are derived for the assumption of a perfect gas. For most cases of practical interest the pressures and temperatures will be such that real gas effects will produce deviations from the conditions predicted by perfect gas theory. The complexity of the chemistry involved requires each case to be considered on its own merits and the use of numerical procedures and machine computation to calculate shock jump properties is usually dictated. Tables and graphs for a wide range of conditions are available for both air[22,23] and many other gases.[24] Further many laboratories have extensive unpublished data on other gases. At present several organizations, notably AVCO-Research and Advanced Development Laboratory have computer codes which can produce extensive shock wave data from basic thermodynamic data of a given gas. In principle then, shock tables can be made available for any gas or mixtures of gases provided the basic thermodynamic data is known.

While no general correction to the perfect gas results can be made a few qualitative remarks are possible. As the gas in question is excited by energetic collisions, it behaves initially as if it were utilizing additional degrees of freedom. The qualitative behavior can be noted by observing the effect of a decrease in γ , that is to say, pressures and densities generally increase and temperatures decrease. If the shock is so strong as to cause complete dissociation and ionization of the gas, it begins to behave as a monatomic gas, with a γ of 5/3. As the intent of this study is to produce an understanding of the basic ideas of the implosion-driven processes, the real gas problem will not be discussed in any detail in order that the simple ideal properties of the implosion dynamics should not be obscured by the complex chemistry.

2.2 Review of Spherical Explosions

Spherically exploding and imploding shock wave phenomena may be readily found in nature.[25] Man-made spherical explosions came into existance essentially with the invention of gunpowder. However it was not until the large scale application of science to warfare in World War II and the resulting atomic bomb that a concerted effort was made to understand the gasdynamics of intense spherical explosions. Prior to World War II the understanding of spherical shocks produced by explosives was essentially on a pragmatic basis.

The general problem of a finite source explosion is sufficiently complicated by the non-linearity of the system of equations even with the simplifying assumption of a perfect gas that computing machines and numerical methods are required for solution. While numerical results are very useful for a specific case, they lack the generality desirable to understand the problem in its entirety. However the simplification made possible by the assumption of an ideal, point source (i.e., massless) explosion makes possible analytic solutions and allows insight into the general problem of explosions.

2.2.1 Classical Point Source Explosion

Three researchers, Taylor[26,27] Sedov[28] and von Neumann[29], independantly and nearly simultaneously obtained solutions for an ideal point explosion in a gas. Sedov's elegant method of solution is somewhat abstract, but analytic, hence exact. Taylor's is such that the physics of the problem remains clear throughout the mathematical manipulations although he resorted finally to a numerical solution. Von Neumann's solution has the advantage that it is analytic and also retains physical clarity. He also provides extensive relations to facilitate the use of the solutions in practical problems. Taylor's approach will be followed in the discussion below as a similar approach will be used in the numerical solution of the implosion problem.

The classical point source explosion solution is based on three assumptions, 1) the resulting blast shock is strong, 2) the pressure immediately behind the shock varies inversely as the shock front radius cubed and 3) the profiles of the physical quantities behind the front are self-similar. The first assumption, that of the strong shock, replaces the complete shock wave relations with their limiting relations, as discussed in Sec. 2.1. It should be noted that were it not for this simplification, a similarity solution would not be possible. The second assumption i.e., that the shock pressure varies as r^{-3} comes essentially from a dimensional argument which notes that, when the energy originally in the quiescent gas is negligible by comparison , the total energy contained in the region behind the blast wave is constant only if $p \sim r^{-3}$. For powers less than or greater than 3, energy is being either added or removed continuously with time. The third assumption is that the self-similar quantities f, φ and ψ, representing pressure, particle velocity and density, do exist. These quantities are assumed initially and the mathematical manipulations seek to show their existence and to finally evaluate them as functions of the nondimensional radius η .

Consider the equations of conservation of mass, momentum and energy which for a perfect inviscid gas can be written for the spherical case

$$\frac{\partial \rho}{\partial t} + \frac{\partial(\rho u)}{\partial r} + 2\frac{\rho u}{r} = 0 \qquad (2.27)$$

$$\frac{\partial u}{\partial t} + u\frac{\partial u}{\partial r} + \frac{1}{\rho}\frac{\partial p}{\partial r} = 0 \qquad (2.28)$$

$$\frac{\partial}{\partial t}\left(\frac{p}{\rho^{\gamma}}\right) + u\frac{\partial}{\partial r}\left(\frac{p}{\rho^{\gamma}}\right) = 0 \qquad (2.29)$$

Equation (2.29) is the "particle isentropic" equation which is valid in the interior region bounded by the blast wave, since shock and other entropy producing mechanisms are assumed absent in that region; aside from the initial variable entropy production by the blast wave. It states that the flow along a given particle path is isentropic although the entropy changes from path to path. The pressure, density and particle velocity behind the shock consistant with the three assumptions are assumed to obey the following

$$\text{pressure} \qquad \frac{p}{p_1} = f_1(\eta)r^{-3} \qquad\qquad (2.30)$$

$$\text{density} \qquad \frac{\rho}{\rho_1} = \psi(\eta) \qquad\qquad (2.31)$$

$$\text{particle velocity} \qquad \frac{u}{U_s} = \varphi_1(\eta)r^{-3/2} \qquad\qquad (2.32)$$

$$\text{where} \qquad \eta = \frac{r}{r_s} \qquad\qquad (2.33)$$

and f_1, ψ and φ_1 are the similarity quantities for pressure, density and particle velocity, respectively. Taking the necessary derivatives, substituting these into Eqs. (2.27), (2.28) and (2.29) and replacing f_1 and φ_1 by their non-dimensional equivalents, f and φ, reduces the set of non-linear, partial differential equations to the following set of ordinary differential equations in the three similarity quantities f, ψ, and φ :

$$-\frac{3}{2}\varphi + (\varphi-n)\varphi' + \frac{f'}{\gamma\psi} = 0 \qquad\qquad (2.34)$$

$$\psi\varphi' + (\varphi-n)\psi' + \frac{2\psi\varphi}{\eta} = 0 \qquad\qquad (2.35)$$

$$-3f + (\varphi-n)f' - \gamma f\frac{\psi'}{\psi}(\varphi-n) = 0 \qquad\qquad (2.36)$$

The only other quantity which appears is γ. These three equations must now be integrated to obtain $f(\eta)$, $\varphi(\eta)$ and $\psi(\eta)$.

Taylor[26] noted that the system could be manipulated to yield the derivatives in a manner that allows step by step numerical integration starting for example, at the shock front. The derivatives written in this form are

$$f' = \frac{f\left\{-3\eta + \varphi(6+ \frac{\gamma}{2}) - \frac{2\gamma\varphi^2}{\eta}\right\}}{(\varphi-n)^2 - \frac{f}{\psi}} \qquad\qquad (2.37)$$

$$\varphi' = \frac{\frac{3}{2} - \frac{f'}{\gamma\psi}}{\varphi - \eta} \qquad\qquad (2.38)$$

9

$$\psi' = \frac{-\dfrac{2\psi\varphi}{\eta} - \psi\varphi'}{(\varphi - n)} \tag{2.39}$$

The three required boundary conditions fixed by the shock relations require that

$$f(1) = \frac{2\gamma}{\gamma+1} \tag{2.40}$$

$$\psi(1) = \frac{\gamma+1}{\gamma-1} \tag{2.41}$$

$$\varphi(1) = \frac{2}{\gamma+1} \tag{2.42}$$

It is a result, rather than a boundary condition of Taylor's solution that $\varphi(0) = 0$, i.e., the velocity vanishes at the origin. This condition must be satisfied if the solution is to have any physical significance. While in principle, one of the above boundary conditions could have been deleted and $\varphi(0) = 0$ substituted in its place, the resulting numerical computations would have become unnecessarily complicated, requiring an iterative procedure on φ. It should be noted that there are no singularities in this system in the region $0 \leq \eta \leq 1$ and that the equations can be integrated numerically without difficulty. The integral that expresses the energy contained within the blast sphere, provided the energy in the quiescent gas is negligible, is

$$\int_0^1 \left(\frac{f}{\gamma(\gamma-1)} + \frac{\psi\varphi^2}{2} \right) \eta^2 d\eta \tag{2.43}$$

is bounded, and the history of the blast is determined by two constants E_0 and ρ_0, where E_0 is the total energy liberated in the blast and ρ_0 the undisturbed density field. Some typical self-similar results are shown plotted in Fig. 7 and show the effect of γ on the resulting profiles. It can be seen from the figure that the pressure is highest, immediately behind the shock front and that initially it decays as η decreases and then leveling off, remains approximately constant at a non zero value as $\eta \to 0$. The decay is most rapid for the largest γ's which also have the highest origin pressures. The particle velocity varies in an almost linear fashion from the shock front to the origin and vanishes at that point. The density approaches zero a short distance behind the shock for small values of γ, but for $\gamma = 3$ extends to $\eta = 0$. The gas engulfed by the shock is entrained in a relatively thin region behind the shock front, and swept along with it. As will be seen subsequently, this general type of behavior has similarities in the implosion case.

2.2.2 Analytic Solutions

Since the publication of the numerical solution to the point source explosion by G.I. Taylor, three independent, different, yet equivalent, analytic solutions have been published by Latter[30], J.L. Taylor[31] and Sedov[28]. Sedov's solution actually predates these two solutions but did not become available in the West until 1959, with the translation of Sedov's book, "Similarity and Dimensional Methods in Mechanics." Sedov's exact solutions have the virtue that all the similarity quantities are given in an explicit, although algebraically unwieldy form through a parameter V and include $v = 1, 2$ and 3 cases. Latter and J.L. Taylor's solutions for the spherical case are much simpler algebraically, although the similarity quantities are available only in an implicit form, hence still require numerical methods to obtain $f(n), \varphi(n), \psi(n)$ directly. Harris[32] has obtained the equivalent solution for $v = 1$. Lin[33] published a numerical solution for $v = 2$ in 1954.

Sedov's Solution[28]

Sedov's solutions take the following form, (the connection between Sedov's notation and G.I. Taylor's notation is indicated):

$$\frac{u}{U_s} = \frac{\gamma+1}{2} \varphi = \frac{(v+2)(\gamma+1)}{4} V \frac{r}{r_s} \qquad (2.44)$$

$$\frac{\rho}{\rho_s} = \frac{\gamma-1}{\gamma+1} \psi = \left[\frac{\gamma+1}{\gamma-1}\left(\frac{(v+2)\gamma}{2} V - 1\right)\right]^{\alpha_3} \left[\frac{\gamma+1}{\gamma-1}\left(1 - \frac{v+2}{2} V\right)\right]^{\alpha_5}$$

$$\times \left[\frac{(v+2)(\gamma+1)}{(2+v)(\gamma+1) - 2[2+v(\gamma-1)]}\left(1 - \frac{2+v(\gamma-1)}{2} V\right)\right]^{\alpha_4} \qquad (2.45)$$

$$\frac{p}{p_s} = \frac{\gamma+1}{2\gamma} f = \left[\frac{(v+2)(\gamma+1)}{4} V\right]^{\frac{2}{2+v}} \left[\frac{\gamma+1}{\gamma-1}\left(1 - \frac{v+2}{2} V\right)\right]^{\alpha_5+1}$$

$$\times \left[\frac{(v+2)(\gamma+1)}{(v+2)(\gamma+1) - 2[2+v(\gamma-1)]}\left(1 - \frac{2+v(\gamma-1)}{2} V\right)\right]^{\alpha_4 - 2\alpha_1} \qquad (2.46)$$

Where the parameter V is given by

$$\frac{r}{r_s} = \left[\frac{(v+2)(\gamma+1)}{4} V\right]^{\frac{-2}{2+v}} \left[\frac{\gamma+1}{\gamma-1}\left(\frac{(v+2)\gamma}{2} V - 1\right)\right]^{-\alpha_2}$$

$$\times \left[\frac{(v+2)(\gamma+1)}{(v+2)(\gamma+1) - 2[2+v(\gamma-1)]}\left(1 - \frac{2+v(\gamma-1)}{2} V\right)\right]^{-\alpha_1} \qquad (2.47)$$

11

and the exponents α's are given by

$$\alpha_1 = \frac{(\nu+2)\gamma}{2 + \nu(\gamma-1)} \left[\frac{2\nu(2-\gamma)}{\gamma(\nu+2)^2} - \alpha_2 \right]$$

$$\alpha_2 = \frac{1-\gamma}{2(\gamma-1)+\nu}$$

$$\alpha_3 = \frac{\nu}{2(\gamma-1)+\nu} \qquad\qquad (2.48)$$

$$\alpha_4 = \frac{\alpha_1(\nu+2)}{2-\gamma}$$

$$\alpha_5 = \frac{2}{\gamma-2}$$

While explicit in u, ρ and p at least in terms of V the complexity of these relations rules out further substitution of these equations into other equations.

Latter's Solution[30]

Latter's analytic solution results from manipulating Eqs. (2.34) through (2.36) into a form that can be integrated directly. He obtained for φ, an implicit function of η

$$\eta = b \; \frac{\left| \dfrac{\varphi}{\eta} - \dfrac{1}{\gamma} \right|^{\frac{\gamma-1}{2\gamma+1}}}{\left| \dfrac{\varphi}{\eta} \right|^{2/5} \left| \dfrac{\varphi}{\eta} - \dfrac{5}{3\gamma-1} \right|^{\frac{13\gamma^2 - 7\gamma+12}{5(2\gamma+1)(3\gamma-1)}}} \qquad (2.49)$$

f and φ can be obtained from the simultaneous solution of

$$f\varphi + (\varphi-\eta) \left(\frac{f}{\gamma-1} + \frac{\gamma}{2} \psi \varphi^2 \right) + c = 0 \qquad (2.50)$$

and

$$\eta^2 (\varphi-\eta) \frac{f}{\psi^{\gamma-1}} = a \qquad (2.51)$$

a, b and c are constants that can be evaluated by applying the boundary conditions at the shock front. c is found to be zero. It was obtained in the original paper by requiring $\varphi(0)$ to vanish in Eq. (2.49). It could also have been obtained by taking $\varphi(1) = 2/(\gamma+1)$. The two are directly equivalent, i.e. taking $\varphi(0) = 0$ will result in $\varphi(1) = 2/(\gamma+1)$ and visa versa. In this case, unlike Taylor's numerical solution, there is no particular virtue in applying one rather than the other. However, it is not a fourth boundary condition as has been stated erroneously at times in the literature. It should also be pointed out that Latter uses a slightly different notation than does Taylor. The F of the former (Latter) is related to the f of the latter

(G.I. Taylor), by

$$F = \frac{f}{\gamma} \qquad (2.52)$$

J.L. Taylor's solutions[31], which was published at the same time as Latter's, is essentially the same, the only different being a matter of notation.

2.2.3 Numerical Solutions of Finite Source Explosions

The numerical solutions for finite source explosions, of which the works of Brode[34,35,36,37,38] are noteworthy examples, require the introduction of an "artificial viscosity", using the method of von Neumann and Richtmyer[39] in order to smooth out the discontinuity at the shock front and to make it amenable to the finite difference technique. With the viscosity term included, the conservation equations for the spherically symmetric case in Eulerian coordinates take the form[30]

$$\frac{\partial u}{\partial t} + u\frac{\partial u}{\partial r} = -\frac{1}{\rho}\frac{\partial(p+q)}{\partial r} \qquad (2.53)$$

$$\frac{\partial \rho}{\partial t} + u\frac{\partial \rho}{\partial r} = -\rho\left(\frac{\partial u}{\partial r} + \frac{2u}{r}\right) \qquad (2.54)$$

$$\frac{\partial p}{\partial t} + u\frac{\partial p}{\partial r} = \frac{\gamma p + (\gamma-1)q}{\rho}\left(\frac{\partial \rho}{\partial t} + u\frac{\partial \rho}{\partial r}\right) \qquad (2.55)$$

where q, the artificial viscosity, is given by

$$q = \tfrac{1}{2} K^2 \; \rho r^2 \; \frac{\partial u}{\partial r}\left(\left|\frac{\partial u}{\partial r}\right| - \frac{\partial u}{\partial r}\right) \qquad (2.56$$

K is an adjustable, multiplicative factor which increases or decreases the effect of the viscosity. The form of the term in brackets is such that for $\partial u/\partial r \geq 0$ the viscosity vanishes. In regions where the wave is spreading naturally, for example, in the rarefaction region behind the blast wave, $\partial u/\partial r$ is positive, q = 0 and the equations reduce to their inviscid form. In compression regions, for example in the shock, the artificial viscosity terms are retained to prevent the wave from steepening and becoming discontinuous. One might expect that the Taylor similarity solution would hold behind the shock, even for cases where viscosity is included. This is not borne out. Latter[30] has obtained similarity solutions for the entire flow field, both upstream and downstream of the shock, for cases where viscosity is retained. The solutions for the region behind the shock, where q = 0, were obtained analytically as noted in Section 2.2.2. The solutions for the compression region through the shock was obtained numerically. Latter found that the inclusion of viscosity effects the entire flow field, including the region behind the shock, but that Taylor's solution is obtained, in the limit as q → 0. Not only are the shock jump conditions altered but also the expansion conditions. While the difference is striking at unreasonably large values of the viscosity parameter K, it is important to note that for small values of K, the difference between Taylor's solution and Latter's solution is not significant.

Pressure and density profiles from spherical explosions for several values of K are shown in Fig. 8. Note that the scale of the distance co-ordinate on the outside of the shock is different from that of the inside in order to clarify the viscosity effects, which are seen to be significant. The density profile, $\psi(r)$, behind the shock front remains essentially unchanged for the range of K considered but for K = 0.349 a peak in density appears ahead of the shock front giving erroneous values for the shock density ratio. The pressure profiles are also altered by the artificial viscosity, the pressures generally increasing as K increases resulting in erroneous values for both the shock pressure ratio and the pressure ratio across the expansion. While the largest values of K shown, gives errors of factors of 2 or more, for the smallest value of K shown, the error is acceptable. Although not shown, the effect on velocity is similar except that the velocity profile is depressed with increasing K. The point made by this important work is that while the artificial viscosity technique makes it possible to solve the equations using finite difference techniques, care must be exercised in selecting the "size" of the viscosity coefficient lest too large a coefficient affect the validity of the results.

Comparison of Some Solutions

It is instructive to compare some of the results of numerical and classical solutions with the experiments as it allows the merits and limitations of each to be assessed. Shown in Fig. 9, which is taken from Glass,[40] is a plot of the overpressure versus the characteristic radius, λ_r, for several different explosions; 1) a numerical point source explosion in perfect air ($\gamma = 1.4$)[38], 2) a numerical point source explosion in real air,[38] 3) the classical self similar solution for $\gamma = 1.4$,[26] 4) a numerical hot sphere finite source explosion[38] 5) a numerical finite source TNT explosion[37] and 6) data from a nuclear explosion[41].

The numerical point source explosions should not be confused with the classical self-similar solution. For these numerical calculations, the energy was added at a point and numerical techniques were used to calculate the resulting flow, in the relevant atmosphere, using the exact equations. However, at high overpressures the classical self-similar solution and the point source explosion are for perfect air indistinguishable. As the shock overpressure decreases on expansion, the classical and the numerical point source solutions diverge, as the assumptions made to obtain the classical solution begin to break down: the shock is becoming weak $p_2/p_1 \sim 10$, the initial pressure ahead of the shock is becoming significant (equivalently, the energy content of undisturbed fluid is becoming significant) and the profiles, as shown in the inserted figures, are no longer self-similar. The numerical solutions ultimately become sound waves which decay as r^{-1}. The numerical point source solution for real-gas air is slightly weaker than the perfect-gas air because energy is used up exciting various internal energy modes of the gas.

The finite source explosions behave much the same as the numerical point explosions, except at high pressures, where the pressures generally fall below the ideal curves. The difference depends on the particular source considered. The hot sphere case (T = 386,000 °K, p = 20,000 atm), follows the ideal curve for overpressures less than $\Delta p \sim 3 \times 10^3$ atm. The hot sphere calculation also shows the effect of secondary shocks which, generated in the initial expansion, implode on the origin, reflect and overtaking the main blast wave, strengthen it. The TNT explosion shows that finite source

14

effects for this case extend to much lower pressures. It does not reach the ideal curve until $\Delta p \sim 10$. The data from the nuclear tests show that the hot gas sphere is a good representation of this type of explosion.

Clearly the classical solution is limited in its application but is a good approximation whenever the blast wave is strong.

2.2.4 Related Explosion Problems

The classical point source explosion problem as treated by Taylor, von Neumann and Sedov, is in fact a special case of a more general explosion problem, albeit that this special case is of more interest. The initial conditions in the unshocked gas ahead of the blast wave, in the Taylor-vonNeuman-Sedov problem are

$$\rho = \rho_o$$
$$p = 0 \qquad\qquad (2.57)$$
$$u = 0$$

In the completely general case, the gas conditions ahead of the blast wave would be known, but arbitrary functions. While the author is not aware of any published attempts at this most general case (its interest would be rather limited) there have been a number of other special cases that have been examined and found to yield self-similar flows. Sedov, for example, has examined the case where the initial conditions are

$$\rho = \text{const } r^{-\omega}$$
$$p = 0 \qquad\qquad (2.58)$$
$$u = 0$$

where, ω may take either positive or negative values. He found that the resulting flow is self-similar. Complete results are given in Ref. 28.

Schindler[42] has investigated the problem where the initial conditions are

$$p = \text{const } r^{-3}$$
$$\rho = \text{const } r^{-2} \qquad\qquad (2.59)$$
$$u = 0$$
$$\Phi_q = \text{const } r^{-1}$$

where, Φ_q is the gravitational potential. The flow quantities, which were self similar, were obtained formally but not explicitly. However, the variation of shock conditions with radius was obtained and found to be

$$p = \text{const } r^{-3}$$
$$\rho = \text{const } r^{-2} \qquad\qquad (2.60)$$
$$u = \text{const } r^{-\frac{1}{2}}$$

The literature contains a few other special cases, for example, variable

15

density conditions related to the change in density through the earth's atmosphere.

A particularily important case from the point of view of the implosion launcher at least, is the explosion (i.e., reflected implosion) in a gas where the initial conditions are

$$p = \text{const. } r^{-\delta}$$

$$u = \text{const } r^{-\delta/2}$$

$$\rho = \text{const}$$ (2.61)

$$\delta = \delta(\gamma)$$

The author knows of no published solution for this case. This is unfortunate since its solution would be of considerable value in the understanding of the conditions left at the origin by the reflected implosion. This case is presently being considered and it is expected that a report covering its solution will be forthcoming in the very near future.

2.3 Similar Solutions for Spherical Implosions

An implosion retains many of the essential features of an explosion, including the compression of the gas and the setting of it in motion in the direction of the shock. The main difference is that the shock is propagating toward the origin with ever increasing strength, rather than away from it in ever decreasing strength as was the situation in the explosion case. Values of η which are now of interest are in the range $1 \leq \eta \leq \infty$ rather than $0 \leq \eta \leq 1$. The same three assumptions that were made in the explosion case will also yield a similar solution for the implosion, except that unlike the case of explosion, only a numerical solution is available at present for the implosion.

The system of equations to be solved has exactly the same form as the explosion system, only that the coefficients of a few of the terms change to reflect the fact that the rate of change of the pressure and particle velocity with radius for an implosion is not the same as for an explosion. Specifically the system of equations to be solved is

$$-\frac{\delta}{2}\varphi + (\varphi-n)\varphi' + \frac{f'}{\gamma\psi} = 0$$ (2.62)

$$\psi\varphi + (\varphi-n)\psi' + (\nu-1)\frac{\psi\varphi}{\eta} = 0$$ (2.63)

$$-\delta f + (\varphi-n)f' - \gamma f\frac{\psi'}{\psi}(\varphi-\eta) = 0$$ (2.64)

which may be compared with Eqs. (2.34) through (2.36). The same boundary conditions at the shock apply. Further for an explosion

$$\delta \equiv \nu \quad ,$$ (2.65)

16

which comes from the requirement that

$$\rho \sim r^{-\delta}$$

(2.66)

but for an implosion, it has been found that

$$\delta = \delta(\nu,\gamma) \neq \nu .$$

(2.67)

The classic work of demonstrating this particular point was done by Guderley[43], who used a series expansion technique for representing the flow near the origin and found the resulting flow to be self similar. He also obtained δ for $\gamma = 1.4$ for both spherical and cylindrical cases, by numerical means. Stanyukovich noted in Ref. 44 that he and Landau obtained a numerical solution for the spherical implosion problem in 1944, however, the original reference was not given. He gives values of δ for $\gamma = 1.0, 1.4, 3.0$ and ∞. Unfortunately only a single significant figure is given so a detailed comparison with the values of others is not possible. Subsequently other values of δ for other cases and gammas have been obtained numerically by Butler[45], for $\gamma = 1.2, 1.4$ and 1.67 and Aiken[46] for $\gamma = 1.67$. Very recently Welsh[47] has recomputed Butler's results and investigated the existence and uniqueness of his solutions. He also calculated δ for $\gamma = 3.0$. These values are compiled in Table 2.

Although no complete analytic solutions for spherical implosions has been obtained to date, progress is being made in this direction at this laboratory. One general equation relating φ, f and ψ has been obtained, which includes the cases $\nu = 1,2,3$ for both implosions and explosions. This equation, the first of a set of three which define the complete analytic solution is

$$\eta^{\nu-1} (\varphi-\eta) f^{\nu/\delta} \psi^{1-\frac{\nu\gamma}{\delta}} = \text{const.}$$

(2.68)

It reduces identically to Latter's result (Eq. 2.51) for $\delta = \nu = 3$. The difficulty in obtaining the other two seems to lie in the energy equation, which in its conventional form diverges because a similar solution exists for an implosion only for infinite energy input. Recall that explosions have a finite energy input. Implosions, by contrast, do not have a finite energy condition.

Partial numerical solutions were available for two cases of interest. For example, for $\gamma = 5/3$ cylindrical and spherical results have been published by Somon, Linhart and Knoepfel[48] and Aiken[46] and $\gamma = 7/5$ by Guderley[43]. However, the published data do not include much of the detailed information required for this present study.

It was necessary for the present problem to obtain additional details for the known cases and to obtain numerical solutions for other values of γ particularly $\gamma > 1.67$, which as stated previously corresponds to explosive products at high densities, and for values of γ near unity which correspond to products of combustion of oxygen and hydrogen. Somon noted that a singularity existed in the range $1 \leq \eta \leq \infty$ which made it difficult to obtain the similarity functions by conventional numerical means. For example, for $\delta = \delta_{exact} + \epsilon$ the numerical code produced one branch of a solution which was non physical, see Fig. 10. For $\delta = \delta_{exact} - \epsilon$ another branch of a solution was obtained which was also non-physical. For $\delta = \delta_{exact}$, in principle a solution could be obtained. On a computing machine, which of necessity must give only an approximation to some value, this last point is not trivial and δ must be known with considerable precision to obtain the correct solutions

for the similarity functions. The precision required is primarily a function of step size, smaller step size requiring more precision in δ. For a step size of η of 0.001 which was used here, 0.1 percent accuracy or better is required to produce accurate solutions for $1 < \gamma \leq 3$. Somon managed to program his routine to integrate through the singularity although no details are given except to note it required "considerable effort". As a side result, he obtained a numerical value of δ for the case in question. He reasoned that the value obtained was the correct one because of the uniqueness of the resulting similarity quantities.

It will be shown below, that from an anlysis of the singular behavior of the implosion equations, an upper limit on δ can be obtained, which is helpful in locating a precise value.

2.3.1 Behavior of the Equations Near the Singularity

The difficulty with the integration is due to a singularity in the equation for f'.

$$f' = \frac{f\ \{-\delta\eta + \varphi[\delta + \gamma\left((\nu-1)-\frac{\delta}{2}\right) - (\nu-1)\frac{\varphi^2\gamma}{\eta}\}}{(\varphi-n)^2 - \frac{f}{\psi}} \quad (2.69)$$

which occurs in the range $1 \leq \eta \leq \infty$. Since the other derivatives, φ' and ψ', can be written in terms of f', any divergence in f' automatically produces divergence in them as well. The equation for f' has two zeros corresponding to points where the numerator vanishes and one singularity corresponding to the point where the denominator vanishes. The denominator vanishes for

$$D_{f'} = (\varphi-n)^2 - \frac{f}{\psi} = 0 \quad (2.70)$$

which is satisfied for

$$\eta_c = \varphi_c \pm \left(\frac{f_c}{\psi_c}\right)^{\frac{1}{2}} \quad (2.71)$$

where the subscript c refers to the value at the singularity. Since $\varphi_c \leq 1$ and $\eta_c \geq 1$ for implosions, only the plus sign has physical significance. The numerator vanishes for

$$N_{f'} = -\delta\eta^2 + \varphi\eta\left[\delta + (\nu-1)\gamma - \frac{\delta\gamma}{2}\right] - (\nu-1)\gamma\varphi^2 = 0 \quad (2.72)$$

Solving for η yields

$$\eta_{z_{1,2}} = \frac{\varphi_c}{2\delta}\left\{\left[\delta + (\nu-1)\gamma - \frac{\delta\gamma}{2}\right] \pm \left[\left(\delta + (\nu-1)\gamma - \frac{\delta\gamma}{2}\right)^2 - 4(\nu-1)\gamma\delta\right]^{\frac{1}{2}}\right\} \quad (2.73)$$

where the subscript $z_{1,2}$ refers to the first and second zero respectively since generally both zeros occur in the range $1 \leq \eta \leq \infty$.

An upper bound on δ can be specified by requiring the two zeros of Eq. (2.73) to be coincident. This results in an analytic expression for $\delta_{max}(\nu,\gamma)$ i.e.,

$$\delta_{max} = \frac{2(v-1)\gamma}{(2-\gamma)^2} \left(2^{\frac{1}{2}} - \gamma^{\frac{1}{2}}\right)^2 \tag{2.74}$$

or inversely in terms of δ

$$\gamma = \left\{ \frac{2\left[(v-1)\delta\right]^{\frac{1}{2}} + 2^{\frac{1}{2}}\delta}{2(v-1) - \delta} \right\} \tag{2.75}$$

for $\delta > \delta_{max}$, the equation has no real zeroes hence a physical solution is not possible.

It is of interest to note that the expression for δ contains a factor $(v-1)$, which for this bound at least, gives values of δ in the spherical case $(v-1 = 2)$ exactly twice the values of δ in the cylindrical case $(v-1 = 1)$. This point has long been suspected, as the ratio of the numerically obtained δ's is very nearly equal to two. Further for the one dimensional case $(v-1 = 0)$, i.e. $\delta \cong 0$. This requirement makes the shock strength a constant, independent of r, a result which can be derived by other means. One can speculate that this $(v-1)$ factor will also appear in the exact expression for δ if such is ever obtained. It is also worth noting that if an analytic expression existed for the implosion problem i.e., $\varphi = \varphi(\eta)$, $f = f(\eta)$, and $\psi = \psi(\eta)$ then an exact value for δ is possible in principle, requiring only the direct substitution of these relations into Eqs. (2.71) and (2.73).

In Fig. 11 the behavior of f' for values of near the exact value, for $\gamma \gtrless 2$ are shown to indicate the cause of the divergence for the approximate value of δ. It can also be seen from the figure that for $\gamma = 2$, $\delta > \delta_{exact}$ that no singularities or zeros occur. A numerical procedure was made which, while integrating the equations from $\eta = 1$ toward $\eta = \infty$ noted the values of η for which the poles and zeros occurred and corrected the value of δ and repeated the integration starting at $\eta = 1$ until the pole and zero coincided to within $\Delta\eta \leq .001$. δ_{max}, as discussed above, was used to aid in the iteration. The results of such a calculation are shown in Fig. 12 and tabulated in Table. 2. From the figure it can be seen that in the region near $\gamma = 2$ the upper bound and the exact numerical values are very close and at $\gamma = 2$, they coincide, ($\gamma = 2$ has only one zero so for this point the analytic representation is exact). Hence, for $1.6 \leq \gamma \leq 2.3$, the analytic relation for δ_{max} can be used as a good approximation to δ. From the table, one notes that the early value reported by Guderley is very precise considering that it was probably done by hand. All of the other values, except Stanyukovich, were obtained using computing machines, and agree among themselves to very high precision. The single exception is Stanyukovich's value for $\gamma = 1$ which at 0.7, disagrees markedly with the vanishing value determined from the present work, but does appear to agree with the present value of δ_{max}. It should be pointed out that "rounding off" errors in the present machine program does introduce an uncertainty in the values of δ for $\gamma \leq 1.2$. However, a complete reversal of the trend with γ would be required to obtain Stanyukovich's value, an unlikely possibility.

A piecewise numerical representation of the present numerical results, which is good within 1.0 percent is

$$\delta = A(\gamma-1)^m$$

where,
$A = 1.000,$ $m = 0.234$ $1.6 \leq \gamma \leq 2.0$
$A = 1.035,$ $m = 0.296$ $1.2 < \gamma < 1.6$
$A = 1.080,$ $m = 0.323$ $1.1 \leq \gamma \leq 1.2$

(2.76)

2.3.2 Numerical Solutions of the Classical Implosion Problem

With precise values of δ available for a wide range of γ, numerical solutions for f, φ and ψ could now be calculated, using the method Taylor applied to the explosion problem. For example, knowing the values at $\eta = 1$ from the shock conditions, Eqs. (2.40) through (2.42) and rearranging Eqs. (2.62) through (2.64) to obtain the derivatives explicitly:

$$f' = \frac{f\left\{-\delta\eta + \varphi\left(\delta + \gamma\left((\nu-1) - \frac{\delta}{2}\right)\right) - (\nu-1)\frac{\varphi^2\gamma}{\eta}\right\}}{(\varphi - \eta)^2 - \frac{f}{\psi}} \tag{2.77}$$

$$\varphi' = \frac{\frac{\delta}{2}\varphi - \frac{f'}{\gamma\psi}}{\varphi - \eta} \tag{2.78}$$

$$\psi' = \frac{-(\nu-1)\psi\varphi/\eta - \psi\varphi'}{\varphi - \eta} \tag{2.79}$$

the numerical integration could proceed from the shock front toward $\eta = \infty$. A numerical code utilizing the above was written, using a step size of 0.001 for $\eta < 3$, and progressively larger values for $\eta \geq 3$. This step size was arrived at as a practical compromise entailing computing time considerations and accuracy after trying a range of values. The results are plotted in Figs. 13, 14, 15, 16 and 17 for values of $\gamma = 1.2$, 1.4, 1.67, 2.0, and 3.0 respectively, for $\nu = 3$. The values for $\gamma = 1.2$, 1.4, 2.0 and 3.0 have not been published previously. Complete graphical and tabular results for an extensive range of γ is expected to be published in the near future.

The properties of the implosion wave can be seen clearly from the figures. The conditions at $\eta = 1$ are fixed by the shock jump requirements (Eqs. 2.40, 2.41, and 2.42). Initially the pressure behind the shock increases as η increases, then decreases to asymptotically approach the value

$$f = f_\infty(\gamma)\ \eta^{-\delta} \tag{2.80}$$

For values of gamma nearest unity, the increase in the pressure behind the imploding wave is greatest, decreasing as gamma increases. For $\gamma \sim 2.57$ the slope of the pressure profile at the shock has vanished i.e., $f'(1) = 0$ and for $\gamma > 2.57$, $f'(1) < 0$, hence the pressure begins to decrease immediately behind the shock with no peaking. The velocity behaves in a somewhat analogous fashion, except for the peaking, decreasing monotonically as η increases. As η becomes large, φ asymptotically approaches the value

$$\varphi = \varphi_\infty(\gamma)\ \eta^{-\delta/2} \tag{2.81}$$

The density, contrary to the explosion case, increases behind the shock for all values of γ less than infinity, approach, as $\eta \rightarrow \infty$

$$\psi = \psi_\infty(\gamma) \tag{2.82}$$

Note that not only does $\psi \rightarrow \infty$ as $\gamma \rightarrow 1$, but also $\psi_\infty/\psi \rightarrow \infty$ as $\gamma \rightarrow 1$. Values of f_∞, ψ_∞ and φ_∞ are plotted as functions of the ratio of specific heats in

Fig. 18 and are tabulated for convenience in Table 3. The only other values, of these quantities that have been published are values of ψ_∞, for $\gamma = 1.67$ from Ref. 48 and for $\gamma = 1, 1.4, 3$ and ∞ from Ref. 44, which are included in Table 3. They are essentially in agreement with the present results, with the exception of Stanyukovich's value for $\gamma = 1$, which as noted previously also gave a different value for δ. He obtained $\psi(\infty)/\psi(1) = 2.72$. The present work gives $\psi(\infty)/\psi(1) = \infty$.

An important feature of implosions is that the thermal and kinetic energy per unit volume, after a transient region, decreases as $\eta^{-\delta}$. This rate of decrease with η is not sufficient to make the total energy, which is given by

$$\int_1^\infty \left(\frac{f}{(\gamma-1)\gamma} + \frac{\psi\varphi^2}{2} \right) \eta^2 d\eta \qquad (2.83)$$

bounded, hence no total energy can be specified in the classical implosion problem, unlike the classical explosion problem which contains a fixed amount of energy. The ratio of internal energy to kinetic energy between the shock front and a shell at η is given by

$$\lambda = \frac{4\pi \int_1^\eta \frac{f}{\gamma(\gamma-1)} \eta^2 d\eta}{4\pi \int_1^\eta \frac{\psi\varphi^2}{2} \eta^2 d\eta} \qquad (2.84)$$

This ratio starts at the shock front with a value[19]

$$\lambda_s = 1 \quad \text{for} \quad \eta = 1 \qquad (2.85)$$

for all values of the ratio of specific heats and all values of ν since it is essentially a consequence of equipartition of energy behind the shock, and because of the asymptotic behavior of f, ψ and φ, which dominates the integral and negates the contribution near the shock front, the ratio approaches a constant as $\eta \to \infty$

$$\lambda_\infty = \frac{2}{\gamma(\gamma-1)} \frac{f_\infty}{\psi_\infty \varphi_\infty^2} \quad \text{for} \quad \eta \to \infty \qquad (2.86)$$

The ratio of internal energy to total energy is a quantity which will be of use later. It is given by

$$\Lambda = \frac{\lambda}{\lambda+1} \qquad (2.87)$$

Because λ increases from unity to asymptotically approach λ_∞ as the integration proceeds from $\eta = 1$ to $\eta = \infty$, Λ also has the same behavior going from $\Lambda = 0.5$ at the shock front to Λ_∞ (γ) as $\eta \to \infty$. Which value to use in a particular problem will depend on whether η is clearly large, in which case Λ_∞ is dictated or if η_{max} is known, as a function of r say, in which case Λ based on λ from Eq. (2.83) is to be preferred.

21

2.4 Implosion in a Sphere

In the preceding sections it has been shown that the self-similar implosion problem is solved in the sense that the self-similar flow properties are known for all implosions. While these self-similar solutions are very helpful in giving insight into the implosion phase of the problem, there are many additional features of the particular problem of an implosion inside a sphere, which are not available from the classical solution. For example, the classical solution shows that the velocity vanishes at infinity. For the implosion in a sphere, the velocity must vanish at the wall. Further, while the classical solution does not permit a limit on the total energy, the total energy for an implosion in a sphere is both fixed and finite. The dynamics of any driving gas, for instance the products of detonation of the explosive for the case at hand, which are driving the implosion, are not accounted for explicitly. Also, the later history, such as the reflection from the origin, the reflection from the sphere wall and subsequent cycling, are not available from the classical theory in its present form. Of all the limitations of the classical implosion, it is felt that the infinite total energy is the most serious, and an effort to account for this in an approximate way is made in Sec. 2.4.1.

An effort has been made by the author to obtain an exact self-similar solution for an implosion in a sphere, as yet unsuccessfully. The main task is to find an analytic representation for the "finiteness" of the implosion which would allow the reduction of the nonlinear partial differential equations to ordinary differential equations. To date none has been found, although a number of different functions have been tried. While it cannot be stated conclusively that a self-similar solution does not exist, the possibility of existance of a solution does not look too promising at this time.

In the following section, an attempt will be made to construct a model which approximates the character of an implosion in a sphere by accounting for the finite energy input, while retaining a self-similar-like character for the flow. This model will then be examined to obtain as much useful information as possible, particularly as it pertains to the launcher problem, as well as to determine the limits of the models usefulness. The results will be compared with the results of numerical experiments for several cases of implosions in spheres. The agreement will be seen to be generally satisfying although several points are not treated rigorously.

2.4.1 A Model of an Implosion in a Sphere

Consider the case of a sphere of radius R_0 containing a gas at rest. On the inside surface of the sphere is assumed to be released, uniformly and instantaneously, an amount of energy E_{total}, or an amount of energy per unit volume of sphere E_V, where E_V and E_{total} are related simply by

$$E_V = \frac{E_{total}}{\frac{4}{3} \pi R_0^3} \tag{2.88}$$

The energy originally contained in the gas at rest is assumed negligible compared with E_{total}. In Sec. 2.3.2 it was noted that the total energy per unit volume behind the imploding shock approaches a value given by const x $(r/r_s)^{-6}$ or r/r_s large. It is assumed for this model that the energy per unit volume distribution behind the imploding shock is given by

$$\epsilon = \epsilon_{peak} \left(\frac{r}{r_s}\right)^{-\delta} \qquad (2.89)$$

where ϵ_{peak} is just the value of the energy immediately behind the shock front. This is equivalent to taking the pressure, particle velocity and density distributions given by Eqs. (2.80), (2.81) and (2.82).

We ask, what are the absolute values of the energy profile behind the shock as the shock implodes toward origin? Conservation of energy requires that this energy distribution, integrated over the entire spherical volume, be equal to E_{total}, that is to say:

$$4\pi \int_{r_s}^{R_o} \epsilon_{peak} \left(\frac{r}{r_s}\right)^{-\delta} r^2 dr = E_{total} = E_v \frac{4}{3}\pi R_o^3 \qquad (2.90)$$

By straightforward integration the peak energy density is determined to be:

$$\epsilon_{peak} = \frac{3-\delta}{4\pi} \frac{E_{total}}{R_o^3} \frac{(r_s/R_o)^{-\delta}}{1-(r_s/R_o)^{3-\delta}} \qquad (2.91)$$

or

$$\epsilon_{peak} = \frac{3-\delta}{3} E_v \frac{(r_s/R_o)^{-\delta}}{1-(r_s/R_o)^{3-\delta}} \qquad (2.92)$$

(In passing, note that if this had been done for an arbitrary value of ν, there would have been obtained instead

$$\epsilon_{peak} = \frac{\nu-\delta}{\nu} E_v \frac{(r_s/R_o)^{-\delta}}{1-(r_s/R_o)^{\nu-\delta}} \qquad (2.93)$$

It follows that the energy profile at any position r, for $r_s \leq r \leq R_o$, is

$$\epsilon = \frac{3-\delta}{3} E_v \frac{(r/R_o)^{-\delta}}{1-(r_s/R_o)^{3-\delta}} \qquad r_s \leq r \leq R_o \qquad (2.94)$$

Equation (2.92) has singularities at $r_s = 0$, and R_o and a minimum at

$$r_{s_{min}} = \left(\frac{\delta}{3}\right)^{1/(3-\delta)} \qquad (2.95)$$

The behavior of Eqs. (2.92) and (2.94) with r and δ can be seen in Figs. 19 and 20 where they are plotted for $\delta = 0$, 1 and 2, in linear coordinates and log coordinates respectively. It can be seen from the figures that the assumed profile has a very strong influence on the magnitude and shape of the peak energy curve. The peak values increase as the profile becomes more peaked i.e., as δ becomes larger. It can also be seen that relatively low values of peak energy are obtained during the wide "mid"-region when $r \sim R_o/2$, and that the highest values of energy are concentrated at the sphere surface and in a relatively small region $r/R_o \sim 0.1$, around the origin. While the logarithmic plot shows clearly the asymptotic behavior of the peak energy density, the linear plot is included to show graphically the very limited region over which the high energy densities exist.

However, pressure rather than energy is the quantity of interest. In Sec. 2.3.2 it was shown that the ratio of internal energy to total energy for a self-similar implosion approaches a constant Λ_∞ for $\eta \to \infty$. If a caloric equation of state is assumed i.e.,

$$e_{int} = \frac{p}{(\gamma-1)\rho} \qquad (2.96)$$

where e_{int} is the internal energy per unit mass, and combining Eqs. (2.87), (2.94) and (2.96), the pressure can now be expressed in terms of r and r_s for the initial conditions R_0 and E_{total} (or E_V)

$$\tilde{p} = \frac{3-\delta}{3}(\gamma-1)\Lambda \; E_V \; \frac{(r/R_0)^{-\delta}}{1-(r_s/R_0)^{3-\delta}} \qquad (2.97)$$

It follows that the shock pressure as a function of shock position is

$$p_s = (\gamma-1) \; \frac{3-\delta}{3} \; \Lambda E_V \; \frac{(r_s/R_0)^{-\delta}}{1-(r_s/R_0)^{3-\delta}} \qquad (2.98)$$

Knowing the shock pressure as a function of position, it is possible to determine the time required for the shock to move from $r = R_0$ to $r = 0$. Assuming a strong shock, Eq. (2.9), and using the definition of M_s, the peak pressure and shock velocity are related by:

$$\frac{p_s}{p_1} = \frac{2\gamma}{\gamma+1} \; U_s^2 \; a_1^2 \qquad (2.99)$$

Combining Eqs. (2.98) and (2.99) to eliminate p_s, gives

$$U_s = \left\{ \frac{\gamma+1}{2} \; \frac{(\gamma-1)}{a_1^2} \; \Lambda \; \frac{E_V}{p_1} \; \frac{3-\delta}{3} \; \frac{(r_s/R_0)^{-\delta}}{1-(r_s/R_0)^{3-\delta}} \right\}^{\frac{1}{2}} \qquad (2.100)$$

But

$$\frac{dr_s}{dt} = U_s(r_s)$$

or $$\qquad\qquad (2.101)$$

$$\frac{dr_s}{U_s(r_s)} = dt \; .$$

Combining Eqs. (2.100) and (2.101) and integrating, the time required to reach a point r is given by

$$t = \int_{R_0}^{r} \frac{1}{a_1} \left[\frac{(\gamma-1)(\gamma+1)}{2\gamma} \; \Lambda \; \frac{E_V}{p_1} \; \frac{3-\delta}{3} \; \frac{(r_s/R_0)^{-\delta}}{1-(r_s/R_0)^{3-\delta}} \right]^{-\frac{1}{2}} dr_s \qquad (2.102)$$

24

hence the implosion phase time, t_{imp}, is given by

$$t_{imp} = \frac{R_o}{a_1} \left[\frac{6\gamma}{(\gamma+1)(\gamma-1)(3-\delta)} \quad \frac{P_1}{E_v} \right]^{\frac{1}{2}} \Phi(\delta)$$

where

$$\Phi(\delta) \int_1^0 \left\{ (1-\zeta^{3-\delta}) \, \zeta^\delta \right\}^{\frac{1}{2}} d\zeta \qquad (2.103)$$

and

$$\zeta = \frac{r_s}{R_o}$$

$\Phi(\delta)$ is tabulated in Table 7 and plotted in Fig. 21. It is seen to take values between 0.4 and 0.6 for values of δ of common interest. It is also worthwhile to determine

$$t = \frac{\displaystyle\int_\zeta^0 \left\{ \left(1-\zeta^{3-\delta}\right) \zeta^\delta \right\} d\zeta}{\Phi(\delta)} \qquad (2.104)$$

for values of ζ_o since this gives the details of trajectory in the non-dimensional r-t plane. Equation (2.104) is plotted in Fig. 22 for $\gamma = 1.1$ and 3. Note that there is very little difference between these two curves. The slope of the curves vanishes at $r/R_o = 1$ indicating infinite velocity at the sphere surface. The imploding shock wave then slows down and traverses most of the sphere at nearly constant velocity, increasing in velocity again as $r/R_o \to 0$, reaching the origin with infinite velocity. As a rough approximation, a linear fit i.e., $r = Kt$, could be assumed for most of the trajectory.

Since the array of constants inside the square root bracket of Eq. (2.103) are essentially all functions of γ, which is held fixed for any given calculation, they could be lumped together in a single constant, simplifying the time for implosion expression to:

$$t_{imp} = K(\gamma) \frac{R_o}{a_1} \left(\frac{E_v}{P_1} \right)^{-\frac{1}{2}} \qquad (2.105)$$

where

$$K(\gamma) = \left[\frac{2\gamma}{\gamma+1} \quad \frac{3}{3-\delta} \quad \frac{1}{\gamma-1} \quad \frac{1}{\Lambda} \right]^{\frac{1}{2}} \Phi \qquad (2.106)$$

If the problem under consideration is such that a single value of γ is sufficient to characterize the entire flow then values of $K(\gamma)$ shown in Fig. 23, can be used. They show that $K(\gamma)$ decreases with increasing γ and is singular at $\gamma = 1$. The values of $K(\gamma)$ calculated lie in a straight line when plotted in logarithmic coordinates. The curve

$$K(\gamma) = 0.795 \, (\gamma-1)^{-0.757} \qquad (2.107)$$

can be used to fit the calculated points with good precision. (For some problems, as will be discussed in the next section, a single value of γ does not characterize the problem and Eq. (2.106) is no longer applicable.)

Before leaving this section, the limitations of this model should be pointed out. By assuming that the limiting similarity profiles hold, the details of the flow immediately behind the shock front are obscured. More importantly the three conservation equations are violated there, hence it should be clear that this is not a rigorous model. Further the finite velocity at the sphere surface has not been accounted for. Initially, when the shock front has propagated only a small distance from the sphere wall, the error from this source will be very large, since the high pressures in this region imply high particle velocity at the sphere surface, which is physically unacceptable, (except for special cases like detonating explosive liners). Later, as the shock approaches the origin region, this error will decrease considerably but will remain finite. The only justification in allowing these physical inconsistancies, is that to remove them would require discarding the model. However, the region of prime interest, i.e., near the origin, will be least affected by these limitations. It is felt that to discard the results obtained from the model because of these faults, would be a mistake, especially when, as will be seen in the next section, this model gives very good predictions for cycle time, trajectories and peak pressures and particularly, since there is nothing better to replace it with at present. It is hoped that further work on the implosion in a sphere problem will subsequently improve this situation.

2.5 Numerical Experiments of Implosions in Spheres

It was recognized early in the program that fairly extensive numerical experiments would have to be performed to provide the details of the dynamics of the flow inside the sphere, particularly since there existed at that time, no body of knowledge either theoretical or experimental for explosive driven implosions in a sphere. Dr. H.L. Brode of the Rand Corporation, who has made many significant contributions in the field of numerical calculations of finite source explosions using detailed equation of states, was contacted and agreed to do several implosion calculations based on parameters thought to be representative at that time. His numerical scheme is very comprehensive and complex but in its essentials, integrates numerically a set of finite difference equations derived from the non-linear partial differential equations of mass, momentum, and energy in Lagrangian form. These are [34,35]

$$\text{mass :} \qquad \frac{1}{\rho} = \frac{1}{3} \frac{\partial r^3}{\partial m} = v \qquad\qquad (2.108)$$

$$\text{momentum:} \qquad \frac{\partial u}{\partial t} = - r^2 \frac{\partial}{\partial m} (p+q) \qquad\qquad (2.109)$$

$$\text{energy:} \qquad \frac{\partial e}{\partial t} = - (p+q) \frac{\partial u}{\partial t} + q \qquad\qquad (2.110)$$

where,

$$u = \frac{\partial r}{\partial t}$$

$$m = \frac{1}{3} \rho_1 R_o^3$$

26

and R_o is the initial position of the Lagrangian surface, with an equation of state,

$$e = e(T,v) \qquad p = p(T,v)$$

or

$$p = p(e,v) \qquad T = T(e,v)$$

$$(2.111)$$

subject to prescribed boundary conditions. Implosions and explosions can be handled with equal ease with his code. The discontinuities at the shock or detonation wave fronts are smoothed out and made amenable to finite difference calculations by using the artifical viscosity technique of von Neumann and Richtmeyer[39].

Detailed calculations for three cases[49] covering a spectrum of values of parameters were done. They include the following: Case 1. This case is the most representative of the prototype in terms of gas initial pressures and explosive yield. A sphere of radius 20 centimeters was assumed filled with a mixture of $2H_2+O_2+7He$ at 100 psi and lined with a 0.1 inch layer of TNT. A gamma law gas was assumed with $\gamma = 1.67$. A real gas calculation for this mixture at 100 psi gives $\gamma = 1.26$ for conditions immediately behind the detonation wave[50], hence care must be taken in the interpretation of the results especially for phenomena where gamma effects are pronounced. The equation of state for the gas was taken as

$$E = 19.5495\,T$$

$$p = 13.033\,T/v$$

where

T is in 10^4 °Kelvin

v is in $cm^3/gram$

$$(2.112)$$

p is in 10^{10} ergs/cm^3

E is in 10^{10} ergs/gram

A detonation wave velocity of 2.70 mm/μsec was programmed. It is ~ 30 percent lower than the accepted real gas value (3.87 mm/μsec).[50] The TNT liner was assumed to have a density of 1.5 grams/cc. The numerical representation taken for the explosive was

$$E = \frac{7.73 \times 10^{-3}T}{8.5 \times 10^{-4}+T^4} + 1200\,T^5$$

$$p = \frac{2.556\,T}{v}\left\{1 + \frac{T^5}{10^{-4}+0.141\,T^5}\right\}\sum_0^5 a_i T^i$$

where

$a_o = 1.14966$

$a_1 = 10.9575$

$a_2 = -288.237$

$a_3 = 2343.39$

$a_4 = -7799.83$

$a_5 = 9236.55$

$$(2.113)$$

where, E, T, P and v are in the same units as in the gas equation of state. This relation follows somewhat the TNT calculations of Jones and Miller[51] with

modifications.[37] A detonation wave velocity of 7.2 mm/μsec was programmed and an energy yield of 4.6037 x 10^{10} ergs/gram (1.095 kcal/gram) was assumed. Output details are available from the instant of initiation at the origin through one complete chamber cycle but terminate two output cycles after implosion, as shown schematically in Fig. 24. This was unfortunate since the conditions at the origin, after the implosion, are those which determine the launcher performance. Hence, while the chamber processes are available in considerable detail, the complete outputs necessary for computing launcher performance are not. It is necessary to assume that the same type of behavior after implosion holds for this case, as was obtained for the other two cases. In short this case is an accurate explosive model with a gamma law gas model, for a representative initial pressure. The radius chosen is a factor of two larger than the present prototype. Case 2 . A sphere of radius 20 centimeters was assumed filled with a stoichiometric mixture of hydrogen and oxygen at 1000 psia and lined with a 0.1 inch layer of COMP B, which is the accepted nomenclature for a 60/40 mixture of RDX/TNT. The equation of state taken for the gas was essentially an extrapolation of the real gas calculations of Moffatt[52]. The numerical representation used was

$$E = 6.57pv + \frac{974.0(pv)^2}{1140.0 + (pv)^4} - \alpha \left[0.101 \times 10^{-3} \text{ Ln } \frac{p}{1.013 \times 10^3} \right.$$

$$\left. - 0.2325 \times 10^{-3} \right]$$

(2.114)

where

$\alpha = 0$ for $pv \leq 1.0465$

$= 8600 \, pv - 9000$ for $1.0465 < pv \leq 3.488$

$= 21.0 \times 10^3$ for $3.488 < pv$

Temperature was not calculated, but presumably could be obtained from other state variables. A detonation wave velocity of 2.7 mm/μsec was programmed which agrees reasonably well with the accepted value of 2.9 mm/μsec.[50] The density of the explosive liner was taken as 1.5 grams/cc. The numerical representation of the equation of state for COMP B was taken as

$$p = \left(\frac{0.01 + 1.77 \, \rho^4}{0.03125 + \rho^4} \right) \rho E$$

(2.115)

$$T = \frac{pE}{45.23 + \frac{10x^3}{91.14 + x^3}}$$

where

$$x = 10(v - 0.4)$$

A detonation wave velocity in the explosive of 8.0 millimeters per micro second was programmed and an energy yield of 4.13 x 10^{10} ergs/gram (0.989 kcal/gram) was assumed. In short, this was an accurate gas and explosive model for a gas loading higher than what is presently anticipated and with a chamber radius a factor of two larger than the prototype.

Detailed results are available from the instant of ignition through one complete cycle, through the collision of the reflected imploding wave with the contact surface and the subsequent implosion of the wave reflected

from that collision, or nearly two complete cycles. Case 3. A sphere of radius 10 cm. was assumed filled with a mixture of a gamma law gas ($\gamma = 5/3$). The composition was assumed to be $2H_2+O_2+7He$ and an equation of state identical with that used in Case 1, was used. No explosive was programmed.

Detailed results are available from a time, slightly after the reflection of the outward propagating spherical detonation wave with the spherical surface, through a reflection at the origin, to after the reflection from the spherical surface a second time and propagation to $r \sim .25 R_0$, i.e., in all, a little less than one and one-half complete cycles. Less detailed graphical results for a few parameters are available for several cycles.

The initial conditions for these three cases are summarized in Table 5 and the range of the outputs are shown schematically in Fig. 24. The output consists of 460 pages of computer-printed material including, at fixed instants of time, the following quantities: cell position, velocity, mass, internal energy, temperature (except for the gas in case 2), density, pressure, kinetic energy, an artificial viscosity parameter as well as a number of indicies concerned with the internal machinations of the program such as stability conditions etc.

The results of these three cases, which can accurately be called "numerical experiments", contain a very large amount of useful and revealing information and have been of inestimable value in the understanding of the wave processes inside the chamber. These results will now be examined in detail, starting with the general trajectories, then progressing through the character at the explosive-metal interface, the implosion phase and its subsequent reflection and the conditions left at the origin by the reflected implosion wave, to uncover the physical principles governing the behavior of the waves.

It is very important to keep in mind in the discussions that follow, the fact that the artificial viscosity technique was used in the calculation of these numerical results. Its inclusion, while making the results possible, introduces a spreading out of the steep fronts, and a subsequent reduction of peak quantities. It is imperative to keep these points in mind in order that phenomena which can be properly classified as "computational effects" can be separated from the true physics of the problem.

2.5.1 <u>Phases of the Implosion Driving Cycle</u>

In order to obtain a suitable perspective, the various phases of the implosion driving cycle will first be examined in the large. Consider Fig. 25, which is a plot of the major wave front locations as a function of time as obtained from the numerical printout for the simplest case, Case 3 - the gas case. A gaseous detonation wave, denoted by D, which was initiated at the origin, propagates outward and reflects from the sphere wall at $r = 10$ cm. An imploding shock wave denoted by S_{imp} then propagates toward the origin, increasing in strength and velocity as noted by the curvature of the trajectory near the origin. It then reflects and propagates outward as an exploding shock denoted by S_{exp}. The shock subsequently continues reflecting and imploding ad infinitum until dissipated. The character of the cycles is very clear for this case as, unlike the explosive driven cases, only one gas is present in the chamber.

29

Consider next the TNT driven case - Case 1, shown in Fig. 26.
The trajectories are somewhat similar to the last case, except that the explosive-driven, imploding shock, as evidence by its greater velocity, is very much stronger. Further, a contact surface separating the driven gas from the products of detonation of the explosive, now appears. It is of interest to note, that to a very good approximation, the contact surface is moving at nearly constant velocity.

The first of many "computational effects" is seen in this figure. It appears that the explosive detonates about 9 microseconds prior to the arrival of the gaseous detonation wave at the explosive surface, which is physically impossible. In the calculations, it was assumed that the detonation wave in the explosive initiated after a threshold pressure was reached at the explosive-gas surface. The detonation wave then propagated toward the wall at constant velocity. Plotted in the figures as the "detonation wave location" are the loci of the maximum pressure points of the gaseous detonation wave. As the artificial viscosity spreads the peak out over several zones, the pressure profile actually extends several centimeters ahead of the maximum pressure location. The threshold pressure chosen was such that the reflection of the leading edge of the wave was sufficient to reach it, hence the detonation wave in the explosive initiates prior to the arrival of the peak of the gaseous detonation wave. In retrospect it would have been better to have had a higher threshold pressure to produce a more realistic timing. However the pressures generated at the explosive gas interface were not known, a priori, and a low enough value was chosen to insure that the calculation of the detonation wave would proceed. It should be carefully noted that this is a computational effect and has no resemblance to the physical situation in a real case. It will be shown in fact, in Sec. 4, that just the reverse happens. The gaseous detonation wave reflects from the explosive and begins propagating toward the origin. After a delay, of typically several microseconds, the explosive detonates. The detonation wave then propagates through the explosive and colliding with the chamber wall, reflects as a shock, moves back through the expanding gas products and overtakes the shock that is being driven ahead of the explosive products. This occurs in a time scale, small enough that the details would be obscured here. In practice, one can assume nearly instantaneous initiation of the detonation wave with little error. The combined shock wave then propagates toward the center decaying first as the finite energy of the explosive requires r^{-1} decay and then increases in strength and velocity as the shock wave becomes truly a spherical implosion wave. Reflecting from the origin, it moves into a strong counter flow. The calculations were terminated shortly after reflection for this case so the details of the subsequent flow are unknown.

Plotted in Fig. 27 are the results of Case 2 (1000 psi - COMP B). For this case the calculations were extended in time and the details of the later flow are evident. The reflected implosion wave propagates outward toward the wall, but collides with the contact surface, which has been following the imploding shock. This collision generates a transmitted wave, which continues toward the wall, and a reflected wave, which returns to the origin. Another wave whose origin is not clear also appears in the flow. Whether this wave is a "computational effect" or a physical fact cannot be determined from the present data. It should be noted that "computational effects" are evident at the time of the initiation of the explosive as before, and at the intersection of the reflected shock and the contact surface in that the two

30

"peaks" never collide. It should also be noted, that for the bulk of its trajectory, the contact surface moves at nearly constant velocity. From one point of view, the interior gas in an explosive driven case is being driven by a nearly constant velocity, spherically imploding piston, as will, a priori, be expected to behave differently from the usual free (undriven) implosion wave behavior. It will be seen later that this is borne out.

2.5.2 Character of the Process at the Explosive-Metal Interface

It is of interest to know the details of the behavior of the flow at the explosive-metal interface, as an understanding of the processes involved will allow estimates to be made of the loading at the wall and in turn permit rational estimates to be made of the depth of plastic flow, say for protective liners. Further these processes dominate the dynamics of the imploding shock initially.

The pressure-time histories at the interface for the two explosive cases are shown in Fig. 28. From the figure it can be seen that the thin layer of explosive behaves as if it were in a one-dimensional frame, i.e, the pressure at the explosive-metal interface varies as $t^{-2/3}$, as predicted for the origin conditions by ideal plane explosion theory. Deviations from this behavior are due to the fact that the data are for a finite-source, plane explosion rather than the ideal plane explosion. The most serious deviation from the ideal theory occurs for Case 2, for times less than one microsecond. The pressures at $t \sim 0.1$ μsec are $\sim 2 \times 10^6$ psi and then the pressure falls rapidly to adjust to the $t^{-2/3}$ - law. This behavior is to be expected since the pressures for a finite source explosion are limited, for vanishing times, to at least less than those produced behind a reflected detonation which for this case is $\sim 6 \times 10^6$ psia. For an ideal explosion the pressures approach infinity as t approaches zero a situation which cannot occur in reality. For times large enough that the details of the source of the explosion are obscured, the behavior should and does approach that of the ideal source. At shorter times, a transition type behavior, connecting in a smooth fashion the maximum pressure of the finite source explosion with the ideal curves is expected and observed. Recall this type of behavior was also seen for finite sources in the spherical case, (see Fig. 9,for example).

One also notes from Fig. 28, that the two ideal approximations to the curves are spaced apart by a factor of ~13. For an ideal plane explosion, the absolute pressure as a function of time, is given by

$$p = K \frac{E_{total}}{\rho} t^{-2/3} \qquad (2.116)$$

i.e., the pressure at a given instant of time varies directly as E_{total}/ρ. For the two cases under consideration a representative value of ρ is difficult to determine exactly, since the density profile varies over the outer half of the sphere. The density in the center region well ahead of the imploding shock is, for Case 2, $\rho = 1.28 \times 10^{-4}$ grams/cc, and for Case 1, $\rho \sim 1.2 \times 10^{-3}$ grams/cc. As noted in Sec. 2.5 the explosive energies as for the two cases are slightly different (by a factor of 1.11), therefore the two curves should be spaced apart by a factor of 11.8. The measured spacing is 13, approximately 10 percent greater. Considering the differences and non ideal nature of the two cases this disagreement is reasonable.

In retrospect, the fact that the explosive does generate a plane type of flow is not surprising, when one recalls that the thickness of the explosive is very small compared to the radius of the sphere. For the above cases

$$\frac{d}{R_o} = \frac{0.254}{20.0} = 1.27 \times 10^{-2} \qquad (2.117)$$

If the thickness of the explosive were increased tenfold or more, one would expect phenomena at the interface would take on more of a spherical character. However it is doubtful that explosive liners greater than ~ 0.5 inches will be used in practice.

The effective value of gamma of the explosive products, which will be used subsequently, can also be determined from the data. In Fig. 29 the variation of pressure with density is plotted for the expanding products of detonation of the TNT and COMP B explosive liners. The slope of the curves in this plane is the effective gamma of the explosive at that state. Gamma in this sense is not the ratio of specific heats but rather the isentropic exponent, a characteristic that relates the pressure and density in the equation

$$p = const \ \rho^{\gamma_e} \qquad (2.118)$$

From the figure it can be seen that the accurate numerical description used in the calculation of the gas state of the products of detonation of the explosives does not permit a single value of gamma to be assigned to the explosive over the range shown here. The slopes vary from a minimum of approximately 0.6 to a maximum of approximately 2.0. A rough approximation for the range shown would be $\gamma_e \sim 1.2$. For explosives at very high densities, isentropic exponents of the order of 3 [53,54] are not uncommon. Clearly this is not the case here. The important points that are made are: 1) that gamma is not high, but moderately low ($\gamma \sim 1.2$), 2) gamma is not constant. These two points will have a strong bearing on arguments made in the next section.

2.5.3 Implosion Phase

After the explosive detonates or the gaseous detonation wave reflects from the outside wall, an imploding shock wave is generated which increases in strength as it approaches the origin. During this phase the conditions at the origin ahead of the shock wave remain constant, the high pressures and temperatures which act on the projectile occur after reflection of the imploding wave. However, an understanding of the implosion phenomena is a prerequisite to the understanding and prediction of the origin conditions after reflection.

While all of the gas properties are changing simultaneously during the implosion, for purposes of organization, the pressure, density and temperature profiles and history and the trajectories will be discussed separately in that order.

Pressure Profiles

Classical implosion theory, which does not include any finite radius effects, predicts that the peak pressure should vary as $r^{-\delta}$. The actual peak pressures attained in the imploding wave are plotted in Fig. 30 as a function of radius for the three cases. For the explosive cases, it is seen that the pressure drops several orders of magnitude during the first few centimeters of inward travel as the effects of the finite amount of energy in the liner are felt and planar flow properties predominate. The pressures then begin to level off approximately midway between the outside wall and the origin and then approach a self-similar type of behavior as they implode toward the origin. A somewhat similar pattern is followed by the gas case, except that the very high pressures generated at the outside wall by the explosive do not exist. For the gas case the slope of the peak pressure curve in logarithmic coordinates approaches a value of 0.905 during the latter part of the implosion phase as predicted by the classical implosion theory for $\gamma = 1.67$. This is to be expected since no exterior driving force is present in the problem and the origins of the imploding wave become obscured near the sphere center.

The explosive driven cases behave quite differently. In the absence of any external driving force one would expect the limiting slopes to be 0.9054 and 0.5719 corresponding to $\gamma=1.67$ and $\gamma = 1.14$, (see Table 2), for cases 1 and 2 respectively. It is seen that the slopes are both 1.21, which if taken literally corresponds to $\gamma = 4.0$. While some explosives do behave initially as if gamma were quite high ($\gamma \sim 3$)[53], as the detonation products expand, γ decreases leveling off at values near $\gamma \sim 1.2$. It was shown in Sec. 2.5.2 that even for the densest regions of the TNT and COMP B liners, gamma never exceeded 2. Clearly the observed behavior is not dependent on any gamma effects of the explosive, and is independent of any effects predicted on the basis of the gamma of the driven gas alone.

It is hypothesized that the observed behavior can be ascribed to the effects of an "imploding piston". Recall from Figs. 26 and 27, which showed the trajectories of the shock and contact surface, that, as a first approximation, the contact surface separating the driven interior gas from the driving products of detonation of the explosive, moves at nearly constant velocity. This surface can be considered as the forward face of a piston moving at the contact surface velocity, since there is no mass flux across it. It is to be expected that the flow produced in front of an imploding piston would behave quite differently from the flow produced by a stationary piston, in much the same manner that a spherically expanding piston produces a flow that behaves differently than the classical explosion flow (effective piston velocity = 0). (The spherically expanding piston problem was also solved by G.I. Taylor[54]). Unfortunately, to the author's knowledge, the spherically contracting piston problem has not been solved. Its solution would shed much light on the dynamics of the implosion wave in the cases where explosives are present.

Also plotted on Fig. 30 is the predicted values of pressure calculated using the "implosion in a sphere model", Eq. (2.92). For the gas case, δ is taken as 0.9054 as suggested by both classical implosion theory and verified by the numerical experiment. It is seen that the comparison in the gas case is very good and that the model does allow the prediction of the peak pressure profiles. For the explosive cases the use of Eq. (2.92), is not valid since there are two gases with different properties to be considered. However, the shape of the profile can be predicted from the terms in Eq. (2.92) contain-

33

ing r_s/R_0 only. δ was taken to be 1.21, as obtained from the plot itself, and as can be seen from the figure, the profiles based on this value of δ show rather good agreement with the data.

If the remaining terms in Eq. (2.92), containing gamma effects, are evaluated based on the gamma of the driven gas, and a comparison is made of the predicted and the numerical results, then the agreement is not very good, the difference being factors of 1.34 and 0.35 for cases 1 and 2 respectively. Basing gamma on an effective value of gamma for the explosive products, $(\gamma \sim 1.2)$ is also unsuccessful.

Better absolute agreement might be obtained if an effective Λ based on a weighting of the two values of γ is defined, and a different representation for the explosive products taken, reflecting the fact that the explosive products undergo an isentropic expansion process rather than a shock process, hence the ratio of internal to kinetic energy will be quite different. It can be concluded that the "implosion in a sphere model" is a good representation of the peak pressure-distance profile and absolute values of pressure for cases where a single value of γ can be determined. For cases where two different gases are used, the snape of the profile is predicted well but an empirical relation must be used at present to predict absolute values of pressure.

It is also of interest to examine the pressure-distance profile at a fixed instant of time. Classical implosion theory predicts that the loci of the peak pressure with distance varies as $r^{-\delta}$, and that the pressure, at a fixed instant of time, also varies with distance as $r^{-\delta}$, (see for example, Eq. (2.66) and (2.80)). In Fig. 31 the pressure is plotted versus radius for the gas case, for several instants of time. It can be seen that the profiles are not as well predicted by the classical theory or the "implosion in a sphere model" as were the peak shock pressure profiles. For the earliest instant of time plotted, (t = 39.48 μsec), the profile is decidedly unlike a classical profile and in fact is representative of a plane wave profile. A direct comparison of this profile with a plane profile cannot be made, since the shock is not strong $(p_2/p_1 \sim 2.5)$, and the effects of the detonation wave profile, which extend to $r/R_0 \sim 0.5$ are most pronounced for times shortly after reflection from the outside wall. At a later instant of time, (t = 51.38 μsec), the profile is achieving a classical like shape but it has taken an asymptotic behavior of $(r/r_s)^{-1.06}$ rather than $(r/r_s)^{-.9054}$ predicted by theory. At the last printed output before reflection (t = 54.45 μsec), the profile is definitely self similar, in the sense that the asymptotic slope remains unchanged from the previous slope and the near shock values are becoming more classical-like in appearance. In short, for early times the profile is decidedly planar. At later times the profiles take on a self-similar, implosion-like character with a slightly greater slope ($\sim 17\%$ in this case) than would be predicted from classical considerations. The fact that the shock strength for the two earliest cases is not sufficient for the shock to be clearly "strong" might be suggested for this breakdown. However, the same behavior will be found in explosive-driven cases, where the shock is and has been strong. The "discrepancy" lies in trying to make the real case of an implosion in a sphere conform, too closely with the classical, implosion from infinity.

It should also be noted that the spreading out of the shock front due to the artificial viscosity technique employed makes it difficult to assign an exact radial position for the superimposed classical implosion

34

profiles. Hence, the curves could shift to the left or right depending on how the shock front position was defined, and the method used here must be explained. In the figure the classical profile is applied to the two latter cases by requiring its peak pressure to coincide with that obtained numerically. For the earliest case ($t = 39.48$ μsec), the shock front location is easily determined. At $t = 51.38$ μsec, this procedure places the shock front approximately midway in the rising portion of the computed profile. At $t = 54.45$ μsec, very close to the origin, the artificial viscosity spreads the front so extensively on this plot that the "middle" of the rising is obscured. The present procedure places the shock front at $r = 0.46$ cm.

Plotted in Figs. 32 and 33 are the pressure profiles plotted for three instants of time for the two explosive driven cases. In general, the same points can be made for these two cases as were made for the previous one, with one exception. The initial behavior of the gas is different. The flow in the explosive case is complicated by the driving gas. From the figure, it can be seen, that not only does an outward propagating shock exist in the flow but also an inward facing wave, which while moderately strong ($p_2/p_1 \sim 5$ to 10) at the times plotted here, is being swept backwards toward the origin. Whether this wave is a computational effect or is part of the explosive-driven implosion phenomenon, cannot be determined from the few data available. One might argue that it is the result of allowing the explosive to detonate prior to the arrival of the pressure peak, as it is seen only in the explosive driven runs. If it were a computational effect it could be removed in subsequent studies by changing the detonation threshold pressure of the explosive to a higher value. There is also the possibility that it is an integral part of implosions in a sphere using explosive liners of finite thickness. For example, secondary, rearward facing shock waves have been found in numerical calculations of finite source explosions and have been observed in practice,[55] hence by analogy the existance of secondary waves in a finite source implosion problem would not be entirely unexpected.

It can be seen from the figures, that the driven gas in the two explosive cases take on a self-similar type of behavior as the shock approaches the origin. In Case 2 the exponent characteristic of the pressure profile is again slightly greater than the predicted exponent, 1.47 as compared to 1.21, a factor of approximately ~ 20 percent. Case 1, which will be seen later, is the most classical like in all respects has a slope of 1.17, only 5 percent lower than the predicted value. On Fig. 32 it should be noted that the absence of a clear cut slope for the profile at 67.78 μsec is due to the fact that the front edge of the imploding shock has reflected and the artificial viscosity is beginning to bulge the incident shock pressure profile as the reflected shock begins to emerge.

Density Profiles

It is of interest to know the peak density as a function of radius and the density profiles at given instants of time as this will allow further insight into the implosion phase phenomenon. In the classical implosion case the peak density should be constant with radius as a strong shock is assumed for the entire implosion phase. The density profiles at fixed instants of time should have distinct rising profiles which approach constants as r/r_s becomes large (see Figs. 13 through 17, for example).

As the artificial viscosity spreads the shock front, it is difficult to assign an exact radial position for the front. However, the peak pressure location can be found with precision and will be used in the following discussion.

In Fig. 34, the density, taken at the pressure peak is plotted as a function of radius. The curves are a companion set to those of Fig. 30. The density is normalized by the density well ahead of the imploding wave, (see Fig. 36, t = 36.54 µs , r = 1.0 cm for example). The striking feature of this figure is that it shows clearly those cases for which the strong shock assumption is not valid. If a strong shock were produced throughout the entire implosion phase, then the density at the peak pressure position should be constant for all radii. Figure 34 shows that only Case 1, the low initial pressure, explosive driven case satisfies the strong shock assumption and then only for the latter quarter of the implosion trajectory. For the other two cases, the shocks are strengthening as they approach the origin, but never attain the strong shock condition for the dimensions shown here. Of course, for very small radial distances i.e., close to the origin the strong shock criteria must ultimately be met. As the density at the peak pressure location is plotted in Fig. 34, rather than density at the shock front the asymptotic value for the density is not the strong shock value $(\gamma+1)/(\gamma-1)$, but is greater than this value by an amount which depends on γ. One notes that the level attained by Case 1 is very close to that predicted by the classical similarity solution for $\gamma = 1.67$. This indicates that while the shock front is spread out and its location is made ambiguous by the artificial viscosity technique, not all of the fine structure of the flow is obscurred by the technique. Knowing beforehand that only Case 1 satisfies the strong shock criteria over any significant part of its trajectory, a detailed look at the density profiles at given instants of time will be more fruitful.

Plotted in Fig. 35 are density profiles at three instants of time for Case 1. For t = 67.78 and 63.67 µsec, the density profiles are seen to approach the classical density profile with minor variations. Even at t = 55.25 µsec, the earliest ins nt of time, where Fig. 34 showed that the strong shock criteria is not fully satisfied, the profile appears classical in character in that it rises above the strong shock value and approaches the classical value. The increase in density above the asymptotic value for the curve for t = 67.78 µsec at r ~ 3 cr is due to the reflection of the front edge of the imploding shock. The increase in density seen immediately ahead of the contact surface is not predicted and may be a computational effect. The density profiles of the two weaker cases are shown in Figs. 36 and 37 for cases 2 and 3 respectively. The gas in Fig. 37 has the same gamma ($\gamma = 1.67$) as the previous case and a direct comparison of the two is possible. At the two earliest instants of time, t = 36.54 and 45.02 µsec, the density profile is quite unlike the classical profile. The peaks in density occurring at roughly the peak in pressure which is indicated by the arrows. The density just reaches the strong shock value the latest time, t = 53.65 µsec, and is still much less than the classical implosion value. However, the profile is tending to become classical like, at least in the sense that the density peak has moved rearward of the pressure peak. Clearly the comparison between the data and the classical implosion profile is not nearly as favorable as it was in Case 1. In Fig. 36 are plotted the profiles for Case 2. The effective gamma of the gas is $\gamma \sim 1.4$, hence the shock density jumps are much greater than the $\gamma = 1.67$ case ($\rho_2/\rho_1 = 8.2$ compared to 4.0). In this case, the density profiles are also non-classical in character because of the relative weakness of the imploding shock. However, for the profile nearest the instant

of implosion, the density peak has moved behind the pressure peak indicating a tendency toward the classical profile.

It can be concluded from data shown on the previous four figures, that a classical-like behavior holds for the implosion phase provided the shock is strong and has been so for most of the implosion phase. For gas cases or cases where the shocks are weak, the density decreases behind the implosion front rather than increases with the result that self similarity of the flow profiles is not obtained.

It should be noted that the 100 psi case is representative of the lower limit of the conditions to be used for launchings. Hence it is clear that the dynamics of the flow in the chamber can only be approximated by a strong shock model, and that the full non-linear exact shock relations must be included, at least over part of the trajectory, if a precise description of the flow is to be obtained.

Temperature Profiles

In the previous two sections it was seen that the pressure and density take on a classical-like behavior provided that the shock is strong and has been so for a significant part of the trajectory. The temperature profiles will now be examined to see if they behave similarly. For the classical case, the peak temperature should vary as r^{-6} and the temperature profile at a fixed instant of time should approach the curve const $x\ r^{-6}$ for $r \gg r_c$.

For a perfect gas, the temperature profiles could be calculated using

$$T = \mathcal{R}\frac{p}{\rho} \qquad (2.119)$$

Hence, for Cases 1 and 3 where gamma was constrained to be $\gamma = 1.67$, the temperature can be obtained directly from the density and pressure. For Case 2, where a real gas was assumed, this cannot be done. Unfortunately the printed output for Case 2 does not include the temperatures, although in principle they could be obtained from p and ρ knowing the complete equations of state, which is not given.

It will be shown in the next section that real gas, stoichiometric oxygen hydrogen for the conditions under discussion, behaves very nearly as if gamma were constant at $\gamma = 1.14$. Using this value, which agrees closely with the detonation calculations of Benoit[50], and information from the real gas calculation for high pressure detonation waves from the same reference, a factor could be determined which allowed the temperature to be estimated from p and ρ. This was

$$T = 7.29 \times 10^{-3}\ p/\rho$$

where

p is in psia $\qquad (2.120)$
ρ is in grams/cc
T is in $^{\circ}$K

For the remainder of this report, where temperatures are quoted for Case 2, they will have been estimated using this equation. Shown in Fig. 38 is the temperature at the peak pressure location versus radius for the three cases.

It is seen that the peak temperature profiles follow generally the profiles obtained for the peak pressure, except that the non-ideal density effects cause the agreement to be not as good as it would have been if the density were more classical-like. For case 1 the curve approaches r^{-5} for $r \leq 0.5$ cm. For smaller r, it falls below this line probably as the result of the artificial viscosity depressing the pressure. For case 3, the curve approaches the $r^{-0.9054}$ curve for $r/R_0 \leq 0.1$ i.e., much closer to the origin, since the implosion required considerably more strengthening to become a "strong" shock than in Case 1. Case 2, which is the explosion-driven, weak-shock case, shows poor agreement with $r^{-1.21}$ curve until nearly $r/R_0 \leq 0.1$, after which it takes on a more classical-like behavior. In short, the peak temperature behaves in a manner consistent with the previous results for peak pressure and density. Although not shown, the temperature profiles taken at various instants of time for the three cases, show a self-similar type profile only very near the origin. They are decidedly planar for times near the beginning of the implosion, in general agreement with the pressure and density behavior.

Implosion Phase Trajectories

It is also instructive to compare the implosion phase shock trajectory obtained from the numerical experiments with the trajectory predicted by the "implosion in a sphere" model. As noted previously, a precise shock front location cannot be determined from the numerical experiments, however the point of peak pressure or maximum artificial viscosity can. In principle, the maximum velocity gradient occurs in the shock front, hence taking the location of the maximum artificial viscosity, as indicative of the shock front location, should entail a minimum of error. While this works well away from solid boundaries or the origin, it will be seen that it fails badly near them. If the pressure profiles were all classical, self-similar profiles, then the shock front position could be determined by correcting for the distance between the shock front and the peak pressure location using the classical theory. It has been shown that the pressure profiles are not all classical-like for the whole trajectory. Hence, a correction based on this assumption would not be valid over the entire range of r. As any method of adjusting the data to account for this effect would be arbitrary, the uncorrected peak pressure location is plotted directly along with the trajectories predicted by the "implosion in a sphere" model.

The data and theory is plotted in Fig. 39, normalizing the distance by the chamber radius and the time by the implosion phase time. For this plot $r = 0$ and $t = 1$ is the position and instant of implosion and $r = 1$ and $t = 0$ is the instant of beginning of the implosion phase. The two predicted trajectories, which in their normalized form are functions only of δ, are given for $\delta = 1.21$, which is applicable to the two explosive driven cases, and $\delta = 0.9054$, which is for the gas case.

The comparison between the numerical experiment and the theory is very satisfying. Cases 2 and 3 have better agreement than does Case 1. But recall that these two cases were the least classical-like hence the peak pressure location plotted here and the shock front location are closest. For Case 1 the pressure profiles were decidedly classical in character. The distance between the shock front and the peak pressure location is 1.25 r, for the classical profile. It can be seen that applying, say, one half of the maximum of this correction to the data, results in a good fit with the theory.

38

Also shown in the figure is the trajectory for Case1 based on the maximum artificial viscosity position. For most of the implosion it is seen that this position is ahead of the peak pressure position, as it should be, and gives better agreement with the predicted trajectory. However, for ζ less than ~ 0.2 the position of maximum artificial viscosity jumps close to the origin and remains there for the remainder of the implosion. This is clearly a computational effect and has no basis in reality. A comparison of the two ways of plotting the "shock location" would indicate that away from the origin the artificial viscosity location is more representative of the shock front position unless the implosion wave is non-classical in which case the peak pressure location is more accurate. Near the origin, the peak pressure location is more accurate. A trajec' ry for a classical infinite-extent implosion is also shown for comparison. w. le it agrees with the implosion a sphere model for the later stage of the implosion, it diverges substantially for earlier times, as is to be expected.

It can be concluded that the "implosion in a sphere" model also provides a good representation of the actual trajectories for the cases at hand. This occurs because the trajectory depends primarily on the pressure, which as was seen previously, is accurately predicted by the implosion in a sphere model.

2.5.4 Conditions at the Origin after Implosion

The implosion phase, during which the shock propagates from the outside wall to the origin, is of interest primarily because it shows the strong effect of the spherical convergence on the shock strength and on the properties of the gas behind the shock. While these properties are of interest, they are not the real point in question. The key point is to be able to predict gas state in the region of the origin, at and after the instant of implosion.

It should be clear from the previous analysis, that as $r \to 0$, i.e., $t \to t_{imp}$, $p \to \infty$, $T \to \infty$ and $\infty \to$ const. This can happen in principle, only in the absence of any viscous, heat-conductive or radiative effects. For any real gas, these effects will limit the pressure and temperature to finite values. The analysis of convective and radiative losses is a problem of considerable importance to implosion-driven launchers since it is probably these effects which will limit their ultimate performance. The complexity of the problem make this a separate task in its own right and preclude its being undertaken as part of the present study. It is hoped that a serious attack on this problem can be started in the immediate future.

In a sense, the finite cell size and artificial viscosity used in the calculations have already limited the maximum recorded pressures and temperatures by spreading the shock front over several cells. The cell or grid size could be reduced at the expense of computing time to obtain finer resolution. However the resulting profiles would then have to be integrated (averaged) over the projectile base area to obtain the accelerating force. The data for times nearest the instant of the implosion, gives as the radii of the central zones, 0.33 cm., 0.89 cm., 0.56 cm for Cases 1, 2 and 3 respectively, hence the numerical results are already averaged over areas comparable to the projectile base area and have finite peak values.

Time History at Origin

The time history of the gas in the origin zone, after the reflection of the implosion wave will now be examined in detail to ascertain the nature of the flow. In Fig. 40 is plotted the pressure in the origin zone as a function of time from the instant of implosion for the three cases. It can be seen that for all three cases the pressure varies as $t^{-3/2}$. The data for Case 1 (100 psia-TNT) are limited to two points but a slope of minus 3/2 is not unreasonable. This point is very significant. As the three cases involved included, explosive-driven cases with both real and perfect interior gases and a non-explosive driven perfect gas case, one can conclude that this result is independent of both the driving technique and of γ and that all cases will behave identically. While this behavior is not sufficient, it is a necessary condition for the existence of a similarity solution for a reflected implosion wave. Recall that the pressure at the origin for an explosion regardless of the ratio of specific heats was

$$p_{orig} = Kt^{-\frac{2\nu}{\nu+2}} \qquad (2.121)$$

For an implosion it appears that the pressure at the origin may have the form

$$p_{orig} = Kt^{-\frac{\nu}{\nu-1}} \qquad (2.122)$$

This result also has considerable bearing on the potential use of the gas produced by the implosion, as for example in the hypervelocity launcher, since it implies a very rapid decay of the pressure and consequently the average pressure will be substantially less than any peak pressures measured or inferred. The point of view of an average pressure will be persued further in Sec. 3.5.

It is of interest to determine in the same manner that was used for the explosive products in Sec. 2.5.2, the ratio of specific heats of the doubly shocked gas in the origin zone. For Cases 1 and 3, $\gamma = 1.67$ should be obtained since this was assumed initially. Case 2 is of interest, since it will indicate how the present representation of real gas stoichiometric oxygen-hydrogen behaves at very high pressure. In Fig. 41 the pressure is plotted versus the density for the gas in the origin zone. For Case 3, the slope of the curve of p versus ρ has a slope of 1.67, which is in agreemen' with the initial constraints. Further, the conditions at the outer wall are also plotted and gamma also found to be $\gamma = 1.67$. The shift in the curve is due to the different state of entropy at this location. For Case 1, only three points exist, but they are sufficient to exhibit a slope of 1.67, as initially assumed. The results from Case 2 are very interesting, as they show that for pressures in the range of 4×10^4 to 8×10^6 psi and corresponding densities of 10^{-2} to 1 gram/cc, that gamma remains essentially constant at a value of $\gamma = 1.14$. From an inspection of the equation of state for the oxygen-hydrogen mixture (Eq. 2.114), there does not appear to be any a priori reason to expect this behavior, i.e., this value of gamma has not been "preprogrammed". That gamma is constant will simplify the discussions and analysis to follow.

After the imploding shock wave reflects from the origin, the gas in the origin zone does not experience any further shocks or compressions, (until the next cycle). In the absence of any entropy producing mechanisms, the flow is particle isentropic and the variation of the other gas variables, density and temperature along a particle path or Lagrangian surface should be calculable from isentropic flow considerations. Recall for isentropic flow

40

between two states 1 and 2, the temperature and density changes are related to the pressure change by

$$\frac{T_2}{T_1} = \left(\frac{p_2}{p_1}\right)^{\frac{\gamma-1}{\gamma}} \tag{2.123}$$

and

$$\frac{\rho_2}{\rho_1} = \left(\frac{p_2}{p_1}\right)^{\frac{1}{\gamma}} \tag{2.124}$$

Since the pressure time history has been shown to follow the relation,

$$\frac{p_2}{p_1} = \text{const.} \; t^{-3/2} \tag{2.125}$$

then it immediately follows that the temperature and density time histories should be

$$T = \text{const.} t^{-\frac{3}{2} \cdot \frac{\gamma-1}{\gamma}} \tag{2.126}$$

and

$$\rho = \text{const.} t^{-\frac{3}{2\gamma}} \tag{2.127}$$

Plotted in Figs. 42, 43, and 44 are the time variations of p, T, and ρ in the origin zone, as obtained from the numerical experiments. In Fig. 42 the data from Case 3 show very good agreement with the predicted slopes. In Fig. 43 the data for Case 2 indicate that for times less than about two microseconds, the spreading due to the artificial viscosity "flat tops" the profiles. If a run with smaller zones or a smaller artificial viscosity coefficient were made, the profiles would be peaked. The flat top shown here is a computational effect, but a similar flat topped behavior would not be unreasonable in a real situation, where convective or radiative losses dominate.

In Fig. 44, results for Case 1 are plotted. The limited amount of data, (three points) and the nearness to the instant of reflection (with its subsequent strong artificial viscosity effect), do not permit a valid comparison with the theory. However, it is not entirely unreasonable to expect from the trend that the data fair with the predicted slopes at later times.

It may be concluded from the above cases that the flow is a particle isentropic expansion flow, and that the state of the gas in the origin zone and its time history are known in the general case, with the exception of the constants in Eqs. (2.125), (2.126) and (2.127).

If an analytic solution for the reflected implosion wave were available, then these constants would be known as for example, as they are in the classical explosion case. As this solution is not yet available and as these constants must be known if any further use is to be made of the analysis developed so far, the following alternate approach is suggested.

There may be several ways of obtaining these constants. One way, which has the advantage that it avoids the singular region, follows. Consider the profiles shown in Fig. 45, which are taken at a fixed instant of time after the reflection of the imploding wave. The pressure and temperature profiles

41

left by the inbound shock are shown by the dotted line which can be calculated using the implosion in a sphere model, for example. If, 1) the shock jump conditions, 2) the ratio of the shock to origin conditions, and 3) the outbound trajectory (such that the shock position and corresponding time are known) then the origin conditions at that instant of time are known, hence the constants can be evaluated. These three points: reflected shock strength, similar profiles behind a reflected implosion, and the outbound trajectory will now be discussed in turn.

Reflected Shock Strength

The overall pressure ratio across a classical reflected implosion wave was determined by Guderley[43] in his classic work on implosions. He obtained an overall ratio of 16.6 and 26.6 for cylindrical and spherical implosions respectively,for $\gamma = 1.4$. An error in the scale of Fig. 4 of his original paper (in German) has caused some confusion but by noting that the exact value for the planar case is $p_5/p_2 = 8$, for $\gamma = 1.4$, the proper vertical scale can be determined. The corrected plot appears in Fig. 46. The curves are normalized by the pressure immediately behind the imploding wave at $r = 1$, $t = -1$ and the time to transit from $r = 1$ to the point of reflection. The normalized trajectory on the $r - t$ plane is shown in the insert on Fig. 46 for $\gamma = 1.4$ and $\nu = 1$. The basic character of the trajectories are the same for $\nu = 2$ and 3, the only exceptions being that the trajectories and particle paths are curvilinear, the particle paths are inclined outbound after reflection, and the reflected waves arrive at $r = 1$ sooner than in the $\nu = 1$ case as can be seen from the pressure-time curve of the same figure.

A very important point concerning the pressure curves was not made explicit by Guderley but can be obtained from an inspection of them. While the "reflected shock" pressure ratio for the one-dimensional case is straight forward in that only a single shock compression is involved, the overall reflection pressure ratio for the cylindrical and spherical cases is composed of two parts, an adiabatic (particle isentropic) compression followed by a shock compression (subsequently there is an adiabatic (particle isentropic) expansion). Further, for the one-dimensional case whether one is interested in the pressure jump as seen by a particle in the flow or by an observer stationary in laboratory coordinates, the reflected shock pressure ratio, p_5/p_2 defined by the ratio of the static pressure across the reflected shock, is the same and is given in Eq. (2.18). It is $p_5/p_2 = 8$ for $\gamma = 1.4$. For the cylindrical and spherical cases, the overall compression experienced by a particle in the flow and the overall compression noted by an observer fixed in the laboratory frame are quite different.

For example, for cylindrical or spherical flows a particle compressed by the inbound shock to a pressure p_2, is put into motion and moves toward the origin. It undergoes an adiabatic compression as it approaches the origin. Its inward motion is terminated by the reflected shock, which is now outbound from the origin. Subsequently, it propagates outward from the origin experiencing an adiabatic expansion. Figure 46 does not apply to this case but rather to an observer fixed at a given radial position and observing the pressure as a function of time. The fixed observer sees the incident shock pass his station at $t = -1$. It is followed by inward flowing gas (along particle paths which come from earlier times) which is undergoing an adiabatic compression by virtue of the cylindrical or spherical convergence. The phenomenon is such that for the cylindrical and spherical cases, the pressure

42

at the fixed observer increases in time until the outbound reflected shock passes, giving an instantaneous pressure increase followed by a monotonic pressure decrease due to the outward diverging flow. It can be seen from the figure, that as, seen by the fixed observer, the adiabatic compression has a greater compression ratio across it ($p/p_2 \simeq 8$), than does the reflected shock ($p/p_2 = 3.33$). From Somon, for $\gamma = 1.67$, the reflected shock has a pressure ratio of $p/p_2 \sim 2.5$, and the adiabatic compression has a strength of $\simeq 5$ giving an overall pressure ratio of $p/p_2 \simeq 12.5$. The ratios, which are tabulated in Table 6 and shown in Fig. 47, are quite different from the larger numbers usually quoted for the "reflected-shock pressure ratio" which should be called "overall compression ratio" on reflection to prevent confusion with the pressure ratio across the reflected shock, which as is seen, is relatively small. A comparison of the two available values indicates, that the strength of the reflected shock part of the total compression, may be roughly approximated by the one-dimensional value divided by $(\gamma+1)$ for spherical implosions.

It is instructive to compare the reflected shock strengths of the numerical experiments with those predicted by classical theory. The direct approach, i.e., plotting the pressure at a point as a function of time to duplicate Fig. 46, was not successful. The spreading of the reflected shock by the artificial viscosity obscurred the profile. An alternate approach which is not so sensitive to the spreading is shown in Fig. 48 for cases 2 and 3. The peak shock pressure is plotted versus the radius for the outbound shock for several instants of time, and loci obtained. The pressure at any point in the gas into which this shock is propagating should, for a classical implosion, be increasing in time up to the instant the reflected shock arrives at that point. However, as seen from the figure for the pressure profiles shown at different times, (for example, $t = 54.45$ and 61.66 μsec for Case 3, and $t = 105.5$ and 116.8 μsec for Case 2), the profile ahead of the reflected shock remains nearly independent of time after implosion for Case 3 and for Case 2, shows only a very small ($\sim 30\%$) increase in pressure. A classical implosion should have shown increases of nearly factors of $\sim 5 - 10$. It is seen that the implosion in a sphere, again produces results which are at variance with classical implosion theory. Since the pressure profiles into which the reflected shock is propagating are nearly constant with time, the difference between that profile and the locus of the peaks of the reflected shock is a rough estimate of the reflected shock strength. As the artificial viscosity has reduced the peak values of the outbound reflected shock by an undetermined amount, this estimate should be considered a lower bound. Values of $p/p_2 \sim 1.7$ and $p/p_2 \sim 4.1$ are obtained for $\gamma = 1.67$ and 1.14, respectively. Predicted values of p/p_2 for the same cases are 2.5 from Somon for $\gamma = 1.67$, and using the numerical approximation $p/p_{2_{3D}} \sim p/p_{2_{1D}}/(\gamma+1)$, gives 8.02, for $\gamma = 1.14$. Both values are about 50% higher than those obtained from the numerical results. A better determination is not possible with the limited data available, but it can be concluded that the values are of the right order of magnitude and in the right direction considering the effects of artificial viscosity.

It appears that the reflection phase of the flow in a finite sphere for weak implosions can be considered to have a pressure profile ahead of the reflected shock, which is fixed at that value experienced at the instant of implosion, and a reflected shock strength that is given by the classical implosion theory. It would be interesting to see if this model also applied to the strong shock finite sphere implosion for which data are not presently available.

43

Profiles of the Flow Behind a Reflected Implosion Wave

While it has not been proven, the evidence suggests that the reflected implosion wave for a classical implosion is self-similar. There exists, at present, no analytical or numerical representation of the profiles behind the reflected wave, however, a step towards obtaining them, albeit in a crude form, can be made by utilizing the results of the numerical experiments. While this is not completely satisfactory, the lack of any other information and the fact that this data is needed presently, is sufficient to justify this approach. If the numerical experiments were more precise, i.e., the pressure peaks were represented accurately, and if both the inward and outward flows were truly self-similar then this approach would yield accurate values. Unfortunately, the peak values are obscured by the action of the artificial viscosity and an exactly self-similar flow is not obtained for either the inbound or the outbound flow. It is unfortunate that Case 1, where the inbound flow is closest to being self-similar, has a limited output, or better values might have been constructed.

It is of interest to note, that the outbound reflected wave does not satisfy the strong shock conditions. Hence, one of the basic assumptions in the usual solution of similar problems is not satisfied. However, the shock has constant strength which is even more useful than the strong shock assumption. Plotted in Figs. 49 and 50 are the pressure, temperature and density behind the reflected shock normalized by the peak values at the shock front versus the radius normalized by the shock front radius, for Cases 1 and 3 ($\gamma = 1.67$) and Case 2 ($\gamma = 1.14$), respectively. The agreement between Cases 1 and 3 is good considering that the only data for Case 1 is for very short times (i.e., distances) after the reflection from the origin when the artificial viscosity effects are still strong, and they have entirely different histories: Case 1 being explosive driven while Case 3 is not. It can be seen that profiles, not unlike a conventional explosion profiles, result. The pressure decays from the shock front and approaches a constant value as $\eta \to 0$. The density decays more rapidly than the pressure, as in the explosion case, but does not vanish as $\eta \to 0$ hence the temperature remains finite at the origin. This is shown clearer in the linear scale of the insert. By comparison, Sómon's results for the profiles at fixed instants of time and as functions of time at a fixed point, for both cylindrical and spherical cases, which are taken directly from Figs. 3 and 4 of Ref. 48, are shown in Fig. 51. From his figures it appears that a singularity in temperature should exist. His figures indicate $\rho \to$ const for $r \to 0$ in the cylindrical case, but $\rho \to 0$ for $r \to 0$ in the spherical case. These results, which are incidental to the main theme of his paper are not discussed, may have been plotted incorrectly. The fact that the velocity field appears to have advanced knowledge of the outbound reflected shock is also unsettling.

In Fig. 50, the profiles are plotted for Case 2, where $\gamma = 1.14$. The profiles are very similar to the preceding case. Again it appears that the density does not vanish for $r \to 0$. However, the asymptotic value is very small. Whether the artificial viscosity has prevented the density from vanishing or whether this is a property of the flow cannot be stated conclusively from the limited data available.

The forgoing profiles were taken at an instant of time that had enough points to adequately define a curve. If the profiles are truly self-similar, then profiles plotted at other times should coincide with this one or equivalently, the ratio of the origin value to the shock value should be independent of time. Plotted in Fig. 52 are values of p_{orig}/p_s and T_{orig}/T_s

44

for radii from reflection to either collision with the wall or contact surface, whichever governs the case in question. It can be seen from the figure, that these values are constant over the inner half of the trajectory. As the profiles into which the shock is propagating become less self-similar away from the origin, the deviation is to be expected. The values for Case 3, indicate a well maintained constant value of the temperature ratio supporting the nonzero density asymptote argument.

Carrying the analysis one step further, the ratios are plotted versus gamma in Fig. 53. The variation of the pressure ratio with gamma is less than the scatter of the data, hence the only conclusion that can be made is that the pressure ratio is constant at $0.85 \pm 20\%$ for all values of gamma. For the temperature ratio, two distinct values are seen, $T_{orig}/T_s = 2.25$ for $\gamma = 1.67$ and $T_{orig}/T_s = 12.6$ for $\gamma = 1.14$. These values, which are plotted in Fig. 53, indicate that the temperature ratio has a singularity at $\gamma = 1$. A possible numerical fit to the two points, which is contrained to be singular at $\gamma = 1.0$, is

$$\frac{T_{orig}}{T_s} = \frac{1.64}{\gamma - 1} \qquad (2.128)$$

as shown in the same figure. It should be kept in mind that this data may be seriously in error, depending on how much the artificial viscosity has depressed the peak shock values. Much additional work will be required to produce more precise values, preferably an analytic solution to the reflected implosion problem.

Reflected Implosion Phase Trajectories

For a classical implosion, both the implosion and reflection trajectories have the same form which is

$$t = K \, r^{\frac{\delta + 2}{2}} \qquad (2.129)$$

The value of the constant for the reflection phase is greater than the value for the implosion phase indicating that the reflected shock moves slower in laboratory coordinates than the incident shock, as can be seen from Fig. 46. For the one dimensional case the reflected phase time to the incident phase time is known, (for example, Ref. 19), and is given by

$$\frac{t_{exp}}{t_{imp}} = \frac{1}{2} \frac{\gamma + 1}{\gamma - 1} \qquad (2.130)$$

which is plotted in Fig. 54. For the cylindrical and spherical cases an analytic expression does not exist but the single points determined for $\gamma = 1.4$ and 1.67 by Guderley and Somon, which are plotted in the same figure show that this ratio has about the same form as the one dimensional case but generally decreases with increasing space index, ν. Using the value for $\gamma = 1.67$ and an estimate of $t_{exp}/t_{imp} = 7.5$, for $\gamma = 1.14$ and Eq. (2.129), the expected trajectories can be constructed. Shown in Fig. 55 are the anticipated trajectories and those actually obtained. It can be seen that they agree neither in slope nor in absolute value. It might be argued that the slopes are approaching the right value as the shock wave approaches the sphere surface.

However, it is in this region where the worst comparison would be expected, not the best, hence the agreement is probably fortuitous. As a rough approximation, a linear trajectory i.e., $r = Kt$ can be assumed, as shown with Case 3. If the trajectories are extended to the outer wall, the time for the reflection phase can be determined. For Case 1, only 3 points are available, and an objective result cannot be obtained. For Cases 2 and 3, the reflected phase time is 140 and 30 μsec, giving for the ratio t_{exp}/t_{imp}, 3.3 and 1.12, respectively. Because Case 2 required a lengthy extrapolation, its precision is not as good as Case 3, which can be obtained accurately. These values are plotted in Fig. 54. It can be seen they have the same trend with ratio of specific heat as the predicted curves, but are lower by a factor of ~ 2 to 3.

It can be concluded that the trajectories for implosions in spheres, are not adequately described by the classical theory, as the flow is becoming less and less classical as the cycle progresses, and numerical descriptions must be sought.

2.5.5 Subsequent Cycles

As noted in the introduction to this section, the detailed print-outs for the three cases cover only one complete implosion. There exists graphical output in the gas case (Case 3) for the pressure at the origin through 3 cycles. Unfortunately, the tabulated information that is implied by these plots is not available. However, even this limited look at later cycles does allow one to sumise what the character of later cycles may be like. The cycle time for the gas case, was 54.4 microseconds. The time between implosions for the first and second, and second and third peaks of the printed output is 55.5 and 54.5 μsec respectively, indicating that for the gas case at least, the cycle time does not appear to change with subsequent cycles. Further, the pressure-time histories of the second and third cycle, shown in Fig. 56, are virtually identical with the first. It would be interesting to be able to compare the temperatures at later cycles, since one would expect that the repeated shock heating would raise the temperature with cycle. This question can only be answered when further data is available.

While the later cycles in the gas case appear, at least as far as pressure and cycle time effects are concerned, to be nearly identical with the first, there is no guarantee that the explosive driven cases, where contact surfaces are found will have similar properties. In fact, it is expected that the shock will refract at the contact surface producing transmitted and reflected shocks which themselves refract ad infinitum. It is to be expected that a fairly steady pressure will be produced after several (5 - 10) cycles have elapsed. The average pressure will probably be close to the steady state pressure which would have been produced by constant volume energy addition. Further, only the first shock is explosive driven and has a large value of δ (δ = 1.21). The subsequent implosions will probably behave as undriven implosions, hence δ will be much less, and consequently the peak pressures of the second and later cycles will be much lower than the first.

While there is no information to verify this, the expected behavior for the explosive driven cases will proably include a strong explosive-driven first cycle, several weaker undriven cycles followed by a steady pressure related to the equivalent constant volume energy addition pressure.

2.5.6 Summary of Properties

From the preceeding sections a considerable amount of useful information was gleaned by a close inspection of the results from the three numerical experiments. It is worthwhile to collect and summarize the key points before proceeding with further analytic work based on these findings.

Generally, the implosion phase of the cycle for an implosion in a sphere can be adequately described by classical implosion theory modified and interpreted in the manner described by the "implosion in a sphere" model. The reflected phase is decidedly unlike the classical model and considerable care and restraint must be used in carrying over classical results. Specifically, the following important points can be made.

1.   The initial motion of the imploding shock wave following the detonation of the explosive at the outside wall, follows ideal plane explosion theory, (Fig. 28).

2.   In the absence of any explosive, the peak pressure of the imploding shock waves with r as $r^{-\delta}$, where δ is given as a function of gamma of the gas as predicted by the classic implosion theory of Guderley. Where explosive liners are used and the total energy of the explosive is at least equal to the energy in the gas, δ is constant at approximately 1.21 and is independent of the gamma of the gas in the interior regions or explosive. This effect is probably due to the explosive products acting like an imploding piston, (Fig. 30).

3.   In the absence of radiative & convective losses, the pressure, velocity, and temperature become infinite at the origin at the instant of implosion, (Figs. 30 and 38).

4.   The radial profiles of the pressure, temperature, and velocity do not correspond exactly to those given by classical theory, but have stronger radial dependences. This effect is probably caused by the wall velocity constraint, (Figs. 31, 32, 33).

5.   The implosion in a sphere model gives a good representation of the peak pressure variation with radius and the implosion phase trajectory, (Fig. 30 and 39).

6.   A strong shock cannot be expected over the entire trajectory unless initial pressures are low and explosive energies are large, (Fig. 34).

7.   The origin pressure after implosion varies as $t^{-3/2}$ for all values of gamma, suggesting the reflected imploding shock obeys a similarity law, (Fig. 40).

8.   The gas conditions in the origin zone after implosion are governed by considerations, i.e., $T \sim p^{\gamma-1/\gamma}$, $\rho \sim p^{1/\gamma}$ as $p \sim t^{-3/2}$, (Figs. 42, 43 and 44).

9.   Stoichiometric-oxygen-hydrogen at very high pressures and densities behaves like a γ-law gas with $\gamma = 1.14$, (Fig. 41).

10. The state profiles behind reflected imploding shocks are approximately self-similar, (Figs. 49 and 50).

11. The reflected trajectories are not adequately described by classical theory, (Fig. 55).

12. The reflected phase implosion time for an implosion in a sphere is less than that predicted by classical theory, (Fig. 54).

3. PERFORMANCE CALCULATIONS

Historically, the development of accurate performance calculations for conventional light gas guns has lagged their appearance by a considerable length of time. While the first guns were reported in 1957[2], it was not until several years later that detailed and accurate performance predictions were finally achieved.[56,57]. It is reasonable to assume that the development of precise performance calculations for a new concept in launchers will also take some time. An effort has been made to achieve as detailed and accurate a performance model as possible in the time scale of the present work. The model which follows is a semi-analytic, semi-empirical one. It attempts to use as much of the physics determined in the previous section as possible, but requires a number of assumptions and empirical relationships to bridge gaps where no firm understanding or data exists. As such it represents the "state of the art". Nevertheless, it should be pointed out that this model does predict many of the observed features of the launcher performance. As such, it has been very useful in understanding the launcher and in optimization studies and design predictions. The existance of such a program should not deter efforts at improving numerical implosion calculations by the addition of more realistic gas parameters, radiative and convective heat losses, as well as boundary layer, model friction effects and ablation. In one respect, the present analysis has the advantage that being semi-analytical, it allows some insight into the reasons for various effects, whereas a completely numerical program has the disadvantage that, given a certain set of initial conditions it produces a certain precise answer, while the reasons are often hidden in the computational details. The present program however, is still sufficiently complex to require the use of an electronic computer.

The performance model replaces the detailed numerical calculations of Brode, such as discussed in Sec. 2.5, by a semi-empirical, semi-analytic relation which gives the pressure-temperature-time history of the gas in the origin region. Since the total amount of mass which has passed out into the barrel is small compared to the total mass of gas in the chamber, it is assumed that the barrel and chamber processes are uncoupled. This is satisfied for the present experiments. For example, assuming a uniform density distribution, the worst condition occurs for the 5/16 inch diameter, 10 foot barrel, which has a barrel to hemisphere volume ratio of 6.8×10^{-2}. The uncoupling of the two processes makes it possible to solve for the chamber flow properties independently of the flow processes in the barrel. The flow in the barrel can then be calculated knowing the chamber origin conditions.

The time dependent origin conditions are taken as the input to a calculation which assumes a "quasi-steady" flow at constant gamma. That is,

the pressure at the base of the projectile is assumed to be that which is obtained by a steady-unsteady (chambered), constant gamma, expansion from the reservoir condition which exists at that instant of time. This force is then summed with a friction force and a counter-pressure force and an acceleration is produced. A small step in time is taken, the motion noted and the calculation repeated with new values corresponding to the new time. The details of the model will now be examined. Particular note should be taken of the assumptions made since they are directly responsible for accuracy of the model. In the last part of this section, the performance predictions based on the model will be compared to the experimentally determined projectile velocities for gas and explosive driven runs and the discrepancies, between predicted and measured quantities, discussed.

3.1 Model of the Wave Dynamics in the Hemisphere

The conditions in the chamber are calculated following the "implosion in a sphere" model developed in Sec. 2.4.1. The pressure and sound speed are known to vary as $t^{-3/2}$ and $t^{-3/4} \cdot (\gamma-1/\gamma)$, respectively. Hence only two constants are required to completely specify these quantities. These constants are fixed for a given case by the chamber size, explosive weight or thickness, explosive energy yield, and the initial gas mixture and pressure. The cycle time is required to complete the model. A characteristic time, t_*, is introduced to produce "flat topped" profiles for $t < t_*$ (see Fig. 57) and in a rough manner attempts to account for the radiative and convective losses in and near the origin. Further, the initial calculations indicated that the calculated performance was unrealistic if all the cycles were considered to be identical. An attempt was made to improve the model by introducing a loss which depends on the particular cycle. It should be kept in mind that this kind of behavior has not been rigorously demonstrated and it may be only an empirical correction which permits better agreement between prediction and experiment. However, mass flux from the chamber and heat losses to the wall would be expected to reduce the pressure with each succeeding cycle. Further, in keeping with the comments made in Sec. 2.5.5 only the first cycle is considered to be explosive driven i.e., $\delta = 1.21$. The second and subsequent cycles (all cycles for a gas case) are based on δ of the particular driven gas being used. Diagrams of the assumed pressure and sound speed history at the origin are shown in Fig. 57. The various supporting calculations and assumptions will now be discussed in detail, starting with the outward propagating detonation wave and progressing through the cycle.

3.1.1 Post-Detonation Wave Conditions

The detonation wave used to initiate the explosive must be considered because it sets the initial conditions ahead of the imploding wave. Unfortunately, it generates flow profiles which are not uniform over the entire region behind the wave, (see for example, Fig. 58). To account for this non-uniformity would be a cumbersome task, hence for the present the initial conditions for the implosion phase are assumed uniform over the entire sphere and taken as equal to the origin conditions of an ideal spherical detonation wave. In other words, the spherical expansion wave that immediately follows the detonation front, is disregarded. Implied in this assumption is that the interaction of the imploding shock wave and the expansion wave is not a dominating feature of the flow.

49

To obtain the properties in the central region, requires the solution of the complete spherical detonation wave problem. In principle this has been done by Sedov[28], but numerical solutions are available only for very few cases. Sedov gives (from plots) as the conditions across the expansion wave of a spherical detonation for $\gamma = 1.67$,

$$\frac{p_{orig}}{p_D} = 0.260 \qquad (3.1)$$

Since the flow behind the wave is isentropic by virtue of the constant detonation wave velocity, the other quantities of interest can be calculated immediately from the pressure using isentropic flow relations. For this case,

$$\frac{T_{orig}}{T_D} = 0.584 \qquad (3.2)$$

$$\frac{a_{orig}}{a_D} = 0.765 \qquad (3.3)$$

These values vary considerably with gamma and since the gammas of interest are more nearly $\gamma = 1.1$, it is necessary to determine these ratios for a range of γ. In principle Brode's numerical results for the implosion in the spheres should yield these parameters directly for $\gamma = 1.14$ and 1.67, but in fact, the artificial viscosity has decreased the peak detonation wave conditions to the point where realistic values cannot be determined. Fortunately, calculations have been made by Manson[58] for a $C_2H_2 + O_2$ mixture, for which $\gamma = 1.13$. He obtained $p_{orig}/p_D = 0.317$ for this case. A linear fit

$$p_{orig}/p_D = 0.330 - 0.107(\gamma-1) \qquad (3.4)$$

was applied to these two values to estimate values for other ratios of specific heat. It appears in Fig. 59. As most of the performance predictions in this work are done for a stoichiometric mixture of oxygen-hydrogen, a value very near to Manson's value is used and no large extrapolations are necesary, hence errors introduced by the liner fit are minimal. (It is anticipated that a numerical code which will calculate the spherical detonation wave ratios for any gamma will be available in the future and the present linear fit could be improved.

The conditions immediately behind the detonation wave in the gaseous mixture were taken from Benoit[50], who did detailed equilibrium real gas calculations for detonation waves in mixtures of the type, $2H_2 + O_2 + nHe + mH_2$ for values of $0 \leq n \leq 6$ and $0 \leq m \leq 6$. In general the values p_D/p_i, T_D/T_i, a_D/a_i, and γ are functions of initial pressure, mixture and initial temperature requiring a three dimensional array for each of the three ratios tabulated. Since the initial temperature for the present experiments is $\sim 298°K$, only one value of temperature need be considered. While a range of initial pressures of from 100 to 1000 psi is possible, the values used in this model were taken for $p_i = 10$ atmospheres, as the variation of p_D/p_i with pressure is small and will not significantly alter the results. The ratio of specific heats is held fixed for the entire calculation at that value obtained for a 10 atmosphere initial pressure. The absolute variation of γ with initial pressure for

the detonation wave properties is small. Unfortunately many of the other
γ-effects in the program occur as $(\gamma-1)$ factors and small variations in γ are
magnified in the results. It is felt that of all the assumptions made in this
performance model that errors introduced by this assumption are primarily
responsible for the discrepancy between predicted and measured values.

3.1.2 Implosion and Reflection Phases

The behavior governing implosion phase of the driving cycle is
taken directly from the "implosion in a Sphere" model of Sec. 2.4.1. The con-
ditions left at the origin by the reflected implosion wave are calculated using
the technique shown schematically in Fig. 45 and discussed in Sec. 2.5.4. For
example, a characteristic radius r_* is assumed and the pressure left by the
inbound wave at this point, $P_{inbound}$, is calculated using Eq. 2.98. As dis-
cussed in Sec. 2.4.1, for gas cases where only a single value of γ is involved,
Eq. 2.98 can be used directly using Λ as obtained from the numerical calcula-
tions of implosion profiles. When an explosive is used this procedure does not
work because Λ is not determined properly. In the absence of any rigorous
method of evaluating Λ for a two-gas mixture, a numerical representation

$$\Lambda = 0.3/(\gamma-1) \qquad (3.5)$$

is used. It predicts the peak pressure curves of Fig. 30 within $\pm$ 30 percent,
and is equivalent to assuming that the ratio of internal to total energy, for
cases having two gases, is 0.3. This pressure is taken as the shock pressure
at that point, for the inbound shock wave. Knowing all of the conditions ahead
of the shock, and the strength, the shock Mach number can be calculated using
Eq. 2.4. The temperature immediately behind the shock is then calculated using
this shock Mach number and the shock temperature ratio, Eq. 2.5.

Next, the pressure immediately behind the outbound shock at r_*,
$P_{outbound}$, is calculated by noting it is the product of the inbound shock pres-
sure and the reflected shock pressure ratio. As noted in Sec. 2.5.4, a good
approximation to the reflected shock pressure ratio appears to be

$$\left(\frac{\gamma+1}{\gamma-1}+2\right)\frac{1}{\gamma+1} \qquad (3.6)$$

which is assumed here. A shock Mach number is calculated from this ratio using
the ideal shock relation, as this shock is weak. The temperature immediately
behind the outbound shock is then calculated using this shock Mach number and
Eq. 2.5.

The origin pressure and temperature corresponding to this point
on the trajectory are calculated from the peak shock values using the results
of Sec. 2.5.4, i.e., Fig. 53

$$P_{orig}/P_s = 0.85$$

$$T_{orig}/T_s = 1.64/(\gamma-1) \qquad (3.7)$$

To complete the calculation, the time corresponding to this
shock position is required, hence the outbound shock trajectory, must be known.
It is assumed that for gas cases the implosion phase time and the reflected
phase time are identical. Where the explosive energy is much greater than the

gas energy it is assumed that the explosion phase time is related to the implosion phase time by a numerical fit to the data of Fig. 54, which is given by

$$t_{exp}/t_{imp} = 0.7/(\gamma-1) \tag{3.8}$$

For cases in between, these two relations are weighted and averaged according to the energy in the gas and in the explosive. The time corresponding to r_* is taken as

$$t_* = t_{exp} \; r_*/R_o \tag{3.9}$$

which follows directly from the assumption that the outbound trajectory is given by

$$r = Kt \tag{3.10}$$

As discussed previously this representation is the best general representation that can be obtained from the limited existing data.

3.1.3 Cycle Time and t_*

The cycle time is defined simply as the sum of the implosion phase time and the reflected phase time. The ratio of explosion phase time to implosion phase time was discussed in Sec. 3.1.2 and only the absolute value of the implosion time is needed. The time for the implosion phase is taken from the "implosion in a sphere" model and is given by

$$t_{imp} = \frac{R_o}{a_1} \left[\frac{2\gamma}{(\gamma+1)} \; \frac{1}{(\gamma-1)} \; \frac{3}{(3-\delta)} \; \frac{1}{\Lambda} \; \frac{P_i}{E_o} \right]^{\frac{1}{2}} \Phi(\zeta) \tag{3.11}$$

with δ being taken as 1.21, and Λ is taken from Eq. 3.5 for cases where explosive liners are used and γ is the gamma of the interior gas. For cases having no explosive liner, δ and Λ are based on the gamma of the gas after the results of Sec. 2.3.

As noted in Sec. 2.5.3, the pressures approach infinity as t goes to zero. This cannot be handled analytically or numerically. Further this implies an infinite impulse hence infinite projectile velocities, which is physically unacceptable. In practice, radiative and convective losses near the origin, finite diaphragm opening times for the first cycle, the possibility of instabilities in the spherical imploding shock resulting in a focal region rather than a focal point, would limit the pressures and temperatures at the origin. It can be assumed that if the appropriate equations were used, as for example the Navier-Stokes equations, that analytic results would also yield finite pressures and temperatures. At present there is no known method of predicting a limit analytically although future work will have to be done along these lines. To reflect the physical situation, the pressure profile is assumed to have a flat top, as shown in Fig. 57, at a value p_* from time zero up to a time t_*, where t_* follows from the assumed value of r_*. For the explosive cases the pressure and temperature, p_* and T_* are calculated using $\delta = 1.21$ for the first cycle. The second and subsequent cycles are based on δ corresponding to the ratio of specific heats of the driven gas as suggested in Sec. 2.5.5. This follows from the fact that only the first implosion of an explosive case is driven. All the later cycles are expected to behave as undriven implosions.

It should be noted that while the first cycle of the implosion has been examined in some detail and that while the indication is that the later cycles may not be substantially different from the first, at least for the gas case, it remains in fact that the repeated shock compression of the gas and losses to the walls through radiation and convection will alter its conditions. At present there exists no information about the conditions in cycles subsequent to the initial one, although extensions of Brode's results could clarify this point. These effects and an overall loss mechanism are lumped together in a "loss relation" which has the form

$$\frac{p(t)_N}{p(t)_1} = (1 - \theta)^{N-1} \tag{3.12}$$

The pressure-time histories for first cycles are taken as calculated above. The pressure histories for the second and subsequent cycles are taken as the first one adjusted by the "loss factor" $(1 - \theta)^{(N-1)}$ where N is the cycle number. The decay parameter θ is essentially a disposable constant (system parameter) which can be evaluated by matching the results of the program with the results of experiment, for a given initial condition. The method of evaluating θ will be discussed in detail in Sec. 3.3.

3.1.4 Comparison With the Numerical Experiments

It is of interest to compare the results of the calculation of the origin conditions with the results of the numerical experiments. The comparison will establish the accuracy of this part of the performance model and will indicate what degree of precision can be expected from the total performance program. It will also allow the source of the deviations between prediction and measurement to be pinpointed. It should be recalled from Sec. 2.5 that the numerical calculations for cases 1 and 3 used an artificially constrained gaseous mixture. The value of gamma for a mixture of $2H_2 + O_2 + 7He$ was assigned a value 1.67 although a gamma of ~ 1.27 would have been more accurate. In order to compare like quantities, the same constraint is made in the present calculations. Since this constraint makes inconsistent many of the detonation wave calculations which are used to calculate sound speed, temperature and pressure prior to the implosion, Brode's values for these parameters are used directly. For Case 2, this step is not necessary and the calculations are made directly from the initial conditions. The results of the calculations and Brode's values are tabulated for comparison in Table 7.

CASE 1: 100 psia $2H_2 + O_2 + 7He$ - 0.1 inch TNT Liner

For this case the assumed initial conditions are: a chamber radius of 20.0 cm., a gamma of 1.67 and post-burn conditions at the sphere center region (which were taken from Brode's results) of 2000°K and 500 psia. A sound speed 0.204 cm/μsec was calculated using this temperature and the state equations, (Eqs. 2.112) assuming a perfect gas The comparison was made at $r_* = 2.0$ cm., which for the assumed trajectory occurred at $t_* = 1.23$ μsec. Brode obtained a time of 1.80 μsec, for $r_* = 2.0$ cm. He obtained a peak pressure and temperature of the imploding shock at this position of 1.25×10^5 psia and 1.0×10^5 °K respectively, whereas the present calculations produced 1.2×10^5 psia and 1.3×10^5 °K, which are in good agreement. On reflection, at t_*, he obtains $p_* = 4.3 \times 10^5$ psia and $T_* = 3.4 \times 10^5$ °K, whereas the present model produced $p_* = 2.2 \times 10^5$ psia and $T_* = 4.4 \times 10^5$ °K. The calculated implosion time of 12.0 μsec. compares roughly with Brode's 17.3 μsec. His total cycle time is not available but the present calculation predicts 24.3 μsec. It is seen that while the implosion phase results are in good agreement, the comparison for the reflection phase is not too satisfying. The predicted pressure is approximately a factor of 2 too low whereas the predicted temperature is approximately 30% too high. Unfortunately this is the best that can be done for the explosive cases with the presently available information. This same order of agreement is obtained in the remaining explosive case. The gas case results however, are in much better agreement.

CASE 2: 1000 psia $2H_2 + O_2$ - 0.1 inch COMP B Liner

For this case, an initial pressure of 1000 psia and a $2H_2 + O_2$ mixture were assumed and the method described in Sec. 3.1.1 was used to calculate the conditions immediately ahead of the implosion wave. This method predicted 6400 psia and 3600°K for the central conditions left by the expanding detonation wave. By comparison, Brode obtained 3500 psia and 1900°K, the difference being a factor of ~ 1.9. This same relative error is carried through the calculation and as seen from Table 7, the predicted pressures and temperatures for the inbound shock and at the origin after reflection remain approximately 1.5 to 2.0 times greater than Brode's values. The predicted cycle time is low, but t_* is predicted favorably.

CASE 3: 100 psia $2H_2 + O_2 + 7He$ - No Explosive

For this case the initial conditions were the same as Case 1 except that no explosive was used and the chamber radius was reduced to 10.0 cm. The comparison is made at $r_* = 1.0$ cm. which for the assumed outbound trajectory occurs at $t_* = 2.44$ μsec. This compares quite favorably with Brode's value of 2.22 μsec. The performance model predicts a pressure of 9330 psia at this time, the numerical experiment gives 9000 psia. The predicted implosion and explosion phase time are 24.4 μsec which agrees well with Brode's values of 26.7 and 27.6 μsec. respectively. However the predicted temperature at t_* of 25,000°K is 40% higher than Brode's 18,000°K. The peak values for the imploding shock at r_*, are in very good agreement with Brode.

In summary, it is seen that the model gives generally realistic values of the parameters. The accuracy for the gas case is good, the error being generally less than ~ 15 percent. However better accuracy is to be desired for the explosive parameters which at present cannot be predicted to within ~ 2. It should be noted that the value taken for r_* has a strong effect on

54

the agreement. The above cases were compared at $r_* = R_0/10$ to be self-consistant. If r_* were taken at twice, or half of this value, then the agreement would change. For example, values for the gas case which were taken at $r_* = 0.5$, 1.0 and 2.0 are shown in Table 8 with the corresponding values from Brode. It can be seen that the inbound shock values are predicted very well for all three cases indicating that the implosion phase is properly represented. On reflection however, the situation deteriorates. For $r_* = 0.5$, the predicted pressure is too low and the temperature too high. For $r_* = 2.0$ the situation is almost reversed. The problem is clearly with the present representations of the reflection phase which as was shown previously in Sec. 2.5, is not nearly as well in hand as is the implosion phase.

3.2 Model of Barrel Processes

The processes by which the gas near the origin flows into the barrel, expands and accelerates the projectile is very complex. An exact computation would include, the time variation of the gas at the origin, gas chemistry effects, viscous and radiative losses, projectile friction, and counter-pressure, to mention a few. Nonequilibrium chemical kinetic effects may also have to be incorporated since the temperatures are very high and densities are large enough that covolume effects may become important. To account for all of these effects would be a formidable task. In the present analysis an attempt was made to account for effects that could be handled analytically. Other factors, some of which (like radiation and ablation) may be dominant, will have to be studied at a later date. In the remainder of this section the details of the assumed expansion process, friction, and counter-pressure representations will be discussed.

3.2.1 Assumed Expansion Model

The time-dependent origin conditions are taken as the input to a calculation which assumes stepwise steady flow at a fixed value of gamma. For example, the pressure on the base of the projectile at any instant is assumed to be that which is obtained by a constant gamma, steady-unsteady (chambered) expansion from the reservoir condition that exists at that instant of time to the velocity which the projectile has at the same instant. As very short (1 μsec) time steps are taken in the calculation, this representation is fairly accurate during the first few cycles. The projectile is still near the origin and the sound speeds are sufficiently high that the time for a sound wave to travel the distance from the origin to the projectile is small compared with the time over which significant changes occur in reservoir properties. During later cycles when the projectile is far from the origin, this criteria is generally not satisfied. For low sound speeds and long barrels it is possible that there may be several shock waves, representing the impulse from several cycles, still moving in the barrel, which have not caught up with and acted on the projectile. However, just as the projectile is not aware of the increased pressures, by the same reasoning, decreased pressures will not have had a chance to act on the projectile. Hence the effects are opposing and are expected to cancel in part.

The chambered driver is accounted for by assuming a "steady-unsteady"[59] expansion. The equations for an infinitely chambered gun were published by Glass[60]. For flow velocities less than sonic a steady expansion is assumed and the pressure at the projectile is given by

$$\frac{p_{proj}}{p_{orig}} = \left[1 - \frac{\gamma-1}{2} \left(\frac{u_{proj}}{a_{orig}} \right)^2 \right]^{\frac{\gamma}{\gamma-1}} \qquad (3.13)$$

When the projectile velocity is sonic or greater, the pressure at the projectile is obtained through a two part expansion, i.e, a steady expansion to sonic conditions followed by an unsteady expansion to the velocity of interest. The pressure ratio across this process is

$$\frac{p_{proj}}{p_{orig}} = \left[\left(\frac{\gamma+1}{2} \right)^{\frac{1}{2}} - \frac{\gamma-1}{2} \frac{u_{proj}}{a_{orig}} \right]^{\frac{2\gamma}{\gamma-1}} \qquad (3.14)$$

3-2.2 Analytic Representation of the Projectile Friction

The state of the friction acting on a projectile in a barrel is very complex, since in reality heat-transfer, ablation, dynamic sliding friction and non-rigid barrel effects all act simultaneously. This problem has not been considered in any detail in the literature. However, estimates of the friction force can be made from simple considerations. Since the friction force is not a dominant one in the dynamics of the projectile, large percentage errors can be tolerated in its determination without substantially effecting the overall performance. In Ref. 61, an analytic estimate of the friction force is given based on a simple model. From the solution of the equation relating the state of the stress in the projectile to the applied loads and the requirements that the stresses along the axis of the projectile be finite and that the deformation of the outside diameter of the projectile vanish, it was shown that the normal stress at the wall are given by

$$p = \frac{\mu}{1-\mu} \cdot \frac{p_3 - p_2}{2} \qquad (3.15)$$

where μ is Poisson's ratio.

For a linear pressure gradient through the projectile the frictional force for a one-caliber projectile is

$$F_{frict} = 2 r^2 f_s \frac{\mu}{1-\mu} \frac{p_3-p_2}{2} \qquad (3.16)$$

where f_s is the coefficient of sliding friction. For the present performance program, f_s and μ were both taken as $1/3$, which is representative of μ over a wide range of materials and roughly true for the coefficient of sliding friction at low velocities for plastics. However, the coefficient of sliding friction generally decreases as velocity increases at least up to several thousand feet per minute. For velocities greater than this, no data exists. The friction force representation assumed here is probably larger than the actual one, hence its effects on the final velocity is probably overestimated.

3.2.3 Analytic Representation of the Counter-Pressure

The projectile moving along the barrel acts as a piston and compresses the gas ahead of it ultimately creating a shock wave which travels at a velocity in excess of the projectile velocity. The shock velocities involved are large hence the pressure behind the shock wave can be several orders of magnitude greater than the pressure initially in the barrel. As this pressure acts counter to the driving pressure, it decreases the acceleration and degrades performance. If the initial pressures in the barrel are kept very low this loss due to counter-pressure can be held to a negligible level. For cases where barrel pressures must be high, for example during photographic flow studies, this effect will degrade performance substantially.

Seigel[62] has shown that the pressure produced by an accelerating piston can be approximated to within 10-15 percent by the pressure produced on the piston at the same instantaneous velocity in a non-accelerating case. The counter pressure p_2 can then be determined directly from the initial pressure and the piston (projectile) velocity, by combining the equation for the pressure jump across the shock

$$\frac{p_2}{p_1} = \frac{2}{\gamma+1} \, U_s^2 \, a_o^2 \tag{3.17}$$

with the equation for the particle velocity (piston velocity) behind the shock

$$\frac{u_2}{U_s} = \frac{2}{\gamma+1} \, \frac{u_p}{U_s} \tag{3.18}$$

which yields

$$\frac{p_2}{p_1} = \frac{\gamma(\gamma+1)}{2} \left(\frac{u_2}{a_o}\right)^2 \tag{3.19}$$

To account for the acceleration effect in an approximate way an arbitrary factor of 1.15 was introduced. The counter pressure equation used in this program was

$$\frac{p_2}{p_1} = 1.15 \, \frac{\gamma(\gamma+1)}{3} \left(\frac{u_2}{a_o}\right)^2 \tag{3.20}$$

3.3 Performance Using Gaseous Driving

The performance model up to this point, predicts the projectile velocity-distance history up to two disposable constants, $t_*(r_*)$ and θ. If the logic of the model is valid then these constants, which can properly be called "system constants", if evaluated for one case should remain valid for all other cases and the velocities predicted should be in agreement with those obtained experimentally. Initially, experimentally determined velocities for two barrel lengths were taken as the pivotal conditions and values of r_* and θ were iterated to obtain values which would match the program to the two velocities. Unfortunately the non-linear nature of the velocity-distance profile did not yield reasonable values for r_* and θ. In the absence of any other workable method, r_* was fixed at the projectile radius and $\theta = 0.05$ was determined by matching the program to the experimentally determined velocity of 6660 ft/sec obtained using a 60-inch barrel, a one caliber polyethelene projectile and an initial pressure of 300 psia of stoichiometric oxygen and hydrogen. This value

is not inconsistent with a physical "feel" for a value of the decay per cycle. Had it been negative or greater than 10-15 percent per cycle then it would have been suspect.

With r_* and θ fixed, the program was "frozen" and performance at conditions away from the pivotal conditions calculated. Shown in Fig. 60 are the predicted values of projectile velocity for a one caliber polyethelene projectile ($\rho = 0.92$ grams/cc) and 60.0 inch barrel for various initial pressures of stoichiometric oxygen and hydrogen, and the experimental values determined by Watson[63] for the same conditions. The agreement is exact at the pivotal condition of 300 psi, but diverges for other pressures. For pressures greater than 300 psia the predicted values are greater than those measured. For pressures less than 300 psia, the performance model predicts lower velocities than those measured. This behavior could be caused by several factors. For example, sound speeds which are too high or gammas which are too near unity would give this behavior. As was shown in the comparison of the model with Brode's results of Sec. 3.1.4, the temperatures based on the model were generally too high for the stoichiometric case (Case 2) and also temperatures were generally too high if r_* were made significantly less than 1.0 cm, ($r_* = 0.279$ in this case). As there is no way to improve these values at present, the prediction must stand on its own merit, until further information allows the model to be refined.

Plotted in Fig. 61 are predicted projectile velocities for initial pressures of 200 and 400 psia for a range of dilutions of $6 > n > 0$ and $4 > m > 0$. The experimental data is from Ref. 63. It is seen that at the stoichiometric conditions ($n = m = 0$) that the predicted velocity at 400 psia is higher than the measured velocity and vise versa for the 200 psia value, as was shown previously. It is also seen that the decrease in velocity that occurs for mixtures away from stoichiometric predicted by the model is much greater than that which is observed. The "jog" in the curve for the 200 psi case is the result of an increase in the number of cycles experienced by the projectile as the dilution is increased for this barrel length. As the dilution is increased, the cycle time decreases making it possible for the projectile to experience an additional cycle before it leaves the barrel. For the 400 psi case, for these initial conditions, the number of cycles (N) was the same (11) for all of the dilutions and no "jog" appears in the predicted curve. The data of Ref. 63 also indicates a smooth transition from detonating combustion, indicated by the filled symbols and deflagrating combustion, indicated by the open symbols, and would suggest that the projectile velocity for gas driven runs is independent of the mode of combustion. This point is discussed further in Sec. 3.5.

The difference between predicted and measured trends with dilution can be explained partly from cycle time considerations. In Fig. 62 the predicted cycle time is plotted versus dilution index and compared with the measured cycle times of Ref. 63. It can be seen that the predicted times are too long by factors ranging from 1.3 to 2.0, and that the decrease in cycle time with dilution is not adequately described. Recall that, as the cycle time decreases more impulses will be felt by the projectile for a given time (or barrel length) hence its muzzle velocity will be greater. The rapid decrease in cycle time observed in practice tends to counter the velocity drop due to dilution effects alone by increasing the number of cycles that are experienced by the projectile. From a close scrutiny of the data it can be seen that for the 400 psia case for example, that "jogs" occur in the measured

58

values at n = 4 and n = 2, that may be the result of additional cycles being experienced by the projectile. However more data will be required, particularly at intermediate values of dilution index, to resolve this point. It should be clear that part of the discrepancy in the predicted performance with dilution comes from the inability of the present model to accurately predict the cycle time variation with dilution. The reason for the poor cycle time prediction is not clear at present.

Plotted in Fig. 63, are the measured and predicted projectile velocities as a function of barrel length for the same projectile and barrel as used previously at initial pressure of 200, 300 and 400 psia. The impulsive type of loading of the implosion launcher is apparent from the figure. The largest fraction of the velocity increase per cycle is felt during the first few microseconds of each cycle. For the remainder of the cycle, the pressure falls very rapidly ($\sim t^{-3/2}$), the velocity increase is very small and the projectile virtually "coasts" along. This acceleration profile is very undesirable and aggravates the projectile integrity problem but is inherent in this type of launcher. To obtain even velocities of the order of 8000 feet per second using a 60-inch barrel and a 400 psi stoichiometric oxygen-hydrogen mixture, say, requires a peak g loading of 7.2×10^6 g's. An equivalent constant base pressure case would require only 2×10^5 g's to obtain the same velocity, more than an order of magnitude less in acceleration, hence it should be clear that the projectile integrity requirements will be considerably more stringent for this type launcher than in a conventional constant base pressure light gas gun. This discontinuous velocity-distance behavior may explain some of the scatter in the data of Ref. 63, since small variations in technique if they coincide with conditions near the beginning of a cycle, can produce substantial variations in velocity. In this respect, comparing the data with a velocity band defined by smooth curves through the curve extremes is probably more meaningful, than comparing it directly with the discontinuous curve.

Plotted in Fig. 64 are the measured and predicted projectile velocities as a function of projectile density, for 0.22 inch diameter, one caliber projectiles using an initial driving mixture of stoichiometric oxygen and hydrogen at 100 and 200 psia. The data corresponds to polyethylene ($\rho = 0.92$ grams/cc) and teflon ($\rho = 2.15$ grams/cc) projectiles and is from Ref. 63. The absolute value of velocity for any particular density is 20-40 percent low as could be seen from the previous figures. However, the trend with density is described reasonably well by the present model.

In summary, it is seen that the predicted values of velocity are generally realistic for the gas case although better precision is certainly to be desired. How much of the agreement is due to the judicious choice of the pivotal condition cannot be determined from the presently available information. This and the other questions will be resolved and the model consequently improved by additional numerical solutions that will allow better resolution of the details of the chamber dynamics than can be obtained from the three numerical cases presently available. The development of complete numerical analysis is presently in progress at UTIAS and is expected to be ready in the near future, at which time many of these questions can be answered.

3.4 Performance Using Explosive Driving

The crucial test of the implosion driven launcher is the proof-firing using explosive-driven implosion waves. While explosive-driven runs

59

have been made, they have been done with such small amounts of explosive because of chamber limitations (see Sec. 5.1.2) that genuine hypervelocities, (30,000 to 50,000 feet per second) have not been obtained to date. In the absence of any "proof" runs, extrapolations must be made to explosive loadings in excess of those actually used. While this is not completely satisfactory, the trends using conservative extrapolations do allow a fairly clear picture of the performance of this driving concept to be made.

Two types of explosive driven runs have been made. The first series using lead azide as the explosive liner was terminated after the hazard of using this material was pointed out. Work was then directed to obtaining a safe explosive liner. After a PETN formulation was developed that would detonate at the desired initial pressure another series of runs was made using the PETN liner. The two series of runs will now be discussed.

3.4.1 Lead Azide Runs

In the discussion of the results of the explosive initiation study in Sec. 4, it will be shown that lead azide has many properties that make it a very desirable material for use in generating implosions. Unfortunately, as pointed out to the author by Duff[64], Havalick[65], and Kauffman[66], even in a slurry with water, in which form it was previously thought to be relatively safe, the hazard of using this material is such as to preclude its use on a day to day basis in any amount over a few hundred milligrams. At the time the hazard was pointed out, a series of runs to determine launcher performance was underway. Of the series, five had already been run. While the series was immediately terminated and no further runs have been made using this explosive, the data obtained from the runs have been of considerable value in understanding and evaluating the implosion driver. From an initiation point of view, these tests are closest to the ideal since the lead azide has been found to be initiated virtually instantaneously at the conditions investigated (100 psia - see Sec. 4.7.5) hence effects due to ignition delay are absent.

During this series of runs, an instrumentation limitation was uncovered. The then existing velocity measuring system was found to be incapable of detecting the 0.22 diameter projectiles at velocities over ~ 9000 ft/sec. As a result, a direct measurement of velocity was obtained only for the single 91 g (wet) charge of lead azide. All the other velocities were inferred from crater depth measurements on lead targets knowing that the penetration varied as $V_{proj}^{2/3}$, [67]. The penetration law was verified by the penetration data that were available at this laboratory at the time. Since that time, the velocity measuring system has been replaced by one capable of detecting projectiles well in excess of any velocities contemplated at this time. Hence this indirect velocity measuring method is no longer used. The penetration data and the assumed extrapolation are shown in Fig. 65. The extrapolation is felt to be conservative. The projectile velocities obtained from the lead azide runs are tabulated in Table 9 and are plotted in Fig. 66.

While there are only 4 data points involved, when compared with the predicted velocities, and analyzed in light of the present understanding of the implosion driving processes they are very useful in assessing the validity of the implosion driving concept. Also plotted in Fig. 66 are several auxiliary curves which will aid in the understanding of the implosion driven launcher. The results and predictions of the stoichiometric gas case are also plotted in Fig. 64 for comparison. For the gas case, a single value of energy is sufficient

60

to categorize the problem so there is no ambiguity in the interpretation of the data. For the explosive runs, the data has been plotted versus the energy content of the explosive liner only, as indicated by the filled symbols and also the total energy (gas energy plus explosive energy) in the chamber as indicated by the open symbols. In the absence of any other information the data appears to define two straight lines. While there is no ambiguity in using the lower end of the curves, which curve to extrapolate to use for the higher end is not clear from the data alone. Plotted also in Fig. 66 are the predicted values of velocity based on the total (gas+explosive) energy. While the absolute value of the predicted velocities is ~ 1.5 times those measured, the theory clearly indicates that a curved line in this plane is to be expected up to total energies of at least ~ 60 Kcal. For total energies greater than 60 kcal., a straight line relating velocity to the square root of energy is indicated.

It should be noted that the predicted performance has a very flat slope for the initial part of the curve indicating that large percentage gains can be obtained for relatively small amounts of explosive. Part of this is due to the inability of the present model to make a smooth transition between a "gas only" and an explosive driven case. However, the data indicates that this is at least in part true, since the slope of the experimental curve is initially very favorable. For the higher total energies the predicted velocities become proportional to the square root of the total energy. The predicted velocities are seen to be about 50% greater than those actually obtained indicating either that losses which have not been considered in the performance program or which have been underestimated, are present or that better performance could be obtained if experimental losses, such as gas "blow by", for example, could be overcome. Using an extrapolation from the two highest energy data points indicates that 350 kcal of energy is required to reach 50,000 ft/sec for this projectile and a 60-inch barrel. As can be seen from the explosive weight scale, this corresponds to an explosive weight of 2.630 kilograms, which for lead azide would yield a liner thickness of 0.985 inches. Increased radiative losses at the higher temperatures implied by this total energy, may make this extrapolation optimistic. For example, the calculated peak temperature for a run using 1000 Kg liner of lead azide is 3.7 x 10^6 °K. At these temperatures radiative losses would be expected to dominate the entire flow. More accurately, the radiative losses will probably not permit the temperatures (and pressures) to reach this level. The calculated maximum pressure and temperature reached at r_* during the explosive driven first cycle is also included in Table 9, and indicates the degree of severity of the environment that the projectile must survive albeit for only a short period of time.

Also shown in this figure is the predicted velocity for a 500 psi case. It has essentially the same shape as the 100 psi curve except that it is translated up and to the right, on this plane, indicating that better performance could be obtained for using higher initial pressures. This point will be investigated in forthcoming experimental work.

A very significant point concerning the overall performance of an implosion launcher is brought out in this figure. Recall in the gas driven runs that the velocities obtained for detonation and deflagration combustion runs were almost identical indicating that the effect of the mode of combustion on performance was unimportant. (It will be shown in Sec. 3.5 that this was the result of a fortuitous choice of operating parameters.) In general, the implosion driven launcher is very sensitive to the mode of energy addition. For example, from the figure it can be seen that if, say 45 kilocalories of energy is re-

61

leased in a gas run (200 psi) the resulting projectile velocity will be 5,700 fps. If the same amount of energy is released, but in a 1:1 ratio of gas energy to explosive energy (100 psi gas and ~ 200 grams of lead azide), ~ 14,000 fps is obtained, 2.4 times as great. Clearly the method by which the energy is added has considerable bearing on the resulting velocity.

Also shown in this figure is the projectile energy in kilo-calories, corresponding to the velocity for a 0.22 diameter, single-caliber, polyethylene projectile, and a grid indicating the percent of total energy that is transferred to the projectile. It is seen that the overall efficiency of the launcher is very low. For gas cases, only 0.1 to 0.2 percent of the total energy is transferred to the projectile. For the explosive runs it starts at ~ 0.2 percent for negligible amounts of explosive and increases as the total energy increases but asymptotically approaches a maximum of ~ 3 percent when the explosive energy becomes much greater than the gas energy. It would appear that the efficiency may improve with increasing initial pressure as evidenced by the higher asymptote of the 500 psia curve.

It should be clear from the discussion at this point that there are possibilities for optimizing the performance of the launcher which have not been examined, and that the launcher performance may be substantially improved by using optimized conditions. Presently an optimization study is being done at UTIAS[66] and results are expected to be released in mid 1967 in a separate publication.

3.4.2 PETN Experiments

After the hazard of using lead azide was pointed out a renewed effort was made at developing a safe explosive liner. In Sec. 4 it is shown, that after further study several additional explosive formulations were found that had the required properties and which were safe to use. Of these PETN was selected as being the most promising for use with the implosion driver. All of the subsequent implosion work has been done with this explosive.

An experimental program was planned which was to determine the effects of the various operating parameters and to "proof" fire the gun. However, it became clear after only several runs had been made, that a number of new problems had been uncovered. The high energy density of PETN (~ 10 times that of lead azide) made it impossible to make liners thin enough to be comparable to the lead azide in energy. For example, a PETN liner containing 25 kilo-calories (equivalent to ~ 200 grams of $P_b N_6$) would be 0.021 inches thick. Maintaining uniformity of thickness in dimensions of this order is beyond present capabilities. In practice, the minimum thickness that can be manufactured reliably is ~ 0.090 inches, which corresponds to a total energy of ~ 100 kilo-calories. Anticipated erosion and damage to the barrel (examples of which are shown in Sec. 5) made it necessary to design an expendable barrel made of thick wall tubing. However barrel straightness and finish were downgraded and bore sizes of only nominal 5/16 and 3/16 inches could be obtained. However, the barrels could be made much longer. As virtually all of the operating parameters, including initial pressure, length, bore, explosive were changed, a direct comparison of the PETN runs with the previous runs is not possible and the PETN data must be considered separately. Liners of nominal 80 and 200 grams were manufactured and run. The results of the experiments are tabulated in Table 10.

The first run (No. 205) using an 81.3 gram liner of PETN and nominal 5/16 inch diameter polyethylene projectile resulted in a measured velocity of 17,650 feet per second, slightly less than one half the predicted value. The crater made in the lead impact plate suggested that the projectile was badly distorted if not in fragments. However, no photograph was obtained of the projectile in flight so the condition of the projectile cannot be positively identified. Subsequently a run (No. 213) using a 91.5 gram liner of PETN resulted in a measured velocity of 10,520 feet per second. The crater left by the impact is shown in Fig. 67. The projectile as shown in Fig. 68 has deformed substantially taking on a "liquid" shape and separated into several smaller pieces. Runs at 209.4 (Run No. 209) and 213.8 grams (Run No. 210) yielded no velocity measurement. Photographs of the projectile in flight, shown in Fig. 69, and the impact plate, shown in Fig. 70, indicate complete breakup of the model.

Magnesium projectiles were then substituted in an attempt to find a projectile configuration which would survive the launch. Unfortunately the higher density also degraded the velocity performance. A 76.3 gram run (Run No. 214) resulted in an intact projectile, as noted photographically and as evidenced by a single large crater at the impact plate (Fig. 71). However a run using a 96.8 gram liner (Run No. 219) resulted in failure of the projectile. Two additional runs at nominal 70 grams of PETN, (Nos. 215 and 216) but using a 0.187 inch bore barrel in an attempt to regain the velocity performance resulted in fragmented projectiles.

A fiberglass projectile made from a rod with fibers running longitudinally and having a density of 1.5 grams/cc was fabricated. A run using 90.8 grams of PETN (No. 218) resulted in a measured velocity of 11,100 feet per second but the photograph of the projectile in flight, shown in Fig. 72 shows that the epoxy which binds the fibers together has failed although the fibers are substantially intact.

A stainless steel projectile (ρ = 5.5 g/cc) using a 74.0 gram PETN liner (Run No. 217) and a 0.187 barrel resulted in an intact projectile however, the velocity was only 3,750 feet per second.

As a result of this data, proof runs at hypervelocities have been temporarily suspended pending the solution of the projectile integrity problem. This problem which is currently under intensive study will be treated in a separate report by Graf[69]. While no specific recommendations can be made at this time, it appears that part of the problem at least is due to the present straightness and finish of the thick wall tubing barrels which are not as well finished as the smooth bore 0.22 inch barrels. This point is supported by the fact that polyethylene projectiles survived intact launches to 15,000 ft per second in the 0.22 inch barrels while they failed at lower velocities in the 5/16 inch thick wall tubing barrels. However, it is possible that the lower velocities are an effect of the failure rather than the cause of it. Present work on improving barrel condition will resolve this point.

3.5 "Average Base Pressure" Considerations

Some insight into the performance advantages and disadvantages of an implosion-driven gun can be had from an analysis of the "average pressure" over a cycle assuming that variations over the projectile radius, finite sound speed effects and other such complications can be neglected. The equivalent constant pressure which will yield the same impulse as the time varying pressure of the implosion driver can be found as follows. The value of the "average" pressure will vary depending on the time over which the average is taken. For long times i.e., where the number of cycles (N) is large, the average is given by

$$\lim_{N \to \infty} \frac{1}{t_{cyc}} \int_{0}^{t_{cyc}} p(t)\, dt = \bar{p} \tag{3.21}$$

Using the "flat top" pressure profile technique to avoid the singularity at $t = 0$, i.e., taking

$$p(t) = p_* \qquad 0 \le t \le t_*$$
$$p(t) = Kt^{-3/2} \qquad t_* \le t \le t_{cyc} \tag{3.22}$$

where

$$K = p_* t_*^{3/2}$$

and is fixed for a given chamber radius, explosive loading etc. and integrating yields

$$\frac{\bar{p}}{p_*} = \frac{t_*}{t_{cyc}} \left[3 - 2 \left(\frac{t_*}{t_{cyc}} \right)^{\frac{1}{2}} \right] \tag{3.23}$$

This relation is plotted in Fig. 73. It can be seen from the figure that the average pressure varies considerably depending on the value of t_*/t_{cyc}. For $t_{cyc} = t_*$ the average pressure and the characteristic pressure are identical. The average pressure then decreases as t_*/t_{cyc} decreases and for $t_* \ll t$ varies as

$$\text{const} \; \frac{t^*}{t_{cycle}} \tag{3.24}$$

The implication of this result is quite clear. If large values of average pressure are to be produced then t_*/t_{cyc} should be as large as possible. In terms of the physical variables this shows that if the cycle time which is a function of the chamber size and the average wave velocity is large then the average value of pressure will be low for t_* fixed. Clearly small chambers and high sound speed gases are desirable.

For cases where $t_*/t_{cyc} \ll 1$ then the average pressure over a cycle will be only a small fraction of the pressure p_*. For practical cases, where the maximum pressure is limited by projectile or other considerations, a very serious limitation will be placed on the performance. From the inverse point of view, the projectile strength requirements can be several orders of magnitude greater than an equivalent (in velocity performance) conventional constant base pressure gun requirements.

One previously unexplained result of the gaseous detonation runs is now clear. Watson[63] found that the velocities for dilutions which could be

made to either detonate or deflagrate depending on the violence of the ignition (small capsules of lead azide were used to detonate a mixture which would otherwise have deflagrated) were nearly the same. This is possible if the cycle time is such as to make the average pressure be nearly equal to the steady pressure that would be obtained in constant volume combustion.

For instance, for a N = 7 mixture initially at 100 psia Benoit[70] predicts an average value of pressure after constant volume combustion of 893 psi. Extrapolating Watson's cycle-time data to this condition yields a cycle time of 55 μsec. If we assume $t_* = 2.5$ μsec i.e., $t_*/t_c = .045$ then from Fig. 73, $\bar{p}/p_* = 0.116$ and since at t_*, $p_* = 7220$ psi it follows that $\bar{p} = 836$ psi or roughly the constant volume combustion value. There are of course other effects which are neglected here. However, the point is made that for the gas cases at hand, the average pressure over a cycle in the detonation case and the pressure in the constant volume case are very nearly the same, hence the resulting performance will be very similar.

4. ONE-DIMENSIONAL EXPLOSIVE INITIATION STUDIES

As noted in the introduction, the key technical obstacle to be overcome in the development of the Implosion-Driven Launcher was the simultaneous and uniform initiation of the explosive liner which generates the imploding shock wave. If this could not be accomplished, then little hope could be held for holding the high degree of symmetry which is required if the high pressures and temperatures at the origin predicted by the theory are to be realized. Accordingly, considerable effort has gone into solving this particular problem. In this section the problem will be discussed in detail, some pertinent initiation theories reviewed, and results of past studies at UTIAS reviewed. The results of a new study are considered at length and finally the feasibility of gas detonation wave initiated, explosive-driven imploding waves is demonstrated.

4.1 Specification of the Problem

It is worthwhile to enumerate and discuss the properties that the explosive liner must have if it is to be useful in this application.

1.   The explosive energy release must be nearly instantaneous and uniform over the entire liner surface. While this implies detonation of the explosive and negates deflagration, it does not necessarily imply full ideal detonation velocity. For example, even if ideal detonation velocity is not reached in the liner (in fact it is to be expected that this will not occur in the thin liners involved, except for perhaps primary explosives such as lead azide, which have extremely short induction distances) the energy release must occur over a short time scale compared to the time scale of the motion of the reflected shock. This requirement can be stated formally. The time it takes for the reflected shock to move a distance characterised by the thickness of the explosive must be of the same order or longer than the time required for the detonation wave to propagate through the explosive

$$\frac{d}{U_{s\ ref}} \geq \frac{d}{D} \tag{4.1}$$

65

or simply

$$D \geq U_{s_{ref}} \tag{4.2}$$

Since the smallest value of the reflected wave velocity i.e., that for the reflection of a gaseous detonation wave is for stoichiometric oxygen-hydrogen mixtures, ~ 2.0 kilometers per second (Sec. 4.7), then

$$D \geq 2.0 \text{ kilometers per second} \tag{4.3}$$

Since the full ideal detonation wave velocity for explosives is in the range 3 to 10 kilometers per second,[71] it is seen that this requirement is easily satisfied even if only two-thirds of the ideal detonation wave velocity is reached. Indeed for some explosives where D is of the order of 10 kilometers per second then $D \gg U_{s_{ref}}$ and the explosive can be assumed to detonate instantaneously. Deflagrating conditions which have wave velocities of the order of 10 millimeters per second[71], that is to say, several orders of magnitude less than the detonation wave velocities, can immediately be disqualified for this reason. Further if there is a delay time characteristic of the time to transit to a detonation say, this must be sufficiently small that the reflected wave has not propagated away from the explosive surface a few times the distance of the explosive thickness. Again since the initial reflected wave velocity is of the order of 2 mm/μsec and since the explosive thickness contemplated are 0.1 to 0.5 inches (2.5 to 13 mm) then the delay times must not be more than ~ 5-10 μsec.

2.   If gaseous detonation waves are to be used as the initiation mechanism then the initial pressure in the unburned gaseous mixture must be of the order of ~ 10-50 atm. The post detonation pressure in the steady - at rest central region, prior to the implosion, is about 5 times the initial loading pressure, hence the imploding shock sees a hot gas at rest with an initial pressure of ~ 50-250 atmospheres. Too great an initial pressure would mean that the relative strength of the imploding wave i.e., its shock Mach number, would be reduced substantially hence the temperature and escape speed would be reduced significantly. If the explosive is initiated in some other manner as for instance by light initiation, this requirement must be modified accordingly.

3.   The explosive liner must be completely safe to handle, insensitive to small jolts such as would be experienced in transporting the liner from the magazine, or installing it in the chamber. This is of particular importance since the liner, which weighs about one pound in its present configuration, would cause fatal injuries to personnel and considerable damage to equipment in the vicinity if it were to detonate accidentally. It will be shown below that several explosive materials which, although ideal in all other respects, are too hazardous to use in an operational situation, although they were tested in a carefully controlled series of experiments.

4.   The liner must have sufficient mechanical strength to hold its shape during transportation, evacuation and pressurization of the chamber. The explosive need not necessarily have mechanical strength itself provided it can be attached to, and will remain attached to a carrier which will provide the necessary shape.

5.   The explosive must be capable of withstanding the evacuation, and pressurization process without igniting or decomposing.

6.   The explosive must be sufficiently homogeneous so as not to introduce significant nonuniformites in the symmetric imploding shock. This is particularly important since it is possible that spherical imploding shocks may be unstable to small disturbances, hence nonuniformites in the shock surface would be magnified during the implosion process.

7.   The explosive liner assembly must be relatively inexpensive. This implies that the explosive must in turn be inexpensive and that the fabrication technique must not be overly complex.

       Of the above seven, the most stringent is the initiation requirement.

4.2 Review of Initiation Theories

       In this section some pertinent initiation theories are reviewed and interpreted in light of the present requirements. Historically, the study of the sensitivity of explosives to initiation has been on an empirical bases. Up until World War II, the drop test[72] was the standard of reference. In this test a small sample of the explosive to be investigated was placed between two metal cylinders and clamped in such a manner as to allow the free vertical movement of the upper cylinder. A known mass was then dropped onto the cylinders from a predetermined height and initiation or failure to initiate noted. Some typical values of critical impact energy obtained using this type of apparatus are given in Table 11 for some common explosives. While this test offers some qualitative measure of the sensitivity, i.e., TNT is found to be less sensitive than lead azide, for example, it does not give any detailed knowledge of the physical processes of initiation, and hence can give only qualitative information for our present purpose.

       A major effort was made during World War II to understand the physics of initiation. While some progress was made it is only in the last decade that quantitative predictions of sensitivity have been made, and then unfortunately only for a very few explosives. The phenomena of initiation can be separated into two distinct types, initiation from weak sources such as flames, of which the works of Bowden and coworkers[73,74] offer much information, and shock initiation. Historically initiation from a flame front and the subsequent transition to detonation was first studied by Kistiakowsky[75] and Ubbelohde[76]. While some of the details of their hypothesis have been subsequently rejected, the concept is generally accepted and later works have been essentially extensions and refinements. They consider the case of a deflagration occurring at a point in the interior of a mass of explosive. As the flame front propagates into the material, pressure and thermal gradients develop. After a sufficient length of time or distance into the explosives, this process accelerates because the reaction rates are very temperature sensitive and very steep gradients (shocks) develop. Behind these shocks the pressure and temperature conditions are such that the reaction time becomes sufficiently short, that it is no longer the limiting factor in the process and a steady state detonation (shock wave followed immediately by a thin reaction zone) develops. The concept of a critical size or critical length to detonate follows immediately from the above.

       The distance to transit from a deflagration to a detonation is much larger than the explosive thickness contemplated for the implosion launcher (0.1 - 0.5 inches). For example Gipson and Macek[77] have measured flame-initiation-to-detonation induction distances of from 6 to 18 cm. for DINA and Pentolite when

initiated by nichrome wires, and Griffith and Groocock[78] have measured burning rates of 0.8 mm/μsec for 100 μsec (8.0 cm.) for granular PETN (ρ = 1.2 g/cc). These distances are about an order of magnitude greater than those required for the implosion driven launcher, hence this mode of ignition does appear to be practical here.

The later stage of the above, where a shock propagates into the explosive and the conditions behind the transmitted shock are sufficiently strong to initiate and support the reaction, a detonation wave will result. If less than a critical value, the shock will decay and a deflagration wave will result.

The "gap test"[79], which has replaced the impact test as the commonly accepted measure of sensitivity, is essentially a controlled shock initiation test. For this test a donor (standardized NOL donor, shown in Fig. 74, is a tetryl charge, ρ = 1.51 g/cc, 5.08 cm. in diameter by 5.08 cm. long) is spaced a known but variable distance from an acceptor charge. This dimension or the material filling the gap, typically lucite or cellulose acetate, is varied to attenuate the shock produced by the donor. Detonation or absence of detonation in the acceptor after a given length is implied by the distortion or absence of distortion of a mild steel witness plate at the further end of the acceptor.

The peak shock pressures applied to the acceptor and the time history have only been recently calculated for the shock test.[80,81] These profiles are known with reasonable precision, hence the test can be considered calibrated in an absolute sense. However, the range of donor dimensions (i.e., pressure profiles) and acceptor dimensions investigated has been relatively small and while good absolute values are obtainable, they are not in a pressure range that is of immediate interest for the present work, being several orders of magnitude greater than those produced by an impinging gaseous detonation wave. This limitation of the "gap test" has been realized by workers in this field and interest in the problem of shock loading at much lower pressures than those produced in the donor - acceptor test, has been revived of late after a dormant period of ~ 20 years. The first reported work (1939) using gaseous detonation waves to initiate explosives was that of Andreev and Maslov[82] who investigated the sensitivity to initiation of detonation waves of PETN, tetryl, picric acid, blasting gelatin and lead azide.

Presently the revival of interest in this area (Refs. 83, 84, 85 for example) has been concentrated on propellents where the emphasis is on finding materials which will not detonate under these high pressure gas loadings rather than those which will, hence this information is not generally of direct use to the specific problem here.

Andreev and Maslov's explosive studies were done in an apparatus similar to the one-dimensional chamber presently used at UTIAS (see Sec. 4.3) except that the total length was greater by a factor of 10, (one meter). As a result their pressure time histories are extended in time. However, it is interesting to note that their pressure limits to detonate PETN pressings are substantially the same as those measured at UTIAS i.e., 10 atm for their work as compared with ~7 atm for the UTIAS tests. This observed insensitivity of explosive initiation to length of time of pulse application can be understood in the light of some recent studies of the initiation process.

Shock Initiation Calculations

Much insight into the initiation process has been given recently by an original work of Hubbard and Johnson[86]. They set up a one-dimensional time dependant, hydrodynamic, numerical code in which the temperature dependant chemical reaction rates were accounted for, and applied this to the problem of a shock propagating into a semi-infinite explosive. By integrating the equations numerically for several pressure-time history inputs they were able to watch the progress of a shock in the material and the subsequent transition to a detonation or deflagration. They assumed an unreacted equation of state of a form that includes covolume effects, i.e.,

$$p(v-b) = (\gamma-1)e \qquad (4.4)$$

where, $\gamma = 3.0$
$b = 0.25$ cm^3/gram

and a chemical reaction rate of the form

$$g = \nu(1-f)^n \exp(-E_a/RT) \qquad (4.5)$$

where, ν = collision rate = 10^{14} sec^{-1}

f = fraction burned

n = reaction order = 1

E_a = reaction energy - 4 Kcal/mole

with

$$e = C_v T$$

where,

$$C_v = 0.30 \text{ cal/g}^o K$$

While these values are generally representative of explosives, together they produce somewhat unrealistic parameters such as a detonation velocity of 13.6 cm/μsec. The value of these numerical experiments is not in the absolute values of calculated results but rather that they show clearly the dynamic behavior of the transition process i.e., transition to detonation or decay to deflagration, as a function of the initial loading conditions.

In Fig. 75b are plotted pressure profiles at three instants of time following the application of a square wave of 10^5 atm amplitude for 0.69 μsec. At a point in the explosive, $x \sim 0.2$ cm, the temperature-time conditions have been such that energy is liberated at a rate faster than it can be conducted away. The pressure and temperature increase vary rapidly to a point such that 0.2 μsec later (at 1.0 μsec) a steady detonation wave has developed. In Fig. 75a are also plotted pressure profiles for the same instants of time, for the same pressure, but of 0.64 μsec duration, 0.05 μsec shorter than the previous case. In this case, the temperature time history is such that the reaction does not "run away" and the pressure wave decays to a deflagration wave. It should be pointed out that the 10^5 atmosphere pressure amplitude was chosen to produce detonations in a reasonable computing time, and was sufficiently low so as not to overdrive the detonation. It should not be taken as representative of any

limiting or critical pressure. From an analysis of a number of numerical experiments such as these the physics of the problem appears. For a short period of time after the shock passes an element, little energy is liberated as evidenced by the slow increase in pressure. After a certain delay or incubation time the energy is released progressively faster until the rate reaches that necessary to support the detonation velocity. This delay is a direct consequence of the sensitivity of the reaction rates with temperature. After one element detonates the high pressures produced quickly ignite the adjacent element with no incubation time and a steady detonation wave is produced. The functional dependence of the delay time on the other parameters is given by Hubbard and Johnson as

$$t_{incub}/\tau \;=\; \frac{1}{\Phi^2}\; \exp \Phi \qquad\qquad (4.6)$$

$$\text{where} \quad \Phi \;=\; \frac{C_v\, E_a}{R\, E_o}$$

$$\text{and} \quad \tau \;=\; \frac{C_v\, E_a}{R}\; (\nu\varphi)^{-1}$$

$$E_o = \text{energy behind the shock}$$

There is a characteristic time τ, which is a function solely of the properties of the explosive but that the fraction of this characteristic time which is taken to produce transition in a specific case depends on a factor containing E_o^2 and an exponential also containing E_o. E_o is the energy state in the shocked explosive hence is a function of the strength of the transmitted shock. Clearly strong shocks decrease the incubation time and vise versa until that level of weakness is reached which will not initiate a detonation in an infinitely long specimen.

In order to obtain absolute values for the incubation time t_{incub}, not only must the usual properties of the explosive be known such as $\overline{C}_v$, Q, etc but also the unreacted Hugonoit. Generally, unreacting Hugonoit's are only presently being sought and reliable detailed information is scarce. Further many explosives are inhomogeneous containing voids and grains of finite size which negates a continuum approach. A comparison with some initiation data was made in Hubbard and Johnson's paper. They noted that their relation predicted a much stronger effect of shock internal energy than was measured. They attributed the discrepancy to lack of realistic equations of state from which to calculate their delays.

While the magnitude of the predicted values may be of little value at the present, the understanding of the processes involved is not. The point that is brought out by their work is that detonation will occur if the temperature-time history of any point in the explosive crosses the curve given by the delay equation. For example, in Fig. 76, which is taken from Ref. 86, the energy (temperature) time histories of 4 pressure pulses are plotted along with the delay equation. For cases B and D the temperature-time history curve did not cross the delay curve defining the detonation boundary and deflagration resulted. Cases A and C crossed the boundary and detonated. The point made is that lower temperatures will cause detonation if held for a longer period of time (this implies long induction distances). Conversely, higher temperatures require shorter times. Clearly the initiation dependence on E_o is very strong, or conversely the curve describing the initiation of detonation limit varies weakly with the time a given temperature is held. The reason that Andreev's

70

and the UTIAS initiation limits for PETN are nearly the same, even though the time of application of the pressure varies by an order of magnitude, is now clear.

Enig[87] of NOL has studied essentially the same initiation problem of Hubbard and Johnson, using a different numerical scheme. He also considers a piston which pushes at constant velocity against one surface of a chemically inert slab the other surface of which is in contact with the explosive. The dynamics of the resulting shock and subsequent growth to detonation or decay to deflagration can be followed as in the previous work. The conclusions that Enig draws are essentially the same as the previous work.

Mader[88] has recently extended this type of calculation to the shock initiation of nitromethane, liquid TNT, and single crystal PETN using realistic equations of state and concludes that the computed pressures and velocities as a function of time agree with the experimental values to within the probable experimental error. However, no published work has been done to define the detonation boundaries for these materials. Mader has also extended the calculations to include the effects of voids. He observed that the interaction of the shock with a void or inhomogeneity produces a local "hot spot" in the explosive of sufficient intensity to cause detonation to occur under conditions that normally would have resulted in deflagrations in the homogeneous material. This point is of considerable significance in the present study since it indicates that the initiation boundary can be substantially lowered by the inclusion of voids.

Work has also been done of late on the effect of thermal pulses on the initiation of explosive materials (chiefly propellants) both by the use of shock tubes where both pressure and temperature effects are combined and radiant pulses from furnaces. In these cases the increase in temperature of the propellant is primarily from the convective (or radiative) heat flux. Delay times of the order of milliseconds are required for ignition.[84],[89] However Cook[71] notes that .."detonating gases are capable, above certain critical pressures, of causing very sensitive explosives such as fined grained, low density PETN to detonate evidently almost directly..", but gives no further information. It will be seen in this section that PETN can be made to detonate by gaseous detonation waves in initial pressures as low as 50 psi. In this low pressure regime it is not clear whether the detonation is caused by shock heating, convective heating, local hot spots due to voids, or a combination of the above. For both shock heating or convective heating the temperature history of the explosive is the key parameter. This is proportional to the transmitted shock strength for shock initiation which in turn is proportional to the initial pressure in the gaseous mixture. If the initiation is due to convective heat transfer, the heat transfer rate can be varied but it is also proportional to the initial pressure of the gaseous mixture, making it difficult to separate the two effects. Definitive experiments have not been performed to date.

With this qualitative understanding or perhaps lack of clear understanding of the initiation process, the search for explosive suitable for use with the implosion driven launcher can be directed specifically to finding an explosive with a low enough transition time for the gaseous detonation wave induced shock wave or rapid enough convective heating that detonation in the solid explosive is reached is less than a few (5-10) μsec or in a distance of less than a few (0.1 - 0.5) inches of explosive.

4.3 Review of Past Work at UTIAS

· It was recognized early in the research that the key technical
obstacle to be overcome would be the initiation of the explosive liner. Some
critics of the technique pointed to the very high pressures required to initiate
secondary explosives and suggested that it was not possible to initiate secondaries
with a gaseous detonation wave. Accordingly, initial efforts were spent in
investigating the initiation properties of explosives under conditions similar
to those experienced in the launcher. Since the results and understanding of
the initiation process would be camoflaged by the three-dimensional nature of
the convergence in the hemisphere it was decided that the shock initiation pro-
blem should be studied by itself in a one-dimensional framework. It was also
decided, at that time, that initial efforts would be concentrated on the initia-
tion by the collision of gaseous detonation waves although other possibilities
for ignition existed. Further by proper design of a one-dimensional experiment,
the amount of explosive used per experiment could be reduced considerably (factors
of 60) hence the hazard of using untested materials reduced. It was felt that the
results obtained in a one-dimensional study could be carried over with little
correction to the hemisphere since the initiation process even in the hemisphere
is essentially one-dimensional in character.

Dr. A. H. Makomaski (now at the National Research Council of
Canada) designed and constructed a one dimensional chamber to be used for the
initiation study[90]. A view of the apparatus is shown in Fig. 77, and a cross-
section is shown in Fig. 78. It is essentially a small cylindrical cavity 1.5
in. dia. and 10 cm. long in a massive high-strength-steel block. The 10 cm.
dimension was chosen to duplicate the radial distance of the hemispherical
chamber, since it was expected that there would be difficulty in producing a
steady-state detonation wave in the gas in such a short distance. Subsequent
results show that this is not a serious problem. The explosive samples were
held in a "witness cup" at one end and an exploding cross wire initiated a
gaseous detonation wave in a stoichiometric oxygen-hydrogen mixture at the other.
The cross wire was chosen to aid in the early formation of a planar wave.

Using this apparatus Makomaski investigated the initiation pro-
perties of PETN pressings at densities of 0.85 and 1.00 g/cc and determined the
lower limit of initial pressure of a stoichiometric oxygen and hydrogen mixture
that will insure a detonation in the PETN for this geometry to be ~ 12.5 atm.
Details are reported in Ref. 90. The criteria for determining if the explosive
had or had not detonated was the presence or absence of significant distortions
of the witness cup which held the explosive. Below 12.5 atm initial pressure,
the dimensions of the witness cups remained essentially unchanged during a run.
Above 12.5 atm initial pressure, the dimensions of the cup changed as a permanent
deformation of the witness cup occurred. The surface of the cup was also bruised
and deformed in a manner suggesting pressures greater than the yield stress of
the witness cup material, which for his studies was ULTIMO 4 (yield $\simeq$ 85,000
psi). The calculated detonation pressure of PETN at a loading density of 1.0 g/cc
is by comparison 7.6×10^4 atm. No other quantitative measurements were reported.

While these results were very encouraging, as they showed
secondary explosives could be initiated in this a fashion, it was felt that
quantitative data of a more precise nature was required to understand and gain
insight into the wave dynamics and initiation process. The question as to the
strength of the gaseous detonation wave, its velocity, if over-driven, remained
unanswered as was the strength of the reflected wave produced by the detonating

explosive. Makowaski did try some incident wave speed measurements using ioniza-
tion probes but concluded that his gages were not suitable for this work although
their simple construction might make them very attractive in less hostile con-
ditions. He also tried photo detectors to measure the wave speed but inade-
quate frequency response of the OAP12 photo diodes prevented any quantitative
measurements. Time did not permit him to try other techniques.

On critical review, it was concluded that the results were most
promising, as initiation of detonation in thin layers of explosives at moderate
pressures was demonstrated on the foregoing basis and that the approach was
sound, but that quantitative data would be required if the wave processes
occurring in the chamber were to be fully understood. Accordingly the first
efforts in the new phase of this work were in the direction of instrumentation.

4.4 One-Dimensional Chamber Instrumentation

The severe environment produced in the chamber by the contained
explosive makes it difficult, if not impossible, to use many measurement tech-
niques. A wave speed measurement is probably the most useful measurement provided
both incident and reflected wave histories can be determined. In principle
several instrumentation techniques could give wave speeds, as for example photo-
graphic streak camera techniques, however ionization probes were chosen since
they are relatively straight forward to design and use. Streak camera techniques
would have required substantial modifications to the existing chamber. An
ionization probe acts essentially as a switch closed by the ionized gas behind
the detonation or shock wave, hence it gives an accurate indication of the time
of arrival of the detonation or shock wave. It has the disadvantage that it
cannot yield any profiles of the properties behind the waves.

After several attempts, an ionization probe that would with-
stand the hostile environment was successfully developed. A view of the final
design of an assembled probe is shown in Fig. 79. A sectional view is shown
in Fig. 80. The probe consists of a single stainless steel electrode potted
with epoxy resin into a holder. The electrode has a maximum diameter at the
lower end greater than the minimum inside diameter of the probe housing so that
the electrode cannot be blown out. The epoxy resin makes a satisfactory vacuum
and pressure seal. Electrical connections are made by a central electrical lead
also potted for strength and the end fitting is a standard BNC connector. The
entire circuit is shielded by the probe housing and connector and minimizes
pickup from electrical disturbances which were present when the capacitor in the
ignition circuit was discharged. This "noise" source was subsequently quieted
(See Sec. 5.1.1).

To date this construction has demonstrated excellent vacuum and
high pre sure holding qualities. An average probe lasts approximately 10 runs
before it breaks down due to imbeded carbon deposits or significant ablation of
the epoxy surface. One probe survived 23 runs in the position nearest the ex-
plosive before being removed from service. The only maintainance required is
the routine cleaning of the exposed surface after each run and a check for
shorts and continuity.

The circuit used for differentiating the signals from the ioniza-
tion probes was a modification of the classical circuit of Knight and Duff[91].
The circuit, shown in Fig. 81a, has been used for many years for velocity mea-

surements in shock tubes and for detonation velocity measurements both in gases and solid explosives. In its original form it senses a single pulse from each probe per run. In principle the circuit could sense waves repeatedly, provided the time constant for recharging capacitor C_1 is less than the time between signals. The time constant for recharging C_1 is essentially R_1C_1, which for the original circuit is 22 milliseconds. The high resistance of R_1 is required to isolate the several sections from one another. By substituting a resistor and diode for this high resistance, where R is now reduced to 4700Ω, the capacitor should in principle recharge in approximately 5 microseconds and yet the separate sections remain isolated due to the high reverse resistance of the diode.

To be exact, it should be noted that the probes are not ideal switches operating in an on-off manner as they have a finite "contact" resistance due to the finite conductivity of the gas. Rather they are detecting a change in contact resistance as if resistors of different values were being switched in and out.

The actual value of R_1 used for this experiment was obtained by trial and error and gives readable signals for the conditions encountered here. If this circuit were to be applied elsewhere under different conditions the optimum values of R_1 would have to be changed accordingly. The circuit as used in this study is shown in Fig. 8lb. Using the modified circuit in conjunction with the robust probe, both the incident detonation wave and the reflected explosive driven wave can be detected in the time scale of the present experiments.

4.5 Direction of Search for Suitable Explosives

As noted in Sec. 4.2, there is little initiation data at conditions near those to be produced by a reflected gaseous detonation wave in the launcher chamber. Most explosive initiation experiments in the literature are for pressure levels several orders of magnitude greater than pressures produced in the gaseous mixture with the exception of Andreev and Maslov's work. Peak pressures produced in the standardized NOL gap test for example are approximately 50 K bars[80] (735,000 psi) whereas the peak pressure produced at a rigid wall by a reflected gaseous detonation wave is 6150 psi for a stoichiometric mixture initially at 10 atmospheres[92]. Accordingly, the search for a suitable explosive had to progress on a pragmatic basis with some skepticism toward the drop-test data, but with the various initiation theories and hypothesis and experience as a guide. In this respect, the wealth of knowledge and experience brought to the project by Professor G.F. Wright of the Chemistry Department, University of Toronto, was of inestimable value in solving this key problem.

From the point of view of initiation, primary explosives are indicated. However, they generally have small energy densities. From the point of view of minimum thickness of liners, secondaries which have large energy densities, are required. In the absence of any hybrid materials, a "sandwich" type of liner having a layer of primary explosive over a secondary is indicated, similar in principle to many commerical explosive products, for example, primers in cartridges or the use of blasting caps to initiate bulk explosives. However, it must be realized that safety is maintained in commercial blasting applications, in part, by attaching the initiator to the bulk explosive shortly before its use. In this way, the only source of initiation is kept

away from the main body of the explosive until initiation is desired. Since the "primer" layer in the liner for the launcher would be in intimate contact with the secondary layer from the time of manufacture, the restrictions on the reliability and safety of the primer are the same as on the secondary, since any spontaneous initiation of the primer would initiate the entire liner, not just the primer. It will be seen below that several "sandwich" types with other desirable properties were developed but had to be discarded because the primer was not sufficiently safe.

Fortunately there are a few explosives which can properly be called hybrids since they can be made to have both the sensitivity properties of primaries and the energy density of secondaries. PETN which was chosen as the most promising explosive for generating implosions is one of these. Its explosive initiation properties vary with the loading density which can be varied over a wide range. At low loading densities its sensitivity to initiation by gaseous detonation wave is comparable to many primaries but without their hazard. Further, its sensitivity to handling or static electricity can be reduced by adding water. It does not have the reputation of detonating spontaneously, and is generally considered to be a "safe" explosive when handled with the care required of materials of this type.

The search for a suitable explosive progressed as follows. Generally, explosives that suggested promise were tested first at moderate initial pressures. If they detonated, the pressure on each succeeding test was progressively lowered until the pressure limit was reached. If a detonation was not clearly evident they were discarded. Several runs were made around the pressure limit to define the limit and indicate approximately the band of uncertainty. However no great effort was expended to obtain high precision for the uncertainty band. Several explosives which could not be made to detonate but which had other desirable properties, for example ease of manufacture or energy content, were tried in combination with a surface layer of more sensitive explosive.

PETN pressings similar to those used by Makomaski were the first to be investigated. While the results reaffirmed that the detonation pressure limit was sufficiently low and cleared up ambiguities in his work, the problem of manufacturing a hemispherical shell from dry crystals of PETN appeared formidable. The emphasis then shifted to primaries such as lead azide, tetracene, nitromannitol which were proportedly safe when wet, and which could be applied in damp paste form. The intent was that the liner could be fabricated wet, then dried, hence armed, inside the chamber in complete safety. For the present conditions, the only one of these to work well was lead azide but the hazard of using lead azide even wet is still sufficiently great as to preclude its use, as noted previously. As will be seen, lead azide worked extremely well alone and also as a primer to initiate less sensitive explosives. It was disappointing that its use had to be abandoned in the interests of safety.

The emphasis then shifted to intermediate types of explosives such as nitrocellulose and PETN and finally to finely divided PETN with a binder in a paste form or in a matrix. In attempts to define the effect of the binder on sensitivity it was noted that pure PETN, when applied in a paste form and dried, had just sufficient strength to support itself in thin layers. By applying the paste to an open core foam plastic matrix, a liner was made which satisfied the strength requirements and could be made in virtually any

thickness. The details of manufacture are given in Sec. 5.2.1. This last formulation, which has a patent pending, was the one used in the bulk of the launcher performance experiments.

In all, 25 different explosives or combinations of explosives were investigated in search for a suitable material. It should not be construed that the PETN formulation chosen for the implosion experiments is an optimum one, rather that it is one out of possibly many that will work in this application.

4.6 Experimental Procedure

The bulk of the explosive samples were prepared at the Chemistry Department of the University of Toronto by Mr. T. Huber under the supervision of Professor G.F. Wright, and arrived with the weight and density predetermined. For dry samples i.e., explosives containing no water, no further initial analysis is required. Some explosives, for example nitrocellulose, nitro-mannitol, mercury fulminate, and tetracene are much less sensitive to initiation by mechanical shock when wet. These explosives were prepared water wet and kept damp until used. Hazardous explosives such as lead azide were handled only in the wet state and an estimate of the water content was made by measuring representative samples, to minimize the amount of handling. The lead azide samples were made up on site to minimize the hazard involved since the University and Launcher Facility, are separated by a distance of ~ 15 miles. "Safe" explosives were dried and measured individually. Samples of the sheet explosive (EL506 and Heller) were cut on site from large sheets using precautions outlined by the manufacturer.

The explosive samples in the witness cups were installed in the one-dimensional chamber and the chamber sections fastened together. For dry explosive samples, the chamber was immediately evacuated to a pressure less than 1 mm hg. Wet explosive samples were dried to a pressure of less than 1 mm hg. by evacuating the chamber at a rate not exceeding 6.7 mm.hg./min. Previous tests in a small vacuum chamber, having a viewing window, using inert materials, having physical characteristics very similar to the explosives used, indicated t hat this pumping rate was sufficiently slow to prevent bubbling of the surface by escaping water vapor. Further with a few samples of explosive used, the chamber was re-opened carefully after the drying cycle and the samples checked to see if they had sufficient structural strength to maintain themselves in the vertical position. In all the check cases the material was intact. It appears that all the samples remained intact after drying provided that reasonable care was taken to prevent jarring the apparatus.

It should be noted that the vapor pressures of the solid explosives used are not an important factor since they are several orders of magnitude lower than the pressure to which the chamber is evacuated. For example, PETN has a vapor pressure of $\sim 10^{-4}$ mm hg.[93] The water and methyl alcohol mixtures that were used for the wet explosives have a vapor pressure of ~ 19 mm hg. and ~ 100 mm.hg. respectively at 72° Farenheit.

The one-dimensional chamber manifolds that are in common with the range (see Sec. 5.1.4) were then evacuated and hydrogen and oxygen gases metered, using $\frac{1}{4}$ of 1 percent test pressure gages, into a mixing bottle where they were allowed to mix by diffusion for several minutes. Then the mixture was allowed to enter the one-dimensional chamber. After several minutes to

allow for diffusive mixing, with any remnants of air in the chamber the charge in the chamber was vented to atmosphere, the chamber refilled and the pressure adjusted to the desired pressure by metered venting. When low pressures (of order 1 - 2 atmospheres) were used, the filling-venting cycle was repeated several times to purge the chamber and insure an accurate composition. In this manner it was felt that errors in mixture due to residual gases in the chamber and lines would be kept to a negligible level. The ignition system capacitors were then charged, the recording oscilloscopes which were previously calibrated were set and the area cleared for firing.

After each firing the chamber was vented to the atmosphere and flushed with helium to remove any hazard due to noxious fumes. The chamber was opened and the explosive cups and ionization probes removed for inspection. The entire inside surface of the chamber was cleaned thoroughly using acetone and steel wool to remove any tenacious deposits and dried with clean rags and dry compressed air. The ionization probes were inspected for damage, cleaned, given an electrical check for high resistance shorts and subjected to a 500 volt potential and monitored electrically and visually for breakdown. This last check was added after electrical breakdown of the probe at 300 volts ignited the gaseous mixture and initiated a run prematurely. Those probes that passed this test were reinstalled; those that failed were repaired or replaced. The crossed bridge-wire, a 4 mil copper cross, 1.2 inches across, was replaced, a new explosive sample and cup installed and the chamber closed up for another cycle. A maximum of 4 samples could be tested in an eight hour day.

4.7 Data and Data Analysis

In this section, it will be shown that from the analysis of the single data source, giving shock or detonation wave front position as a function of time, a considerable amount of useful information can be obtained for both the wave dynamics inside the chamber and the initiation properties of the explosives. While the results are all interrelated, for purposes of organization the raw data will be discussed first, followed in order by the analysis and results of the x-t diagram data, the wave-speed data, detonation pressure limit data, plane explosion considerations, detonation delay data and witness cup distortion data. After each of these areas are examined in detail the key points, will be summarized.

4.7.1 Raw Data

Two typical photographic records are shown in Fig. 82. Figure 82a is the result of a run using a nominal 200 psi mixture of stoichiometric oxygen hydrogen and 1.3 grams of PETN cloth. Not the clean signals obtained for both the incident gaseous detonation wave, "breaks" 1, 2 and 3 and the reflected wave, "breaks" 3', 2' and 1'. The reflected wave is essentially the shock generated by the reflection of a gaseous detonation wave since the explosive did not detonate for this initial pressure. It is worth noting in passing that "break" 3' while large enough to be read clearly is not as large as the 3 initial breaks or the remaining two since the capacitor in the circuit for the 3' section, while it has recovered enough to give a readable signal, has not completely regained its original charge. Figure 82b by comparison, is the result of a similar run using PETN cloth but with an overcoating of PETN in a sandwich configuration. The point to be investigated was whether the cloth could be detonated by a thin booster layer of PETN, which detonates at this

77

pressure. In this particular case the overcoating explosive detonated as expected, but the cloth did not, hence the reflected wave is strengthened only by the addition of the primer energy. Its velocity, as noted by the closer spacing between the timing signals of the reflected wave in comparison with the previous record, is faster than that generated by the deflagrating run, but is not as fast as would be the case if both materials had detonated. The timing marks shown in the lower sweep of each trace are 10 μsec timing markers from a Tektronix 601 time mark generator.

As a matter of course, two sets of data were obtained for each run, the data for the sweep speeds indicated and also at twice the time sensitivity shown in these two figures, i.e., at 5 microseconds per division, using a dual beam oscilloscope and a delayed second sweep. The faster sweep records allowed better time resolution i.e. by about a factor of 2, although the photographic quality is not as good as the ones shown. In practice they both gave essentially the same result and the two oscilloscopes were run in parallel every test to insure that data would be obtained and as a check against time calibration errors.

The estimated accuracy of the overall measurement is ± 250 nanoseconds in time and ± 0.25 mm. in space.

4.7.2 (x-t) Diagrams and Wave Speed Measurements

(x-t) Diagrams

The raw time-distance data was first plotted in the (x-t) plane to prevent the mis-reading of the traces i.e., taking a "noise break" as the signal, since the timing signals for both the incident and the reflected waves must of course be self consistant. Invariably misreading a "noise break" for a signal resulted in an inconsistant (x-t) diagram, and could be immediately detected and rectified. Typical (x-t) plots are shown in Figs. 83, 84, 85, 86 and 87 for stoichiometric oxygen-hydrogen mixtures alone, lead azide, PETN pressings, nitrocellulose and superfine PETN respectively. Pertinent data for all the runs are given in Table 12. The essential features of (x-t) diagrams for the 20 other materials tested are similar to the five given here and will not be repeated. The wave diagrams shown have been adjusted in time so that the detonation wave arrives at the reflecting surface at time t = 0. This will clarify the effects of the various parameters.

From the figures the general similarity of the wave diagrams can be seen as well as the fact that the trajectories, as evidenced by the data fit to smooth curves, can be accurately determined in both space and time. A number of important points can be seen from an inspection of these figures. Firstly, the incident wave which clearly is a detonation from its velocity, does not move at constant velocity but is initially overdriven by the exploding wire ignition source. It decays in the length of the chamber towards a steady plane detonation wave,as evidenced by the curved trajectory but is still slightly over-driven by the time it reaches the explosive surface. The amount of overdriving of the detonation wave is a function of the initial pressure as the phenomena is, initially at least, related to an ideal plane explosion, hence the blast wave should vary as E/ρ or for these experiments, $1/p_i$ since E is constant. The energy for the exploding wire (or more accurately the energy stored in the ignition capacitors) was held constant for the entire study, at

78

135 joules corresponding to a capacitor bank voltage of 6 kv. However only a fraction of this energy actually appears in the gas. The remainder is dissipated in the thyratron and cables.

The decrease in over-driven detonation wave velocity with pressure is best seen from the initial slopes of the curves in Fig. 83. As the over-driving is a transient phenomena and the actual amount of energy dissipated by the exploding wire was not measured and apparently varies from run to run, scatter exists in the trajectories, particularly at lower pressures. At higher pressures the overshoot and scatter is much reduced (see for example the results plotted in Fig. 86 where the trajectory is a straight line indicating the detonation wave velocity is constant).

Secondly, it can be seen that the reflected gaseous detonation wave of Fig. 83, for example, where no explosive is used appears to accelerate as it propagates from right to left. This is due to the expansion wave that immediately follows the incident detonation wave and has an almost linear velocity gradient behind it. The particle velocity varies from a maximum value at the detonation front to zero at a point roughly half of the distance travelled by the detonation front, (see for example Fig. 58). The reflected shock wave first enters a gas with a high counter velocity, and then moving through and out of this region moves into a gas at rest. To a fixed observer in the laboratory the shock wave accelerates. The pressure ratio of the shock increases in this interaction although the absolute pressure behind the shock decreases.

For cases where the explosive deflagrated, for example run No. 121 of Fig. 86 and run No. 194 of Fig. 87, the resulting reflected wave trajectory is essentially identical to the gas cases of Fig. 83 since the energy release by the explosive is so slow that it does not have time to add any significant energy to the reflected wave. For those cases where the explosive has detonated, for example, all the runs of Figs. 84 and 85, run No. 49 and 121 of Fig. 86 and run No. 199 and 202 of Fig. 87, the reflected shock trajectory flattens indicating much higher reflected shock velocities than in the deflagrating cases. The shocks also decay with distance as they adjust to and approach a $p \sim r^{-1}$ decay required by an ideal plane explosion, rather than accelerate as they did in the deflagration cases. The effect of the rarefaction behind the gaseous detonation wave is negligible for the detonating explosives. By measuring the reflected wave velocity and comparing it with the reflected wave velocity of a gas only case, it could be determined whether or not the explosive had detonated.

The complicated wave diagram obtained during the first few micro-seconds after reflection, as for example in Fig. 84 will be discussed with the ignition delay measurements of Sec. 4.7.5.

Velocity Measurements from (x-t) Data

The average velocity between probe stations was obtained by dividing the distance between stations by the time required to traverse that distance. By plotting the average velocity versus distance the dynamics of the wave motion can be seen. Plotted in Fig. 88 are data from a representative sample of the initial conditions and explosives investigated. All of the data are included in Table 12. The reflected wave data is plotted "mirror reflected"

across the reflecting surface to unscramble the dynamics of the two different waves (incident and reflected). For the incident wave, only the wave velocities for typical stoichiometric oxygen and hydrogen cases are plotted since the incident waves for the explosive runs are the same since they occur in the same mixture. In an attempt to evaluate the extent of the overdriving at the time that the wave has reached the reflecting surface, curves are drawn for $1\frac{1}{2}$, 3 and $4\frac{1}{2}$ percent increment in velocity at the reflecting surface assuming a r^{-1} decay of the velocity increment with distance. This decay of the increment of the excess velocity over the detonation velocity appears to be reasonable, in light of the trends shown in Fig. 89, which is a plot of the increment in velocity over the detonation velocity versus the distance from the induction point. The data is from Bollinger[94], however it is for lower pressures than considered here. It would appear based on this decay law that overdriving by as much as 5 percent in velocity may have occurred for low initial pressures. Since pressure behind a detonation wave varies as the velocity squared, the peak pressures could be as much as 10 percent greater than the predicted Chapman-Jouguet pressure for a steady detonation wave at the same mixture and initial pressure.

While the incident wave velocities are similar in character, the reflected wave velocities vary considerably depending on the particular explosive and the initial pressure. For gas alone cases or for cases where the initial pressure is lower than the pressure to insure detonation, the reflected wave moves at relatively slow velocity, increasing in velocity as it propagates through the gaseous detonation wave particle velocity profile, as noted previously. For initial pressures greater than that required to insure a detonation in the explosive, much higher velocities, up to 4 times the reflected wave velocity in deflagration cases, are measured. The high velocities then undergo a transition, begin to decay and approach the $V \sim r^{-2}$ required by an ideal plane explosion. Correlation of these velocities with plane explosion theory is given in Sec. 4.7.4.

For most of the low initial pressures investigated the detonation wave was overdriven, hence a direct comparison of the wave velocity with the predicted steady detonation wave velocity is not possible. However for run Nos. 49, 114, and 121 shown in Fig. 86 the initial pressure was high enough and the ignition phenomena was such that the wave decayed to a steady detonation before reaching station 1 and travels the remainder of the chamber at a constant velocity of 3.06 km/sec. As shown in Fig. 90 this velocity compares well with the predicted steady detonation velocity for these conditions.[94]

Before leaving the discussion of the wave velocities, it is worthwhile to elaborate on one of the questions posed by Makomaski[90], that of the strength of the incident wave. As noted, the gaseous detonation wave generated by the exploding wire, is initially overdriven, decays rapidly, and reaches a velocity slightly in excess of Chapman-Jouguet velocity prior to colliding with the explosive surface. This particular point is not of trivial importance in the study of the initiation phenomena. In the spherical geometry of the launcher the initially overdriven detonation wave damps out very quickly (as $r^{-3/2}$) and is probably moving at the C-J velocity when it collides with the explosive. By insuring that the detonation wave velocities in the one and three-dimensional experiments are the same at the instant of reflection, the peak pressures generated on reflection will be the same. As shown previously, it is primarily the peak pressure which determines whether or not an explosive will detonate. The pressure profiles of detonation waves in the different geometries are quite different as can be seen from Fig.

80

58. The planar $(\nu = 1)$ and cylindrical$(\nu = 2)$ cases (curves from Ref. 95 for stoichiometric oxygen-hydrogen) have much smaller gradients behind the detonation wave than does the spherical case $(\nu = 3)$ (Ref. 58 $\gamma = 1.13$) which has by comparison a very steep pressure profile. Further the plane detonation wave profile cannot be made to match the spherical profile by a simple shortening of the one-dimensional chamber size although in principle a better approximation to the spherical chamber case could be had by a much reduced ($\sim$ 1/3) length of one-dimensional chamber which is clearly not practical here. However, as it is primarily the pressure peak and, not the length of time application that is important in the initiation, the results obtained in the one-dimensional chamber are generally valid for the three-dimensional case provided the detonation wave velocities are kept the same. The last condition while not satisfied exactly for all initial conditions investigated, is close enough so as not to cause major discrepancies in the detonation pressure limit.

4.7.3 Detonation Pressure Limits

Using the velocity data and, as will be discussed in Sec. 4.7.6 the cup distortion data, it was possible to determine the lower limit of pressure for which a given explosive sample would detonate. No attempt was made to define the boundary with high precision since the emphasis in this study was primarily on finding explosives with acceptable properties rather than the precise definition of their properties. Specific results showing the regions of detonation, deflagration and no combustion are shown in Fig. 91. The circular symbols are the results of this study. The square symbols are results of others. Filled symbols indicate detonations, half filled symbols indicate deflagrations and open symbols signify no combustion. A combination ("sandwich") case is listed as a detonation only if both materials detonated. For example, a (SF) PETN/PETN cloth run at 13.7 atm is considered a deflagration as only the top layer of PETN detonated. For some runs at very low initial pressures the explosive neither detonated nor deflagrated but the surface melted.

From Fig. 91 and Table 13 which are arranged generally in order of increasing sensitivity, it can be seen that of the explosives investigated there are 9 explosives or explosive combinations that will detonate for initial pressures in the gaseous mixture of 11 atmos or less. These are lead azide, superfine PETN, a lead azide-PETN mixture, superfine PETN/No.1 Paste combination*, superfine PETN/No.2 Paste combination, PETN powder, PETN pressings and nitrocellulose. Those that will not initiate at this condition are Nos 1 and 2 pastes, blasting gelatin, PETN-EL-506 combinations, tetracene, cast PETN, picric acid, tetryl, mercury fulminate, lead azide/Heller combinations, lead azide/EL-506 combinations, nitromannitol, corregated nitrocellulose, αHMX, PETN fabric, superfine PETN/PETN fabric combinations, Heller, EL-506, DINA, and lead azide-polyurethane mixtures. This last material would not even ignite at 300 psia. If the initial pressure can be increased to 20 atmospheres then No. 1 and No. 2 pastes, PETN/EL-506 combinations, tetracene and cast PETN become available. It is also possible that other materials, for example, mercury fulminate and nitromannitol, may have suitably low initiation pressures, however the study was directed to finding materials that would detonate at low values ($\sim$ 10 atm) of initial pressure, and detailed tests of these explosives were not made.

---

* Trade names - composition defined in Sec. 4.7.7.

While the present tests of lead azide were not carried below 1 atm, it is interesting to note that Andreev and Maslov[82] observed that lead azide initiated at initial gas pressures as low as 210 mm. Their experiments were done in a tube 1.0 meters long. However, this would not have a strong effect on the measured limit. From a pressure point of view, lead azide is an excellent initiator. It is unfortunate that it is not acceptable from safety considerations. Other materials reported by Andreev and Maslov include picric acid, tetryl, "blasting geletin" and cast PETN. The only other comparable work using gaseous detonation waves is that of Makomaski,[90] who determined that EL-506 and cast mixtures of DINA and PETN would not initiate at initial pressures of 98 atm. He also found that PETN pressings of 1.0 and 0.87 g/cc would detonate at initial pressures of 13 atm. but would deflagrate, as evidenced by the lack of substantial deformation of the cups, at 12 atm. The present study indicates that detonation extends to below 8.98 atm. for PETN but deflagration occurs at 6.12 atm. This apparent discrepancy is probably due to t he inability of the distortion measurements to give the finer details. These details are discernable when the wave speeds are measured.

It is important to note that PETN becomes easier to initiate as the packing density (related inversely to the fineness of the explosive and the quantity of voids) decreases. For example, cast PETN requires 15 to 20 atm. to detonate, PETN pressings require 6-8 atm. The very fine grained Superfine PETN requires only 2-3 atm. to detonate. Whether this is due to the voids and their subsequent local hot spots or to improved heat transfer from better surface area to volume ratio cannot be determined from the present data.

Some insight into the initiation phenomenon can be gained from a comparison of the present data with some data from PETN initiation studies obtained using a different initiation method. Seay and Sealy[96], used explosive driven shocks at relatively low pressures to initiate PETN pressings at a density of 1.0 g/cc. They obtained not only an initiation limit but also the depth of penetration required to detonate. Their data, shown in Fig. 92, gives the distance required to detonate versus the pressure induced by the impinging wave. It is of interest to note that their data indicates the depth of penetration varies as the cube of the pressure. They also predict a pressure of ~3 K bars (~ 45,000 psia) to initiate PETN in a distance of 0.15 inches. This pressure is equivalent to the pressure produced on reflection by a stoichiometric-oxygen mixture initially at ~ 1000 psia. The lower pressure measured in the present tests may be due to the heat transfer from the hot gas products of stoichiometric oxygen-hydrogen. In Seay and Sealy's tests the shock was transmitted through either brass or lucite plates. The temperature of the shock processed brass or lucite is at least an order of magnitude less than the peak temperature in the gaseous detonation wave, (4145°K)[50] which will further increase by about an order of magnitude on reflection from a solid surface. From this comparison it appears that the heat transfer may play an important role in the initiation by gaseous detonation. However further work is required to resolve this point.

It might also be argued that the explosive, particularly the lead azide, is initiated by radiative heating from the incident detonation, particularly since this mode of initiation has been identified by Roth[97]. He showed that lead azide could be initiated by the radiant heat flux to the explosive surface by shocks travelling at 8.3 millimeters per microsecond in 17 psi initial pressure of argon. His results show that when the critical

temperature of $910° \pm 30°K$ is reached by the lead azide, it spontaneously detonates. Because of the high temperature of the shock processed argon $(29,000°K)$ the radiation could be considered as that from a black body at that temperature. The wide difference in temperature, ~4100°K for the detonation waves as compared to 29,000°K for the argon shock, and the fact that the radiative flux is a strong function of temperature negates this possibility in the present tests. Further, if the lead azide were initiated by radiant heating then the explosive could initiate prior to the arrival of the detonation wave. This was not observed in the present experiments. Roth's experiment does indicate that some explosives can be detonated by a purely thermal pulse, independent of shock heating.

4.7.4 Shock Velocity - Explosive Yield Considerations

In Sec. 4.7.2 it was seen that for pressures greater than a threshold pressure the explosives would detonate, as evidenced by the substantially enhanced velocity of the reflected wave. It is instructive to examine the reflected wave velocities produced by different explosives at different initial pressures for possible correlation parameters.

For an ideal plane explosion the strength of the blast wave varies with distance as

$$\frac{p_2}{p_1} = K_1 \; \frac{E_{tot}}{\rho} \; r^{-1} \tag{4.7}$$

and for the shock velocity

$$U_s = K_2 \left(\frac{E_{tot}}{\rho} r^{-1} \right)^{\frac{1}{2}} \tag{4.8}$$

Hypothesising that the present situation can be approximated by a plane explosion case and since the composition of the gaseous mixture is held constant at $2 c + C_2$ and the location of the probes fixed, it should be observed experimentally that

$$U_{s_{ref}} \sim \left(\frac{E_0}{p_i} \right)^{\frac{1}{2}} \tag{4.9}$$

if this hypothesis is valid. Plotted in Fig. 93 is the reflected wave velocity extrapolated to the explosive surface using the (x-t) plane and velocity data, versus E_0/p_i for all explosive runs where complete or partial detonations occurred. For partial detonations only the energy of the detonating layer is used in evaluating E_0. It is seen that the data follows this variation for a wide range of E_0/p_i. Velocities less than 1.79 mm/μsec were not observed since the reflected gaseous detonation wave sets a minimum to the velocity at this value. Values greater than about 7 mm/μsec are also not observed. The data appears to be asymptotically approaching a constant velocity ~ 8 to 10 mm/μsec as $E_0/p_i \to \infty$. As the velocity is taken at the explosive surface where finite source effect are important this behavior is not unexpected. For example, the calculated front velocity for TNT at a density of 1.5 grams/cc driving air at 0.01 mm. hg. is 10.7 mm/μsec. As the detonation temperatures (sound speeds) of most explosives are grouped in the range 5500 $\pm$ 1000,[71] this "escape" velocity can be taken as representative of explosives in general. For driven gas initial pressures greater than 0.01 millimeters the front velocity should decrease proportionately. What is observed is not inconcistent with this view.

It is to be expected that for points away from the explosive where the finite character of the source is becoming obscured that the agreement with ideal plane explosion theory would be better. Plotted in Fig. 92 is the average velocity taken between the probes furthest from the explosive versus E_o/p_i. It is seen that the agreement is improved.

In order to calculate E_u/p_i it is necessary to have accurate values of E_o and p_i. A precise value for p_i is immediately available as one of the initial conditions of the experiment. E_o, the energy per unit surface area is not so easily obtained, since accurate data at various loading densities is not available for all explosives. A word is necessary to explain the values taken here.

To reduce the lead azide data, two extrapolations had to be made as Q could only be found for a loading density of 4.0 g/cc (Q = 0.22 kcal/gm)[71] for which the corresponding detonation velocity in the explosive is 5.1 mm/μsec. Using these values as initial points the detonation velocity at $\rho = 1.67$ gm/cc was calculated using the accepted detonation velocity-density[71] variation relation:

$$D = D^* \rho^* + M^* (\rho - \rho^*) \tag{4.10}$$

where M^* from the same reference is 0.560 mm-cc/gm-μsec. The value of D obtained in this manner is 3.75 mm/μsec. The energy release varies approximately as the detonation velocity squared,[99] for an ideal explosive hence the energy release at 3.75 mm/μsec is

$$Q = Q^* \left(\frac{D}{D^*} \right)^2 \tag{4.11}$$

= 122 calories/gram.

The energy release of tetracene was assumed to be 0.4 kcal/gm. Nitrocellulose has a value 0.965 kcal/gm.[100] For PETN at the various loading densities considered here, values of Q were obtained from interpolating calculated values of Cook.[71] The results of his calculations for various assumptions are shown in Fig. 95. Included in the figure are two measurements of the heat of detonation made recently by Ornellas, Carpenter and Gunn,[101] using a bomb calorimeter. They report 1.487 ± 3 and 1.499 ± 5 kcal/gm for confined and unconfined charges of PETN at a density of 1.74 gm/cc. These two values differ from Cook's calculated values by less than 2%. This amount of disagreement between precise calculated and measured properties is better than what is generally to be found in explosive research at this time. The disagreement comes primarily from lack of knowledge of the precise equations of state for the explosive and explosive products. Of late, cor iderable interest has been shown in this area as evidenced by the flood of papers at recent symposia[102] on this topic. However there is no general accord as to what the precise equation of state is for any given explosive although many reasonably accurate descriptions are available. It has been suggested by Davis, Craig and Ramsey[103] that perhaps the assumption that an equation of state exists is false, since in order to properly apply equilibrium thermodynamics to the problem, the chemical reaction rates must be much faster than any other process in the time scale of interest. Information about reaction rates in solid phase detonations is non-existant .

4.7.5 Detonation Delay Measurements

It can be seen from the (x-t) diagrams (Figs. 84 through 87) of the explosive cases that result in detonations that the reflected wave trajectory extrapolated back to the explosive surface, does not interesect with the incident wave trajectory. The fine details of the trajectories at the explosive-gas interface cannot be obtained from the present measurements. From what is known of the physics, it can be surmised that the initial reflected trajectory is that of the reflection of a gaseous detonation wave. After a short delay in which explosive burning begins to build up to a detonation, a left running shock is created that out-races the original reflected shock, overtakes and strengthens it. In some cases, for example lead azide at $p_i \sim 6$ atm, (run Nos. 58 and 67 of Fig. 84), the explosive detonates virtually instantly and no intermediate shocks exist. In other cases, for example superfine PETN at $p_i \sim 3$ atm (run No. 199 of Fig. 87), the delay is such that the initial reflected wave is nearly halfway back across the chamber before it is overtaken.

By extrapolating the incident and reflected wave trajectories to the reflecting surface, a delay time for initiation, characteristic of the explosive at that initial pressure, but not an exact explosive initiation delay time in any absolute sense, can be determined. The characteristic delay time is defined as the time between the extrapolated incident and reflected waves at the explosive-metal interface. As was seen from Fig. 84, the lead azide is initiated almost instantaneously or at least in times less than ~ 1 μsec. This property is a very desirable one, since it satisfies the criteria of nearly simultaneous initiation of the explosive. Unfortunately, it is not possible to determine whether the explosive initiates at the front surface or on reflection of the shock from the explosive-metal interface. From the extreme sensitivity of the lead azide it is summized that the explosive probably initiates at the gas-explosive interface except when the initial pressures become very low. The other explosives require the increased pressure on reflection of the shock at the explosive-metal interface for initiation if shock heating is indeed the mechanism. For initial pressures of 89 and 92 psi (Run Nos. 67 and 58), the ignition delay time of lead azide is effectively zero, or at least less than 1 μsec. For run No. 170 where the initial pressure was reduced to 30 psi in order to gain a high value of E/p_i or 48.8, hence a high reflected shock velocity, the delay time for lead azide increases to a measurable 4 μsec. In this case the reflected detonation wave propagated outward approximately 1 cm. before being overtaken by the strong shock produced by the detonating lead azide. The other explosives investigated behave similarly but generally have longer delays than does lead azide as can be seen from the other (x-t) diagrams.

Characteristic ignition delay data obtained in the fashion is plotted versus initial pressure in Fig. 96, and tabulated in Table 14. While the data is insufficient to make quantitative predictions of the variation of delay time with initial pressure, qualitatively it does appear to have the strong dependence on pressure. The PETN pressings at 1.00 gm/cc, nitrocellulose, tetracene, and the PETN paste formulations have essentially the same initiation delay characteristics. The PETN pressing at 0.87 gm/cc and the less dense "super fine" PETN ($\rho = 0.59$ gm/cc) appears to give generally shorter delay times, in that order, in qualitative agreement with the hot spots theory or the concept that the fine particles have favorable surface to volume ratios hence are more sensitive to convective heat fluxes.

It should be appreciated that this method of determining the ignition delay of the explosive is very rough. The actual ignition process and the dynamics of the interaction of the gaseous detonation wave and the explosive is very complex. In all probability the detonation wave reflects from the gas-explosive interface producing a transmitted shock wave which propagates into the explosive, compacting it in the case of porous explosives, and a reflected shock. Subsequently, the transmitted shock reflects from the explosive-solid interface. At some point in the explosive a critical condition of pressure and temperature, is reached for a given period of time either through shock heating, convective heating, local hot spots or a combination of effects and the explosive detonates. To assume that PETN for example, initiates instantaneously at the gas-explosive interface as was suggested by Makomaski[90] is clearly not valid in light of the present delay time data. It must be recalled that his data was limited and a time resolved display of the events was not possible.

It is possible that an explosive could detonate after a sufficiently long delay time ($\sim$ 20-30 µsec) that its effect on the reflected wave would not be felt in the dimensions of the present apparatus. This is an academic point for the implosion driven launcher since the requirement is that the explosive detonate in time to be available to strengthen the imploding wave. As such, any explosives which would not initiate soon enough to be effective in the length of the one-dimensional chamber, i.e., within $\sim$ 10 µsec, would be of no use in the implosion driven launcher. However the delay time could be relaxed proportionately for larger diameter chambers.

4.7.6 Witness Cup Distortion Data

The witness cups that hold the explosive samples provide additional information as to the type and "quality" of the explosive combustion. It was this single data source which was used by Makomaski to determine the detonation limit for the PETN pressings. In all cases where the measured reflected wave velocity was comparable to that of a reflected gaseous detonation wave, no damage marks could be found on the surface of the cup. These two pieces of coroborating evidence are taken to show conclusively that the explosive deflagrated. In all cases where the reflected wave velocity showed an enhanced velocity, damage marks were visible on the cup surface. For sandwich type samples, where only the top layer detonated, the damage was limited to the sides of the cup where the detonating explosive was in intimate contact with the cup.

Two representative types of damage marks are shown in Fig. 97. For PETN pressings, grooves separating cells, seen in Fig. 97a, were found suggesting very high pressures locally. This sort of pattern would be produced if detonations were initiated at only a few isolated points in the explosive. The grooves would be produced by the collision of detonation waves, which substantially increase the pressure over the C-J value and are the loci of the collision points. This type of behavior wherein the explosive detonates at only a few points would be expected to produce bulging and distortion in the shock which is generated. Whether or not the observed cell size ($\sim$ 1 centimeter) is sufficient to destroy the spherical symmetry for an implosion case is not known but it is unlikely that it is favorable to the implosion.

In contrast to this behavior, the damage marks produced by the explosives that are known to initiate nearly instantaneously, such as lead azide, were homogeneous over the entire surface as shown in Fig. 97b Superfine. PETN also produced uniform markings even to initial pressures as low as 50 psia.

86

This is taken to indicate that the explosive not only detonated but initiated at a large number (100's/cm² or greater) of points. This property is very desirable for the generation of a symmetric imploding wave. It is this uniformity of initiation property along with the low initiation pressure which prompted the decision to use the superfine PETN for the implosion work.

4.7.7 Summary and Discussion by Type and Conclusions

The results for the various explosives and explosive combinations are discussed by type below.

Lead Azide ($Pb N_6$)

The dextrinated lead azide used in this study was obtained from E.I. DuPont, DeNemours and Company of Pompton Lakes, New Jersey. It was certified to comply with military specification MIL-L-3055A. Analysis by the supplier indicated the material to be 93.31 percent pure, 0.49 percent soluable in water have a density of 1.67 g/cc and "aggregates free from needled-shaped crystals having a maximum dimension greater than 0.1 millimeter[104]. The sensitivity of lead azide to initiation increases rapidly as the size of the particles increases. Crystals 1 mm. in length or greater are liable to explode spontaneously probably because of internal stresses. Dextrinated lead azide, as used here can be stored for long periods of time probably because the growth of the crystals is inhibited by the dextrination process. "Service lead azide" which is not inhibited, is known to become more sensitive with time, when stored under water probably because of the growth of the crystals.[105]

Approximately 10 pounds of lead azide were consumed without mishap during the study. However, as pointed out by Duff[64] and Kauffman[66] this should be taken as good fortune rather than evidence of reliability, as lead azide has been known to initiate without external cause. While this is of little consequence when using a few milligrams, it could cause fatal injuries in the amounts used here. As such, its use at this laboratory has been subsequently discontinued.

This was very disappointing since the initiation properties of lead azide are very close to ideal. For pressures, as low as 15 psia the measured delay time is only 4 μsec. For pressures of ~ 100 psia the delay time is less than 1 μsec. However, the energy density of lead azide is low, ~ 1/10 that of PETN hence a liner of lead azide would have to be ~ 10 times as thick as an equivalent secondary explosive liner. However, a mixture of lead azide and PETN was observed to retain the sensitivity characteristics of the lead azide, at least to 6 atm initial pressure, and also the high energy density of PETN. Lead azide was not able to detonate EL-506 or Heller even in fairly thick layers probably as a result of the low detonation pressure at this loading density (~ 5.7 x 10⁵ psi at ρ = 1.67 g/cc).These last few points are academic in view of the decision not to use this material.

Lead Azide - Polyurethane

Samples of a 75% lead azide - 25% polyurethane explosive developed by Abegg, Fisher, Lawton and Weatherill [106] of Aerojet General Corp. were also tested. Its chief virtue is that it has a low detonation pressure, (not to be confused with low initiation pressure) compared to pure lead azide. As it can be made in flexible sheets, manufacture in a hemispherical shell would be simpli-

fied. Unfortunately, pressures up to 300 psia did not initiate even deflagration in the explosive hence this material is clearly not suitable for use with the implosion driver. Further, difficulties experienced with the manufacture of the samples indicate that the hazard of this material is comparable with lead azide in its usual form.

Heller

Heller, a solid propellant that was developed by the Canadian Armament Research Establishment has properties closely resembling JPN propellant[107] It was investigated also because in sheet form, it could be readily manufactured into shells. Unfortunately, it will not detonate at initial pressures of 12 and 18 atms. When used in combination with a primer layer of lead azide it also shows no tendency to detonate. It is this property which has made it a reliable solid propellant, but which negates its use in the implosion driven launcher.

Tetracene

Tetracene (1-Guanyl-4-nitrosoaminoguanyl tetrazene) is commonly used as an intermediate booster in detonators to increase their efficiency. It is relatively sensitive to heat and has been used commerically mixed with other materials in explosive rivets which are initiated by heat. As evidenced by the enhance reflected wave velocity at 270 psi, it appears to detonate. However, the damage to the witness cups was slight and generally non uniform. Further, the measured delay times were the longest at a given initial pressure of any of the detonating explosives that were investigated. For these reasons it does not offer much promise for use with the implosion driven launcher.

EL-506

EL-506 is the trade name of a product containing PETN and "other ingredients" which is formed into a tough, flexible, rubber like, product and marketed in thin sheets (0.084 to 0.0328' by E.I. DuPont[108]. The ease by which it could be manufactured into hemispherical shells made it very attractive. However, its sensitivity compared with raw PETN is much reduced by the addition of the "other ingredients" to the point where it will not detonate at 98 atm initial pressure. Further a lead azide primer layer will not initiate it at 90 psia, but a PETN primer layer at 250 psia will. However, if a PETN primer layer is required, it is simpler to make the entire liner from PETN, hence there is no advantage to using the PETN/EL-506 combination.

Nitromannitol (Mannitol Hexanitrate)

This material is commerically available from Atlas Chemical Industries, Wilmington, Del. It is used commonly in detonators and is considered to be "almost" a primary. It has a sensitivity to impact and friction comparable to nitroglyccerin[105]. Its inability to detonate at 91 psi was surprising in light of this data. Subsequent investigation showed that it can be obtained in two forms, a grain form having grain size of ~ 1 mm. which is in common use in detonators and a crystaline form which has long thin "fiber like" crystals about 0.1 mm in diameter which is not commercially available. The grain type was used in the present tests. In light of the other results it is summized that the crystaline form is more sensitive and might have been detonable at moderate pressures. As several suitable materials had been found by the time this information was known, further study of nitromannitol was not persued.

Nitrocellulose

The nitrocellulose used in this study was nitrated to 13.45% nitrogen which is close to the maximum nitrogen content (14.14%). It was pressed to a wet density of ~ 1.8 g/cc. The dry density was ~ 1.3 g/cc. As evidenced by the uniformity of the markings on the witness cups, the low pressure limit $11.2 < p_i < 11.6$, and high enegy content, nitrocellulose is very suitable for use in the implosion driven launcher. However, the pressing of the fiberous nitrocellulose into a shell with uniform thickness and density has not been attempted. As the fibers provide structure, an additional matrix for strength is not required as with the PETN. It is possible that a shell could be manufactured by pressing smaller segments, the density and thickness of which could be controlled, which could then be cemented in place in the metal shell. As such, this material is a suitable back-up material if for any reason the use of PETN has to be discontinued.

PETN

Of all the explosives tested in this application, PETN shows the most promise. Pentaerythritol tetranitrate ($C_5H_8O_{12}N_4$) is made by nitrating pentaerythritol, a white crystalline compound of formaldehyde and acetaldehyde. Its chemistry, derivatives and effects are well known[93]. Further, total production of pertaerythritol in 1958 was 1.41×10^6 pounds of which ~ 1 percent is the explosive, hence it is readily available and inexpensive.

In the present study, a number of different formulation of PETN were investigated. Initially tests of pressings of PETN crystals at $\rho = 1.0$ and 0.87 g/cc indicated that this configuration would detonate for initial pressures less than 8.98 atm, and showed that the delay times were both reasonable (< 10 μsec) and decreased with increasing initial pressure. However, manufacturing a hemispherical shell from dry crystals of PETN did not appear possible, and this material was temporarily abandoned.

Later several proprietary formulations of PETN were suggested by Canadian Safety Fuse Ltd. These included a PETN fabric, and Superfine PETN (SF-PETN) combined with binders and separately. The PETN fabric, details of which are proprietary, could be manufactured in a hemispherical shell, but would not initiate at 200 psia nor in conjunction with a primer layer of PETN, although a standard blasting cap is sufficient for initiation. The No. 1 and No. 2 PETN pastes which were composed of 65% Superfine PETN 5 - 10μ, 29% water and 6% binder and 74% medium fine PETN 10-15μ, 22% water and 4% binder respectively, were developed by Welsh[109] of Canadian Safety Fuse in an attempt to solve the manufacturing problem. The pastes which have the consistancy of putty can be fabricated in virtually any shape. The results of the initial experiments indicated that the binder was reducing the sensitivity of the pastes perhaps by coating the individual crystals. Configurations using superfine PETN layers on the pastes showed that the initiation properties were improved but it was difficult to make the superfine PETN adhere to the paste.

In an attempt to define the effect of the binder on sensitivity a quantity of the paste was washed, and allowed to dry undisturbed. Dried, it remained an integral, yet somewhat fragile solid, which would maintain its shape provided it was not jarred. Subsequent tests showed that pure superfine PETN could be mixed with water, dried, and would have the same property. To improve the strength of the dried form and as a guide for thickness, an open

89

pore foam plastic, which could be cut in thin layers was first cemented to the witness cup and the pores filled with PETN. The strength of the resulting liner was markedly improved.

Tests of this configuration at 3.4 atm (~ 50 psia) showed it would detonate, but with a 12 μsec delay. At 6.8 atm (~ 100 psi) the delay was reduced to a nominal 3.6 μsec. Further the markings on the witness cups indicate uniform ignition over the entire surface. For $p_i \leq 1.7$ atm the PETN surface showed melting but no deflagration, hence the deflagration region for this material is rather narrow.

On the basis of low initiation pressure, uniformity of ignition, explosive yield, and ease of manufacture, the superfine PETN formulation is ideally suited for use with the implosion driven launcher. A further advantage of this formulation is its low detonation pressure. As can be seen from Fig. 98, which shows data from Cook[71], the detonation pressure can be related to the density by

$$ p_D = K \rho^2 \tag{4.12} $$

where

$$ K = 7.8 \times 10^4 \text{ atm-cm}^6/\text{gm}^2 $$

for PETN. Reductions in density can bring about substantial reduction in detonation pressure. The SF-PETN formulation has a density of 0.588 g/cc. The corresponding detonation pressure is 2.65×10^4 atm (~ 3.9×10^5 psia). The detonation pressure at 1.0 g/cc is 7.7×10^4 atm a factor of ~ 3 higher. This property alleviates the problem of protecting the chamber from high pressures generated on detonation.

4.8 Alternate Initiation Schemes

The gaseous detonation wave initiation technique described in this section is only one of a number of ignition schemes that have been proposed. It has the advantage that it is simple and straight-forward. However, it requires expolosives that can be initiated by fairly weak shocks and the driving gas is made up largely of the products of combustion i.e., dissociated high temperature water. It was also seen both experimentally and theoretically that the best performance is obtained using a stoichiometric mixture primarily because gamma is a minimum for this case. A pure hydrogen driver which has a room temperature gamma of 1.4 has been studied by Bjork[110] and found to have a low value of gamma(~ 1.24)for high temperatures Further, its low molecular weight is much less than that of the water vapor left by the combustion of the stoichiometric oxygen mixture, hence it is a very favorable driving gas.

To take advantage of these properties requires a different ignition technique. It has been suggested by Wright[111], that a light sensitive explosive applied to the surface of the explosive liner,when exposed to a intense light pulse, as say from an exploding wire, would detonate and subsequently initiate the under layer. The initiation would be virtually instantaneous since the light is received everywhere instantaneously. Further, the driving gas composition can be chosen arbitrarily. Silver azide has the necessary properties and has recently been studied elsewhere[112,113,114] in this connection. Safety aspects require that the sensitive layer be applied in situ, perhaps by precipi-

90

tating silver azide onto a granular explosive layer from a solution of silver nitrate, by passing acetylene through the liquid. Apparatus for the investigation of this technique was started but is temporarily shelved.

Another technique which was proposed, investigated and found lacking is the multipoint initiation technique. It was proposed that if the explosive could be initiated at enough points that the initially perturbed (scalloped) imploding sphere might be sufficiently smooth to allow most of the implosions ideal character to be retained. Experiments performed by Kennedy at IITRI and reported by Glass and Kennedy[115,116] used 91 detonators spaced around the outside of a hemisphere which was lined with EL-506. The time resolved wave front showed that the initial "jetting" at the detonators completely destroyed the symmetry. It appears to be of little use in generating implosions although the technique might be useful for investigating instabilities where perturbations are purposely introduced.

4.9 Verification of Initiation Results in the Hemispherical Chamber

While the demonstration that explosives exist that will detonate under moderate pressure loadings with a small time delay, in a one-dimensional framework is necessary, it is not sufficient to guarantee that the same explosive will behave similarly in a hemispherical chamber. Four differences in conditions are to be noted. Firstly, the pressure-time history of the reflecting detonation wave in the spherical case is foreshortened in time over what it is in the one-dimensional chamber. Secondly, the spherical detonation wave requires a high degree of symmetry if the wave is to reach every point of the explosive simultaneously. The one-dimensional investigation while very useful in other ways, gave no information as to the quality of the planeness of the wave. Thirdly, the variation from point to point of the ignition delay of the explosive must not be too large. If the delay is not uniform over the entire liner, the initial spherical symmetry will be lost. Finally, it was feared that the spherical implosion would be unstable to small disturbances. It was reasoned that since explosion waves are stable in that shock front disturbances are damped out with time due to the geometrical divergence and that plane waves are neutrally stable, that implosion waves would be unstable due to geometrical convergence.

There appears to have been very little work done on the stability of implosion waves. Zaidel and Lebedev[117] have analysed the case for $\gamma = 7$, $\delta = 3$ and determined it to be stable. However, these conditions are not very representative of the case at hand. Butler[118] has analysed an imploding wave for various mathematical representations of disturbances and found some representations to be stable. However, the connection between the representations and physical reality is not clear. The verification of stability in this study would have to be experimental.

An experiment was conceived which would provide conclusive answers to most of the above questions. The nozzle insert which fairs in the hemispherical chamber with the barrel was replaced by a solid copper plug 1.5 inches in diameter and 0.5 inches thick. The plug served to seal the chamber and provided a witness plate for the implosion. Two runs were proposed. The first using a stoichiometric mixture of oxygen and hydrogen at 500 psi would indicate the degree of symmetry of the expanding spherical detonation wave provided that the subsequent implosion wave, which results from the reflection of the gaseous detonation wave at the outer

wall, was stable. Calculations indicated that the pressures on implosion would be greater than the yield strength of the copper block hence the region of high pressure around the focussing region would be evident.

The implosion print, captured by the copper block is shown in Fig. 99a. From the figure the symmetric indentation ~ 2 mm dia at the very centre is evident and is proof of a very high degree of symmetry of both the exploding detonation wave and the imploding shock wave. Spaced on either side of the center depression are two less pronounced depressions which may have been caused by subsequent cycles. The marks around the periphery are peaning marks from installing the block.

Next, a similar run was made using a 100 psia stoichiometric oxygen-hydrogen mixture and an 81 gram liner of PETN. Any deviations in character from the previous run would be caused by the explosive. The resulting print is shown in Fig. 99b. The near perfect symmetry and the effect of the extremely high pressures generated by the implosion is clearly evident. The entire copper block has yielded and had begun to extrude down the barrel before the pressure was relieved.

While the questions of the detonation wave symmetry, significance of ignition delay time jitter and the validity of carrying across the results of the one-dimensional study to the hemispherical case have been answered by these crucial experiments, the question of the stability of the imploding wave is not completely settled. However, it can be stated that if the implosion is unstable, its rate of divergence is sufficiently low as to not to destroy the symmetry of the implosion for the dimensions and conditions experienced here. Whether or not an implosion in a hemisphere several times this size, would retain this degree of symmetry is not known. Future work with the hemispherical chamber will be done in an attempt to define the parameters which control the symmetry of the implosion.

Implosion Pressure Measurements

The imprints of the implosion left in the copper witness block provide a direct but not unambiguous measurement of the pressures produced on implosion. Yielding of the block occurs for pressures greater than the yield strength of the material, hence the outer edge of the yielded region fixes the radial position of the implosion pressure which is equal to the yield stress of the copper provided the material is assumed to yield instantly. This assumption must be taken with reservation since it will require a finite length of time to displace the surface of the yielded regions. As such the pressure "measured" in this manner will be low by an undetermined amount. A sample taken from the same bar as supplied the witness blocks was subjected to a compression test and the static yield strength in compression determined to be 28,750 psi[119].

An inspection of the copper block from the gas run showed yielding has occurred out to $r = 0.5 \pm 0.1$ cm. For the explosive run, the entire block had yielded hence pressures greater than the yield stress extended beyond $r = 1.83$ cm. An estimate of the radial limit of the yielding that would have been obtained for a larger block was made by plotting the deflection versus radius and extrapolating to zero deflection. This resulted in $2.6 < r < 5.2$ cm. which could be in considerable error as the extrapolation is large and the slope of the curve is relatively shallow.

92

These values are plotted in Fig. 100 with the peak pressures behind the incident and reflected shock waves for both cases using the implosion in a sphere model. As shown previously (Sec. 3.1.4) the predicted pressures in the stoichiometric case are about a factor of 2 greater than those predicted by Brode for the same initial conditions, hence the predicted curves may be too high by this amount. On the other hand the measurements are low by an unknown amount. In view of this, it would appear that the pressures obtained on implosion are in substantial agreement with what is expected for both the gas and the explosive driven cases, at least up to the 28,750 psi point. Whether this agreement would extend closer to the origin is a matter of conjecture which only further measurements can resolve.

5. IMPLOSION DRIVEN LAUNCHER EXPERIMENTS

In this section the procedural details of the experiments which were conceived and carried out using the prototype implosion driven launcher will be discussed. The performance was discussed in detail in Sec. 3. The existing apparatus will be described with particular attention paid to the limitations imposed on the performance by the weaknesses in the prototype chamber, as well as suggested steps that can be taken to overcome this and other limitations.

5.1.1 Launcher

The implosion driven launcher is composed of essentially three assemblies, a hemispherical chamber, a barrel and auxiliary (ignition, gas, vacuum, filling etc.) systems. A view of the launcher shown in the firing position is given in Fig. 101.

The chamber is essentially an 18-in. dia. high-strength steel block into which has been machined an 8-in. dia. hemisphere. A view of the chamber in the opened position is shown in Fig. 102. As holes and "cutouts" introduce stress concentrations and reduce its strength the chamber proper has no "cutouts" in the walls in order that its strength be as great as possible. The chamber block is closed by a circular top plate which is placed on top of the chamber, (see Fig. 2). In the plates (several different models exist) are machined O-ring grooves for pressure and vacuum sealing, connections for the barrel, high voltage feed throughs for bringing in the ignition wires, pressure connections for venting and filling the chamber and in two of the plates, numerous instrumentation ports. These have been used at various stages in the launcher project[120,121] for a variety of instrumentation, heat transfer gages, pressure gages, and ionization (time of arrival) gages in particular. These ports have been designed such that other instrumentation, for example photo gages, windows for photographic studies etc., could be incorporated without difficulty. As these ports substantially reduce the stiffness of the plate, one top plate has only three holes: gas inlet, ignition and barrel connection, for the purpose of containing higher performance runs. As will be seen later, even this plate is not sufficiently stiff to contain the amounts of explosives that it is desired to use. The others are severely limited in explosive applications. The side of the chamber is threaded to receive a coupling ring which screws down onto the chamber and holds the top plate and chamber in contact.

A previous student experienced difficulty in unscrewing the coupling ring after runs in which O-rings were extruded between the chamber and top

93

plate. When this occurs essentially a giant friction device is produced which requires a large measure of brute force to release. To overcome this, 24-1¼ inch diameter threaded holes were machined in the top plate and fitted with socket head set screws. The coupling ring is then brough to within ~ 1/16 of an inch of the top plate and the remaining clearance taken up with the set screws. While this solved this particular problem, it substantially weakened an already marginal design. This point will be discussed further in Sec. 5.1.2. The chamber assembly is fitted with a ring trunnion and is free to rotate through its center of gravity about a cross range axis allowing the chamber to be tilted over for firing and to be positioned vertically for loading. The carriage is free to move fore and aft to accommodate various length barrels and the chamber is fitted with adjusting blocks for vertical and cross range fine positioning.

Provision has been made in the top plate to fit an assortment of barrel types. To date two different types have been used: smooth bore 0.22-in I.D., 1-in. O.D. barrels of nominal 4 and 5-ft lengths have been used, and high-pressure tubing types. The 0.22 in. barrels were fabricated by the Canadian Arsenals Small Arms Division* for this laboratory and have performed admirably in service. The maximum barrel length obtainable for this bore is limited to five feet. Unfortunately the erosion which occurs in the high performance runs, makes it necessary to cut off and remachine the breech end of the barrel to remove the enlarged bore after only a few runs. Some examples of erosion are shown in Fig. 103. The erosion shown in Fig. 103a is the result of 6 to 8 runs using constant volume combustion of stoichiometric oxygen-hydrogen diluted with helium or hydrogen at initial pressures of 100 to 500 psia.[120] In an attempt to avoid this problem, replaceable inserts were designed for the entrance region to the barrel. However, it was found that the barrel still eroded downstream of the joint between the main part of the barrel and the insert,[63] probably as the result of the increased heat transfer due to the tripped flow. An example of the erosion of the insert caused by a single gaseous detonation run using 500 psia of stoichiometric oxygen-hydrogen is shown in Fig. 103b. It can be seen that the higher pressures and temperatures of the detonation driven run considerably increase the erosion. The barrels are too expensive ($150/unit) to use in this fashion on a day-to-day basis, and have been used primarily for low performance work and on special occasions, for explosive work.

An alternate barrel design which uses Aminco** type No. 45-12110 and No. 45-11220 heavy wall tubing and which has been reamed and polished has also been used. The quality of the bore finish does not compare favorably with the smooth bore 0.22-in. barrels and may have been responsible for some of the projectile damage. Presently steps are being taken to improve the finish. As the raw material cost for these barrels is ~ $4.00/ft and as approximately 6 in. at the breech end must be removed after each run, the barrel costs are very favorable provided the finish can be improved. An example of the erosion produced in the barrel by a single 81 gram PETN run is shown in Fig. 103c. The erosion which is very severe, extends to about 20 calibers downstream of the entrance to the barrel.

---

* Canadian Arsenals, Small Arms Division, Long Branch, Ontario, Canada.

** American Instrument Company Inc., Silver Spring, Maryland.

The 0.22 in. dia. barrels are sufficiently stiff and short that no support other than at the chamber and muzzle end is required. The length and outside diameter of the Aminco tubing barrels is such that support must be provided at several stations along the length of the barrel, to maintain alignment. At present, alignment is taken from the outside diameter of the barrel. It is possible that variations in the wall thickness and concentricity of the bore may in fact result in a non-aligned bore as the manufacturer's specifications require the variation in straightness to be only less than .020 in./ft. Future improvement in launcher performance will require an improvement both in barrel finish and alignment, as they are both very important at high velocities.

Auxiliary Systems

The high pressure gas lines and the associated vacuum system, gages and valves, necessary for evacuating and filling the chamber are incorporated into an integrated system for the entire range facility and serve both the hypervelocity launcher and the one-dimensional chamber. The system is discussed in Sec. 5.1.4.

Ignition is accomplished by discharging a capacitor through a 5C22 hydrogen thyratron into an exploding wire which is held fixed at the origin of the hemisphere. Minimum capacitor voltages of 6KV and a capacity of 7.5 mfd (135 joules) are sufficient to initiate a detonation wave for most of the operating conditions encountered. Of the stored energy (135 joules) only a fraction probably is dissipated in the exploding wire. The remainder is lost in the thyratron and cable. Earlier work[63,120,121] was done with exploding wires, some as long as 1.0 in., and with other arrangements such as spark gaps and small explosive charges. While long wires are acceptable for deflagrating combustion they are entirely unsatisfactory for generating spherically symmetric detonation waves. Further, care must be taken to assure a good electrical connection at the inside of the electrical feed-throughs or arcing can initiate the detonation at this point as well as at the gap. Problems with unsymmetric detonation waves noted in Ref. 121 were subsequently traced to this source.

For the present work an exploding wire ~ 1/16 in. long and 0.002 in. dia. was positioned at the origin. This technique was developed in conjunction with Watson[63] who used it to obtain excellent symmetry characteristics. Symmetry was taken from time of arrival measurement of the outward moving detonation wave at three radial positions. The high degree of symmetry can also be inferred from the focussing results of Sec. 4.9.

During the initial few firings of the chamber and range it was noted that strong electrical interference from the exploding wire and its associated circuitry was present on all of the oscillograph traces. This same electrical interference was noted by Makomaski[90] and prevented any quantitative pressure measurements. The problem was traced to a number of ground loops in the circuitry, which were picking up the strong field created during the discharge of the ignition capacitors. This type of interference is fairly common among facilities or devices using high currents, as for example electrically driven shock tubes and pulsed-plasma devices using capacitor discharges. It can be avoided simply by removing the ground loops i.e., insuring that all grounds connections return to a common ground by a single path. In this case the removal of the loops reduced the interference to a tolerable level. The noise was further reduced to virtually zero by shielding the entire ignition unit, using RF suppressing capacitors on lines leading into the unit, using double

95

shielded coaxial cable on the cable connecting the ignition unit and the chambers and using a shielded connector at the chamber. No further trouble from this source has been experienced since these modifications were incorporated.

5.1.2 Chamber Strength Considerations

The peak pressures that are generated inside the chamber by the detonating explosive are much higher than those usually encountered in gun or shock-tube operation. Accordingly a critical review of the original design calculations was undertaken before any explosive runs were attempted, to ensure that unexpected failure would not occur and to place an upper limit for safe operation on the existing launcher. The chamber was designed by a previous student in 1960,[122] and first assembled in 1961.[123] However, it was not hydrostatically checked until the present work.

In the sections that follow it will be shown that the original design calculations were based on very optomistic and in some cases highly unrealistic models. As a result, the strength of the chamber is not nearly the assumed 100,000 psi steady state design condition. Subsequent modifications to the chamber assembly by other students further reduced its strength till it was more like 5,000 psi steady state a factor of 20 less than originally planned. Some improvements have recently been made in the form of triangular back-up rings, a stiffened top plate to bring the limiting pressure to approximately 23,000 psi. A design has been made that can contain 100,000 psi steady state, the original design goal. However, it has not yet been built pending future launcher developments.

Chamber Block

The chamber block was probably designed using thick wall spherical pressure vessel theory. Detailed calculation do not exist for the record, but the dimensions of the block seem to support this hypothesis. Provided that the internal pressure p is less than $\sigma_y/0.65$, the maximum tensile stress which occurs on the inner surface and in the direction of the circumference is given for thick wall spherical pressure vessels by[124]

$$\left(\frac{r_o}{r_i}\right)^3 = \frac{\sigma_y + 0.4\,p}{\sigma_y - 0.65\,p} \tag{5.1}$$

The maximum hemisphere that can be included in the chamber has a radius of 9.0 in. The inner radius is 4.0 in., the minimum guaranteed tensile strength of the material (Atlas, Steels Company AHT-28)[125] is 170,000 psi, hence from Eq. 5.1, the maximum steady state uniform pressure that will produce yielding at the inside surface is 252, 000 psi.

This figure is to be regarded with reservation as the stress at the inside radius will be different since the actual chamber is not spherical but hemispherical. An estimate of chamber strength can be made from hemispherical considerations if the free diametrical plane is considered as a thin "washer like" ring. Applying Lame's thick wall cylinder criteria, the maximum pressure for yielding at the inner radius is [124]

96

$$p = \sigma_y \frac{(r_o{}^2 - r_i{}^2)}{(r_o{}^2 + r_i{}^2)} \tag{5.2}$$

$$= 114{,}000 \text{ psi}$$

a factor of 2.2 lower. While the peak pressures produced by the explosive at the inner wall are well in excess of these two figures, the "average" pressure is considerably less. However the application of any kind of "average pressure" taken over an arbitrary time interval is not a realistic criteria as the time interval can be adjusted to give essentially any desired "average" pressure. The realistic strength of the chamber can only be obtained by doing a complete dynamic analysis, which is beyond the scope of the present work, but is presently being investigated at UTIAS. In the absence of a complete dynamic analysis the static design criteria has been applied, and indicates a positive factor of safety at 100,000 psia for the chamber block.

Top Plate

The top plate which closes the chamber is subjected to the same high pressures. The existing plate was fabricated from a circular slab of AHT-28, 18.0 in.dia. and 2.5 in. thick, heat treated to give a yield stress of 190,000 psi. The O-rings limit the diameter over which the chamber pressure acts to 8.625 in. The O-ring groove is 0.203 in. in depth leaving a minimum thickness of 2.297 in.

The design calculations for this piece are a matter of record and can be scrutinized critically. The plate design was based on a thin circular plate plate theory, assuming clamped edges as in case "a" of Fig. 104. The radius of the opening was taken as 4 in. instead of 4.31 (a factor of 1.16 in stress and 1.34 in stiffness), and the equation for stress was erroneously taken with a t^3 in the denominator instead of t^2 (another factor of 2.5 in stress). Further, the maximum thickness was used rather than the minimum. No account of the instrumentation and barrel attachment holes was made. It was further assumed that the coupling ring would not deflect, hence a clamped edge constraint applied. This last assumption is highly unrealistic as the coupling ring is considerably thinner than the top plate (1.750 inches compared to 2.50 inches) and has a large 8.5 inch diameter hole in the center, consequently it lacks the stiffness sufficient to justify the clamped edge constraint. Later modifications reduced the stiffness of the coupling ring even further.

In short, the calculation was both erroneous and highly optimistic. The calculations showed a design limit of 238,000 psi. If the calculations are performed correctly for this highly unrealistic model, the design limit is closer to 108,000 psi. The relation for maximum stress versus pressure is shown in Fig. 105. Figure 106 shows the maximum deflection at the center for this model, to be 0.018 inches at 108,000 psi, which would have been acceptable provided this model were valid, which clearly it is not.

As seen in Fig. 107, which shows the various existing and proposed top plate designs, the top plate was originally designed to be held down by direct contact with lower face of the coupling ring. This design was very susceptable to jamming and was consequently modified in 1964 by the addition of two rows of set screws at $r = 5.875$ in. and $r = 7.50$ in. While this solved a

97

serious jamming problem it further reduced the stiffness of the plate by the addition of weakening holes and by moving the radius of the restraining force from 4.25 in. to 5.875 in. This case is represented schematically by case C of Fig. 104. Since the strength varies as r_o^2, moving the restraining force location by this small amount reduced the strength by a factor of 1.91 and stiffness by a factor of 3.65. The weakening due to the holes is not calculable by simple means, but is probably of the same order.

. It was desirable to confirm the strength and stiffness calculations by a hydrostatic test of the assembled chamber. A strength check, i.e., to measure stress on the inside of the chamber, as for instance using strain gages, would be difficult. The simplest and most straight-forward method of verifying the model is a deflection-pressure test, which was performed using a number of dial indicators spaced across the top plate and coupling ring. While some of the indicators actually measured deflection of the coupling ring, the coupling ring is directly in contact with the top plate at two rows of set screws hence the measurement is directly the top plate measurement at those places and approximately the top plate measurement at places away from them. The slopes of the measured deflection-pressure curves are plotted as deflection per unit pressure versus radius in Fig. 108. This mode of presentation permits both deflection-pressure information and deflection profile to be presented in one figure. The "volcano" like shape of the curve rather than the "bell" shape anticipated is a consequence of the 2.680 in. (across flats) hexagonal plug in the center, and the fact that the coupling ring is not providing a clamped edge constraint. It is seen that the deflection at the center is approximately 36 times that predicted using the optimistic clamped edge model.

While it cannot be stated conclusively that the original (no holes) coupling ring design was inadequate, as the additional set screw holes have made it impossible to measure the deflection for a "no hole" case, it seems highly unlikely that the original coupling ring had adequate stiffness to justify a clamped edge constraint for the top plate. The deflection at the center which corresponds to incipient yielding is 0.093 in. However, the O-rings would have extruded prior to this in a manner shown in Fig. 109. Taking the deflection at the first O-ring (from Fig. 108 as δ = 4.1 p μin/psi and an analytical representation for the extrusion data[126] supplied by the O-ring manufacturer, as

$$p_{failure} = 11.4 \ \delta^{-.61} \text{ kpsi/thousandth}$$

$$1500 \leq p \leq 10,000 \text{ psi} \qquad (5.3)$$

and solving, yields as the limit pressure for the existing top plate as 4820 psia. The extrusion data is probably conservative, hence this limit is probably low.

It should be noted that this apparatus was used by Watson for constant volume combustion[120] and detonation[63] driving. No trouble was experienced with runs producing average pressures up to ~ 2500 psia. Runs producing pressures in the range of 5000 psi generally caused the first O-ring to fail while the second one held. Those runs attempted which yielded pressures in excess of 10,000 psi caused both O-rings to fail. These results are in general agreement with the present analysis and suggest that a safe limit on the existing top plate is ~ 5000 psi if both O-rings are required to hold. Pressures up to approximately 10,000 psi can be contained if inner O-ring failure can be tolerated, however the action of the hot gases leaking past the O-ring has a deleterious effect on the "O"-ring seating surface and this type of operation should not be attempted.

A more realistic analytical model of the existing top plate is that given for a uniformly distributed localized load, freely supported at the edge as shown in Fig. 109c. The maximum stress for this model is given by:

$$\sigma_{max} = 4.5 \left(1 - \frac{2}{3} \frac{r_o}{r}\right) \frac{r_o^2 p}{t^2} \qquad (5.4)$$

For the geometry under consideration ($r = 9.0$ inches, $t_{min} = 2.297$ inches)

$$\sigma_{max} = 10.9 \, p \qquad (5.5)$$

Assuming a maximum allowable stress of 190,000 psi gives a pressure limit of 17,400 psi. This relation is also plotted in Fig. 105. The deflection at the center for this model is given by

$$\delta_{max} = \frac{1.41 \, r^2 r_o^2 p}{t^3 E} \qquad (5.6)$$

which for this case yields

$$\delta_{max} = 5.82 \times 10^{-6} \, p \qquad (5.7)$$

This relation plotted in Fig. 106. One notes the excellent agreement between this prediction and the measured deflection of the existing top plate. This is partly fortuitous since no account has been made for the holes, a factor which is probably balanced by the coupling rings contribution to stiffness.

It should be clear that for the existing top plate the O-rings set the upper limit in the pressure at ~ 5000 psi, but that even if this criteria could be removed only modest gains (to 17,400 psi) could be made due to the inherent lack of strength of the existing top plate.

Improved Top Plate

It should be clear from the last section that the existing top plate was hopelessly inadequate for use with explosive driving. An improved seal design would not help much since the pressure to produce yielding was only 17,400 psi, hence a new top plate was required, one having a substantial improvement in both strength and stiffness.

Two top plate assemblies were designed. The design to contain 100,000 psi (named the "high-pressure top plate") required both a new top plate and coupling ring to meet the requirement. The lowest bid for the fabrication of the assembly was $4,500.00, about twice the original cost of the chamber, and an uncommonly long delivery time. It was decided to design and build a less costly top plate, the "improved top plate", by using the existing nut, improving the O-ring design and increasing the thickness of the top plate at the expense of the load being taken up by fewer threads along the side. At 100,000 psi the shear stress in the threads is 73,400 psi assuming that only $\frac{1}{2}$ of the threads are effective. Since the yield strength in shear is 105,000 psi (0.62 of the yield in tension)[125] the threads have a safety factor of 1.43.

The improved top plate, as seen in Fig. 107c, is stepped. It has a thickness of 3.000 in. at the periphery and is 5.000 in. thick at the center step, which is 8 in. in diameter. The number of holes is reduced to the absolute minimum of 3; - one each for barrel, ignition lead, and gas fill line instead of the original 13.

The step provides primarily for stress relief around the holes. Theoretically the ratio of deflection for stepped plate simply supported to a plate of uniform thickness simply supported, for uniform loading, is given by[119]

$$\frac{\delta_{stepped}}{\delta_{uniform}} = 1 - \left[1 - \left(\frac{t_o}{t_i}\right)^3\right]\left(\frac{r_i}{r_o}\right)^4\left[1-8\log\left(\frac{r_i}{r_o}\right)\right]$$

$$(5.8)$$

where subscripts o and i stand for outer and inner respectively. For the case in point, this ratio is 0.881 or the step reduces the center deflection by 12%. This contribution will be most noticeable in the center region. The major portion of the improvement comes from the increased thickness of the plate 3.00 in. instead of 2.5 in. (or 2.790 in. instead of 2.797 in. at the O-ring groove) giving a factor of 1.49 improvement in strength and a factor of 1.82 improvement in stiffness. These relations are plotted in Fig. 105 and 106. The calculated pressure that will just produce yielding is 25,900 psia. The deflection at the center using Eq. 5.6 and accounting for the factor 0.881 calculated for the step is given by

$$\delta = 2.93 \times 10^{-6} \, p \qquad (5.9)$$

The original O-ring design was also replaced by one using a triangular metal backup ring on a suggestion from the O-ring manufacturer. The triangular ring, shown in Fig. 109 which is made from a ductile material, deflects into the space left by the deflecting top plate preventing the O-ring from extruding and insuring a pressure-tight seal at pressures that would have caused extruding for the conventional design. If the back-up ring is assumed to fail by shearing, a pressure to fail, which is a function of the gap dimension, can be calculated. The results of such a calculation[127] are shown in Fig. 110. The limiting steady chamber pressure is given by the intersecting curves, which for the brass rings is 38,000 psi. Doubling the shear stress of the material to 76,000 psi by using stainless steel rings, say, increases the limit pressure to only 49,000 psi, an improvement of a factor of 1.26. This cannot be carried ad infinitum since a ductile metal is required to deflect and seal the gap. The figure does show the powerful effect of plate stiffness. Increasing the stiffness by a factor of 2 results in an improvement in limit pressure of a factor of 1.57 (to 60,000 psia) even using brass and increasing the stiffness by a factor of 4 gives a factor of 2.35 (to 91,500 psia) for this model. It is clear that the O-ring can be made to withstand very high pressures without extruding by the use of triangular back-up rings provided the deflection is kept very small.

To verify these calculations a hydrostatic test of the improved top plate was also carried out. While hydrostatic testing is much safer than using high-pressure gases, say, the elastic strain energy in the apparatus is the same and considerable damage could be caused if the structure were to fail. Accordingly, the pressure intensifying equipment which can produce up to 100,000 psi was located remotely from the apparatus. The apparatus was located in the blast room which is separated from the rest of the range by a one-foot thick reinforced concrete wall. The dial gage readings were monitored remotely using mirrors and a telescope. Loading was stopped at 26,700 psi after it was noted that the deflection - pressure curve had changed slope.

The deflection measured at the center is plotted on Fig. 106. We note that the predicted values and the measured values agree quite well, lending

support to the calculations. The deflection per unit load is plotted as a function of radius in Fig. 108. A substantial reduction of the deflection curve with a general flattening in the center due to the increased plate thickness in this region is observed. The deflection is caused primarily by the outer edges and the poor constraint of the coupling ring. If the coupling ring could also be stiffened a considerable improvement in the maximum pressure limit would be obtained.

As with the previous test, no strength (strain gage) measurements were made. However the yield limit was found in an indirect manner. Figure 111 shows deflection load curves taken for several stations. At ~ 23,000 psi the slope changes abruptly. It appears that yielding has occurred at some plate in the plate and that the increase in load is being taken up only at the expense of an increase in rate of deflection with load. That is to say part of the plate is now in the plastic range with a corresponding increase in slope of the strain - stress relation. This value compares favorably with the predicted yield of 25,900 being ~ 12% lower than the prediction. No measurable set was noticed when the pressure was released. However it is expected that a permanent set would be produced if plastic regions extended significantly, that is, if this pressure limit (23,000 psi) were exceeded by a significant amount.

It should be clear that the improved top plate can withstand steady pressures up to 23,000 psi, a limit which comes from strength considerations rather than O-ring extrusion considerations. Further increase in the pressure limit could come only by stiffening the coupling ring. However the much stronger "high pressure top plate" assembly would be more desirable than an improved coupling ring.

5.1.3 Sacrificial Metal Liners

The pressure generated at the explosive/metal interface, as discussed in Sec. 2.5.2, is for short times, several orders of magnitude greater than the yield strength of the metal of the chamber, hence plastic flow, distortion and possibly fatigue failure will result. As there are no known materials that can withstand these stresses, a design predicted on a philosophy of disposable elements is necessary. Ideally, an inexpensive disposable "sacrificial" liner that protects the surrounding chamber from damage by containing the plastic flow is required.

Fortunately, the problem of the propagation of plastic-elastic waves in solids has been attacked in the very recent past, and some theoretical results are available. The essence of the plastic-elastic wave propagation problem is as follows. When a solid experiences at a boundary a normal stress (pressure) greater than its yield strength a shock wave is propagated into the material. Because the plastic and elastic waves travel at different velocities, the shock wave bifurcates into separate plastic and elastic waves. The plastic wave moves at a slightly slower velocity (~ $0.8\ C_e$) than does the elastic wave which propagates at a velocity given by

$$C_e = \left(\frac{E}{\rho} \right)^{\frac{1}{2}} \tag{5.10}$$

If the problem is planar and if the driving pressure is maintained, both waves propagate to infinity. In the case of cylindrical and spherical geometries, the

geometric divergence causes a reduction in the stress levels until at some point the plastic wave vanishes even for steady pressures greater than the yield stress. If the driving pressure is decreasing with time, relief waves will continuously weaken the strength of the plastic wave and limit its penetration into the solid. For the purposes of protecting the launcher chamber from plastic flow, a sacrificial liner having a depth equal to or greater than the depth of penetration of the plastic wave is required.

Prof. R. C. Tennyson of UTIAS, who is currently working on some related problems, studied this problem at our request and was able to deduce an empirical general relation from the work of Freidman et al[128], which predicts the depth of plastic flow in a given material for cases where the pressure-time history is of the form

$$p = p_o e^{-\alpha t} \tag{5.11}$$

where

$$p_o = n \, \sigma_y$$

and

$$n \geq 1$$

From his analysis the radial depth of plastic flow r_p is given by[119]

$$r_{pl} = R_o \, \frac{n + \dfrac{0.151 \, \alpha n R_o}{C_e}}{1 + \dfrac{0.151 \, \alpha n \, R_o}{C_e}} \tag{5.12}$$

This relation is plotted in Fig. 112. If the second term in the denominator is smaller than the first, i.e., $n \gg C/0.151 \, \alpha \, R_o$, then (5.12) becomes

$$r_{pl} = R_o \, \frac{1 + \dfrac{0.151 \, \alpha \, R_o}{C}}{\dfrac{0.151 \, \alpha \, R_o}{C}} \tag{5.13}$$

or in terms of the depth of penetration, d_{pl}

$$d_{pl} = r_{pl} - R_o = \frac{C_e}{0.151 \, \alpha} \tag{5.14}$$

The depth of penetration of plastic flow is directly proportionately to the sound speed of the liner material and inversely proportional to the time constant of the unloading rate, which is in turn related inversely to the explosive thickness, and the initial gas pressure. Low sound speed liner materials, i.e., low elastic modulus and high density, thin explosive layers, and low gas initial pressures are desirable. The difficulty in applying Eqs. 5.12 through 5.14 is that of fitting a "reasonable" exponential to the $t^{-2/3}$ time decay of the pressure at the explosive metal interface, since the time constant α is continuously variable for a $t^{-2/3}$ decay. The problem of generalizing the analysis to include different loading profiles is presently being considered by Prof. Tennyson. However, no additional results are available at this time.

Unfortunately, very little experimental data exists on dynamic plastic flow penetration in general and none for cases which would be applicable to the present problem. Several exploratory runs were made in the 1-D chamber .. . in an attempt to estimate the thickness of liner required to protect the hemispherical chamber. Lead discs 0.040 in. thick were placed between nominal 1-2 gram layers of PETN and the face of the explosive cups. A close inspection of the surface of the explosive cup after the explosive had detonated for a 100 psia run showed that plastic flow penetrated through the shims in tests where one or two shims were used but that it would not penetrate through three shims. In other words, the depth of plastic flow in lead for this loading ($\rho = 0.588$ gm/cc d $\sim$ 0.1 in., p_i = 100 psia) was between 0.080 in. and 0.120 in. As a rough rule of thumb, at this packing density, for a given thickness of explosive, an equal thickness of lead should be used for each 100 psi of initial pressure. For example, for a 0.1 inch liner of PETN at an initial pressure of 150 psi, would require a 0.150 in. or $\sim$ 3/16 in. lead liner to protect the chamber from damage by plastic flow. How far this rule of thumb can be extrapolated cannot be determined from the · limited data presently available.

To utilize commercially available materials, lead liners of 1/16, 1/8 and 3/16 of an inch were made, and have worked satisfactorily in service. After numerous explosive driven runs, the present wall surface indicates no damage except for very localized ($\sim$ 1/16" dia.) deformations. It is hypothesized that these are the results of shock wave interaction and reinforcements that occur when a void of this dimension is left in the explosive liner, as the dimensions are of the same order as the cell size in the open core foam matrix used as a structure for the explosive. From a long term point of view, either the explosive liner manufacturing tolerance will have to be tightened to preclude the voids or the sacrificial liner thickness will have to be increased to protect against the localized higher pressures.

5.1.4 Launcher Laboratory and Instrumentation

An elevation view of the UTIAS Hypervelocity Launcher Facility is shown in Fig. 113. The implosion driven launcher is located in a blast room which is separated from the rest of the range by a 12 in. thick reinforced concrete wall. The remainder of the walls of the room are of the "blow out" type and are designed to blow out at a small pressure differential and prevent any buildup of pressure. Access to the blast room is through two-2.0 in. thick steel doors. Gases are stored in high pressure bottles behind a protective shield in this room.

The range is located in a high bay area, 80 ft. long and is composed of a blast chamber, three range sections and an impact section. The present blast chamber which is 2.0 ft. dia. by 6.0 ft. long and has a volume of 18.8 cu. ft. serves to contain the bulk of the expended driving gases. At present, it is connected directly to the rest of the range. Future plans call for increasing the volume of the chamber and providing a quick-acting shut-off valve to isolate the rest of the range and trap most of the driving gases. The range proper consists of three sections which can be isolated from one another by thin plastic diaphragms and evacuated to different pressures. The gases simulating the atmosphere under investigation can be set independently in each section to allow several different experiments to be performed during a single run. Section 1, which is 2.0 ft. in diameter by 15.0 ft. long, has twelve 8.0 in.dia. windows arranged four to a station. Recently, two

103

additional sections 3.0 ft. dia. by 18.0 ft. long have been added to extend the capability of the range. They contain 16 observation ports each, arranged in sets of four per station. An impact section containing instrumentation for impact work is currently in the planning stage.

Views of the range are shown in Fig. 114 and 115. The projectiles that are accelerated in the launcher, are released in the blast chamber, which serves to contain most of the driving gases and the resulting explosive products. The velocity and orientation of the projectile is measured during its traverse of Section 1 by three light screen velocity detectors and three spark shadowgraph-schlieren systems. Sections 2 and 3 have not been used to date and a temporary impact station has been installed between Sections 1 and 2.

The velocity measuring system which was originally in the range was a photomultiplier-light screen type. The system was apparently designed for large models having low velocities, as the 0.22 in. one caliber projectiles could not be detected at velocities greater than ~ 9000 fps. The present velocity system which was purchased to replace the old one was designed and manufactured by the Aerophysics Branch of Computing Devices of Canada, Ltd.* It is also of the light-screen-photomultiplier type, but has the capability of measuring 1/32 in. dia. particles up to velocities of 30,000 fps and 0.22 in. dia. projectiles at velocities well in excess of any contemplated for this facility at this time. The units produce a 6.0 volt pulse with a 20 nano-second rise time and a 100 μsec. duration. A 40 millisec. one shot feature is incorporated in the circuit and precludes spurious signals from sabot, debris, wake etc. The system has been in operation over one year and has performed admirably. The only maintainance required is the occasional changing of a battery and routine cleaning of the associated range windows with each run.

The range also has three in-house designed and built shadowgraph-schlieren systems which are located in the first range section. They have a field of view of 6.0 in. dia. and a spark light source with an effective pulse width of 200 nanosec. They have been used to date primarily for verifying projectile integrity and orientation and occasionally for flow field studies.

Range Control Center

Adjacent to the blast room and the range, in a room which has 12-in. concrete block walls, sand filled and reinforced with rods, is a "human-engineered" range control center. The entire operation of the range with the exception of explosive loading and special instrumentation can be controlled from this one location. A view of the control room is shown in Fig. 116. Controls on the center and right panels are for the vacuum pumps and valves for evacuating the range sections which may be controlled jointly or separately and pressure instrumentation for monitoring the pressures. Provision is also made for metering air or other gases into the sections, also jointly or separately. On the left panels are the controls for evacuating and loading gases into either the one-dimensional chamber or the hemispherical launcher chamber.

A schematic of the system is shown in Fig. 117. The gas cylinders (hydrogen, oxygen and helium) are located behind a protective panel in the driver room. Solenoid-operated fail safe shut-off valves are provided between

* Computing Devices of Canada Ltd., Ottawa 4, Ontario.

the hydrogen and oxygen regulators and their respective high-pressure lines to allow these gases to be shut off in case of an emergency. The high-pressure lines are routed overhead to a mixing manifold. At the mixing manifold each gas line is connected to the main manifold through two-solenoid operated valves, a coarse valve that has a 1/32 in. orifice that permits high flow rates for flushing and large volume flows, and a fine valve that is connected in series with a metering valve, that allows fine adjustments. The mixing manifold assembly can be seen in the background of Figs. 101 and 102.

By adjusting the metering valve, extremely low flow rates can be obtained. By operating the remote switches for these solenoid valves the pressures in the chamber can be set with an accuracy equal to a hand operated valve. Keeping high pressure manifolds out of the control room is the prime advantage of this system. However, valve life is essentially unlimited since the valves are opened and closed with the same force and over-tightening and subsequent leakage inherent in hand-operated valves is eliminated. This source of wear can be an irritating maintainance problem particularly when many different people are allowed to operate the system, each with his own "feel" as to how tight a valve must be turned off to prevent leaking. Ignition voltage and firing controls are located in the center panel. A system of interlocks is incorporated into the system and provides essentially "fool proof" operation, i.e., certain otherwise hazardous functions are rendered in-operative unless conditions which are safe for their operation are satisfied. For example: valves connecting vacuum gages to the manifold cannot be opened unless a pressure of one atmosphere or less exists in the manifold, metering valves are inoperative until vacuum gages have been isolated, etc. Further the launcher cannot be fired unless all valves, switches, door interlocks etc. are in the "safe" position.

Because of the human engineering that went into the design of the control panel, new operators can learn how to operate the entire range in a very short time. The layout of the graphic flow diagram plus the associated signal lights greatly simplifies training. Another factor that facilitates operator training is the system of safety interlocks. Since a new operator does not have to worry about damaging the apparatus by accidently pushing the wrong button, he can concentrate fully on learning the operation of the system.

5.2 The Explosive-Liner Package

The high degree of symmetry, which is required to obtain the high pressures and temperatures on implosion, can be attained only if the tolerances on the explosive package are stringently maintained. Variations in explosive thickness or uniformity, ignition asymmetry would produce asymmetries which would seriously degrade launcher performance. Tests in which symmetry was purposely perturbed indicated that performance falls rapidly as the symmetry is degraded. For example, using gaseous detonation driving, a decrease in performance of more than 30 percent was obtained by changing from a "point source" 1/16 in. long to an ignition wire 1.0 in. long. An explosive run in which the upper part of the explosive liner had become detached, did not even succeed in bursting the diaphragm. The same run under normal conditions would have produced peak pressures if at least one order of magnitude greater than the burst strength of the diaphragm. In short the quality and uniformity requirements of the explosive liner cannot be overstressed.

Lead liners of a thickness necessary to contain the plastic flow, were fabricated by a local manufacturer from sheet lead using spinning techniques. As a single male mandril was used for all sizes, some final fitting and trimming was necessary to match the contour of the existing chamber. The liners were washed in solvent to remove the oil used in the spinning operation and four previously prepared orange peel segments of open core foam plastic* were cemented in place in each. The plastic was trimmed at the edge and set aside to dry. The liner and plastic matrix was weighed using a chemical balance an accuracy of ± 1.0 mg. The PETN which was previously prepared in a slurry with approximately 50 percent water was poured into the shell and forced into the pores of the plastic using a rubber spatula. Care was taken to see that all the pores were filled in order to prevent local high pressures which penetrate the liner. Final touches to bring the thickness even with the top of the plastic foam matrix were made using a paint brush damped with water. The assemblies were placed in a warm air draft to dry. The drying cycle takes several hours for a 100 gram liner. The dryness of the PETN can be determined from the color and texture of the surface by experience. Good results require that the liner be completely dry before using or the measured weight will be incorrect. After the drying cycle, the assemblies were weighed again to determine the weight of the dry PETN. The assemblies were then stored for later use. As the PETN is dry, it is more sensitive to initiation and crumbling, hence handling consistant with a delicate device and explosive materials is required. The lead liners, particularly the 1/16 in. ones, are easy to deform and require light handling.

A view of a mock-up showing the steps taken in the manufacture of the explosive package is shown in Fig. 118. Section 1 shows the lead liner prior to the loading of the explosive. Sections 2 and 3 show the application of the open core foam plastic matrix, which is used to provide strength for the explosive and as a gage for thickness. Section 4 shows the PETN after it has been dried.

To use for a run, the completed package need only be placed in the chamber and seated securely against the chamber wall. A thin coating of releasing agent has been found helpful in the assembly of the explosive package in the chamber and also facilitates the removal of the liner after a run. In

---

* Scott Paper Company, Chester, Pennsylvania, U.S.A.

the absence of the releasing agent, the lead adheres to the chamber. An
example of the remains of a liner package after a run is shown in Fig. 112.
The melted lead which accumulates in the bottom of the chamber during the
run is a result of the heat transfer from the hot gases to the liner. It is
felt that the melting occurs late in the cycle and does not compromise the
sphericity of the chamber during the time the projectile is in the barrel.

6. FUTURE WORK

It should be apparent from the preceding sections that many
of the questions and problems that existed at the inception of the present work
such as the explosive initiation problem and the physics of the implosion in a
sphere, have now been answered. It should also be clear that other problems
have been uncovered, which must be solved for a complete understanding of the
implosion driven launcher, and if the device is to be completely successful.
In this section, these problems will be enumerated and suggestions made as to
their possible solution.

6.1 Problem Areas in the Present Work and Suggested Extensions

The key technical problem at this point is projectile inte-
grity. If projectiles that can withstand the very high and repeated accelera-
tions that are inherent in the implosion driving concept cannot be found, then
this technique is not practical. This would be most unfortunate since high
performance is inherent in the device provided the projectiles can withstand
the accelerations. At present, the mood among workers in this field is pessi-
mistic. However, it is important to note that up to the present, relatively
little serious work has been done on this problem, which affects all launchers,[69]
this particular one more so than the others. Work has begun at this laboratory[69],
on this specific problem. It is suggested that the research should first de-
fine the actual mode of failure, as so far, no clear-cut evidence exists as
to just how the projectile fails. After determining the failure mode, effort
can be applied logically to prevent failure, if possible, through rational
projectile design, materials selection or improvement of the properties of
materials.

Another very important area of study, is one of losses. The
hot gas in contact with the wall gives rise to a convective heat loss. This
is true not only during the cycling of the shocks in the chamber but also for
the gas that is driving the projectile in the barrel. The high temperatures
near the origin also generate a high radiative heat loss, which while being
partially blocked by the gas behind the shock, has essentially a transparent
gas ahead of it and a nearly "black" cold sink at the wall. The radiative flux
is not only a loss mechanism but can also preheat the unshocked gas and signi-
ficantly alter the shock conditions. The problem of radiative coupled flows
is difficult in itself. The additional complication of hemispherical symmetry
and imploding shocks would make this a first rate analytical and experimental
research problem. Experimentally, the temperature at the shock front, and
radiative fluxes could be determined using spectroscopic techniques or total
flux measuring gages.[129,130]. If the loss rates are high enough, the surface
of the chamber, the nozzle entrance, and the barrel will ablate significant
amounts of dense material into the flow thereby lowing the performance. Studies
of all these aspects are essential in order to obtain realistic results for com-
parison with experiment.

As mentioned in Sec. 3, to obtain a complete performance program required a number of questionable assumptions, for example the assumption that the pressures at the projectile are related to the pressures at the origin of the sphere at the same instant of time. To make the next step, i.e., to account for the shocks and expansions that are propagating up and down the barrel, requires a finite-difference calculation such as was done by Seigel[56]. Even Seigel's program, which is one of the most recent does not account for projectile friction, nor radiative or convective losses. While this program is presently being adapted to the geometry of the implosion driver and an optimization of the launcher is being done by Sevray[68], from a long range point of view the extension of this program to include both laminar and turbulent gas friction, projectile friction, and convective and radiative losses, should be done. Considering that it has taken nearly a decade to advance this far in the state of the art of performance predictions of hypervelocity launchers, these last effects are not going to be incorporated in a short period of time, but must be done if accurate performance predictions are ever to be obtained.

There are several well-defined analytical problems. The solution, either numerical or analytical of the special case of an explosion with initial conditions

$$\rho = \rho_c$$
$$p = p_o r^{-\delta}$$
$$u = U_o r^{-\delta/2}$$

(6.1)

which corresponds approximately to the reflection of an implosion, would shed considerable light on a phase which is not well in hand at present. Also an analytic solution of the classical implosion problem might allow further use of the resulting relations if they were sufficiently simple. An analytic solution would also yield δ as a function of γ, which is known only numerically to date.

The problem of an "implosion in a sphere" as attempted in this work, could be refined. While a "self-similar" solution, in the usual sense, does not appear likely, a solution that gives a plane-like character initially and then approaches a form resembling the classical implosion at later stages and explains some of the present anomalies would be very useful.

Finally, it is important to note that the absolute stability of the implosion wave has not been proven in the present work. However, it can be concluded that if the implosions are unstable, the rate of divergence is sufficiently low that complete loss of symmetry does not occur in the distances of the present experiments. A proper analysis of the stability of an imploding shock, which is very much a part of the launcher concept is a task that will require much physical insight and mathematical skill.

6.2 Extension to Larger or Faster Facilities

Presently under study is the feasibility of a launcher for accelerating a 1.0 in. dia., one-caliber projectile to 50,000 fps. Initial estimates are based on a projectile density of 1 g/cc, although projectiles of this density, capable of withstanding pressures in the 10^6 psi range, have as yet not been produced. Initial estimates suggested a chamber size of 30 in. dia. However, it appears that much smaller chambers may be better suited to the task. A study model of a 30 in. I.D. launcher is shown in Fig. 120.

Using the present performance model an estimated performance plot for this type of launcher is shown in Fig. 121. It should be kept in mind that at present only half the estimated velocity has been attained in practice. The figure shows that 1.5×10^4 Kcals (~ 10 kg of PETN) would be required to attain 50,000 fps. Preliminary calculations indicate that a chamber can be made to contain this amount of explosive in safety. A smaller chamber would decrease the amount of explosive needed and improve the strength to size ratio of the device. These figures which are included only to indicate what performance may be expected from this type of launcher should be considered preliminary as detailed performance estimates must await the improvement of the present performance predictions and an optimization of the entire launch cycle.

7. CONCLUSIONS

Several key technical problems of the implosion driven launcher project have been successfully solved in the present work, among them the generation of stable, centered implosions by detonating, safe, secondary explosives initiated by gaseous detonation waves. A fuller understanding of the processes that occur inside the implosion chamber has also been obtained. Unfortunately, the last obstacle, projectile integrity, has not been overcome as yet although several distinct possibilities exist that may offer a successful solution.

The explosive initiation studies conducted in the one-dimensional chamber have demonstrated that there are several explosives or explosive combinations that will initiate when subjected to a detonation wave in a gaseous mixture at moderate initial pressures (3 - 15 atm). The delay time to initiate the detonation for these explosives is also short enough (< 10 μsec) to be nearly instantaneous for the conditions of this problem. Some of the materials are rejected for safety reasons. Others, PETN and nitrocellulose for example, are free from undue hazard. The superfine PETN formulation that offers the most promise has been successfully manufactured into thin hemispherical shells and successfully detonated in a hemispherical cavity. The resulting spherical implosion wave was apparently stable and had a high degree of symmetry. This is probably the first time an implosion has been generated in this fashion. The pressure measurements made using copper witness plates at the origin indicate that the pressures generated were in substantial agreement with those predicted.

The results of three numerical implosion experiments have been analyzed and have given much insight into the physics of implosions. The striking difference between driven and undriven implosions has been noted and explained. The physical laws governing the flow behind the reflected implosion have been uncovered, and an approximate physical model made which accounts for the differences between the classical implosion from infinity and the implosion in a sphere. In short, the physics of the implosion cycle is now known although some finer points and the effects of radiation and viscosity require further study. Such investigations have already been started.

A semi-empirical model of the implosion driven launcher performance has been made. It uses much of the physics of implosions in spheres but requires some questionable assumptions to bridge gaps in the complete understanding of the implosion and reflection processes. This model was used to calculate the performance of the implosion driven launcher.

Two series of explosive-driven runs have been made; one using lead azide liners, which were accomplished before the hazard of using this material was fully appreciated; the other series made use of the superfine PETN formulation developed subsequently in the one-dimensional explosive initiation study. The lead azide runs which used a barrel with excellent finish and bore characteristics, yielded velocities as high as 15,000 fps for a 0.22 inch one-caliber polyethylene projectile. The projectiles also survived intact, launch cycles having computed peak accelerations of 5×10^6 g's. The PETN runs which were done in a different barrel configuration with less favorable finish produced velocities up to 17,650 fps for 0.312 inch one-caliber polyethylene projectiles. The peak calculated peak g' leadings for these cases were from 100 to 500×10^6 g's. The projectiles were generally distorted at the lower g loadings and were fragmented at the higher loadings. While it is clear that the acceleration profile is playing an important role in the break-up of the projectiles it is also clear that the poor bore finish and concentricity are contributing to the failure. Work on improving barrel finish is currently in progress.

The projectile problem is presently being investigated from two points of view: a detailed study of the failure modes of the projectile in anticipation of rational projectile design or materials improvement programs; methods of tailoring the pressure-time history produced by the implosion to make it more favorable for projectile survival. Since there is considerable latitude in the performance of this device, some of this can be sacrificed to obtain a more favorable acceleration profile.

In all, it can be concluded that a considerable amount of progress has been made in the present study in the bringing of the unique Implosion Driven Launcher concept into practical reality.

REFERENCES

1. Langweiler, H.   Z. Tech. Physik 19, 416, 1938.

2. Crozier, W.D.   High-Velocity, Light-Gas Gun, Journal of Applied
    Hume, W.   Physics, Vol. 28, No. 8, Aug. 1957.

3. Curtiss, J.S.   An Accelerated Reservoir Light-Gas Gun. NASA TN-
                            D 1144, 1962.

4. Charters, A.C.   How an Accelerated Reservoir Light Gas Gun is Used
    Curtiss, J.S.   in a Hypervelocity Free Flight Range, General
                            Motors Engineering Journal, Second Quarter, 1963.

5. Denardo, B.P.   Penetration of Polythelene into Semi-Infinite
                            2024-T351 Aluminum up to Velocities of 37000 feet
                            per second, NASA TN D-3369, March 1966.

6. Lukasiewicz, J.   Constant Acceleration Flows and Application to High-
                            Speed Guns, Arnold Engineering Development Center,
                            AEDC-TR-66-81, Nov. 1966.

7. Moore, E.T.   Explosive Gas Guns for Hypervelocity Acceleration,
    Mumma, D.   Fourth Hypervelocity Techniques, Symposium, Arnold
    Godfrey, C.S.   Air Force Station, Tennessee, Nov. 1965.
    Bernstein, D.

8. Eckerman, J.   Performance of a Three-Stage Arc Heated Light-Gas
    McKay, W.L.   Gun, AVCO-Research and Advanced Development, Division
                            TM 63-21, April 1963.

9. Swift, H.F.   NRL Hypervelocity Accelerator Development, Proceedings
    Porter, C.D.   of the Sixth Symposium on Hypervelocity Impact,
    Condon, J.J.   Cleveland, Ohio, 1963.
    Baker, J.R.

10. Howell, W.G.   Electrical Augmentation of a Light Gas Hypervelocity
    Orr, W.R.   Projector, Advances in Hypervelocity Techniques,
    Krill, A.M.   Proceedings of the Second Symposium on Hypervelocity
                            Techniques, University of Denver, 20-21 March 1962.

11. Thom, K. H.   Theory of an Electromagnetic Mass Accelerator for
    Norwood, J. Jr.,   Achieving Hypervelocities, NASA TN D-886, June 1961.

12. Rosen, F.D.   A Magnetically Augmented Rail Gun, Seventh Hyper-
                            velocity Impact Symposium, Vol. 1 - Techniques,
                            Tampa, Florida, Nov. 1964.

13. Lunc, M.   Accelerator for Jets Formed by Shaped Charges,
    Nowak, H.   Bulletin Polish Academy of Sciences, Vol. 12, No.5,
    Smolenski, D.   p. 295, 1964.

14. Wenzel, A.B.   Technique for Launching 0.001 to 25 Gram Discrete
    Gehring, J.W.   Projectiles at Velocities up to 54100 Feet per
                            Second, Proceedings Fourth Hypervelocity Techniques
                            Symposium, Arnold Air Force Station, Nov. 1965.

111

15. Riddell, F.R. From ICBM Re-entry to Meteorite Entry, National
    Winkler, H.B. IAS-ARS Joint Meeting, Los Angeles, California,
                   13-16 June, 1961.

16.   Bulletin And Annual Progress Report, Institute for
                Aerophysics, University of Toronto, 1959.

17. Glass, I.I. Shock&Combustion Wave Dynamics in an Implosion-
                 Driven Hypervelocity Launcher, UTIAS Review No. 25,
                 1965.

18.   High Speed Aerodynamics and Jet Propulsion, Vol. III,
                Fundamentals of Gas Dynamics, H.W. Emmons, Editor,
                Princeton University Press, 1958.

19. Glass, I.I. Handbook of Supersonic Aerodynamics, Section 18,
    Hall, J.G.   Shock Tubes, NAVORD Report 1488, Vol. 6, Dec. 1959.

20. Wright, J.K. Shock Tubes, John Wiley and Sons, New York, 1961.

21. Courant, R.   Supersonic Flow and Shock Waves, Interscience
    Freidrichs, K.O. Publishers, New York, 1948.

22. Feldman, S. Hypersonic Gasdynamic Charts for Equilibrium Air,
                 AVCO-Everett Research Laboratory, Research Report
                 40, 1957.

23. Laird, J.D. Shock Tube Gas Dynamic Charts - Part 1: Equilibrium
    Heron, K.   Argon-Free Air from 3000 to 40,000°K, AVCO-Research
                 and Advanced Development Division, TM 64-12, 1964.

23. Heron, K. Shock Tube Gas Dynamic Charts - Part 2; Martian
               Atmospheres (Models G,H,I,J and K) AVCO-Research and
               Advanced Development Division, TM 65-23, 1965.

25. Sandage, A.R. Exploding Galaxies, Scientific American, Vol. 211,
                   No. 5, Nov. 1964.

26. Taylor, G.I. The Formation of a Blast Wave by a Very Intense
                  Explosion, I, Theoretical Discussion, Proceedings
                  of the Royal Society, A, Vol. 201, 1950.

27. Taylor, G.I. The Formation of a Blast Wave by a Very Intense
                  Explosion, II, The Atomic Explosion of 1945,
                  Proceedings of the Royal Society, A, Vol. 201, 1950.

28. Sedov, L.I. Similarity and Dimensional Methods in Mechanics,
                 Academic Press, Inc., New York, 1959.

29. von Neumann, J. John von Neumann Collected Works., Vol. VI,
                     MacMillan Co., 1963.

30. Latter, R. Similarity Solution for a Spherical Shock Wave,
                Journal of Applied Physics, Vol. 26, No. 8, Aug. 1955.

31. Taylor, J.L. An Exact Solution of the Spherical Blast Wave Problem, Phil. Mag. Vol. 46, 1955.

32. Harris, E.G. Exact and Approximate Treatments of the One Dimensional Blast Wave, NRL Report 4858, Naval Research Laboratory, Washington, D.C., Nov. 1956.

33. Lin, S.C. Cylindrical Shock Waves Produced by Instantaneous Energy Release, Journal of Applied Physics, Vol. 25, No. 1, 1954.

34. Brode, H.L. Numerical Solutions of Spherical Blast-Waves, Journal of Applied Physics, Vol. 26, No. 6, 1955.

35. Brode, H.L. Numerical Calculations of Blast Waves, The Rand Corp., P-1933, Feb. 1960.

36. Brode, H.L. The Blast From a Sphere of High Pressure Gas, The Rand Corp., P-582, Jan. 1955.

37. Brode, H.L. The Blast Wave from a Spherical Charge of TNT. Physics of Fluids, Vol. 2, No. 2, 1959.

38. Brode, H.L. The Blast in Air Resulting from a High Temperature, High Pressure Sphere of Air, Rand Corp. Report RM-1825-AEC, 1956.

39. von Neumann, J.
    R chtmyer, R.D. A Method for the Numerical Calculation of Hydrodynamic Shocks, Journal of Applied Physics, Vol.21, 1955.

40. Glass, I.I. Aerodynamics of Blasts, CASI Journal, Vol. 7, No.3, 1961.

41. Glasstone, S.
    Editor The Effects of Nuclear Weapons, U.S. Government Printing Office, 1957.

42. Schindler, G.M. On an Extension of Taylor's Blast Wave Solution. RM62TMP-6, TEMPO, General Electric Company, Santa Barbara, Calif., Feb. 1962.

43. Guderley, G. Strong Spherical and Cylindrical Shock Waves in the Neighborhood of the Center of the Sphere of the Axis of a Cylinder, Report of the Institute for Gasdynamics of the Herman Goring Aviation Research Institute, Braunschweig (Luftfahrtforschung, Vol. 19, No. 9, pp. 302-312, Oct. 1942).

44. Stanyukovich Unsteady Motion of a Continuous Media, Pergamon Press, 1960.

45. Butler, D.S. Converging Spherical and Cylindrical Shocks, Armament Research Establishment Report 54/54, Forth Halstead, Kent, Dec. 1954.

46. Aiken, A.W.   Metropolitan-Vickers-Research Report 5090, 1956.

47. Welsh, R.L.   Imploding Shocks and Detonations, Report No.
                         AS-66-1, College of Engineering, University of
                         California, Berkeley, January 1966.

48. Somon, J.P.   Contribution a La Theorie des Chocs / Convergenes
    Linhart, J.G.   dans un Plasma, Nuclear Fusion: 1962 Supplement
    Knoepfel, H.   Part 2, pp. 717-726 (in French)

49. Brode, H.L.   Private communication.

50. Benoit, A.   Properties of Chapman Jouget Detonations in Stoi-
                         chiometric Hydrogen-Oxygen Mixtures Diluted with
                         Helium and Hydrogen, Institute for Aerospace Studies,
                         University of Toronto, Tech. Note No. 104, Dec.1966.

51. Jones, H.   Detonation of Solid Explosives., Proc. Roy. Soc.,
    Miller, A.R.   London, Vol. A, 194, 480, 1948.

52. Moffatt, W.C.   The Thermodynamic and Electrical Properties of
                         Dissociated Combustion Gases Magnetogasdynamics
                         Laboratory Report 61-5, Massachusetts Institute
                         of Technology, May 1961.

53. Jacobs, S.J.   Recent Advances in Condensed Media Detonations,
                         Journals ARS, Vol. 30, No. 2, Feb. 1960.

54. Taylor, G.I.   The Air Wave Surrounding an Expanding Sphere,
                         Proc. Royal Society, London, A186, 1946.

55. Boyer, D.W.   Blast from a Pressurized Sphere,
    Brode, H.L.   UTIA Report No. 48, 1958.
    Glass, I.I.
    Hall, J.G.

56. Piacesi, R.   Computer Analysis of Two-Stage Hypervelocity Model
    Gates, D.F.   Launchers, U.S. Naval Ordnance Laboratory, White
    Seigal, A.E.   Oak, Maryland, NOLTR 62-87, Feb. 1963.

57. Wilenius, G.P.T.   The Constant Base Pressure Light Gas Gun,
    Cowan, P.L.   Proceedings Third Hypervelocity Techniques
    Cloutier, M.   Symposium, Denver, Col. 17-18, March 1964.

58. Manson, N.   Propagation des Detonations et des Deflagrations
                         dans les Melanges Gaseux, Compt. Rendes, 222,
                         46, 1946 (from Ref. 25).

59. Flagg, R.F.   Detailed Analysis of Shock Tube Tailored Conditions,
                         RAD-TM-63-64, AVCO Research and Advanced Development
                         Division, Sept. 1963.

60. Glass, I.I.   Hypervelocity Launchers, Part 2: Compound
                         Launchers - Driving Techniques, UTIAS Review No.
                         26, Dec. 1965.

61. Glass, I.I.   Hypervelocity Launchers Part 1: Simple Launchers,
                           Institute for Aerospace Studies, University of
                           Toronto, UTIAS Review 22, Jan. 1963.

62. Seigal, A.   U.S. Naval Ordnance Laboratory, White Oak, Maryland,
                           Private Communication.

63. Watson, J.D.   Implosion Driven Hypervelocity Launc'.er Performance
                           Using Gaseous Detonation Waves, Masters Thesis,
                           Institute for Aerospace Studies, University of
                           Toronto, June 1966.

64. Duff, R.E.   Private Communication.

65. Harvalik, Z.V.   Personal Communication. U.S. Army Engineers
                           Research and Development Laboratories, Ft. Belvoir,
                           Virginia.

66. Kauffman, J.V.R.   Private Communication, Picatinny Arsenal, N.J.

67. Christman, D.R.   Target Strength and Hypervelocity Impact, AIAA
                           Journal, Vol. 4, No. 10, Oct. 1966.

68. Savray, P.   Optomization Studies of the UTI AS Implosion
                           Driven Hypervelocity Launcher, (to be published)

69. Graf, W.   An Experimental and Theoretical Study of Pro-
                           jectile Integrity in an Implosion Driven Hyper-
                           velocity Launcher (to be published).

70. Benoit, A.   Thermodynamic and Composition Data for Constant-
                           Volume Combustion of Stoichiometric Mixtures of
                           Hydrogen-Oxygen Diluted with Helium or Hydrogen,
                           UTIAS Technical Note No. 85, Nov. 1964.

71. Cook, M.A.   The Science of High Explosives, American Chemical
                           Society Monograph, Reinhold, 1958.

72.   U.S. Army Technical Manual 9-1910 and U.S. Air
                           Force Technical Order 11A-1-34, Washington, D.C.,
                           14 April 1955.

73. Bowden, F.P.   Initiation and Growth of Explosion in Liquids and
    Yoffe, A.D.   Solids, Cambridge University Press, Cambridge,
                           England 1952.

74. Bowden, F. P.   A Discussion on Initiation and Growth of Explosion
                           in Liquids and Solids, Proc. Roy. Soc., London,
                           Vol. A-246, 1958.

75. Kistiakowsky, G.B.   Initiation of Detonation of Explosives, Third
                           Symposium on Combustion Flames and Explosives,
                           Williams and Wilkins Co., Baltimore, 1949.

76. Ubblohoe, A.R.

Transition from Deflagration to Detonation: The Physico-Chemical Aspects of Stable Detonation, Third Symposium on Combustion, Flames and Explosives, Williams and Wilkins Co., Baltimore, 1949.

77. Gipson, R.W.
Macek, A.

Flame Fronts and Compression Waves During Transition from Deflagration to Detonation in Solids. Eighth Symposium on Combustion, Cal. Inst. of Technology, Aug. 28-Sept. 3, 1960.

78. Griffith, N.
Groocock, J.M.

Journal Chemical Society, p. 4154, 1960

79. Price, Donna
Jaffe, Irving

Large Scale Gap Test: Interpretation of Results for Propellants. Journal ARS, Vol. 31, No. 5, May 1961.

80. Price, D.
Petrone, F.J.

Detonation Initiated by High-Pressure Gas Loading of a Solid Explosive, Journal of Applied Physics, Vol. 35, No. 3, March 1964.

81. Lutzky, M.

U.S. Naval Ordnance Lab. Tech. Report 62-19, Jan. 1962.

82. Andreev, K.K.
Maslov, V.P.

Action of Gas Explosion on Solid Explosives, Comptes Rendes (Doklady) de l'Academie des Sciences de l'URSS, Vol. 25, No. 3, 1939.

83. Summerfield, M.
McAlevy, R.F.

The Shock Tube as a Tool for Solid Propellant Ignition Research, Jet Propulsion, 66, 478, 1958.

84. Baer, A.D.

Ignition of Composite Rocket Propellants, Ph.D. Thesis, University of Utah, 1959.

85. Erikson, T.A.

Pure Shock Environmental Testing of Condensed-Phase, Unstable Materials, ARS Journal Vol. 30, No. 2, Feb. 1960.

86. Hubbard, H.W.
Johnson, M.H.

Initiation of Detonations, Journal of Applied Physics, Vol. 30, No. 5, May 1959.

87. Enig, J.W.

Growth of Detonation from an Initiating Shock, Proceeding 'rd Symposium on Detonation, Princeton Univ., Sep 1960.

88. Mader, C.L.

Shock and h   .ock Initiation of Homo-
geneous Exp   .ysics of Fluids, Vol. 6,
No. 3, Mar.

89. Keller, J.A.
Baer, A.D.
Ryan, N.W.

Ignition of Ammonium Perchlorate Composite Pro-pellants by Convective Heating, AIAA Journal, Vol. 4, No. 8, Aug. 1966.

90. Makomaski, A.H.   Preliminary One-Dimensional Investigation of the Initiation of Low Density PETN by Hydrogen-Oxygen Detonation Waves, UTIAS Technical Note 83, Feb. 1965.

91. Knight, H.T.
    Duff, R.E.   Precision Measurements of Detonation and Strong Shock Velocity in Gases, Review of Scientific Instruments, Vol. 26, No. 3, March 1955.

92. Edwards, D.H.
    Williams, G.T.
    Breeze, J.C.   Pressure and Velocity Measurements in Detonation Waves in Hydrogen Oxygen Mixtures. Jour. Fluid Mech. Vol. 6., No. 4, 1959.

93. Berlow, E.
    Barth, R.H.
    Snow, J.E.   The Pentaerythritols, ACS Monograph No. 136, Reinhold Publishing Corp., 1958.

94. Bollinger, L.E.   Formation of Detonation Waves in Hydrogen-Oxygen Mixtures from 0.2 to 2 Atmospheres Initial Pressure in a 54-Meter Long Tube, NASA TN D-2256, April 1964.

95. Lee, J.H.   Inviscid Hypersonic Flow of a Detonating Gas, Paper Presented at CASI Astronautics Symposium Toronto, Feb. 15-16, 1965.

96. Seay, G.E.
    Sealy, L.B. Jr.   Initiation of a Low-Density PETN Pressing by a Plane Shock Wave, Jour. Appl. Phys., Vol. 32, No. 6, June, 1961.

97. Roth, J.   Initiation of Lead Azide by High Intensity Light, Journal of Chemical Physics, Vol. 41, No. 7, Oct. 1964.

98. Lundborg, N.   Front and Mass Velocity at Detonation in Evacuated Chambers, Proceedings Fourth Symposium on Detonation, U.S. Naval Ordnance Laboratory, Oct. 12-15, 1965.

99. Rosciszewski, J.   Solid Propellant Driven Shock Tube, ARS Journal, Vol. 32, No. 9, Sept. 1962.

100. Tomlinson, W.R., Jr.   Properties of Explosives of Military Interest, Picatinny Arsenal, TR 1740, Rev. 1, April 1958.

101. Ornellas, D.L.
     Carpenter, J.H.
     Gunn, S.R.   A Detonation Calorimeter and the Heat and Products of Detonation of Pentaerythritol-tetranitrate (PETN), Proceedings Fourth Symposium on Detonation, U.S. Naval Ordnance Laboratory, Oct. 12-15, 1965.

102. Jacobs, S.J.
     Editor   Proceedings Fourth Symposium on Detonation, U.S. Naval Ordnance Laboratory, Oct.12-15, 1965.

103. Davis, W.C.
     Craig, B.G.   Failure of the Chapman-Jouget Theory for Liquid and Solid Explosives, Proceedings of the Fourth Symposium on Detonation, U.S. Naval Ordnance Laboratory, Oct. 12-15, 1965.

104. White, D.H.   Primate Communication, E.I. DuPont DeNemours and
                           Co. Explosives Dept. Pompton Lakes, N.J.

105. Davis, T.L.   The Chemistry of Powder and Explosives, Vol. II,
                           Wiley and Sons Inc. 1943.

106. Abegg, M.T.   Low Detonation Pressure Explosive Combinations,
     Fisher, H.J.   Proceedings of the Symposium on Explosives and
     Lawton, H.C.   Hazards and Testing of Explosives, Sept. 8-13,
     Weatherill, W.T.   1963, New York.

107. Wimpress, B.H.   Internal Ballistics of Solid-Fuel Rockets,
                           McGraw-Hill Book Company, 1950.

108.   DuPont EL-506 Series Flexible Sheet Explosive-
                           Explosive Specialties Technical Information,
                           E.I.DuPont DeNemours and Co. (Inc.) Wilmington,
                           Deleware.

109. Welsh, D.M.   Private Communication, Canadian Safety Fuse Co.
                           Ltd., Brownsburg, Que.

110. Bjork, R.L.   The Atomic-Hydrogen Gun, Rand Corp. Report RM-1707,
                           1961.

111. Wright, G.F.   Private Communication, Chemistry Dept. University
                           of Toronto.

112. Nevill, G.E., Jr.   Impulsive Loading Using Sprayed Silver Acetylide-
     Hoese, F.O.   Silver Nitrate, Experimental Mechanics, Sept. 1965.

113. Bowden, F.P.   The Thermal Decomposition of Explosive Crystals,
     Camp, M.   Eighth Symposium (International) on Combustion,
     Montagu-Pollock, H.M. Williams and Wilkins Co. Baltimore, Md., 1962.

114. Deb, S.K.   Ignition and Sensitized Reactions in the Explosive
     Evans, B.L.   Inorganic Azides, Eighth Symposium (International)
     Yoffe, A.D.   on Combustion, Williams and Wilkins Co.,
                           Baltimore, Md., 1962.

115. Kennedy, J.E.   Multipoint-Initiated Implosions from Hemispherical
     Glass, I.I.   Shells of Sheet Explosives, UTIAS T.N. 99, Dec.1966.

116. Kennedy, J.E.   Generation and Evaluation of Implosion Driven by
                           Multiple-Point Initiated Detonation, Illinois
                           Institute of Technology Research Institute Final
                           Report K6071, April 1965.

117. Zaidel, R.M.   The Stability of One Case of a Spherical Converging
     Lebedev, V.S.   Shock Wave, Soviet Physics-Doklady, Vol. 135, No.2,
                           Nov. 1960.

118. Butler, D.S.   The Stability of Converging Spherical and Cylindri-
                           cal Shock Waves, Armament Research and Development
                           Establishment, Ft. Halstead Report B 18/56, Aug./56.

119. Tennyson, R.C.   Institute for Aerospace Studies,
                         Private communication.

120. Watson, J.D.   The Performance of the UTIAS Hypervelocity Launcher
                         using Deflagrating Gaseous Combustion, Bachelor
                         of Science Thesis, Dept. of Engineering Science,
                         University of Toronto, Dec. 1964.

121. Benoit, A.   An Experimental Investigation of Spherical Combustion
                         for the UTIAS Implosion Driven Launcher, UTIAS Tech.
                         Note No. 71, Sept. 1963.

122.   Annual Progress Report 1960. Institute for Aero-
                         physics, University of Toronto, Oct. 1960.

123.   Annual Progress Report 1961, Institute for Aero-
                         physics, University of Toronto, October 1961.

124. Marks, L.S.   Editor, Mechanical Engineers Handbook, Fifth Edition,
                         McGraw-Hill Book Company, Inc., New York, 1951.

125.   Atlas Select Alloy Machinery, Steels-Technical
                         Handbook, Atlas Steels Company, Welland, Ontario,
                         Canada.

126.   Parker O-Ring Handbook No. 5700, Parker Seal
                         Company, Culver City, California, Sept. 1963.

127. Graf. W.O.   Private communication. Institute for Aerospace
                         Studies, University of Toronto.

128. Freidman, Morton B,   Spherical Elastic Plastic Shock Propagation,
     Bleich, Hans   Journal of the Engineering Mechanics Div. ASCE,
     Parnes, Raymond   Vol. 91, No. EM3, Proc. Paper 4377, June 1965.

129. Flagg, R.F.   Stagnation Point Radiative Heat Transfer Measure-
                         ments at Super Satellite Velocities, Proceedings
                         of the Plasma Phenomena and Measurements Conference,
                         San Diego, Calif. Oct. 29-31, 1963.

130. Flagg, R.F.   An Experimental Determination of Stagnation Point
                         Radiative and Convective Heat Transfer Rates at
                         Entry Velocities in Simulated Planetary Atmospheres,
                         AVCO-RAD-TM 64-43, Sept. 1964.

TABLE 1
LIMITING VALUES OF PRESSURE, TEMPERATURE, DENSITY PARTICLE VELOCITY AND FLOW MACH NUMBER
FOR INCIDENT AND REFLECTED SHOCKS

γ	n	Incident					Reflected			Overall		
		p_{21}/M_s^2	T_{21}/M_s^2	ρ_{21}	U_2/U_s	M_f	p_{52}	T_{52}	ρ_{52}	p_{51}/M_s^2	T_{51}/M_s^2	ρ_{51}
1	∞	1	0	∞	1	∞	∞	2	∞	∞	0	∞
1.1	20	1.048	.0499	21	0.952	4.26	23	2.091	1..	24.10	0.104	231
1.2	10	1.091	.0992	11	0.909	2.89	13	2.167	6	14.18	0.215	66
1.4	5	1.167	.1944	6	0.833	1.89	8	2.286	3.500	9.340	0.445	21
1.667	3	1.250	.3125	4	0.750	1.34	6	2.400	2.500	7.500	0.750	10
2	2	1.333	.4444	3	0.667	1.0	5	2.500	2	6.667	1.111	6
3	1	1.500	.7500	2	0.500	0.58	4	2.667	1.500	6	2	3
4	0.667	1.600	.9600	1.667	0.400	0.41	3.66	2.750	1.333	5.867	2.640	2.222

TABLE 2

TABLE OF EXPONENTS FOR SPATIAL VARIATION OF PRESSURE FOR SPHERICAL IMPLOSIONS

x	This Report	Butler[45]	Guderley[43]	Somon[48]	Welsh[47]	Stanyukovich[44]
			δ For Spherical Implosions			
∞						3
4.2	1.219					
4.0	1.211					
3.8	1.199					
3.6	1.188					
3.4	1.166					
3.2	1.159					
3.0	1.143				1.14262	1.1
2.8	1.123					
2.6	1.099					
2.4	1.072					
2.2	1.039					
2.0	1.000					
1.8	.9475					
5/3	.9053	.905385		.904		
1.6	.8810	.788728				
1.4	.7887		.792			0.8
1.2	.6416	.641513				
1.15	.5846					
1.14	.5719					
1.10	.5107					
1.05	.4008					0.7
1	.0000					

TABLE 3

CONSTANTS FOR THE ASYMPTOTIC BEHAVIOR OF THE SPHERICAL IMPLOSION SIMILARITY SOLUTIONS

γ	f_∞	Φ_∞	ψ_∞	λ_∞	Λ_∞	ψ_∞(Stanyukovich[44])	ψ_∞(Somon et al[48])
--	--	--	--	--	--	∞*	--
1.14	3.984	0.6833	106.2	1.006	.5015	--	--
1.2	3.447	0.6579	59.53	1.114	.5270	--	--
1.4	2.868	0.5874	20.07	1.477	.5954	16.2	--
1.667	2.659	0.5076	9.549	1.964	.6626	--	9.548
1.8	2.658	0.4727	7.471	2.207	.6882	--	--
2.0	2.574	0.4221	5.559	2.591	.7215	--	--
2.4	2.616	0.3494	3.843	3.306	.7678	--	--
3.0	2.606	0.2682	2.735	4.337	.8144	2.90	--
3.4	2.579	0.2290	2.353	5.087	.8357	--	--
4.0	2.587	0.1862	2.019	6.104	.8592	--	--
∞	--	--	--	--	--	1	--

*$\psi(\infty)/\psi(1) = 2.72$ Present report gives $\psi(\infty)/\psi(1) = \infty$

**$\psi(\infty)/\psi(1) = \infty$

TABLE 4

TABLE OF VALUES OF THE INTEGRAL $\Phi(\zeta)$ FOR $0.5 \leq \delta \leq 1.5$

$$\Phi(\zeta) = \int_1^0 \left\{ \left(1 - \zeta^{3-\delta}\right)\zeta^\delta \right\}^{\frac{1}{2}} \, d\zeta$$

δ	$\Phi(\zeta)$	δ	$\Phi(\zeta)$
0.50	0.6283	1.00	0.4792
0.52	0.6213	1.02	0.4741
0.54	0.6145	1.04	0.4691
0.56	0.6078	1.06	0.4640
0.58	0.6012	1.08	0.4591
0.60	0.5946	1.10	0.4542
0.62	0.5881	1.12	0.4493
0.64	0.5818	1.14	0.4445
0.66	0.5755	1.16	0.4397
0.68	0.5693	1.18	0.4350
0.70	0.5631	1.20	0.4303
0.72	0.5571	1.22	0.4256
0.74	0.5511	1.24	0.4210
0.76	0.5452	1.26	0.4164
0.78	0.5393	1.28	0.4119
0.80	0.5335	1.30	0.4074
0.82	0.5278	1.32	0.4029
0.84	0.5222	1.34	0.3985
0.86	0.5166	1.36	0.3941
0.88	0.5111	1.38	0.3898
0.90	0.5056	1.40	0.3854
0.92	0.5002	1.42	0.3812
0.94	0.4949	1.44	0.3769
0.96	0.4896	1.46	0.3727
0.98	0.4844	1.48	0.3685
		1.50	0.3643

TABLE 5

SUMMARY OF INITIAL CONDITIONS FOR NUMERICAL EXPERIMENTS OF BRODE AND COMPARISON WITH PROTOTYPE INITIAL CONDITION

Parameter	Prototype	Case 1	Case 2	Case 3
Gas	$2H_2 + O_2$ + Helium and/or Hydrogen Dilution Real Gas	$2H_2 + O_2$ + 7 He $\gamma = 5/3$	Analytic Re-presentation of stoichiometric Oxygen-Hydrogen	$2H_2 + O_2$ + 7 He $\gamma = 5/3$
Pressure	75 - 200 psia	100 psia	1000 psia	100 psia
Explosive	0.1-0.5 inch liner of PETN @ .59 g/cc	0.1 inch liner of TNT @ 1.5 g/cc	0.1 inch liner of COMP B @ 1.5 g/cc	none
Chamber Radius	10 cm	20 cm	20 cm	10 cm
Range of Numerical Experiment	--	Instant of Initiation at Origin Through Reflection at Origin	Instant of Initiation at origin Through Two Complete Cycles	From Reflection of the Detonation Wave at Periphery Through 1 cycle

TABLE 6

OVERALL COMPRESSION AND REFLECTED SHOCK STRENGTH RATIOS FOR PLANAR, CYLINDRICAL AND

SPHERICAL IMPLOSIONS AND SOME RESULTS FROM NUMERICAL EXPERIMENTS

γ	Planar	Cylindrical		Spherical		Numerical Representation $\left(\frac{\gamma+1}{\gamma-1}+2\right)^{\frac{1}{\gamma+1}}$	Numerical* Experiment
		Total Compression	Reflected Shock	Total Compression	Reflected Shock	$\nu = 3$	$\nu = 3$
1.14	--	--		--		8.02	4.1
1.4	8	16.**	4.6**	26.6**	3.33**	3.33	--
1.67	6		3.3***		2.5***	2.25	1.7

*   Values are probably low due to action of artificial viscosity on peak values

**   From Guderley, Ref. 43

***   From Somon, Ref. 48

TABLE 7

VALUES OF INITIAL CONDITIONS AND CHAMBER PARAMETERS OBTAINED FROM BRODE'S
CALCULATIONS AND THE IMPLOSION IN A SPHERE MODEL

Initial Conditions	Parameter	Brode	Implosion in a Sphere
Case 1	$p_{inbound}$ (psi)	1.25×10^5	1.2×10^5
100 psia	$T_{inbound}$ (°K)	1.0×10^5	1.3×10^5
$2H_2 + O_2 + 7He$ $\gamma = 1.67$	t_* (psec)	1.80	1.23
$p_{burned} = 470$ psia	p_* (psi)	4.3×10^5	2.2×10^5
$T_{burned} = 2000°K$	T_* (°K)	3.4×10^5	4.4×10^5
$a_{burned} = 0.204$ cm/μsec	t_{imp} (μsec)	17.3	12.0
$R_o = 20$ cm	t_{exp} (μsec)	N.A.*	12.3
0.1 inch TNT liner	t_{cyc} (μsec)	N.A.	24.3
$r_* = 2.0$ cm			
Case 2	p_{burned} (psia)	3.5×10^3	6.4×10^3
1000 psia	T_{burned} (°K)	1.9×10^3	3.6×10^3
$2H_2 + O_2$ (real gas)	$p_{inbound}$ (psia)	2.0×10^5	2.9×10^5
$R_o = 20$cm	$T_{inbound}$ (°K)	3.0×10^3	1.4×10^4
$r_* = 2.0$cm	t_* (μsec)	9.3	9.31
0.1 inch COMP B liner	p_* (psia)	9.8×10^5	2.0×10^6
	T_* (°K)	4.0×10^4	2.5×10^5
	t_{imp} (μsec)	42.5	35.3
	t_{imp} (μsec)	N.A.	93.1
	t_{cyc} (μsec)	N.A.	128.4
Case 3	$p_{inbound}$ (psi)	4.9×10^3	4.9×10^3
100 psia	$T_{inbound}$ (°K)	6.6×10^3	7.1×10^3
$2H_2 + O_2$ 7He	t_* (μsec)	2.22	2.44
$\gamma = 1.67$	p_* (psi)	1.0×10^4	9.3×10^3
$p_{burned} = 470$ psia	T_* (°K)	1.8×10^4	2.5×10^4
$T_{burned} = 2000°K$	t_{imp} (μsec)	26.7	24.4
$a_{burned} = 0.204$ cm/μsec	t_{exp} (μsec)	27.6	24.4
$R_o = 10$ cm	t_{cyc} (μsec)	54.4	48.8
no explosive			
$r_* = 1.0$ cm			

N.A.* Not Available.

TABLE 8

COMPARISON OF CHARACTERISTIC CHAMBER PARAMETERS OBTAINED FROM BRODE'S CALCULATIONS AND THE

IMPLOSION IN A SPHERE MODEL FOR SEVERAL VALUES OF r_* FOR CASE 3

Parameter	$r_* = 0.5$			$r_* = 1.0$			$r_* = 2.0$		
	Brode	IIAS*	Error	Brode	IIAS	Error	Brode	IIAS	Error
$P_{inbound}$ (psi)	9.1×10^3	9.1×10^3	~ 0	4.9×10^3	4.9×10^3	-0	2.7×10^3	2.6×10^3	-4%
$T_{inbound}$ (°K)	1.1×10^4	1.2×10^4	$+10\%$	6.6×10^3	7.1×10^3	$+6.5\%$	4.6×10^3	4.6×10^3	~ 0
t_* (μsec)	1.15	1.22	$+6\%$	2.22	2.44	$+10\%$	4.20	4.88	$+17\%$
P_* (psi)	2.9×10^4	1.7×10^4	-7.0%	1.0×10^4	9.3×10^3	-7.5%	3.6×10^3	5.0×10^3	$+39\%$
T_* °K	2.7×10^4	4.1×10^4	$+50\%$	1.8×10^4	2.5×10^4	$+39\%$	1.2×10^4	1.6×10^4	$+33\%$

*IIAS = Implosion in a Sphere

TABLE 9

TABLE OF INITIAL CONDITIONS AND PREDICTED AND MEASURED VELOCITY VALUES FOR THE LEAD AZIDE RUNS USING

0.22 INCH DIAMETER ONE CALIBER PROJECTILES IN A 60.0 INCH BARREL

Run No.	Explosion Weight (Grams)	Explosion liner (inches)	Explosive (Kcal)	E_{total} (Kcal)	Experimental Velocity (feet per sec)	Predicted Velocity (feet per sec.)	Difference	Calculated P_{max} (psia)	Calculated T_{max} (°K)
80	93.5	0.035	11.4	33.8	9,400	13,800	+47%	9.1×10^5	9.3×10^5
81	72.9	0.027	8.9	31.3	7,100	12,700	79%	8.4×10^5	8.7×10^5
82	230.0	0.086	28.1	50.4	14,300	20,500	43%	1.4×10^6	1.4×10^6
85	199.0	0.075	24.3	46.6	15,000	18,500	24%	1.3×10^6	1.3×10^6

E_{Gas} = 22.4 kilocalories @ 100 psia for an 8 inch diameter chamber and $2H_2 + O_2$

$E_{Pb N_6}$ = 0.122 Kcal/gm,@ ρ = 1.6 gm/cc

TABLE 10

INITIAL CONDITIONS AND MEASURED AND CALCULATED LAUNCH PARAMETERS FOR PETN IMPLOSION DRIVEN RUNS

Run No.	Projectile Material	Dia. (inches)	Density (g/cc)	Explosive Wt. (grams)	Energy Total (Kcal)	barrel (inches)	v_{meas} (ft/sec)	v_{pred} (ft/sec)	$\frac{v_{pred}}{v_{meas}}$	Acc_{max} (g's)	Remarks
205	Polyethylene	.312	0.92	81.3		120	17,650	38,500	2.2	2.5×10^8	Distorted
213	"	"	"	91.5		111	10,520	39,200	3.7	2.8×10^8	Distorted
209	"	"	"	209.4		120	--	62,300	"		Fragmented
210	"	"	"	213.8		110	--	63,200	-	5.4×10^8	Fragmented
214	Magnesium	.312	1.80	76.3		108	9,100	23,200	2.6	1.2×10^8	Survived Launch
219	"	"	"	96.8		100	11,600	25,300	2.2	1.5×10^8	Fragmented
216	"	.187	"	70.9		117	--	31,900	-	1.9×10^8	Fragmented
215	"	"	"	74.5		118	--	32,000	-	2.0×10^8	Fragmented
218	Fiberglass	.312	1.5	90.8		102	11,100	27,700	2.4	1.6×10^8	Fragmented
217	Stainless Steel	.187	5.5	74.0		111	3,750	14,900	4.0	6.6×10^7	Survived Launch

p_i = 200 psia of $2H_2 + O_2$

PETN Energy Constant 1.235 Kcal/Gram

PETN Density 0.588 g/cc

E_{Gas} = 44.8 Kcal

TABLE 11

CRITICAL VALUES OF IMPACT ENERGY FOR IMPACT SENSITIVITY TESTS (REF. 72)

EXPLOSIVE	PICATINNY ARSENAL (cal/cm^2)	BUREAU OF MINES (cal/cm^2)
AN	-	> 2.6
COMP C4	1.2	> 2.6
TNT	0.9	2.6
COMP B	0.77	1.8
50/50 Pentolite	0.77	0.68
50/50 Amatol	0.72	2.3
NG	c 6	0.16
EDNA	0.6	1.0
Torpex	0.48	0.96
Tetryl	0.47	0.61
RDX	0.47	0.77
PETN	0.35	0.4
Lead azide	0.29	0.26
Mercury fulminate	0.12	0.12
Diazodinitrophenol	0.12	0.12
Tetrazene	0.12	0.17

TABLE 12

PERTINENT DATA FROM ONE-DIMENSIONAL EXPLOSIVE INITIATION STUDY

Run No.	Explosive	Weight (grams)	Initial Pressure (psi)	Incident Velocity 1-2 (mm/μsec)	Incident Velocity 2-3 (mm/μsec)	Reflected Velocity 3'-2' (mm/μsec)	Reflected Velocity 2'-1' (mm/μsec)	Velocity at surface (mm/μsec)	τ_{delay} (μsec)	Detonation	E_a/p_1 (cal/cm²-atm)
1	-	-	240	2.90	2.90	-	-	-	-	-	-
4	-	-	266	3.31	3.23	-	-	-	-	-	-
5	-	-	211	2.93	3.05	-	-	-	-	-	-
6	-	-	151	4.06	4.43	-	-	-	-	-	-
7	-	-	371	4.10	3.46	-	-	-	-	-	-
8	-	-	112	3.40	3.20	-	-	-	-	-	-
9	-	-	167	3.40	3.12	-	-	-	-	-	-
10	-	-	84	3.63	3.54	-	-	-	-	-	-
11	-	-	84	3.31	3.54	-	-	-	-	-	-
12	-	-	314	3.70	3.60	-	-	-	-	-	-
13	-	-	332	3.33	-	-	-	-	-	-	-
14	-	-	282	3.71	3.28	-	-	-	-	-	-
15	-	-	249	2.96	-	-	-	-	-	-	-
16	-	-	304	5.11	3.17	-	-	-	-	-	-
17	-	-	235	2.93	2.93	-	-	-	-	-	-
32	-	-	90	4.10	3.10	1.93	2.05	-	-	-	-
40	-	-	180	5.73	3.34	1.97	2.35	-	-	-	-
42	-	-	270	3.53	3.37	1.98	2.35	-	-	-	-
54	-	-	105	3.86	3.18	1.94	2.10	-	-	-	-
65	-	-	89	4.23	3.18	-	-	-	-	-	-
66	-	-	91	-	3.23	-	-	-	-	-	-
112	-	-	177	4.02	3.07	1.96	1.98	-	-	-	-
169	-	-	100	3.10	2.99	1.84	2.06	-	-	-	-
173	-	-	82.8	3.05	3.18	2.01	2.01	-	-	-	-
18	PETN	4.229	160	3.31	3.25	5.45	5.08	5.98	7.7	Yes	47.2
19	PETN	4.229	132	3.10	3.16	-	-	-	-	No	37.9
20	PETN	4.229	199	3.38	3.29	5.22	5.22	5.43	7.0	Yes	32.4
21	PETN	4.229	233	4.14	3.88	-	-	-	-	Yes	-
22	PETN	4.229	176	-	-	-	-	-	-	No	43.0
23	PETN	4.229	176	-	-	-	-	-	-	No.	-
37	PETN	4.229	90	4.10	3.40	2.07	2.14	-	-	Yes	-
38	PETN	3.69	270	4.37	3.44	4.23	3.23	4.63	2.5	Yes	2?.2
43	PETN	4.229	180	3.63	3.41	5.45	4.95	6.20	6.3	Yes	~2.0

Stoichiometric Oxygen-Hydrogen Only (Run Nos. 1–173)

PETN Pressings (Run Nos. 18–43)

TABLE 12 (con'd)

PETN and PETN Combinations

Run No.	Explosive	Weight (grams)	Initial Pressure (psi)	Incident Velocity 1-2 (mm/μsec)	Incident Velocity 2-3 (mm/μsec)	Reflected Velocity 3'-2' (mm/μsec)	Reflected Velocity 2'-1' (mm/μsec)	Velocity at surface (mm/μsec)	τ_{delay} (μsec)	Detonation	E_a/P_1 (cal/cm²atm)
125	Fabric	1.3	200.5	3.31	3.05	1.93	2.25	–	–	No	–
126	SF/Fabric	0.4/1.3	201.0	3.53	3.13	2.59	2.75	2.65	–	Yes/No	3.65
130	No.1	(2.0)	201.0	3.26	2.97	2.16	2.87	–	–	Yes	–
131	No.1	(2.0)	190.0	3.37	2.98	1.93	2.12	–	–	No	–
176	No.1	(2.0)	205.0	3.25	3.12	3.00	3.81	–	–	Yes	–
178	No.1	(2.0)	225.0	3.12	3.05	1.96	2.35	–	–	No	–
179	No.1	(2.0)	225.0	3.18	3.07	1.95	2.46	–	–	No	–
129	No.2	(5.0)	180.0	3.63	3.05	1.84	2.03	–	–	Yes	–
132	No.2	(2.0)	195.0	–	–	2.67	2.72	–	–	No	–
175	No.2	(2.0)	200.0	3.17	3.12	3.60	–	–	–	Yes	–
177	No.2	(2.0)	210.0	3.26	3.07	2.46	3.10	–	–	Yes	–
185	No.2	(2.0)	312.0	–	–	–	–	–	–	Yes	–
124	SF/No.1	1.0/(5.0)	200.0	3.20	3.00	4.65	4.82	–	–	Yes	–
127	SF/No.1	0.9/(5.0)	161.0	3.10	3.03	1.93	2.03	–	–	Yes	46.8
182	SF/No.1	0.5/(2.0)	50.4	3.25	3.05	4.88	4.25	–	–	No	–
128	SF/No.2	0.2/(5.0)	180.0	3.12	3.07	5.08	3.97	5.58	13.3	Yes	33.1
180	SF/No.2	0.5/(0.2)	125.0	3.12	2.78	1.97	2.38	–	–	Yes	–
181	SF/No.2	0.5/(0.2)	100.0	3.55	3.05	3.08	2.68	–	–	Yes	–
183	SF/No.2	0.1/(0.2)	150.0	–	3.56	2.23	3.47	–	–	No	–
184	SF	Test patch	150.1	3.23	3.07	–	–	–	–	Yes	–
186	SF	"	150.1	3.00	2.93	–	3.52	–	–	Yes	–
188	SF	"	99.5	3.34	3.02	–	–	–	–	Yes	–
189	SF	3.2	50.1	2.94	2.89	–	–	–	–	Yes	–
190	SF	2.4	25.1	3.00	3.17	1.98	1.86	–	–	No comb	–
194	SF	2.65	50.1	3.28	3.12	3.81	3.81	–	–	Yes	49.5
199	SF	1.5	50.1	3.28	3.12	3.81	3.81	–	–	Yes	49.5
202	SF	2.25	100.0	4.10	3.10	4.33	4.02	5.05	3.7	Yes	37.4

Tetracene

Run No.	Explosive	Weight (grams)	Initial Pressure (psi)	Incident Velocity 1-2 (mm/μsec)	Incident Velocity 2-3 (mm/μsec)	Reflected Velocity 3'-2' (mm/μsec)	Reflected Velocity 2'-1' (mm/μsec)	Velocity at surface (mm/μsec)	τ_{delay} (μsec)	Detonation	E_a/P_1 (cal/cm²atm)
27	Tetracene	(4.0)	140	–	–	–	–	–	–	No	–
30	Tetracene	(4.0)	90	3.05	2.93	–	–	–	–	No	–
34	Tetracene	(4.0)	90	4.02	3.31	2.06	2.24	–	–	No	–
35	Tetracene	(5.3)	180	3.56	3.29	2.94	2.38	3.29	9.5	Partial	12.46
36	Tetracene	(4.3)	270	2.72	2.63	3.05	2.82	3.32	6.0	Yes	6.74
39	Tetracene	(6.1)	270	3.98	3.39	2.93	2.38	3.03	6.5	Yes	9.60
41	Tetracene	(10.0)	270	4.06	3.37	2.01	2.27	–	–	No.	–

TABLE 12 (concluded)

Category	Run No.	Explosive	Weight (grams)	Initial Pressure (psi)	Incident Velocity 1-2 (mm/μsec)	Incident Velocity 2-3 (mm/μsec)	Reflected Velocity 3'-2' (mm/μsec)	Reflected Velocity 2'-1' (mm/μsec)	Velocity at surface (mm/μsec)	τdelay (μsec)	Detonation	E₀/p₁ (cal/cm²atm)
Nitrocellulose	48	NC(corr)	(3.0)	180	4.77	3.63	2.18	2.72	4.77	9.0	No	-
	49	NC	(3.0)	180	3.12	3.00	3.74	3.05	-	-	Yes	21.8
	51	NC	(3.0)	90	-	-	-	-	-	-	No.	-
	52	NC	(4.0)	135	-	-	-	-	-	-	No	-
	113	NC	(4.0)	156.6	3.53	3.25	1.95	1.95	-	-	No	-
	114	NC	(4.0)	170.5	3.05	3.05	5.85	4.82	6.54	7.2	Yes	31.6
	115	NC	(4.0)	160.5	3.12	3.17	1.78	2.07	-	-	No	-
	121	NC	(4.0)	165.3	3.18	2.84	1.84	1.94	-	-	No	-
Lead azide	57	Lead azide	thin layer	92.0	-	-	-	-	-	-	Yes	-
	58	Lead azide	(2.62)	92.0	4.37	3.34	2.85	2.85	2.85	~0	Yes	4.60
	59	Lead azide		91.5	-	-	-	-	-	-	Yes	8.64
	61	Lead azide	(6.1)	91.5	-	3.46	3.98	3.46	3.92	~0	Yes	9.17
	67	Lead azide	(6.3)	89.0	2.82	3.17	3.31	3.40	3.70	~0	Yes	87.0
	68	Lead azide	(10.1)	15.0	4.76	3.89	6.35	7.76	7.06	-	Yes	-
	73	Lead azide	5.7	74.0	-	-	-	-	-	-	Yes	-
	170	Lead azide	11.3	30.0	3.07	3.09	6.69	7.07	6.88	4.0	Yes	48.8
	171	Lead azide	11.5	?.7	-	-	-	-	-	-	Yes	-
	172	Lead azide	5.0	30.2	-	-	-	-	-	-	Yes	-
	174	Lead azide	5.2	30.0	4.02	3.17	9.52	5.68	5.68	-	Yes	22.5
Miscellaneous	44	αHMX	5.0	180	3.28	3.28	1.91	2.20	-	-	No	-
	45	EL-506	4.5	180	3.93	3.34	2.24	2.14	-	-	No	-
	71	EL-506	4.5	181	3.02	3.20	1.81	2.07	-	-	No	-
	46	Heller	4.5	180	2.82	2.94	1.50	1.97	-	-	No	-
	47	Heller	4.5	270	3.66	3.34	1.93	2.24	-	-	No	-
	50	DINA	5.0	180	2.68	2.89	2.15	2.40	-	-	No	-
	55	Nitromannitol	(3.9)	91.0	3.18	3.20	-	-	-	-	No	-
	56	"	(2.8)	91.0	3.81	3.18	-	-	-	-	No	-
	60	Mercury Fulminate	(6.5)	92.0	3.28	2.81	2.07	1.98	-	-	Yes	-
	62	PETN, Pb N6(mixed)	~5	89.7	-	-	-	-	-	-	Yes	-
	63		~5	89.7	3.23	2.94	3.76	-	-	-	Yes	-
Combination	69	Pb N6/Heller	(4.2)/4.5	89	4.06	3.12	2.66	-	3.76	-	Yes/No	6.12
	70	Pb N6/EL-506	(4.2)/4.5	91	3.26	3.00	2.90	-	2.76	-	Yes/No	5.97
	72	Pb N6/EL-506	(3.7)/4.5	89	2.93	3.40	2.46	2.46	-	-	Yes/No	5.40
	122	PETN/EL-506	0.7/4.5	220.5	3.26	3.05	2.46	2.72	3.02	-	Yes/No	6.22
	123	PETN/EL-506	1.0/4.5	250.0	3.53	3.40	5.22	4.50	6.06	-	Yes/Yes	33.8

( ) Indicates wet weight

TABLE 13

INITIAL PRESSURE OF $2H_2 + O_2$ TO INITIATE DETONATION IN EXPLOSIVE BY IMPINGING GASEOUS DETONATION WAVE

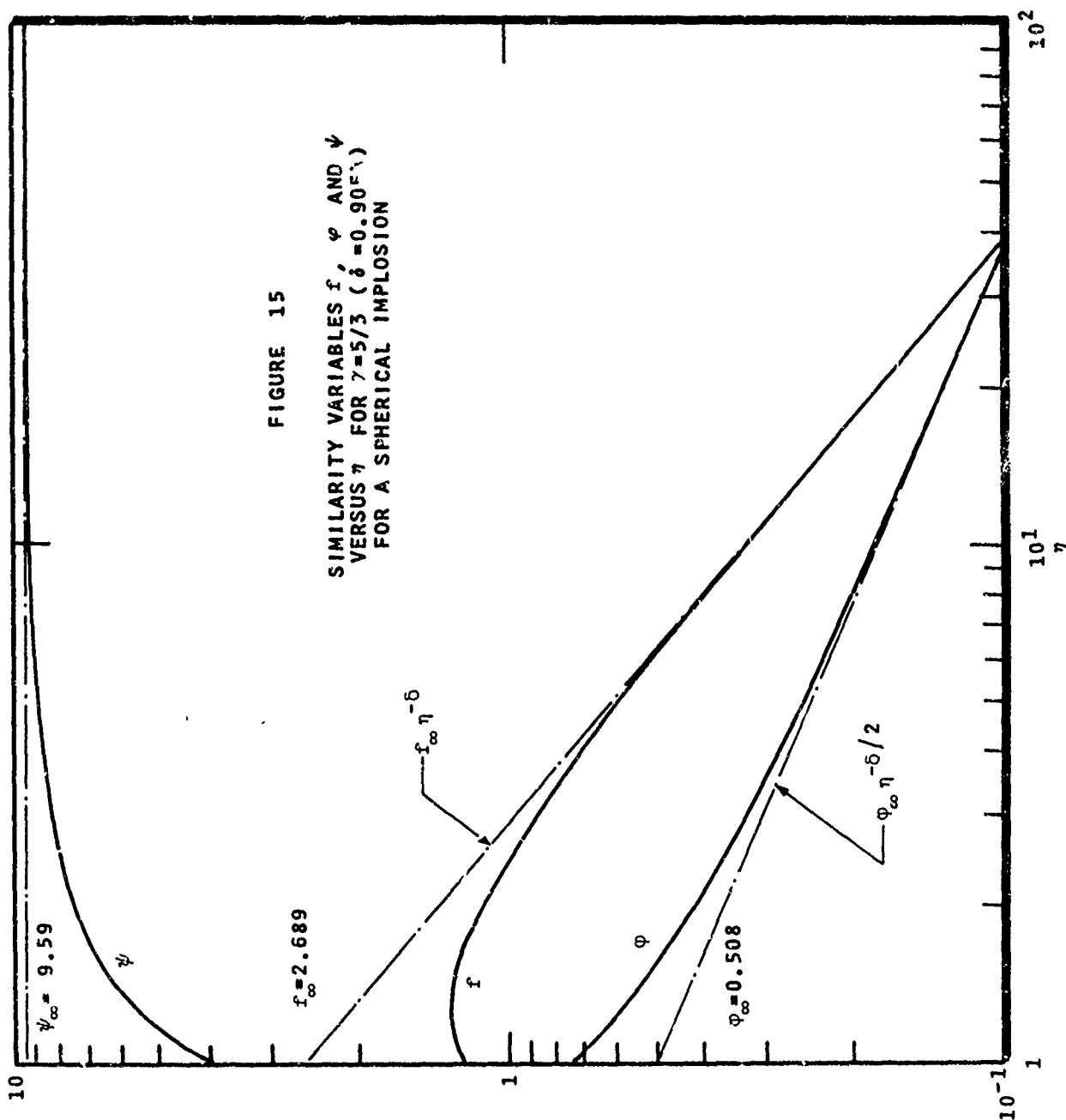| Explosive	Initiation Pressure (Atmos)
Lead azide	$p_i < 0.026$
Superfine PETN	$1.71 < p_i < 3.42$
Lead azide - PETN mixture	$p_i < 6.1$
Superfine PETN/No. 1 Paste*	$3.43 < p_i < 10.9$
Superfine PETN/No. 2 paste*	$p_i < 6.8$
PETN "powder"[82]	$p_i < 10$
PETN pressings (present tests)	$6.12 < p_i < 8.89$
PETN pressings[90]	~ 12.5
Nitrocellulose	$11.2 < p_i < 11.6$
No. 2 paste	~ 14
No. 1 paste	~ 15
Blasting gelatin[82]	$10 < p_i$
PETN/EL-506	$13.6 < p_i < 17.0$
Tetracene	$12.2 < p_i < 18.4$
Cast PETN[82]	$15 < p_i < 20$
Picric acid[82]	$24 < p_i < 30$
Tetryl[82]	$1 \ll p_i$
Mercury fulminate	$6.25 < p_i$
Lead azide/Heller	$6.25 < p_i$
Lead azide/EL-506	$6.25 < p_i$
Nitromannitol	$6.25 < p_i$
Corregated nitrocellulose	$12.3 < p_i$
αHMX	$12.4 < p_i$
PETN fabric	$13.7 < p_i$
Superfine PETN/PETN fabric	$13.7 < p_i$
Heller	$18.4 < p_i$
EL-506[90]	$98. < p_i$
DINA[90]	$98 < p_i$
Lead azide-polyurethane	$20 \ll p_i$

* Depends on thickness of top layer

TABLE 14

Measured "Delay" Times For Initiation of Detonations in Explosives

Explosive	Density (g/cc)	Sample Weight (grams)	Delay Time (μsec)	Initial Pressure (atmos)
Lead azide	1.67	11.3	4.0	2.04
	1.67	6.3	<1.0	6.05
	1.67	2.62	<1.0	6.25
	1.67	6.1	<1.0	6.22
Nitrocellulose	-	3.0	9.0	12.2
		4.0	7.2	11.6
PETN	1.0	4.229	7.7	10.9
	1.0	4.229	7.0	13.5
	1.0	4.229	6.3	12.25
PETN	0.87	3.69	2.5	18.35
PETN(SF)	0.588	2.25	3.7	6.8
	0.588	1.50	12.0	3.41
Tetracene	-	5.3	9.5	12.2
	-	4.3	6.0	18.4
	-	6.1	6.5	18.4
No. 1 PETN Paste/ (SF) PETN	-	5.0/0.9	4.6	10.9
No. 2 PETN Paste/ (SF) PETN	-	5.0/0.2	6.5	12.25

FIG. 1   MAXIMUM LAUNCH VELOCITIES AND WEIGHTS - 1966 (REF. 6)

TOP PLATE

BARREL

RETAINING NUT

CHAMBER BLOCK

EXPLOSIVE LINER

8 INCH DIAMETER
HEMISPHERICAL CAVITY
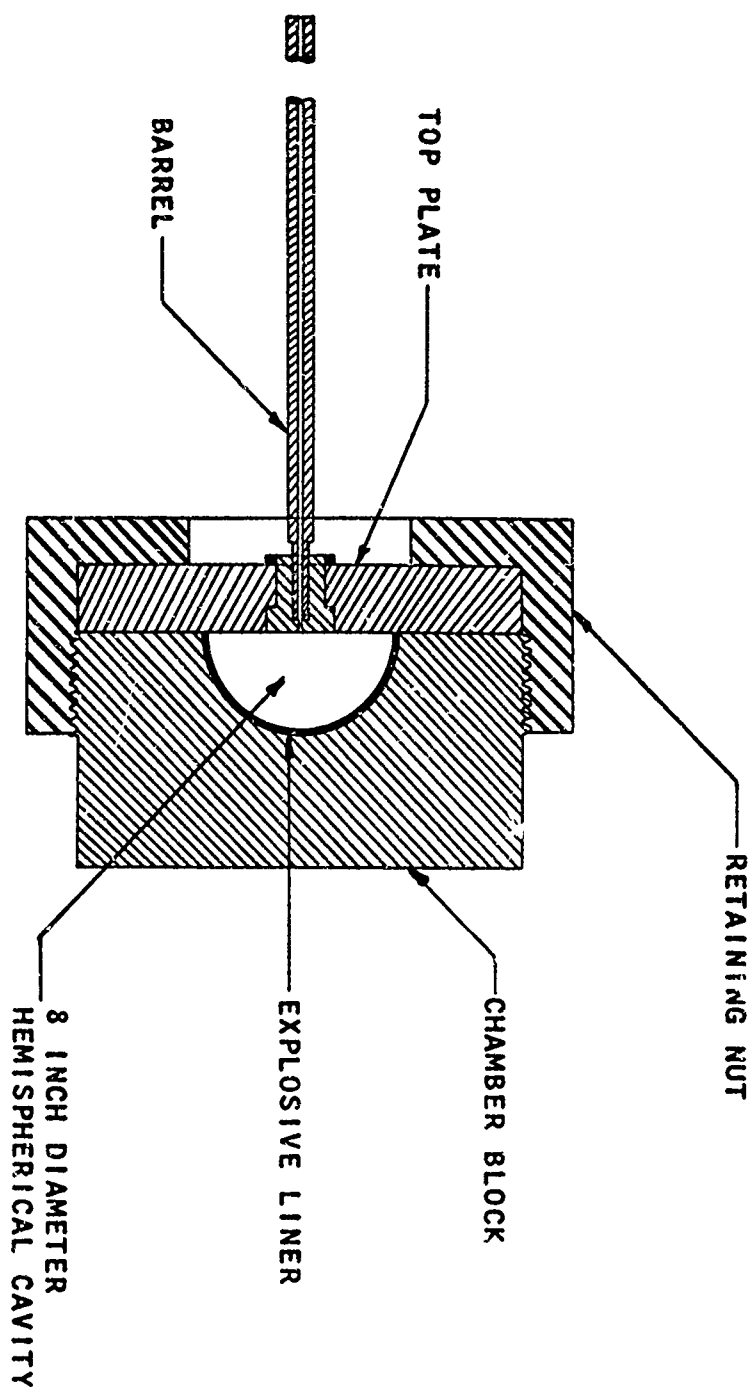
FIG. 2 SCHEMATIC OF THE UTIAS IMPLOSION-DRIVEN HYPERVELOCITY LAUNCHER

BARREL

PROJECTILE
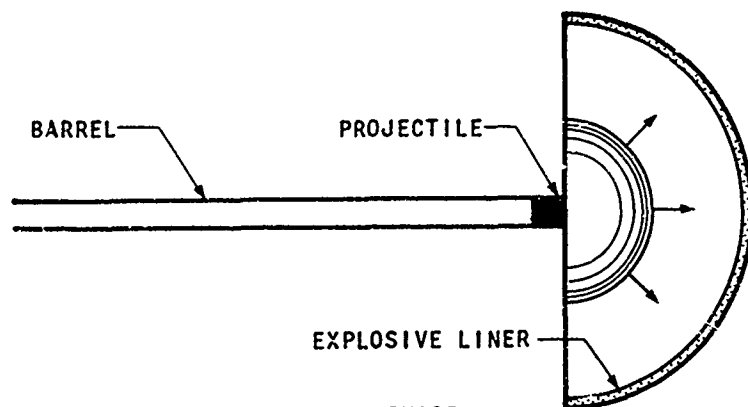
EXPLOSIVE LINER

3A   IGNITION PHASE

A GASEOUS DETONATION WAVE PROPAGATES OUTWARD
FROM THE ORIGIN IN A $2H_2+O_2+nHe+mH_2$ MIXTURE
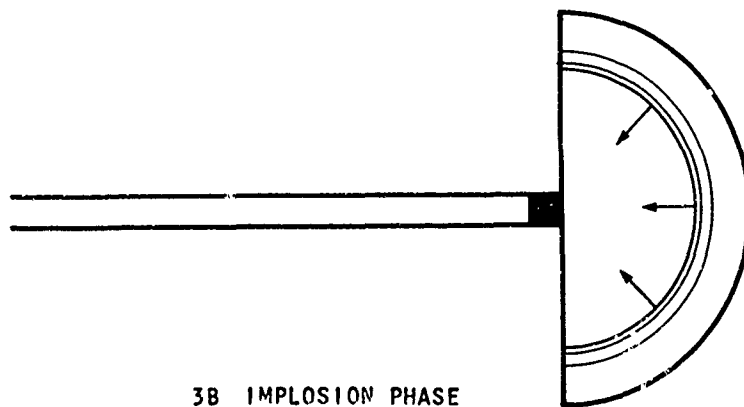
3B   IMPLOSION PHASE

THE DETONATION WAVE IGNITES THE EXPLOSIVE LINER
WHICH IN TURN GENERATES A STRONG IMPLODING WAVE
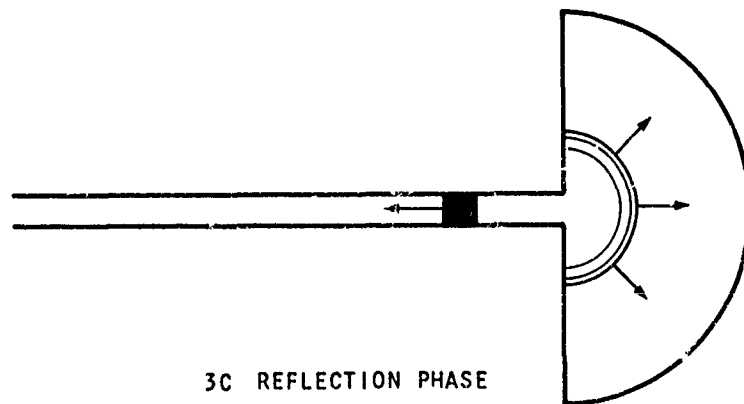
3C   REFLECTION PHASE

THE IMPLOSION WAVE REFLECTS FROM THE ORIGIN LEAVING A REGION
OF HIGH PRESSURE - HIGH TEMPERATURE GAS WHICH BURSTS
THE DIAPHRAGM AND ACCELERATES THE PROJECTILE

FIGURE 3   SCHEMATIC OF THE PRINCIPLE OF OPERATION OF THE IMPLOSION DRIVEN
HYPERVELOCITY LAUNCHER

FIGURE 4

ASYMPTOTIC BEHAVIOR OF THE STRONG NORMAL SHOCK
PRESSURE, TEMPERATURE, AND DENSITY RATIOS, FLOW MACH NUMBER
AND PARTICLE VELOCITY FOR $1 \leq \gamma \leq 3$

RATIO OF SPECIFIC HEATS γ
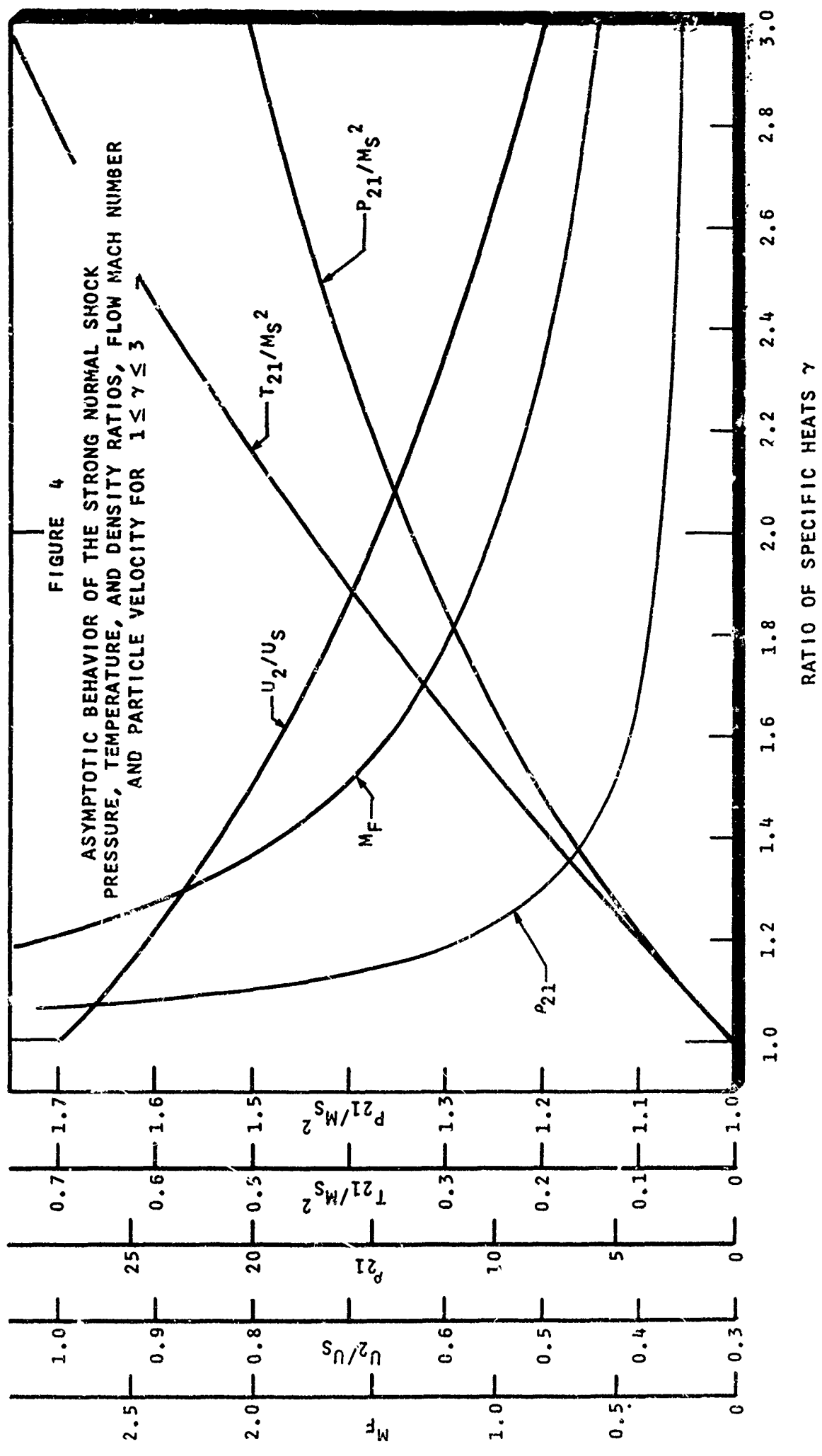
FIGURE 5

ASYMPTOTIC BEHAVIOR OF THE REFLECTED SHOCK PRESSURE,
TEMPERATURE AND DENSITY RATIOS FOR $1 \leq \gamma \leq 3$

FIGURE 6

ASYMPTOTIC BEHAVIOR OF THE FINAL TO INITIAL PRESSURE,
TEMPERATURE AND DENSITY RATIOS ACROSS A REFLECTED PLANE SHOCK
FOR $1 \leq \gamma \leq 3$
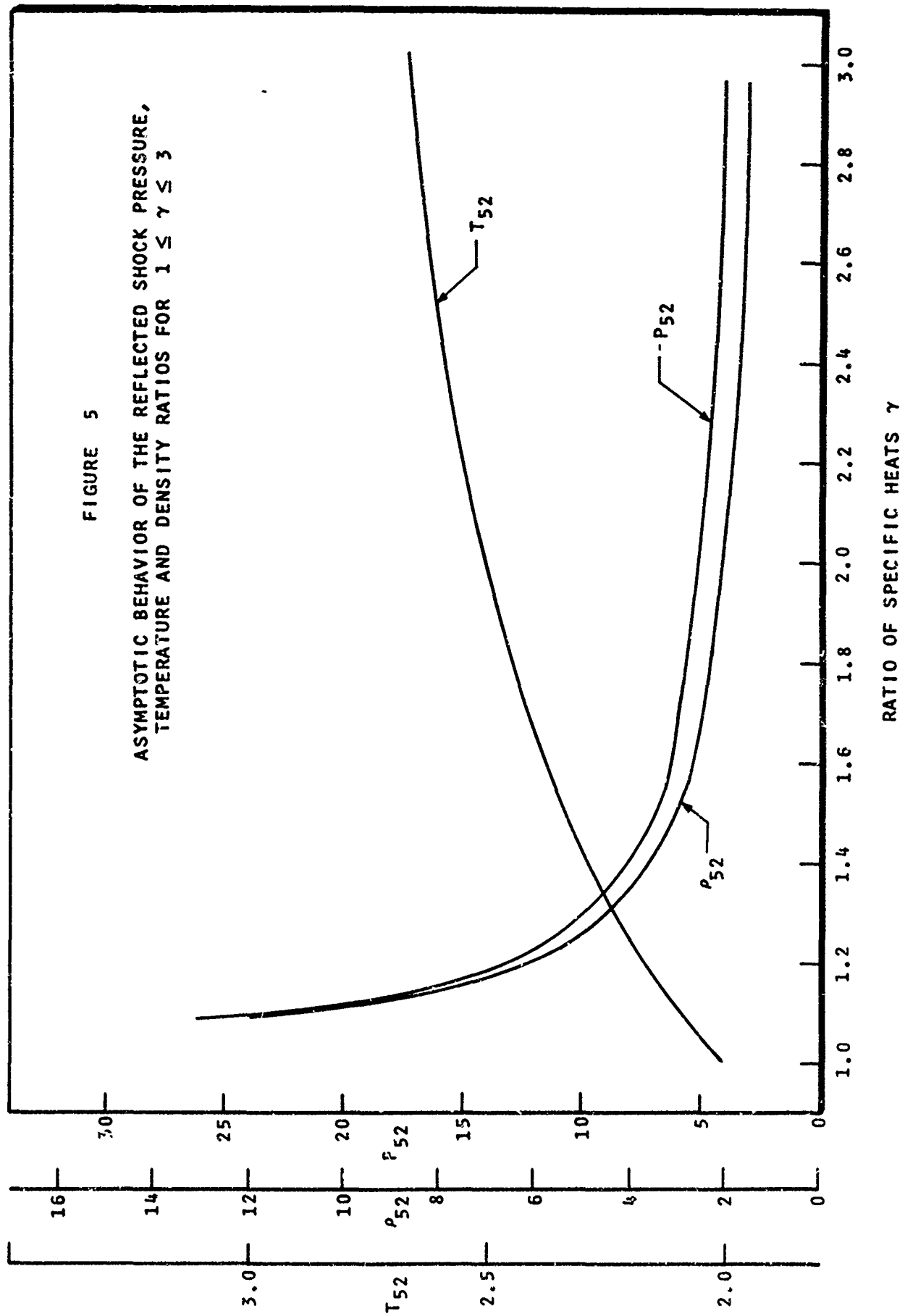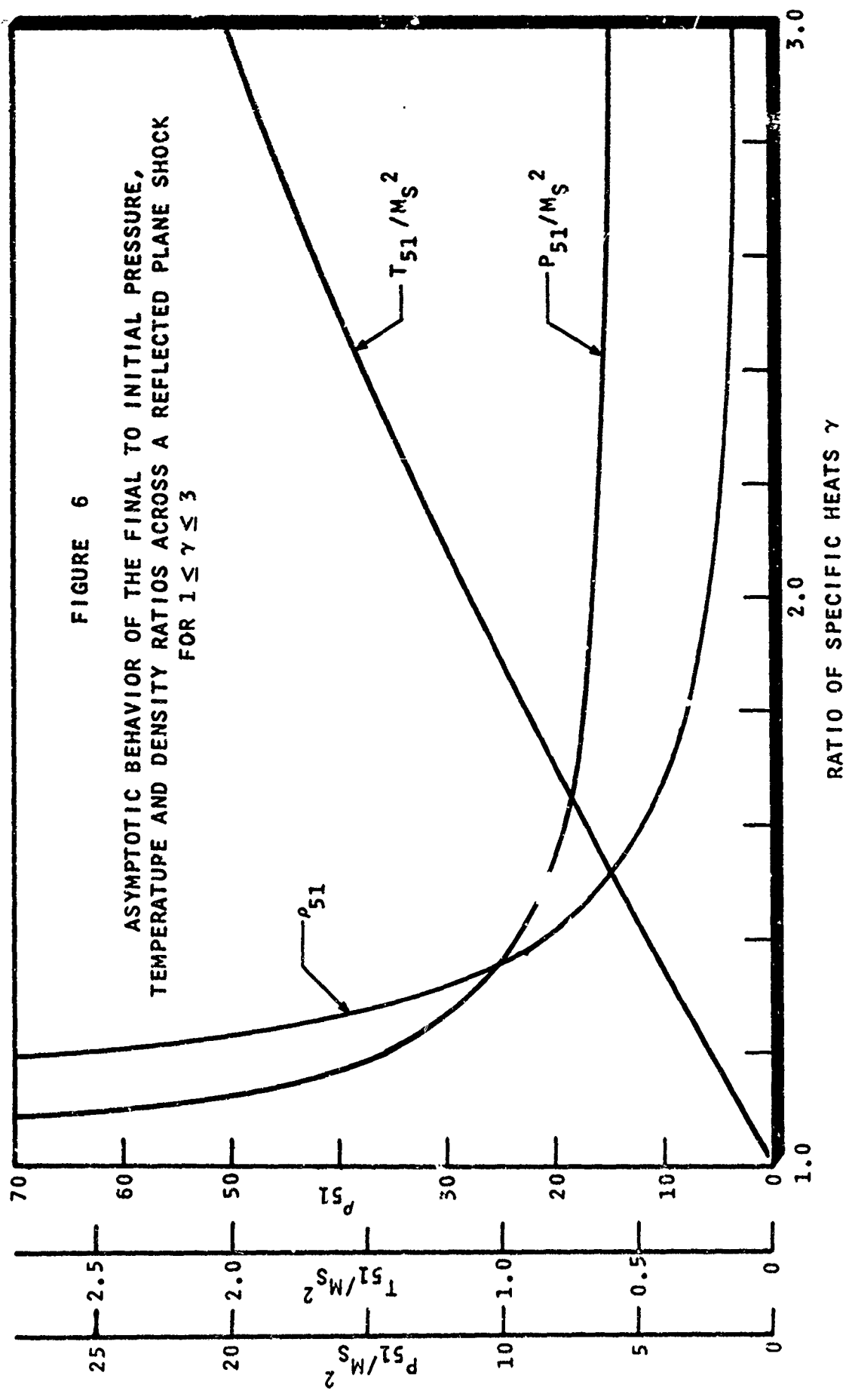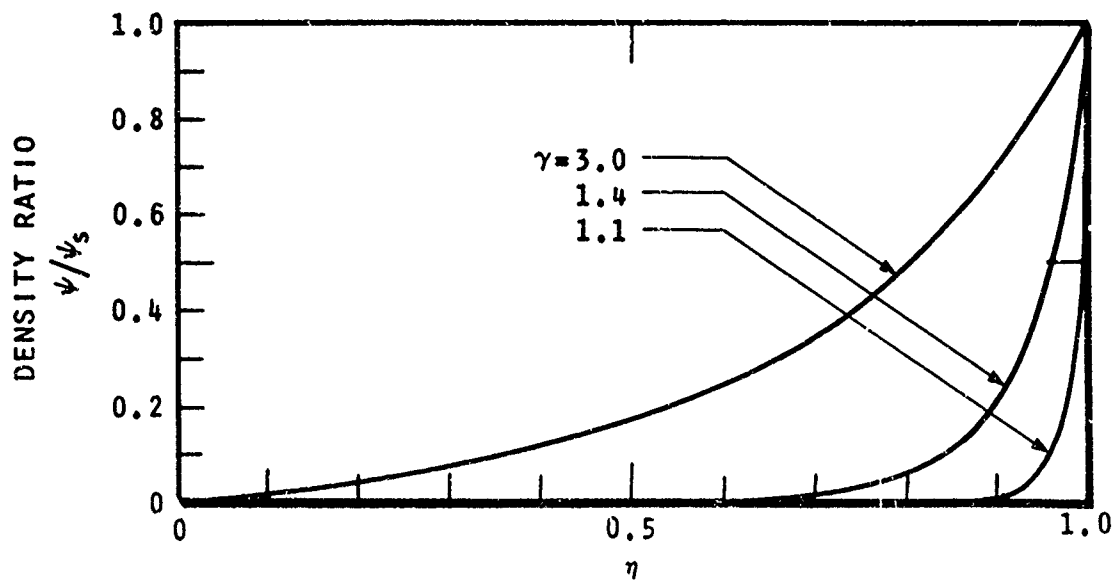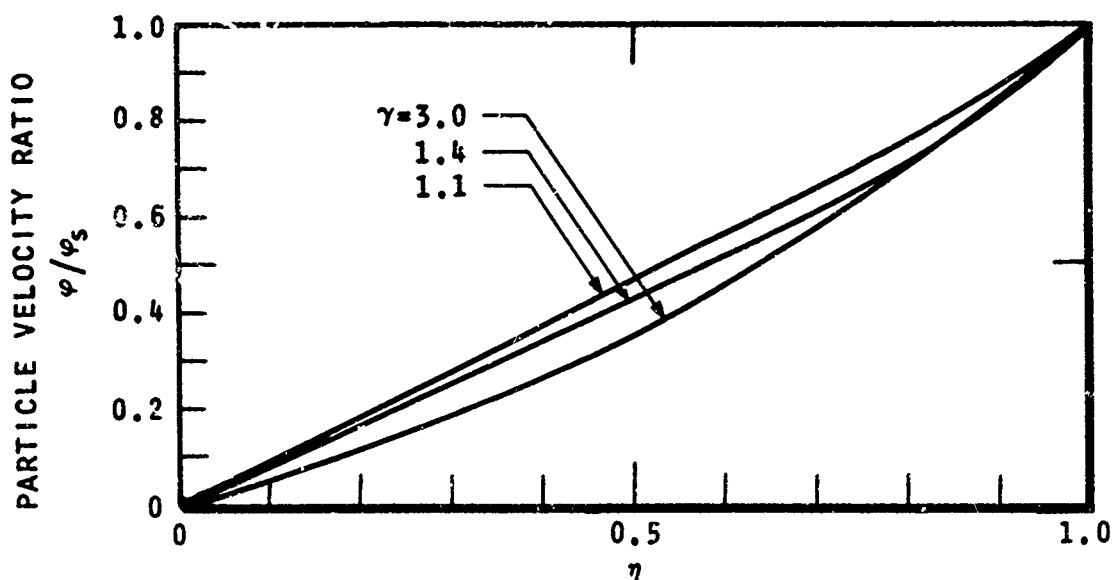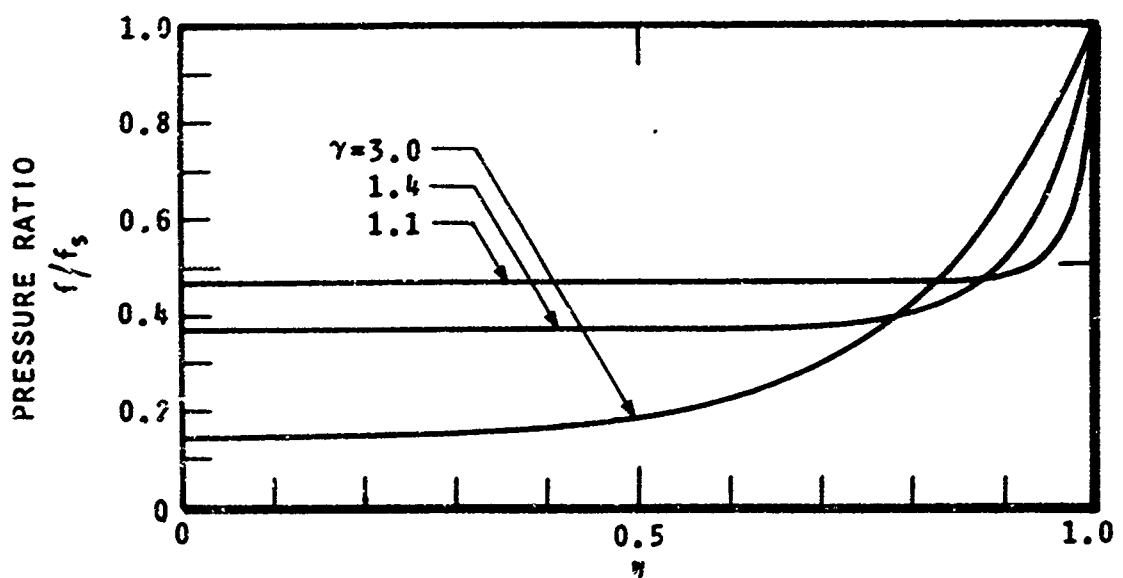
FIGURE 7 SIMILARITY PARAMETERS f, φ, AND ψ FOR AN IDEAL
POINT SOURCE EXPLOSION FOR $\gamma = 1.1$, 1.4 AND 3.0
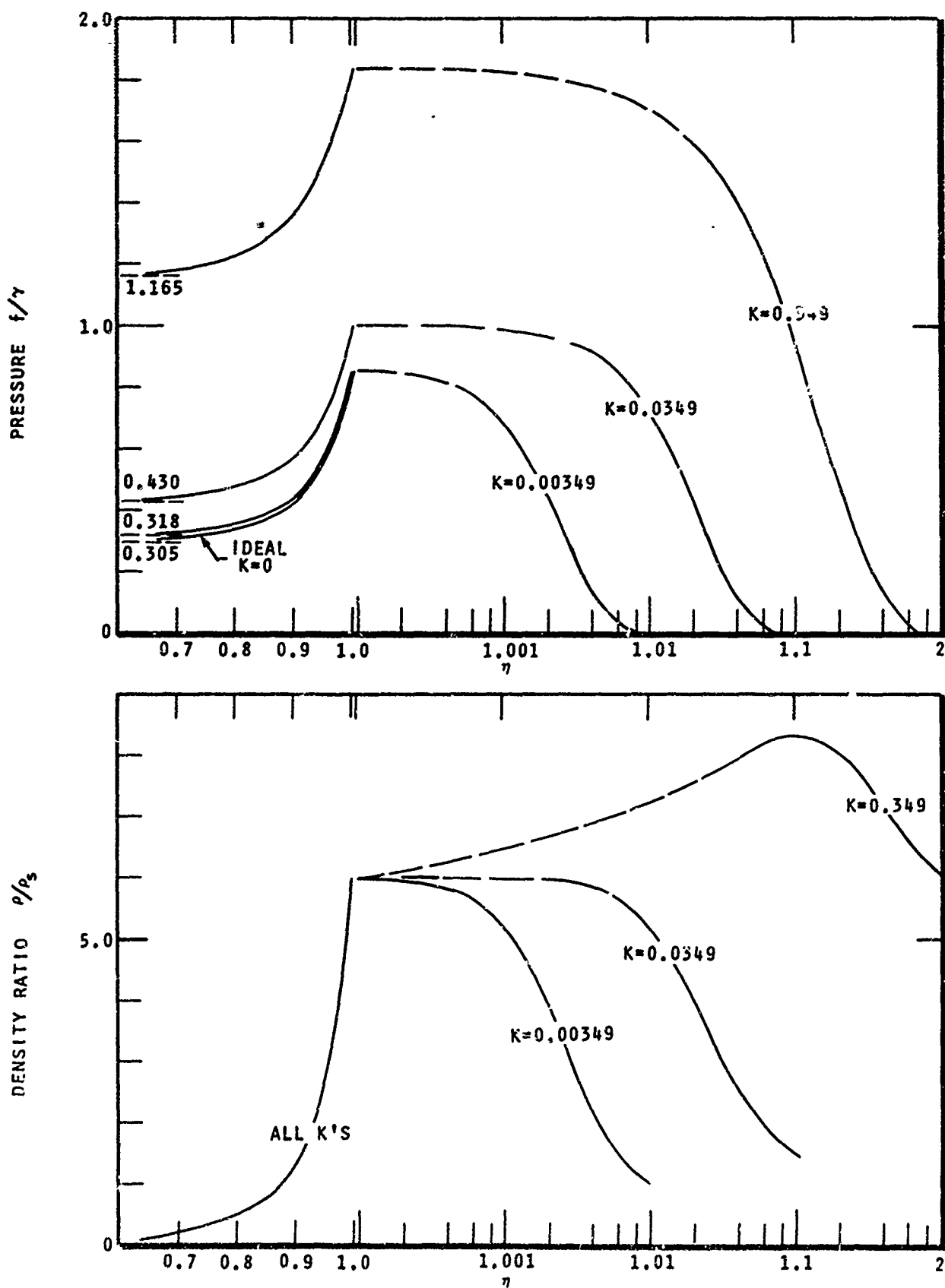
FIGURE 8 SIMILARITY VARIABLES f, φ AND ψ FOR A SPHERICAL EXPLOSION
(γ=1.4) FOR SEVERAL VALUES OF THE VISCOSITY PARAMETER K
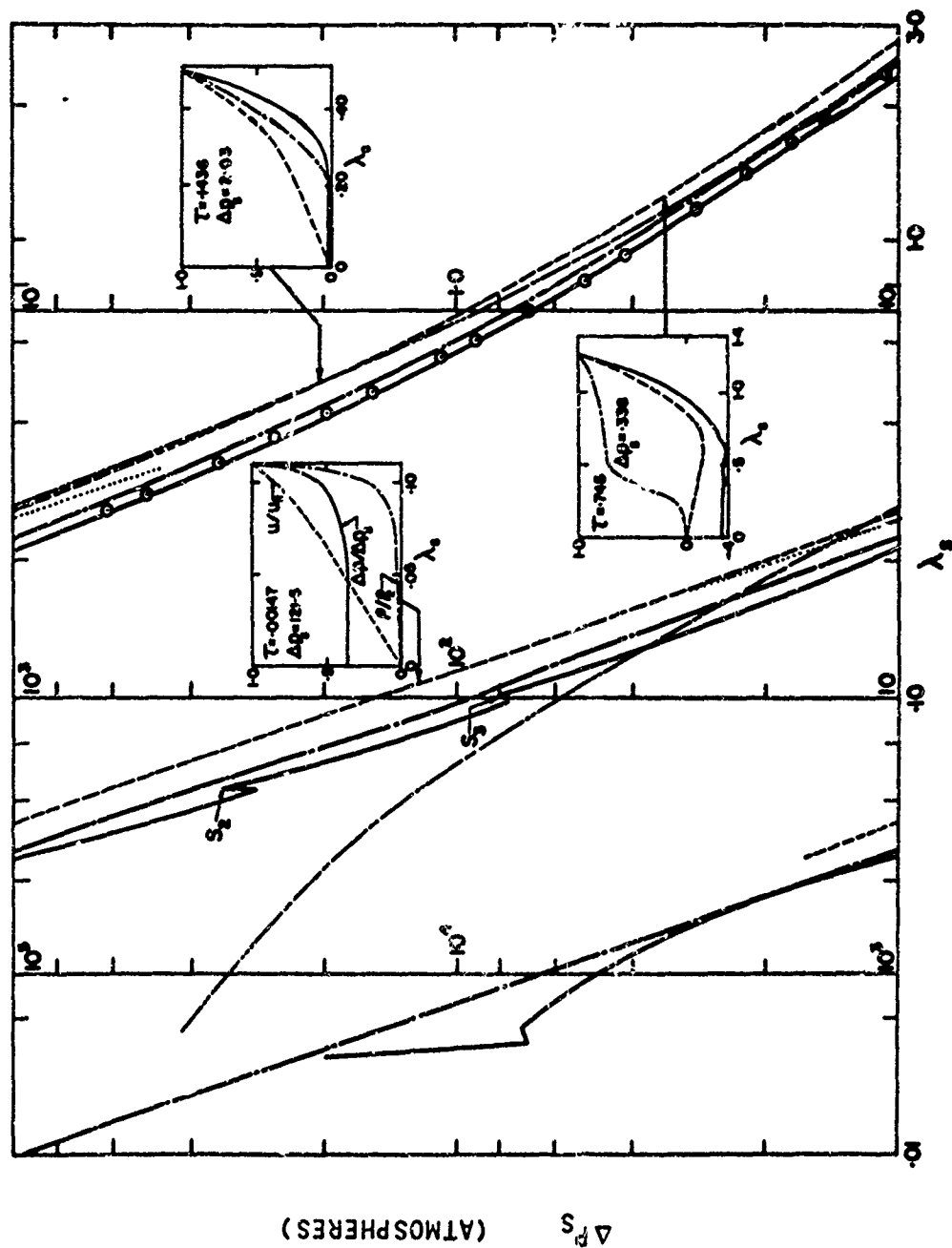
FIGURE 9   VARIATION OF PEAK OVERPRESSURES WITH SHOCK RADIUS

TAYLOR
POINT SOURCE PERFECT AIR
POINT SOURCE IMPERFECT AIR
HOT SPHERE
TNT
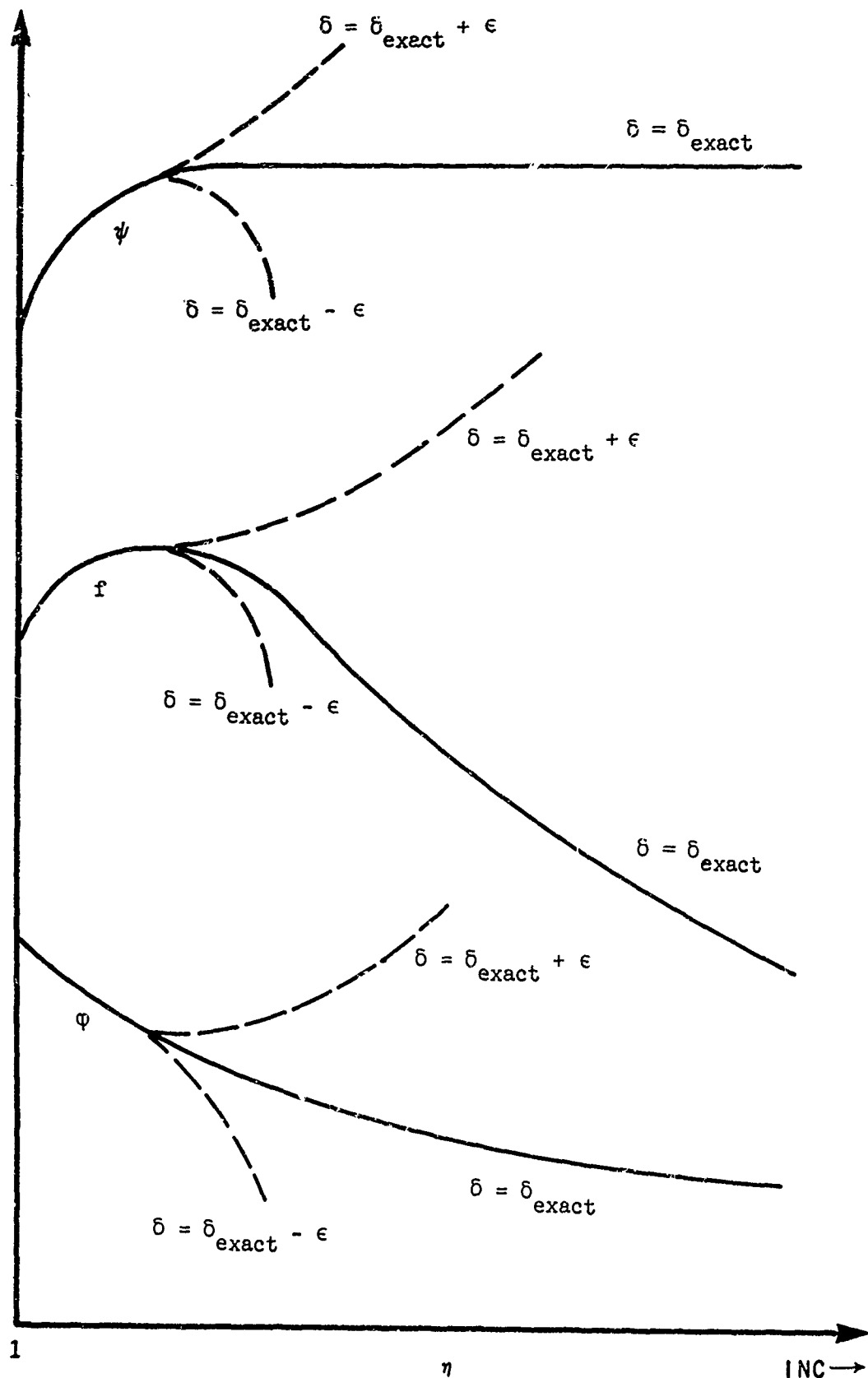
FIGURE 10 SCHEMATIC OF THE VARIATION OF f, φ AND ψ WITH δ FOR VALUES OF δ IN THE VICINITY OF THE EXACT VALUE
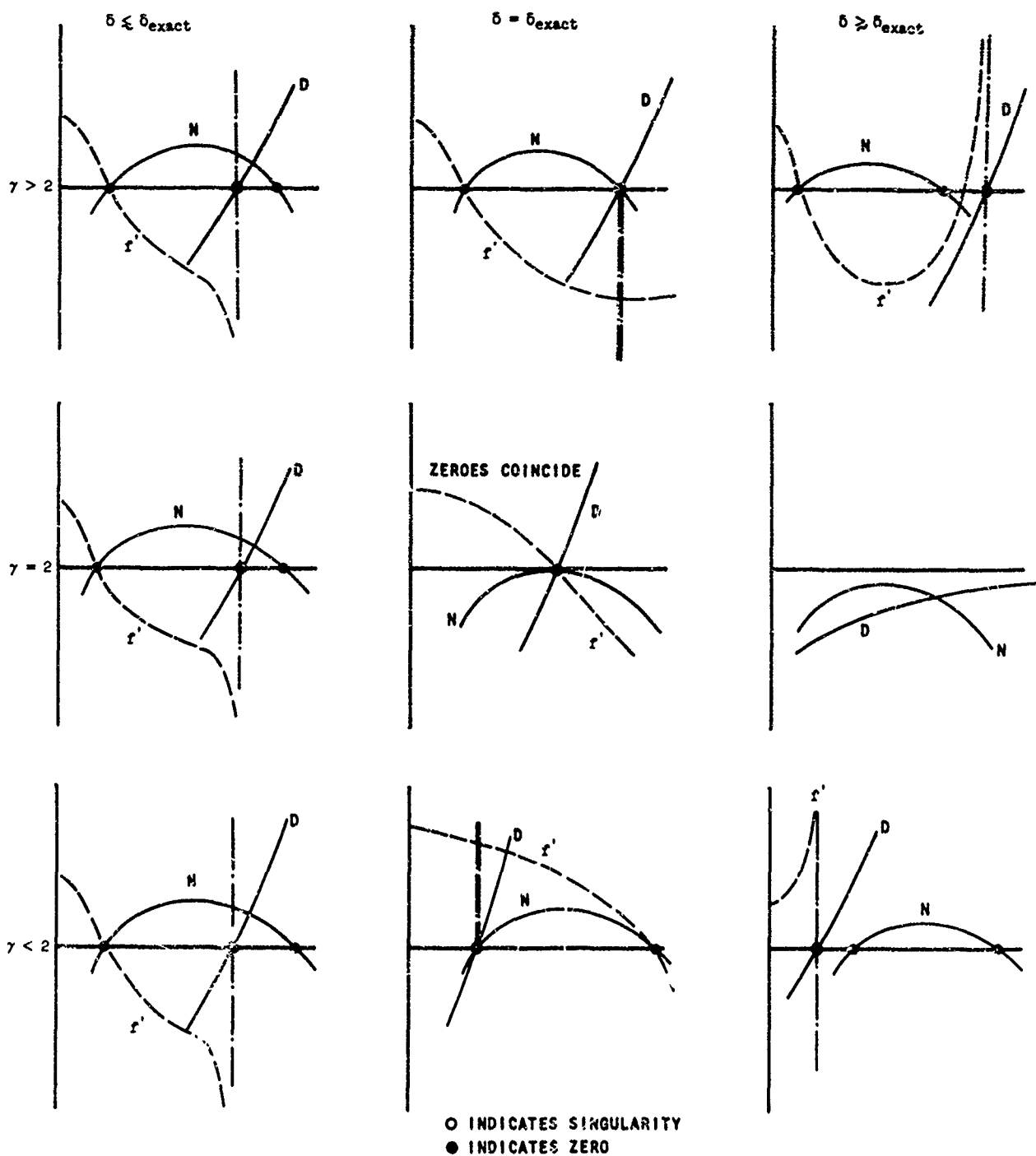
FIGURE 11

SCHEMATIC OF THE BEHAVIOR OF f', N AND D IN THE REGIONS AROUND THE SINGULARITIES AND ZEROES FOR $\gamma \leqq 2$ AND $\delta \neq \delta_{exact}$
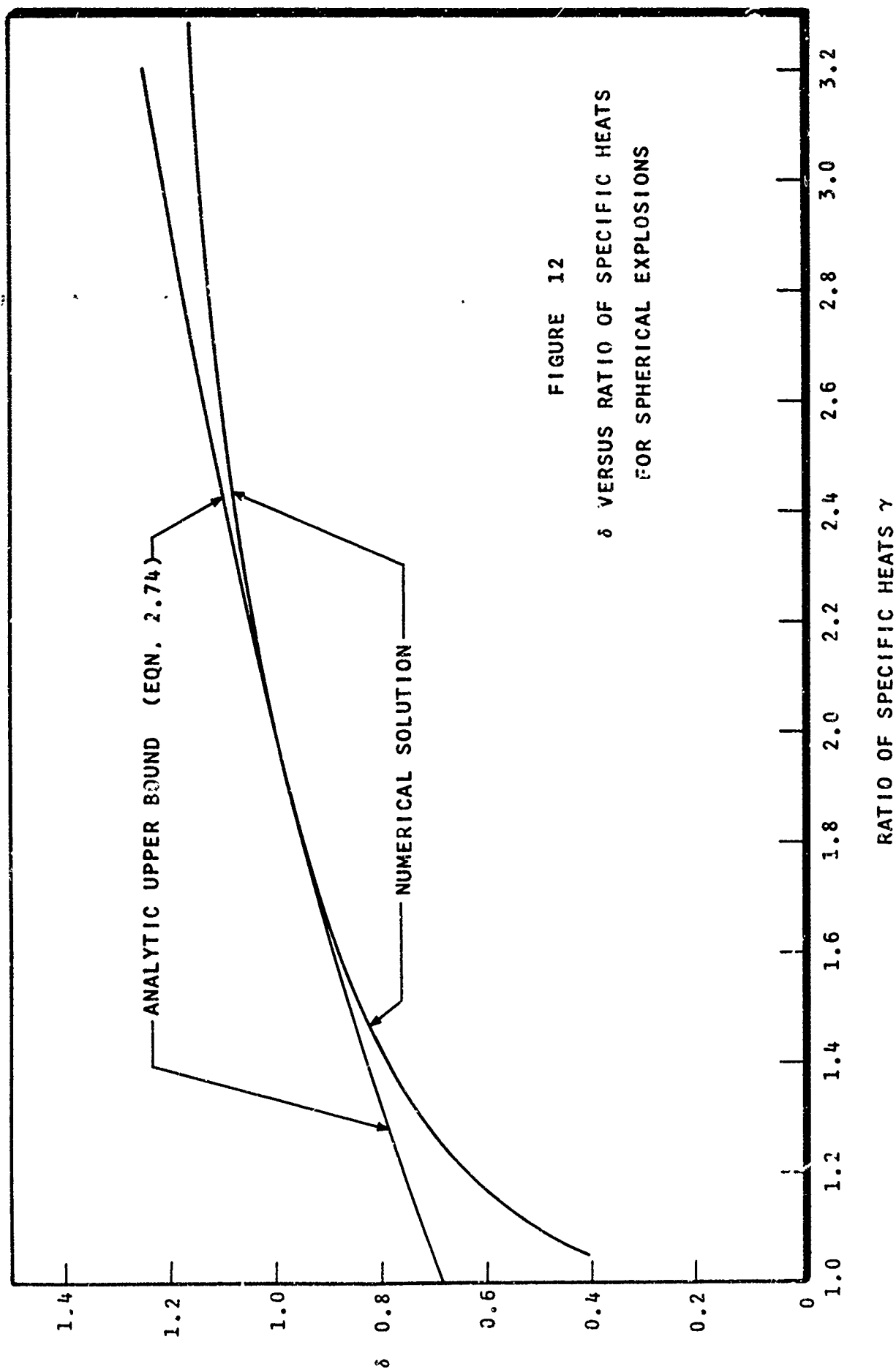
FIGURE 12

δ VERSUS RATIO OF SPECIFIC HEATS
FOR SPHERICAL EXPLOSIONS

TABLE 13

INITIAL PRESSURE OF $2H_2 + O_2$ TO INITIATE DETONATION IN EXPLOSIVE BY IMPINGING GASEOUS DETONATION WAVE

Explosive	Initiation Pressure (Atmos)
Lead azide	$p_i < 0.026$
Superfine PETN	$1.71 < p_i < 3.42$
Lead azide - PETN mixture	$p_i < 6.1$
Superfine PETN/No. 1 Paste*	$3.43 < p_i < 10.9$
Superfine PETN/No. 2 paste*	$p_i < 6.8$
PETN "powder"[82]	$p_i < 10$
PETN pressings (present tests)	$6.12 < p_i < 8.89$
PETN pressings[90]	~ 12.5
Nitrocellulose	$11.2 < p_i < 11.6$
No. 2 paste	~ 14
No. 1 paste	~ 15
Blasting gelatin[82]	$10 < p_i$
PETN/EL-506	$13.6 < p_i < 17.0$
Tetracene	$12.2 < p_i < 18.4$
Cast PETN[82]	$15 < p_i < 20$
Picric acid[82]	$24 < p_i < 30$
Tetryl[82]	$1 \ll p_i$
Mercury fulminate	$6.25 < p_i$
Lead azide/Heller	$6.25 < p_i$
Lead azide/EL-506	$6.25 < p_i$
Nitromannitol	$6.25 < p_i$
Corregated nitrocellulose	$12.3 < p_i$
αHMX	$12.4 < p_i$
PETN fabric	$13.7 < p_i$
Superfine PETN/PETN fabric	$13.7 < p_i$
Heller	$18.4 < p_i$
EL-506[90]	$98. < p_i$
DINA[90]	$98 < p_i$
Lead azide-polyurethane	$20 \ll p_i$

* Depends on thickness of top layer

TABLE 14

Measured "Delay" Times For Initiation of Detonations in Explosives

Explosive	Density (g/cc)	Sample Weight (grams)	Delay Time (μsec)	Initial Pressure (atmos)
Lead azide	1.67	11.3	4.0	2.04
	1.67	6.3	<1.0	6.05
	1.67	2.62	<1.0	6.25
	1.67	6.1	<1.0	6.22
Nitrocellulose	-	3.0	9.0	12.2
		4.0	7.2	11.6
PETN	1.0	4.229	7.7	10.9
	1.0	4.229	7.0	13.5
	1.0	4.229	6.3	12.25
PETN	0.87	3.69	2.5	18.35
PETN(SF)	0.588	2.25	3.7	6.8
	0.588	1.50	12.0	3.41
Tetracene	-	5.3	9.5	12.2
	-	4.3	6.0	18.4
	-	6.1	6.5	18.4
No. 1 PETN Paste/ (SF) PETN	-	5.0/0.9	4.6	10.9
No. 2 PETN Paste/ (SF) PETN	-	5.0/0.2	6.5	12.25

FIGURE 15

SIMILARITY VARIABLES f, φ AND ψ VERSUS η FOR $\gamma=5/3$ ($\delta=0.90^{r}$) FOR A SPHERICAL IMPLOSION

FIGURE 16

SIMILARITY VARIABLES f, φ AND ψ
VERSUS η FOR $\gamma = 2$ ($\delta = 1.0$)
FOR A SPHERICAL IMPLOSION

FIGURE 17

SIMILARITY VARIABLES f, φ AND ψ
VERSUS η FOR $\gamma = 3$ ($\delta = 1.143$)
FOR A SPHERICAL IMPLOSION

$\varphi_\infty = 2.680$

$f_\infty = 2.602$

$\varphi_\infty \eta^{-\delta/2}$

$f_\infty \eta^{-\delta}$

$\psi_\infty = 2.734$

FIGURE 18

CONSTANTS f_∞, φ_∞ AND ψ_∞ VERSUS γ
FOR THE
SPHERICAL IMPLOSION SIMILARITY SOLUTIONS

● CALCULATED VALUES
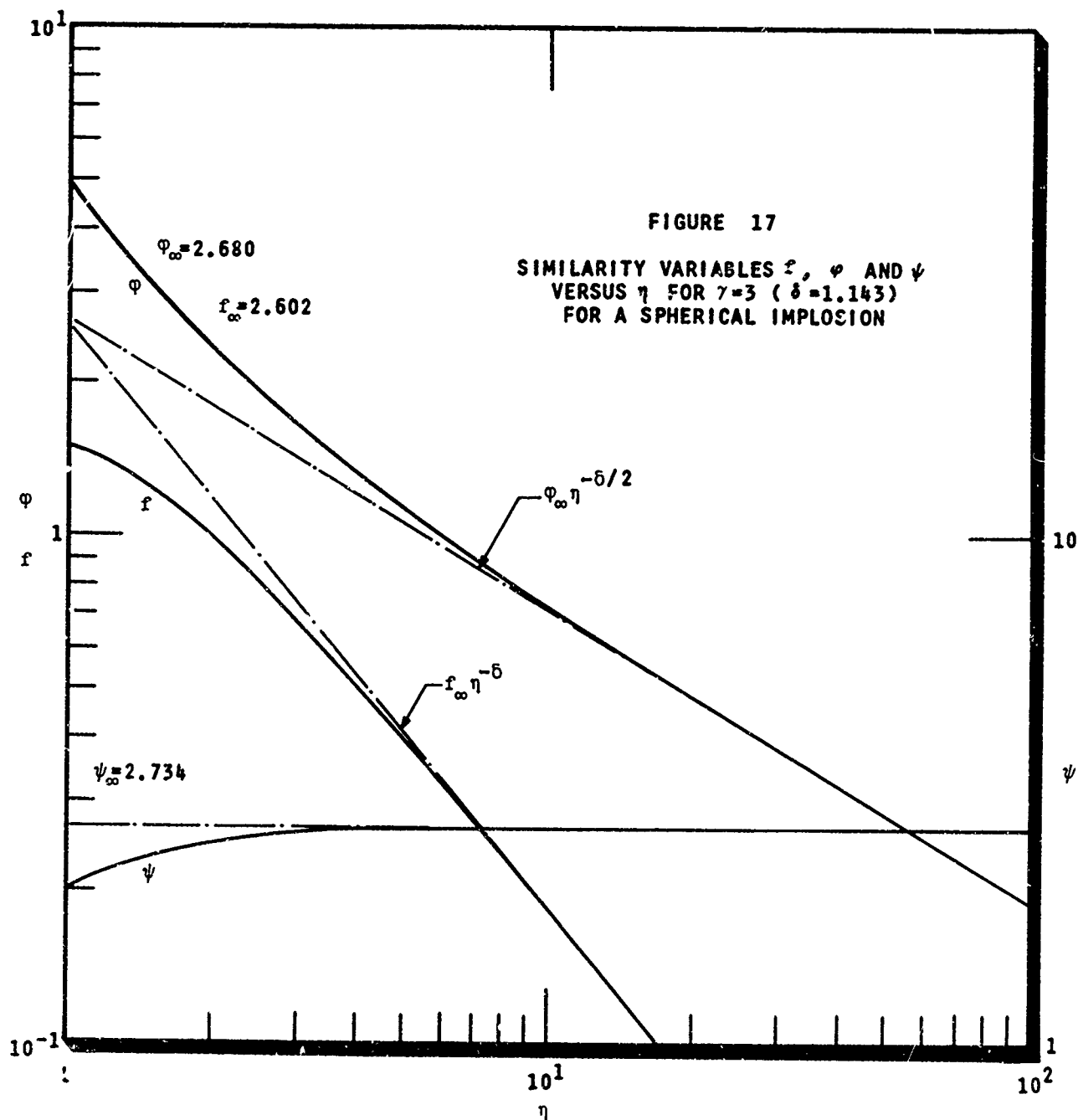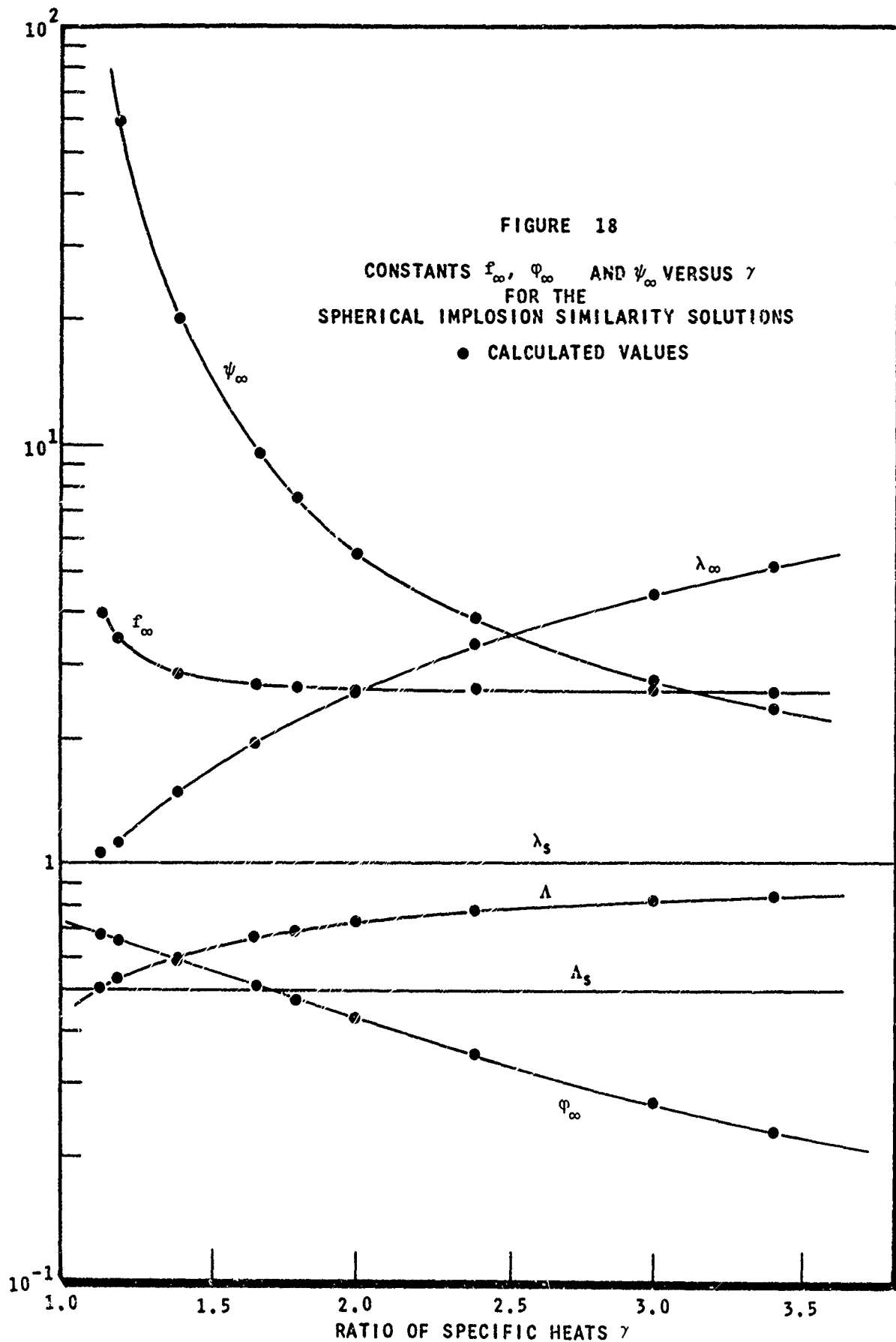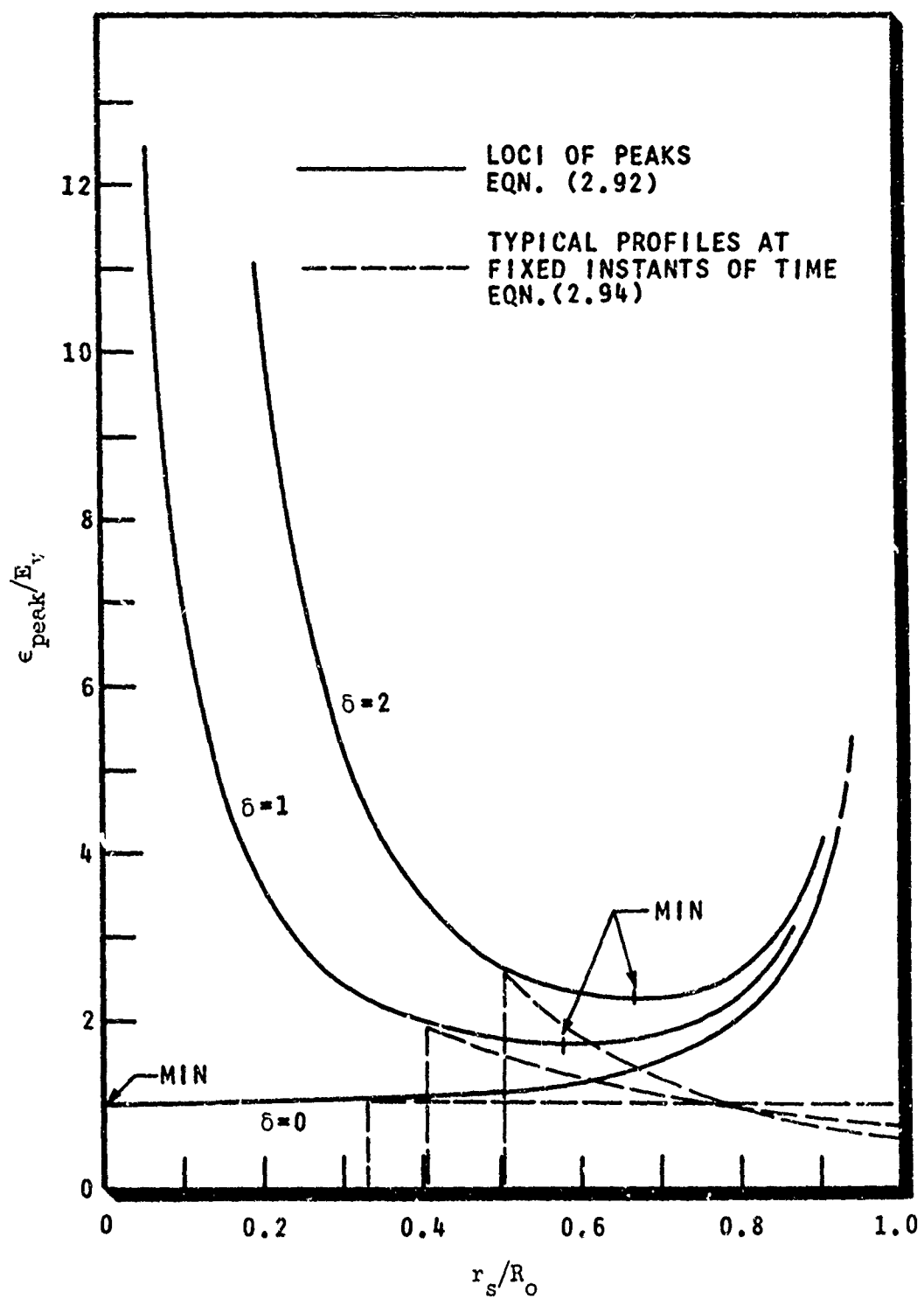
FIGURE 19 ϵ_{peak}/E_v VERSUS r_s/R_o FOR $\delta = 0$, 1 AND 2

FIGURE 20
LOG ϵ_{peak}/E_v VERSUS LOG r_s/R_o
FOR $\delta = 0$, 1, AND 2

$\delta = 2$

$\delta = 1$

MIN

LOCI OF PEAKS EQN. (2.92)

TYPICAL PROFILES AT FIXED
INSTANTS OF TIME EQN. (2.94)

$\delta = 0$

ϵ_{peak}/E_v

r_s/R_o
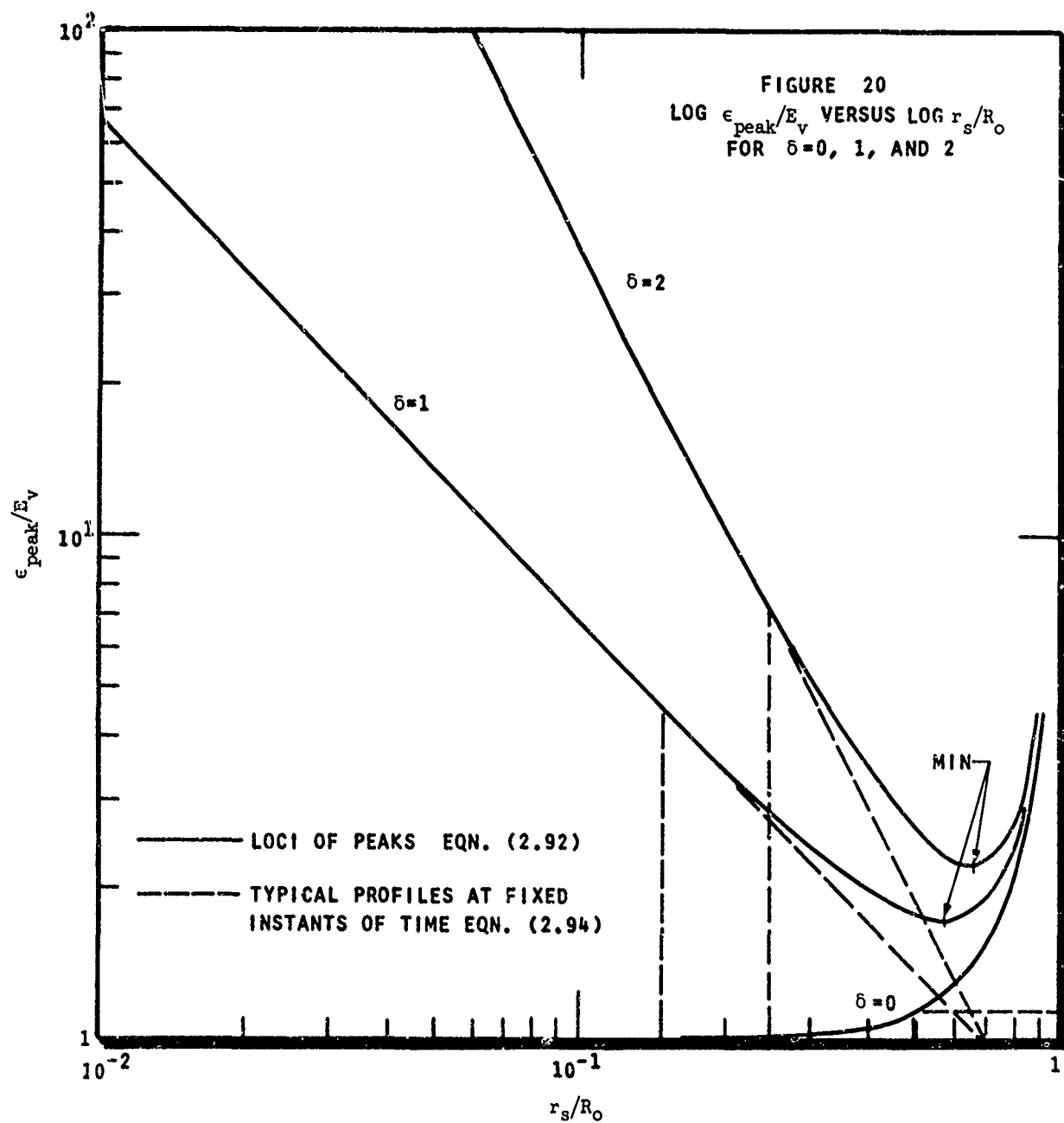
FIGURE 21

VALUE OF THE INTEGRAL $\Phi(\zeta)$ VERSUS δ AND γ

$$\Phi = \int_0^1 \left\{ \left(1 - \zeta^{3-\delta} \right) \zeta^\delta \right\}^{\frac{1}{2}} d\zeta$$

RATIO OF SPECIFIC HEATS γ

$\Phi(\zeta)$

FIGURE 22
$\hat{t}$ VERSUS ζ FOR $\gamma = 1.1$ AND 3

$$\hat{t} = \int_{\zeta}^{0} \left\{ \left(1 - \zeta^{3-\delta} \right) \zeta^{\delta} \right\} d\zeta$$

$\zeta = r_s/R_o$
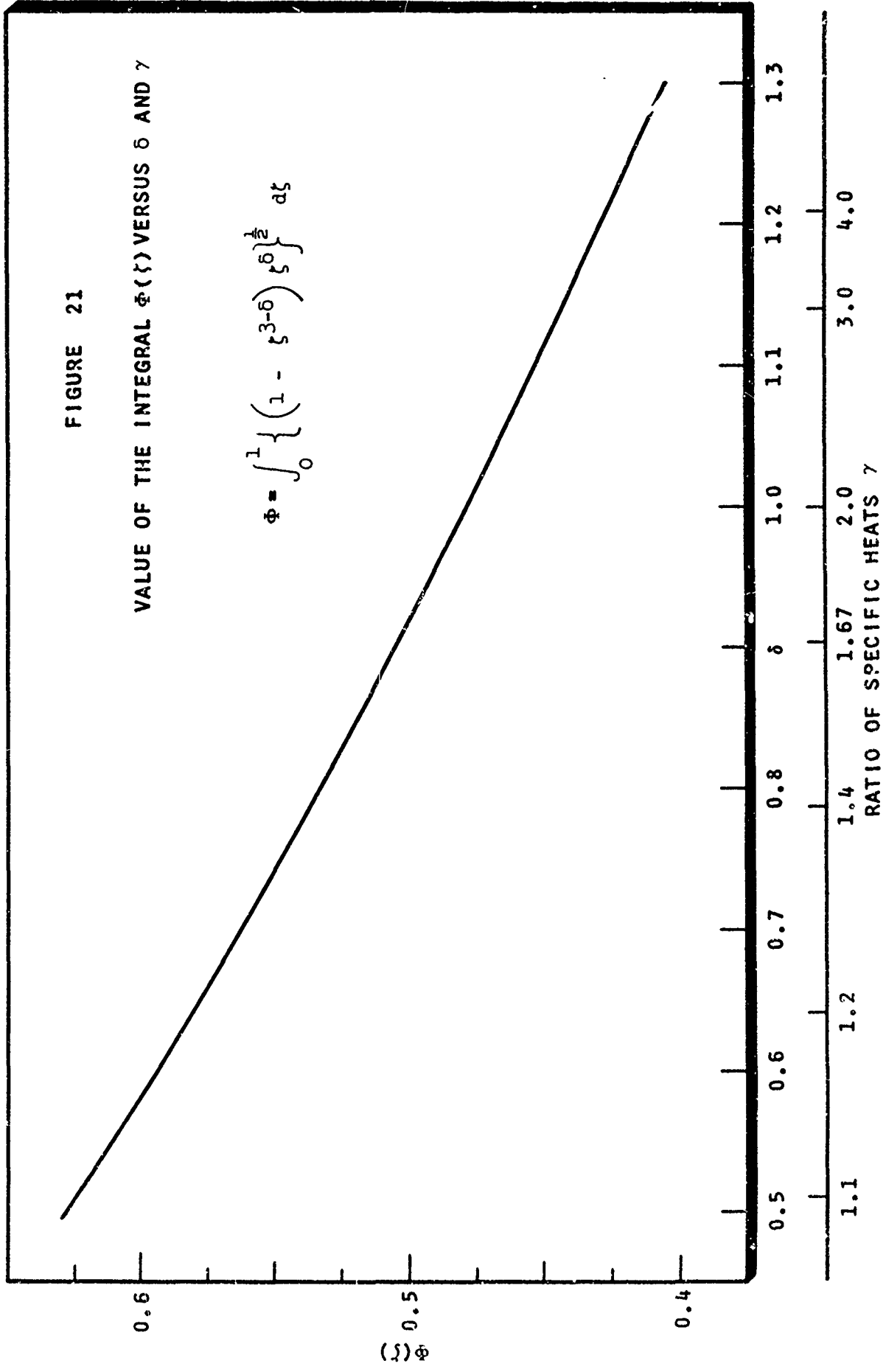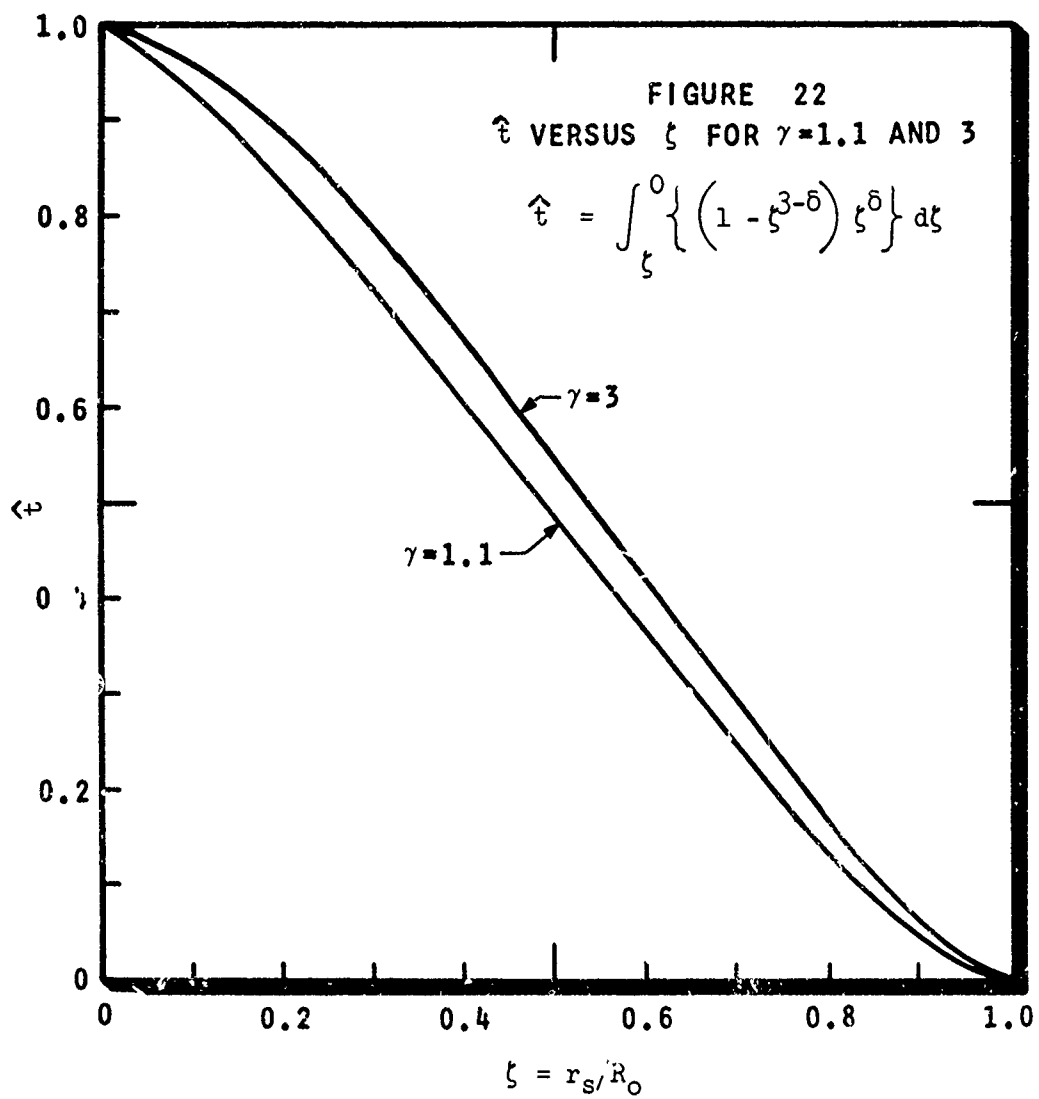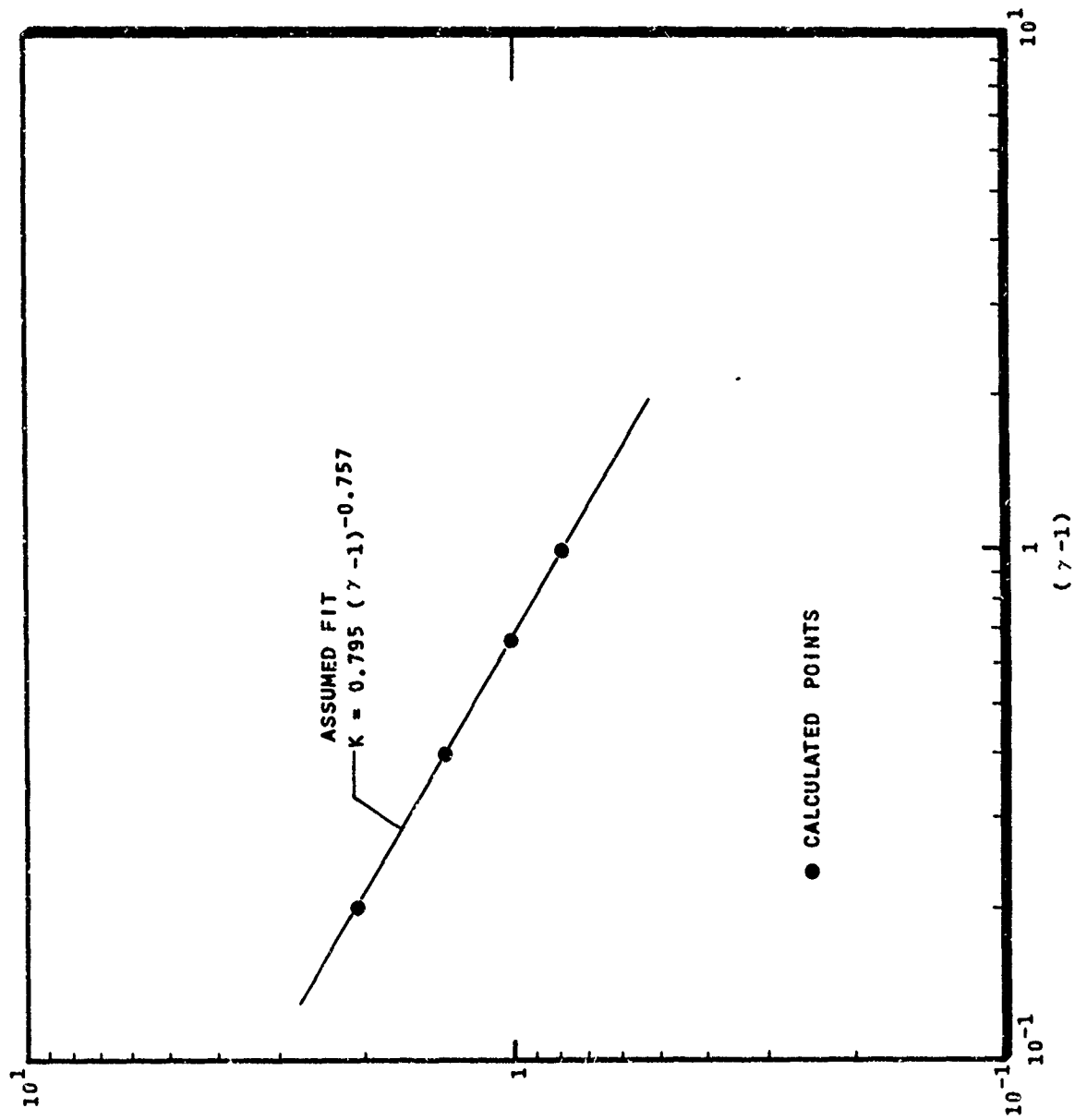
FIGURE 23   K(γ) VERSUS (γ -1)
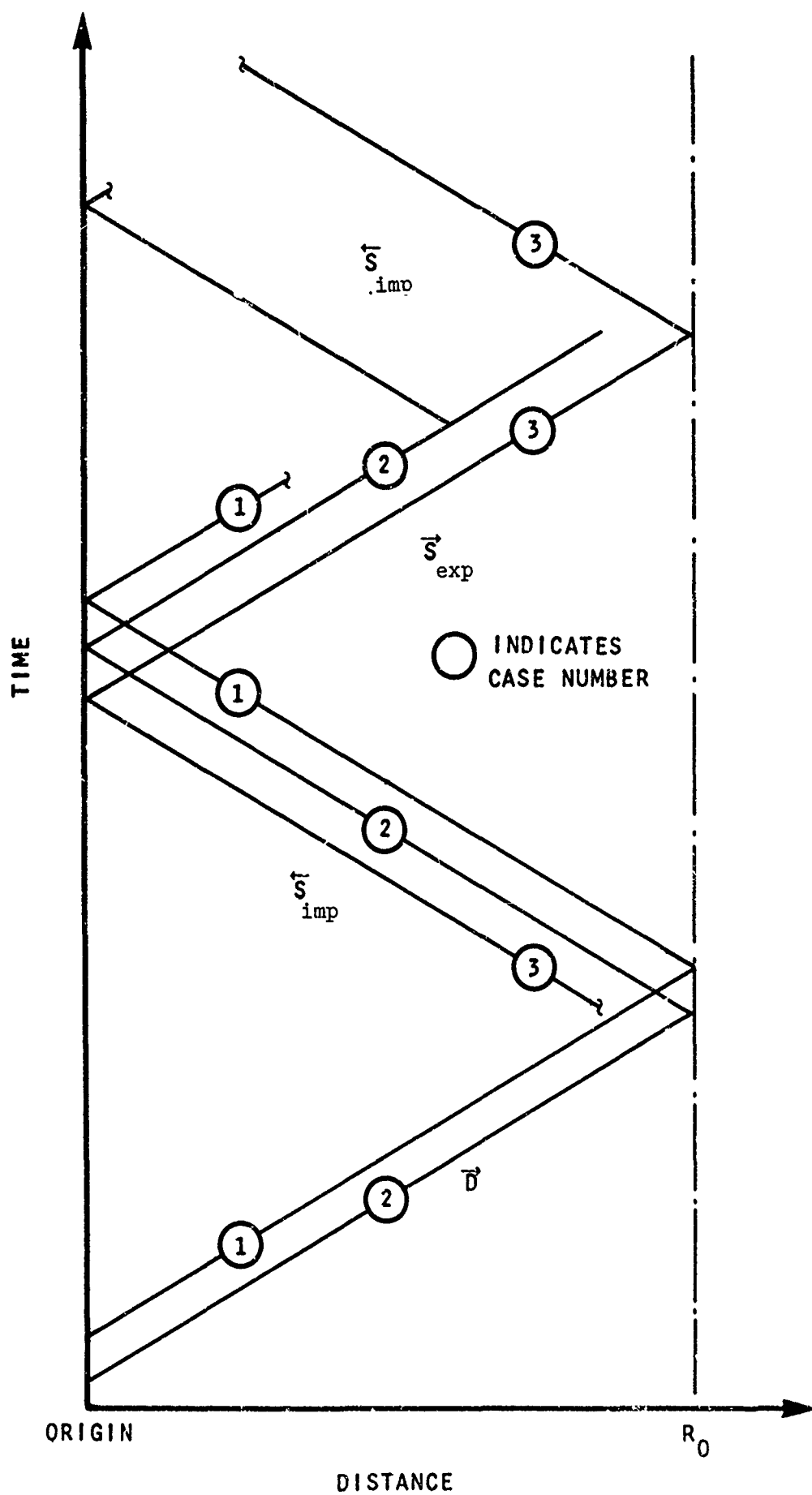
FIGURE 24 SCHEMATIC OF THE EXTENT OF THE X-T PLANE
COVERED BY THE NUMERICAL EXPERIMENTS OF BRODE

FIGURE   25

WAVE TRAJECTORIES FOR CASE 3
100 PSIA OF A MIXTURE OF $2H_2 + O_2 + 7H_e$
($\gamma = 1.67$) IN A 10.0 CM. RADIUS SPHERE

TIME t (MICROSECONDS)

DISTANCE r (CENTIMETERS)

FIGURE 26

WAVE TRAJECTORIES FOR CASE 1
100 PSIA OF A MIXTURE OF $2H_2 + O_2 + 7He$
WITH A 0.1 IN. TNT LINER
IN A 20.0 CENTIMETER SPHERE

$SLOPE^{-1} = 2.7$ KM/SEC

TIME t (MICROSECONDS)

DISTANCE r (CENTIMETERS)
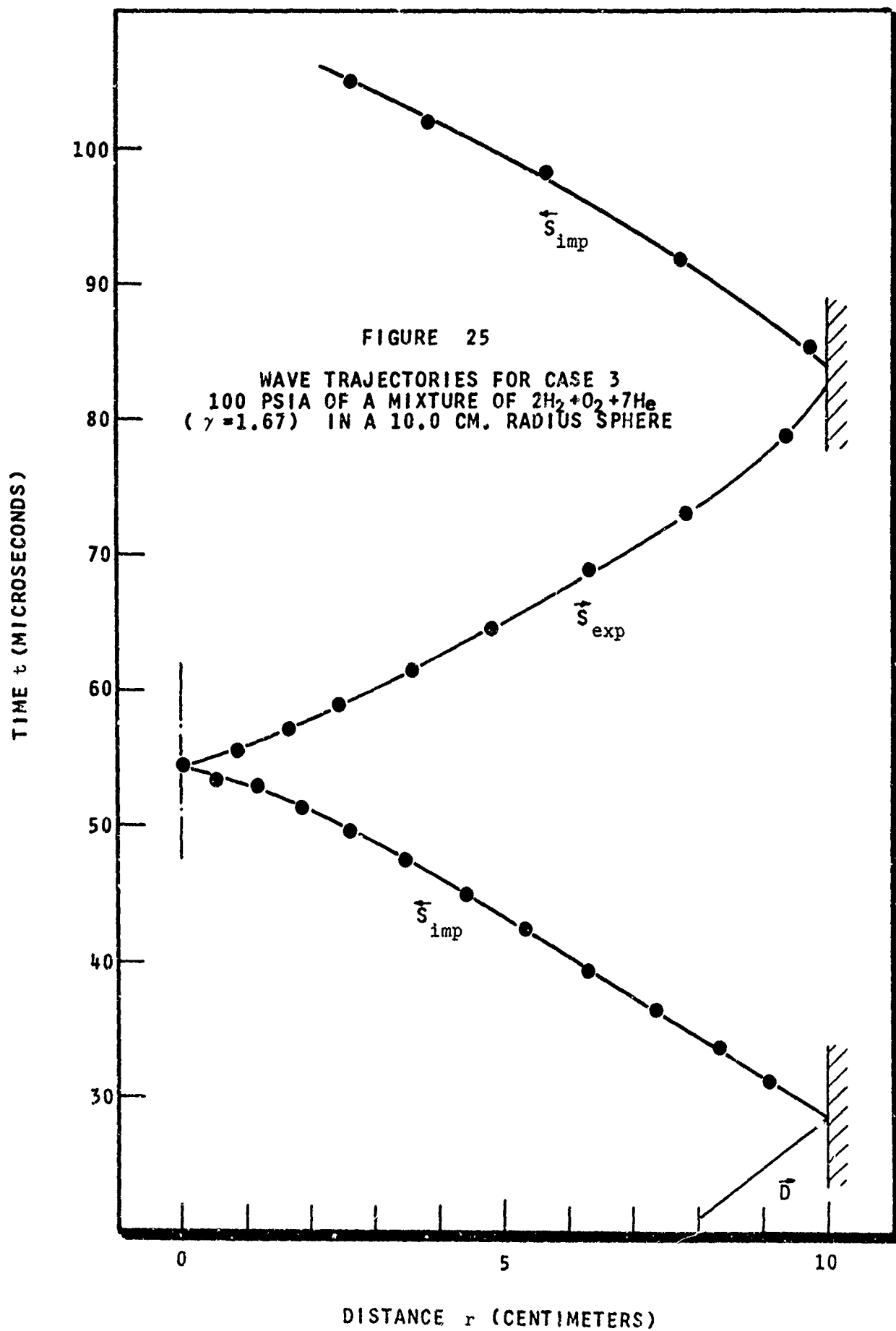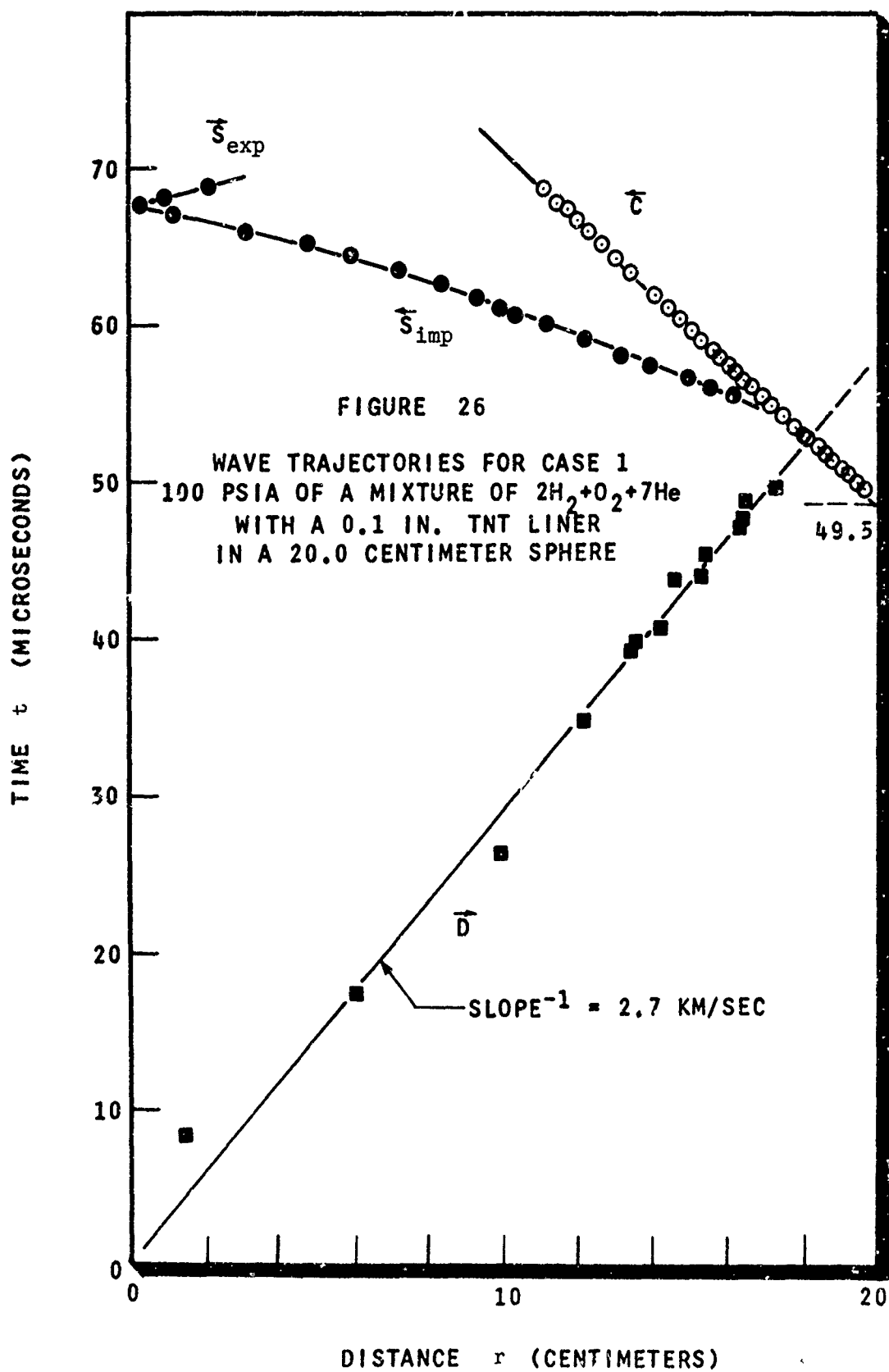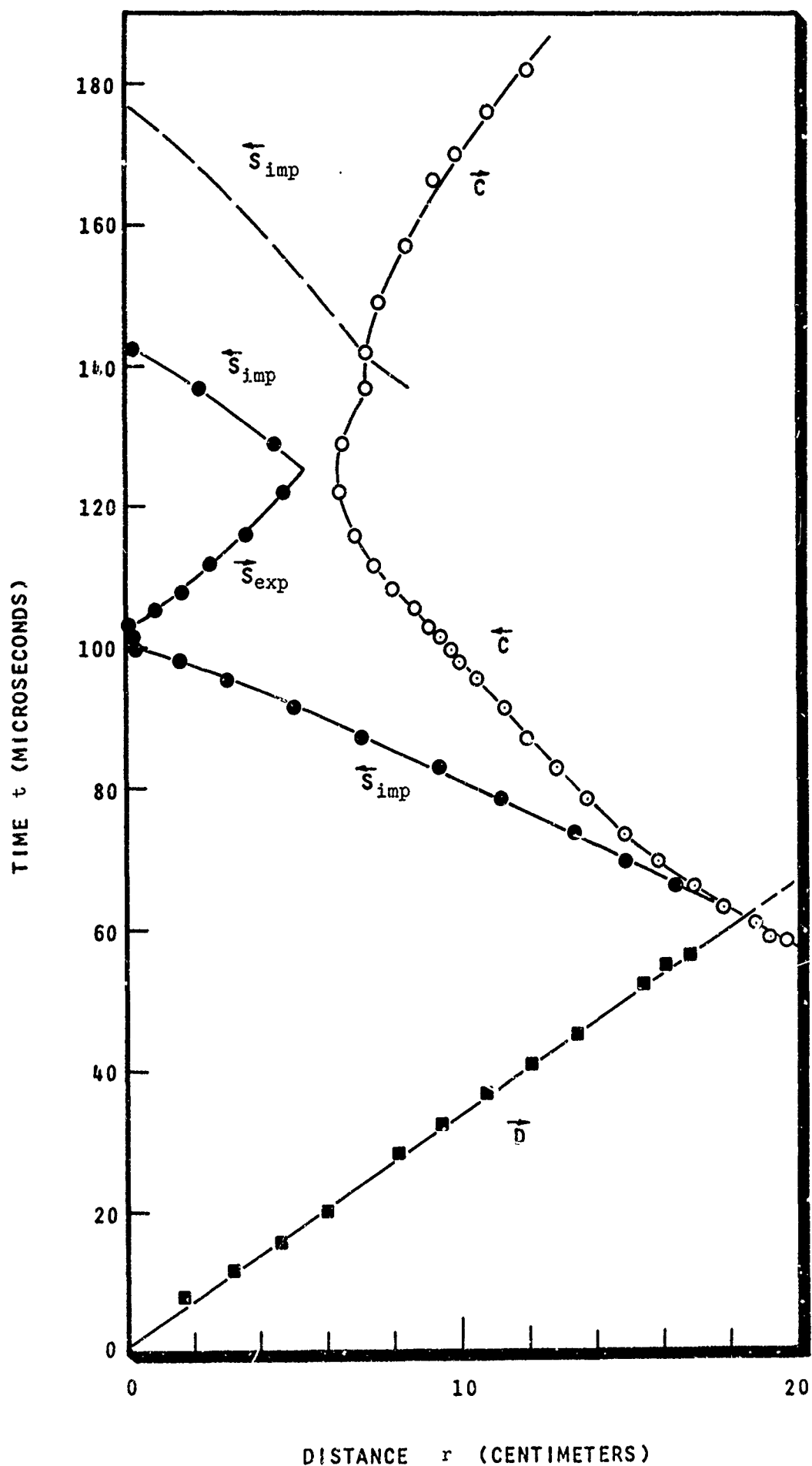
FIGURE 27 WAVE TRAJECTORIES FOR CASE 2 - 1000 PSIA OF A STOICHIOMETRIC
MIXTURE OF OXYGEN AND HYDROGEN IN A 20.0 CM. SPHERE WITH A
0.1 IN. LINER OF COMP B

FIGURE 28

PRESSURE AT THE EXPLOSIVE/METAL INTERFACE
AS A FUNCTION OF TIME FROM REFLECTION OF THE DETONATION WAVE
FOR THE EXPLOSIVE DRIVEN CASES

O CASE 1 (100 PSIA - TNT)
□ CASE 2 (1000 PSI - COMP B)

$p \sim t^{-2/3}$ ORIGIN CONDITIONS
PLANE EXPLOSION THEORY

13X

TIME FROM REFLECTION t (MICROSECONDS)

PRESSURE AT THE EXPLOSIVE/METAL INTERFACE p (PSIA)

FIGURE 29

VARIATION OF THE PRESSURE WITH DENSITY
FOR THE EXPANDING PRODUCTS OF DETONATION
FROM THE NUMERICAL EXPERIMENTS

FIGURE 30
PEAK PRESSURE VERSUS RADIUS
FOR THREE CASES OF IMPLOSIONS
IN A SPHERE
△ CASE 1 100 PSI - TNT
□ CASE 2 1000 PSI - COMP B
○ CASE 3 100 PSI

SHAPE CALCULATED
FROM IMPLOSION
IN A SPHERE MODEL

$r^{-1.21}$

ABSOLUTE VALUE CALCULATED
FROM IMPLOSION IN A SPHERE
MODEL EQN. (2.92)

$r^{-0.9054}$

PEAK PRESSURE p (PSIA)

RADIUS r (CENTIMETERS)

CLASSICAL ASYMPTOTE $r^{-0.9054}$

CLASSICAL PROFILE

SLOPE ~ -1.06

$t = 54.45 \mu SEC$

$t = 51.38 \mu SEC$

$t = 39.48 \mu SEC$

FIGURE 31

PRESSURE VERSUS RADIUS AT THREE INSTANTS OF TIME
CASE 3 - INITIAL CONDITIONS $2H_2 + O_2 + 7H_e$
($\gamma = 1.67$) AT 100 PSIA IN A 10.0 CENTIMETER SPHERE

RADIUS r (CENTIMETERS)
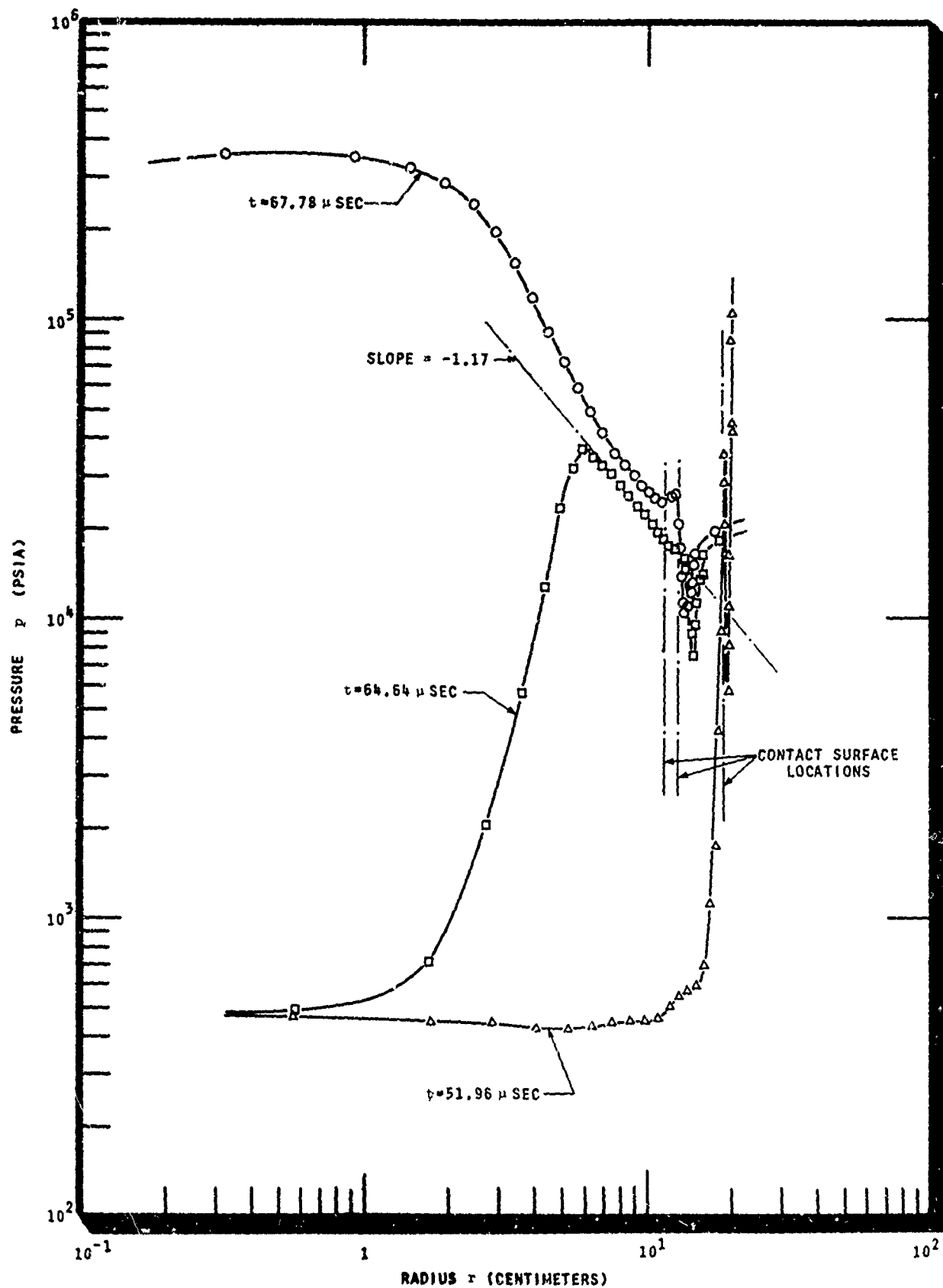
PRESSURE p (PSIA)

FIGURE   32   PRESSURE VERSUS RADIUS AT THREE INSTANTS OF TIME FOR
AN IMPLOSION   CASE 1 - INITIAL CONDITIONS $2H_2+O_2+7He$
($\gamma=1.67$) AT 100 PSIA AND A 0.1 INCH LINER OF TNT
IN A 20.0 CENTIMETER SPHERE

FIGURE 33 PRESSURE VERSUS RADIUS AT THREE INSTANTS OF TIME FOR AN IMPLOSION CASE 2 INITIAL CONDITIONS $2H_2+O_2$ (γ =1.14) AT 1000 PSIA AND A 0.1 INCH LINER OF COMP B IN A 20.0 CENTIMETER SPHERE
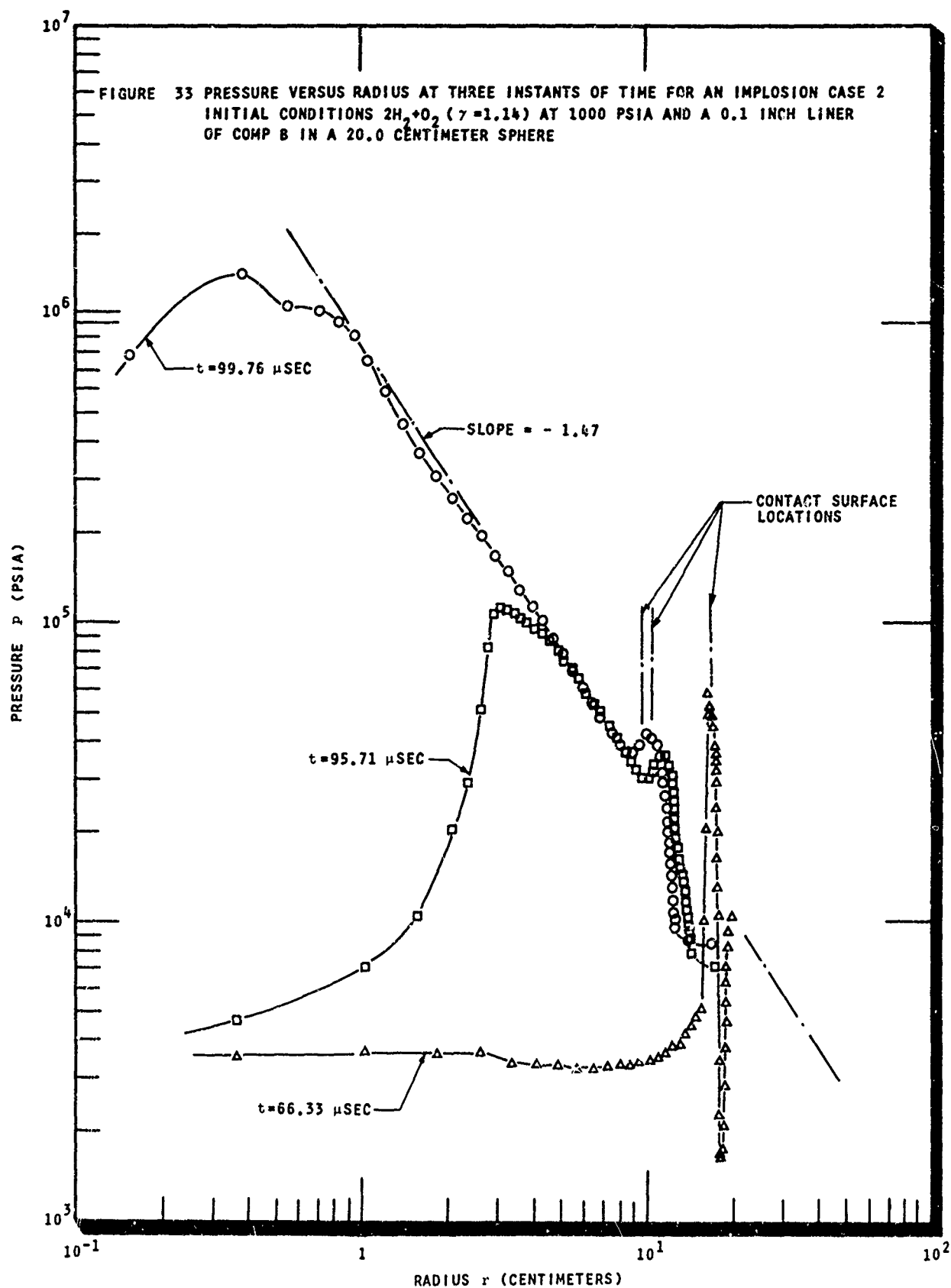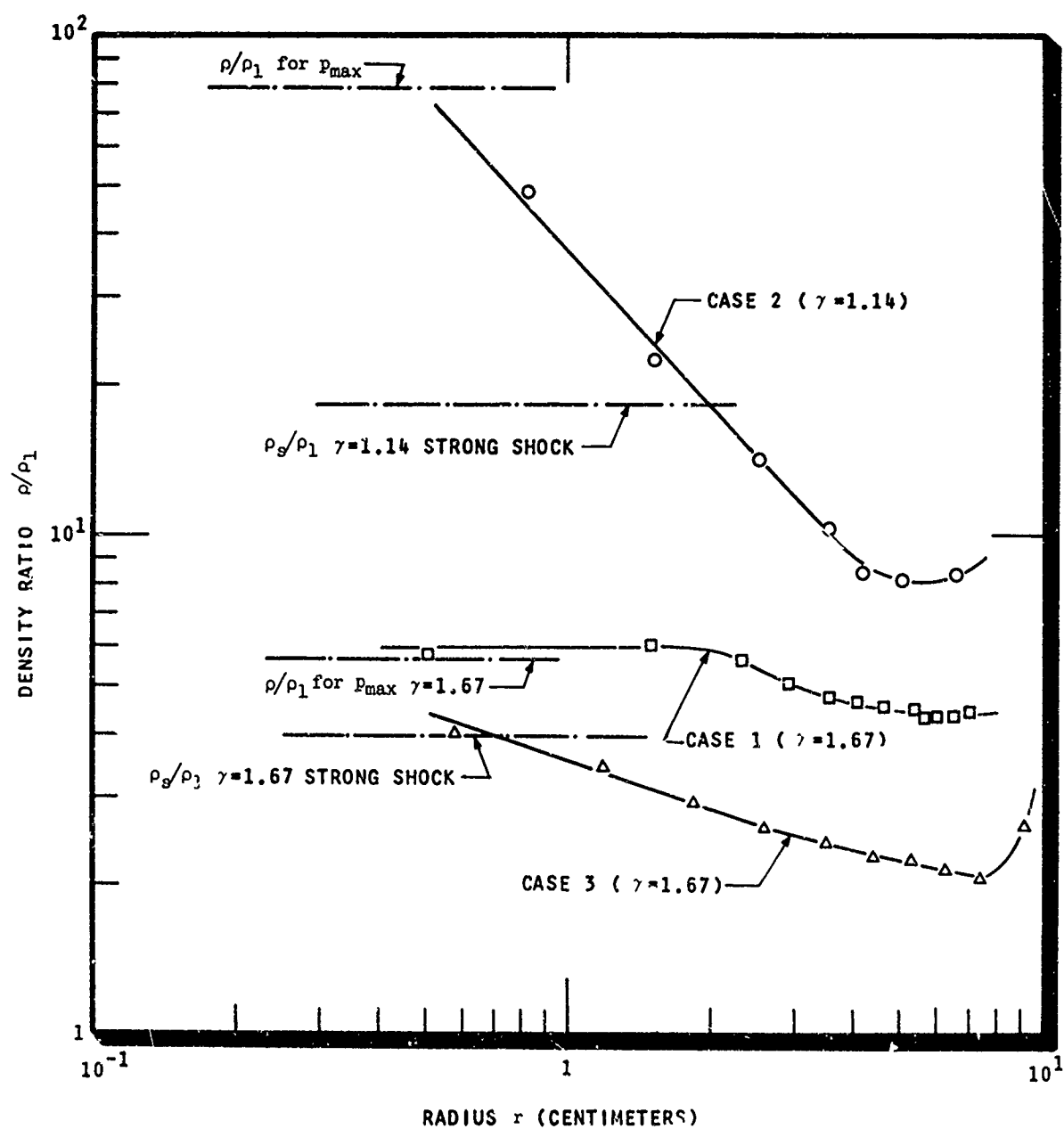
FIGURE 34 DENSITY RATIO AT THE PEAK PRESSURE LOCATION BEHIND AN IMPLODING SHOCK WAVE VERSUS RADIUS FOR THREE CASES

FIGURE 35

DENSITY VERSUS RADIUS AT THREE INSTANTS OF TIME
FOR AN IMPLOSION. CASE 1 INITIAL CONDITIONS
$2H_2+O_2+7He$ ($\gamma=1.67$) AT 100 PSIA AND A 0.1 INCH TNT
EXPLOSIVE LINER

FILLED SYMBOLS INDICATE
PEAK PRESSURE LOCATION

CONTACT SURFACE
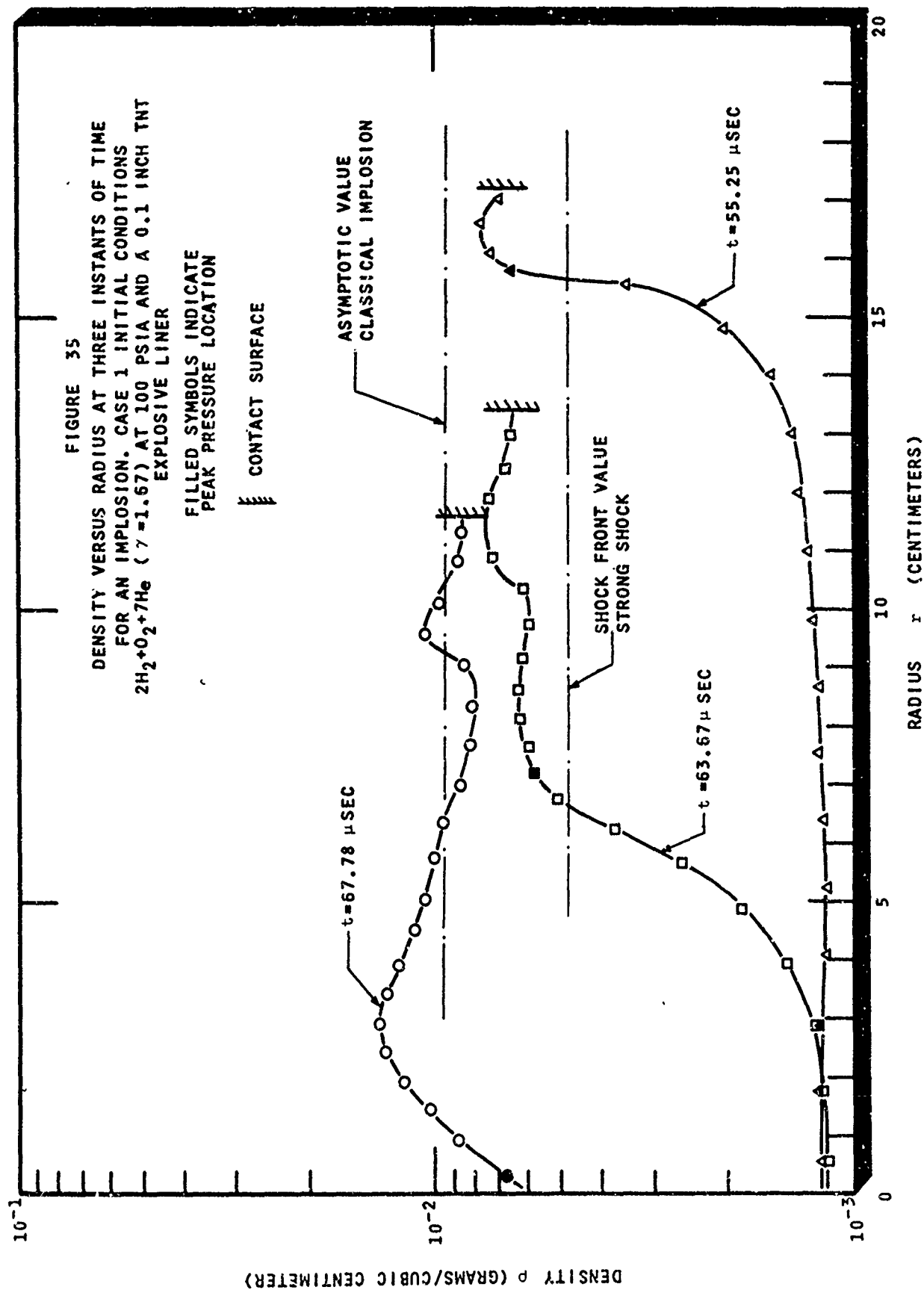
FIGURE 36

DENSITY VERSUS RADIUS AT THREE INSTANTS OF TIME FOR AN IMPLOSION
CASE 3 INITIAL CONDITIONS $2H_2 + O_2$ ($\gamma = 1.14$) AT 1000 PSIA AND
A 0.1 INCH LINER OF COMP B IN A 20.0 CENTIMETER SPHERE

FILLED SYMBOLS INDICATE
PEAK PRESSURE LOCATIONS

FIGURE 37

DENSITY VERSUS RADIUS AT THREE INSTANTS OF TIME FOR AN IMPLOSION
CASE 3 INITIAL CONDITIONS $2H_2 + O_2 + 7He$ ($\gamma = 1.67$) AT 100 PSIA
IN A 10.0 CENTIMETER SPHERE

FILLED SYMBOLS INDICATE
PEAK PRESSURE LOCATION

FIGURE 38

TEMPERATURE AT THE PEAK PRESSURE LOCATION
BEHIND AN IMPLODING SHOCK WAVE VERSUS
RADIUS FROM THREE NUMERICAL EXPERIMENTS

△ CASE 1
○ CASE 2
□ CASE 3

TEMPERATURE T (DEGREES KELVIN)

PEAK PRESSURE LOCATION r (CENTIMETERS)

$r^{-1.21}$

$r^{-1.21}$

$r^{-0.9054}$

FIGURE 39

NORMALIZED TRAJECTORIES AS DETERMINED FROM PEAK PRESSURE AND PEAK ARTIFICIAL VISCOSITY LOCATIONS OF THE NUMERICAL EXPERIMENTS AND THE SHOCK FRONT POSITION PREDICTED BY THE IMPLOSION IN A SPHERE MODEL

△ CASE 1 100 PSIA - TNT PEAK P
▲ CASE 1 100 PSIA - TNT PEAK Q
○ CASE 2 1000 PSIA - COMP B PEAK P
□ CASE 3 100 PSIA - NO EXP PEAK P

FIGURE 40

PRESSURE IN THE ORIGIN ZONE
VERSUS TIME FROM REFLECTION
FOR THREE IMPLOSION CASES

PRESSURE IN THE ORIGIN ZONE p_{orig} (PSIA)

$t^{-3/2}$

O CASE 1 100 PSIA – TNT
□ CASE 2 1000 PSIA – COMP B
△ CASE 3 100 PSIA – NO EXP

TIME FROM REFLECTION t (MICROSECONDS)

FIGURE 41
PRESSURE VERSUS DENSITY AFTER REFLECTION
FOR THE GAS IN THE ORIGIN ZONE
FOR THREE IMPLOSION CASES

FIGURE 42

ORIGIN ZONE PRESSURE, TEMPERATURE AND
DENSITY VERSUS TIME FROM REFLECTION FOR
CASE 3 (100 PSI $2H_2+O_2+7He$ $\gamma = 1.67$)

O PRESSURE
□ TEMPERATURE
△ DENSITY

FIGURE 3
ORIGIN ZONE PRESSURE, TEMPERATURE AND
DENSITY VERSUS TIME FROM REFLECTION FOR
CASE 2 (1000 PSIA $2H_2+O_2$ - COMP B)

FIGURE 44 ORIGIN ZONE PRESSURE, TEMPERATURE AND DENSITY VERSUS TIME FROM REFLECTION FOR CASE 1 (100 PSIA $2H_2+O_2+7H_e$ -TNT)
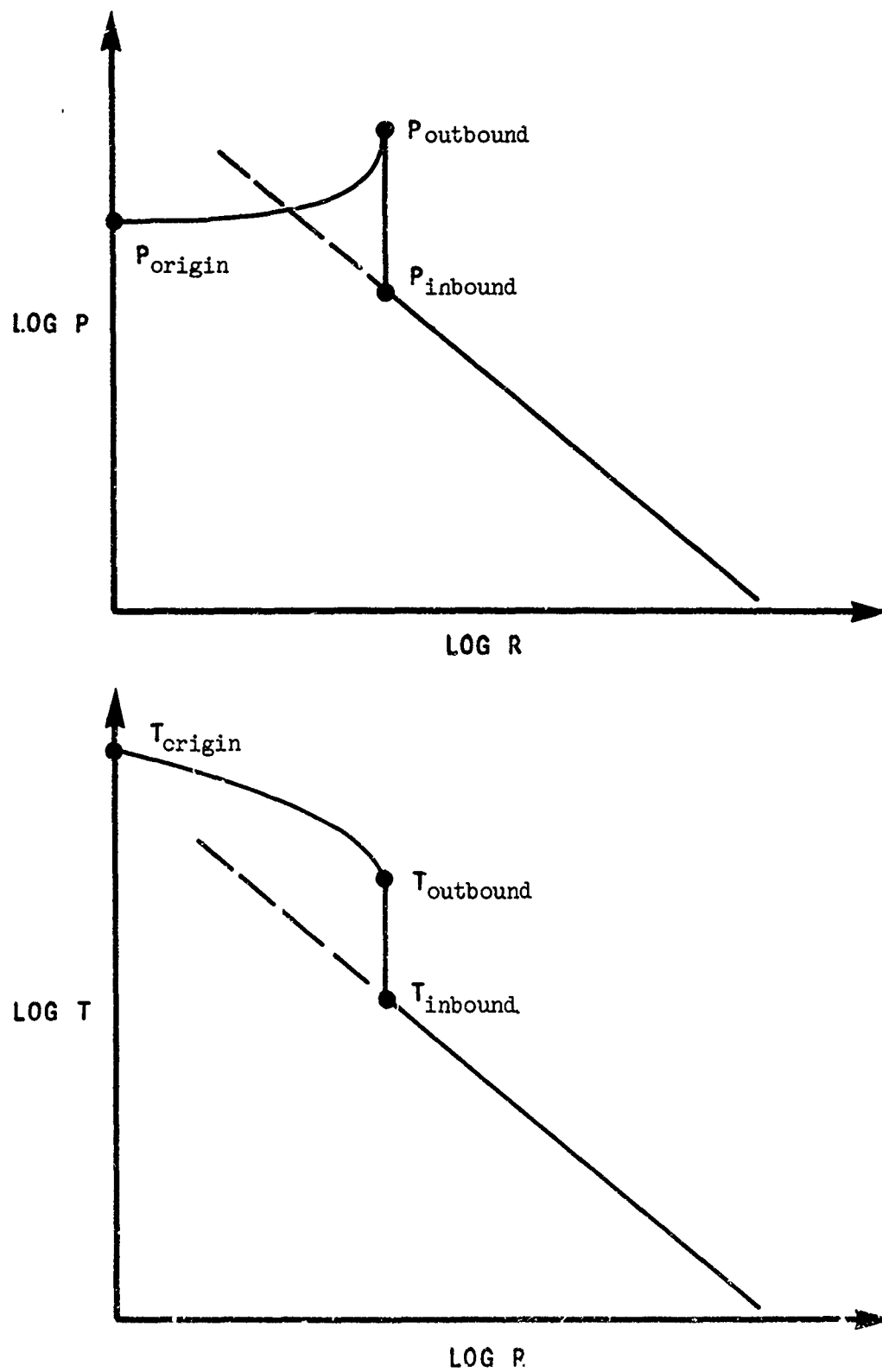
FIGURE 45 SCHEMATIC OF THE PRESSURE AND TEMPERATURE PROFILES
AFTER REFLECTION OF AN IMPLODING SHOCK WAVE IN A SPHERE

FIGURE 46

PRESSURE AT A FIXED POINT AS A FUNCTION OF TIME FOR
PLANE, CYLINDRICAL AND SPHERICAL SHOCK WAVES
(REF. 43 CORRECTED)
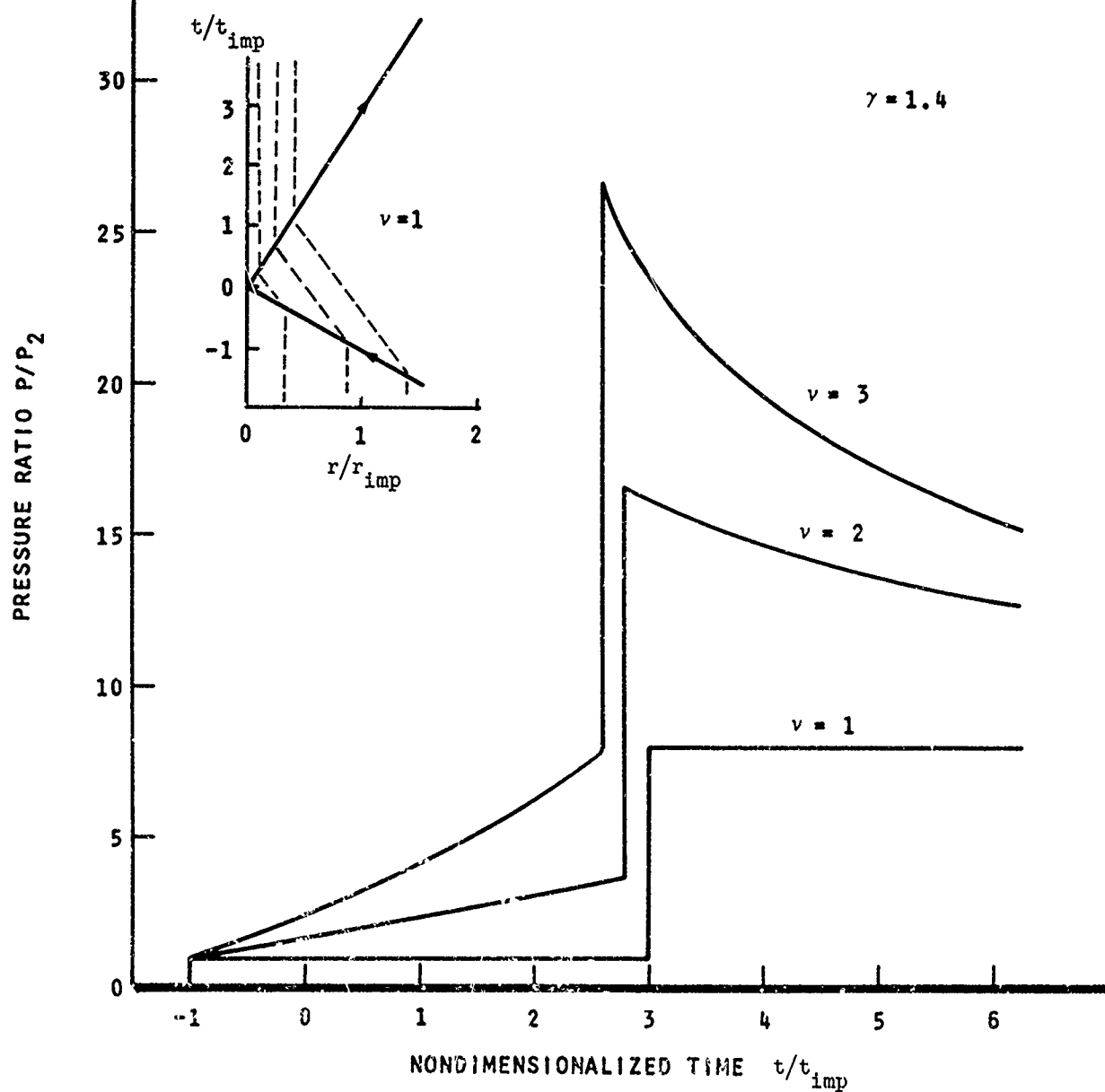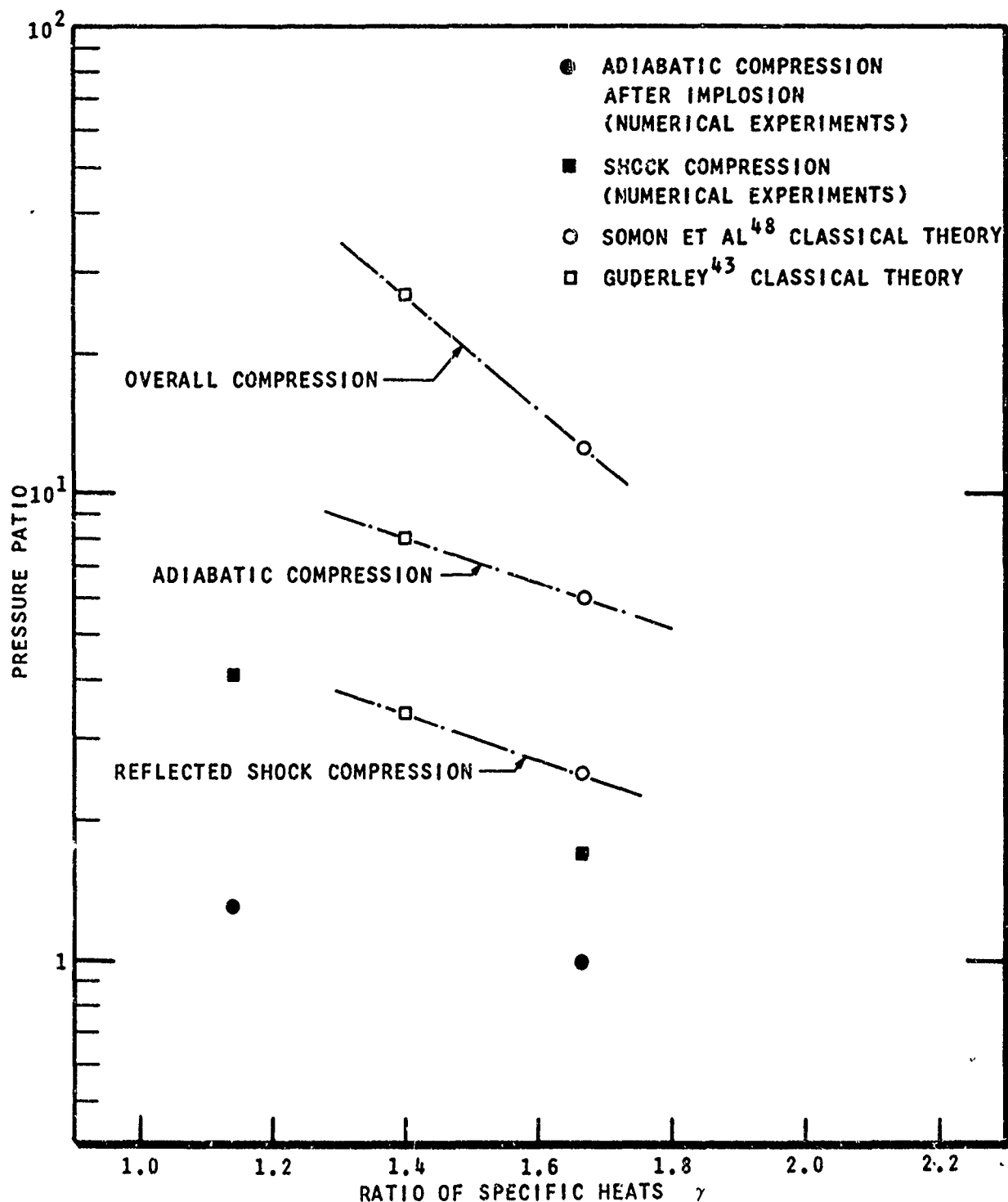
FIGURE 47 REFLECTED SHOCK, ADIABATIC AND OVERALL COMPRESSION RATIOS VERSUS
RATIO OF SPECIFIC HEATS FROM CLASSICAL IMPLOSION
THEORY AND THE NUMERICAL EXPERIMENTS

FIGURE 48 PEAK REFLECTED SHOCK PRESSURE AND PRESHOCKED PRESSURE PROFILES AS A FUNCTION OF RADIUS FOR CASES 2 AND 3

FIGURE 49

PRESSURE, TEMPERATURE AND DENSITY PROFILES
BEHIND A REFLECTED IMPLOSION WAVE FOR $\gamma = 1.67$
FROM THE NUMERICAL EXPERIMENTS

OPEN SYMBOLS   CASE 3
FILLED SYMBOLS CASE 1

T/T_S

P/P_S

ρ/ρ_S

NONDIMENSIONAL RADIUS η

FIGURE 50

PRESSURE, TEMPERATURE AND DENSITY PROFILES
BEHIND A REFLECTED IMPLOSION WAVE FOR $\gamma = 1.14$
AS OBTAINED FROM THE NUMERICAL EXPERIMENTS

T/T_S

P/P_S

ρ/ρ_S

ρ/ρ_S

NONDIMENSIONAL RADIUS η

A. REFLECTED SHOCK PROFILES

B. VARIATION OF FLOW PROPERTIES AT A FIXED POINT WITH TIME

FIGURE 51   REFLECTED SHOCK PROFILES AND THE VARIATION OF THE
PROPERTIES AT A FIXED POINT VERSUS TIME FOR CYLINDRICAL AND
SPHERICAL IMPLOSIONS - SOMON ET AL (REF 48)

FIGURE 52

RATIO OF ORIGIN CONDITIONS TO PEAK SHOCK CONDITIONS
FOR PRESSURE AND TEMPERATURE VERSUS SHOCK POSITION
FROM THE NUMERICAL EXPERIMENTS

□ CASE 1
△ CASE 2
○ CASE 3

FIGURE 53

RATIO OF ORIGIN CONDITIONS TO PEAK SHOCK CONDITIONS
FOR TEMPERATURE AND PRESSURE VERSUS
THE RATIO OF SPECIFIC HEATS AS OF OBTAINED FROM
THE NUMERICAL EXPERIMENTS

$T_{orig}/T_S = 1.64/(\gamma-1)$

$P_{orig}/P_S = 0.85$

$(\gamma-1)$

FIGURE 54

RATIO OF REFLECTED IMPLOSION PHASE TIME
TO IMPLOSION PHASE TIME
VERSUS RATIO OF SPECIFIC HEATS
FROM CLASSICAL THEORY AND NUMERICAL EXPERIMENTS

$\nu = 1 \quad t_{exp}/t_{imp} = (\gamma+1)/2(\gamma-1)$

$\nu = 2$
$\nu = 3$
(REF. 43 AND 48)

● NUMERICAL EXPERIMENTS

$(\gamma - 1)$

FIGURE 55

REFLECTED IMPLOSION TRAJECTORIES FOR THREE
SPHERICAL IMPLOSIONS AS OBTAINED FROM
NUMERICAL EXPERIMENTS AND CLASSICAL THEORY

FIGURE 56

ORIGIN ZONE PRESSURE
VERSUS
TIME FROM REFLECTION
FOR THREE SUCCEEDING CYCLES

CASE 3

O FIRST CYCLE

□ SECOND CYCLE

△ THIRD CYCLE

PRESSURE P (PSIA)

TIME FROM REFLECTION t (MICROSECONDS)

FIGURE 57

SCHEMATIC DIAGRAMS OF THE ORIGIN ZONE PRESSURE AND TEMPERATURE
VERSUS TIME FOR THE PERFORMANCE MODEL

FIGURE 58

PRESSURE PROFILES BEHIND GASEOUS
DETONATION WAVES

ν	GAS	REFERENCE
1	$2H_2+O_2$	96
2	$2H_2+O_1$	96
3	$\gamma=1.13$	58

FIGURE 59

P_{ORIG}/P_D VERSUS RATIO OF SPECIFIC HEATS

FIGURE 60

MEASURED AND PREDICTED PROJECTILE VELOCITIES VERSUS INITIAL PRESSURE OF STOICHIOMETRIC OXYGEN AND HYDROGEN FOR A ONE CALIBER POLYETHYLENE PROJECTILE

$n = 0.22$ INCHES
$L = 60.0$ INCHES
$\rho_{PROJ} = 0.92$ G/CC

PROJECTILE VELOCITY V_{PROJ} (FEET PER SECOND)

10^4
9
8
7
6
5
4
3
2
10^3

PREDICTED
400 PSIA

N = 11

N = 15

PREDICTED
200 PSIA

N = 16

FIGURE 61

MEASURED AND PREDICTED PROJECTILE VELOCITIES VERSUS
DILUTION INDEX FOR A 0.22 INCH DIAMETER ONE CALIBER
POLYETHYLENE PROJECTILE IN A 60.0 INCH BARREL
AT 200 AND 400 PSIA INITIAL DRIVING PRESSURE

$2H_2 + O_2 + nHe + mH_2$

SYMBOL PRESSURE COMBUSTION

Symbol	Pressure	Combustion	
●	400 PSIA	DET	
○	400 PSIA	CVC	(REF 63)
■	200 PSIA	DET	
□	200 PSIA	CVC	

N = NO. OF CYCLES

7   6   5   4   3   2   1   0   1   2   3   4

n ◄─── ───► m

DILUTION INDEX

FIGURE 62 MEASURED AND PREDICTED
CYCLE TIMES
VERSUS DILUTION INDEX

$R_0 = 10.0$ CM.

$2H_2 + O_2 + nHe + mH_2$

FIGURE 63

MEASURED AND PREDICTED PROJECTILE VELOCITIES VERSUS BARREL LENGTH
FOR A 0.22 INCH DIAMETER ONE CALIBER POLYETHYLENE PROJECTILE AND
STOICHIOMETRIC OXYGEN HYDROGEN AT 200, 300 AND 400 PSIA INITIAL PRESSURE

FIGURE 64

MEASURED AND PREDICTED PROJECTILE VELOCITIES
VERSUS PROJECTILE DENSITY FOR A 0.22 INCH DIAMETER
ONE CALIBER PROJECTILE AND AN INITIAL DRIVING MIXTURE
OF STOICHIOMETRIC OXYGEN AND HYDROGEN AT
100 AND 200 PSIA

PENETRATION VERSUS PROJECTILE VELOCITY FOR 0.22
INCH DIAMETER POLYETHYLENE CYLINDERS IMPACTING ON LEAD TARGETS

FIGURE 65

FIGURE 66

MEASURED AND PREDICTED PERFORMANCE USING LEAD AZIDE AND 0.22 INCH DIAMETER
ONE CALIBER POLYETHYLENE PROJECTILES IN A 60.0 INCH BARREL AND A
STOICHIOMETRIC OXYGEN - HYDROGEN MIXTURE AT 100 PSIA

FIGURE 67

VIEW OF THE LEAD IMPACT PLATE FOLLOWING AN IMPACT WITH A
DISTORTED NOMINAL 5/16 INCH DIAMETER ONE CALIBER
POLYETHYLENE PROJECTILE (V = 10520 FPS)
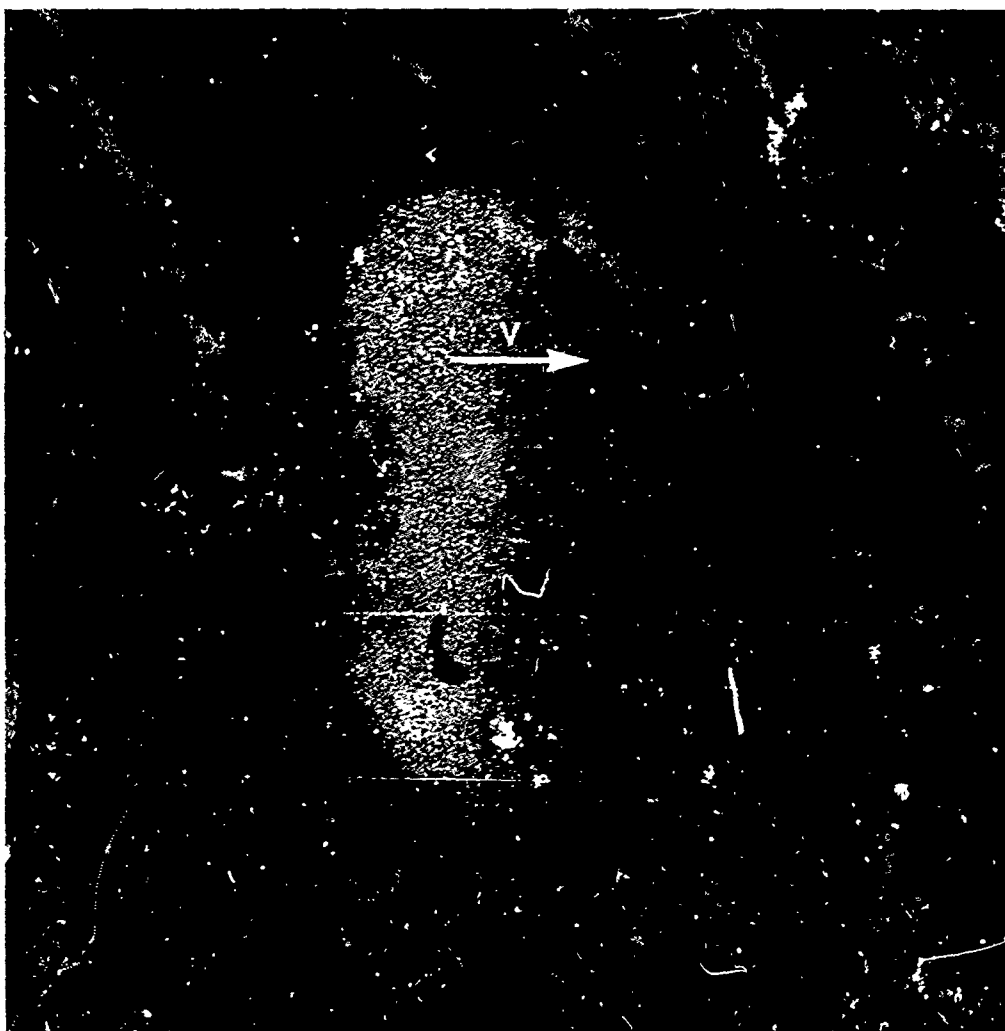
FIGURE   68

PHOTOGRAPH OF A DISTORTED 5/16 INCH DIAMETER ONE CALIBER
POLYETHYLENE PROJECTILE AT 10520 FEET PER SECOND AFTER A
91.5 GRAM PETN LAUNCH   (RUN NO. 213)
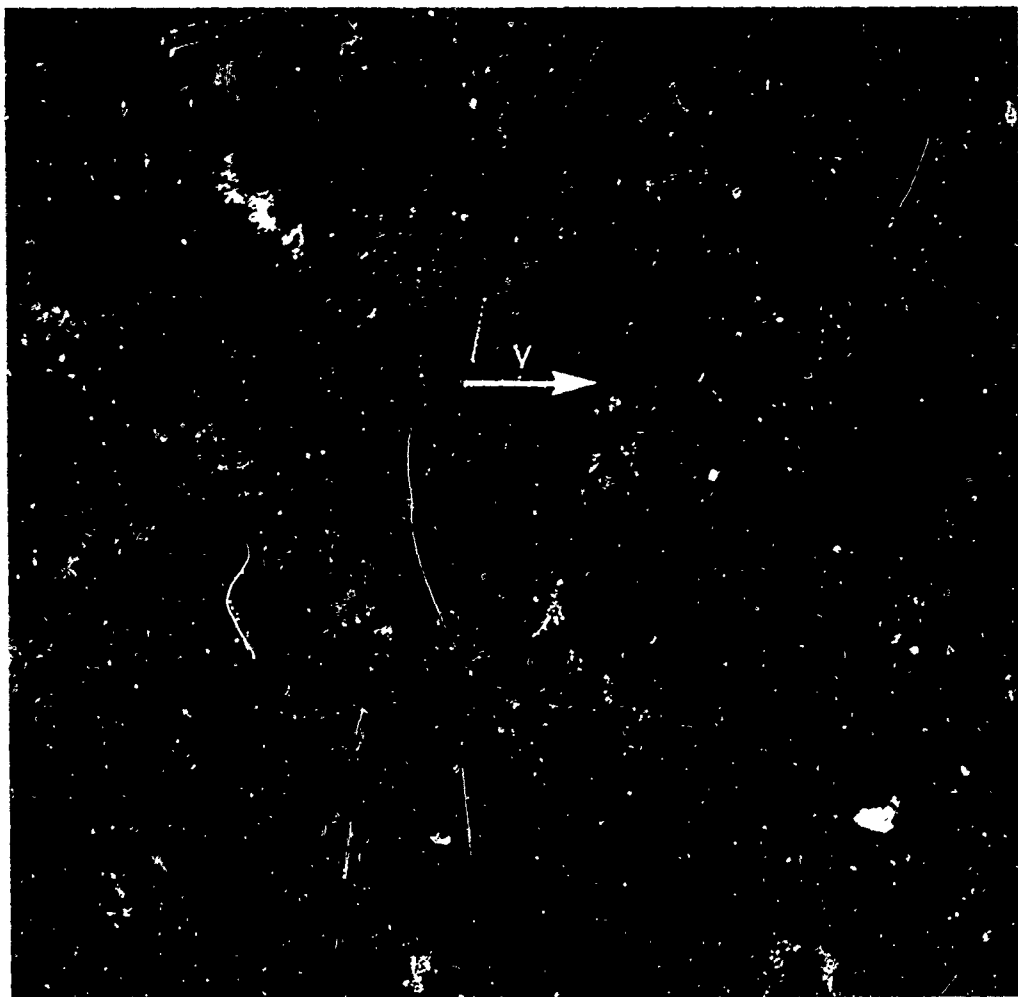
FIGURE 69

PHOTOGRAPH OF A FRAGMENTED 5/16 INCH DIAMETER, ONE CALIBER
POLYETHYLENE PROJECTILE AFTER A 209.4 GRAM PETN LAUNCH
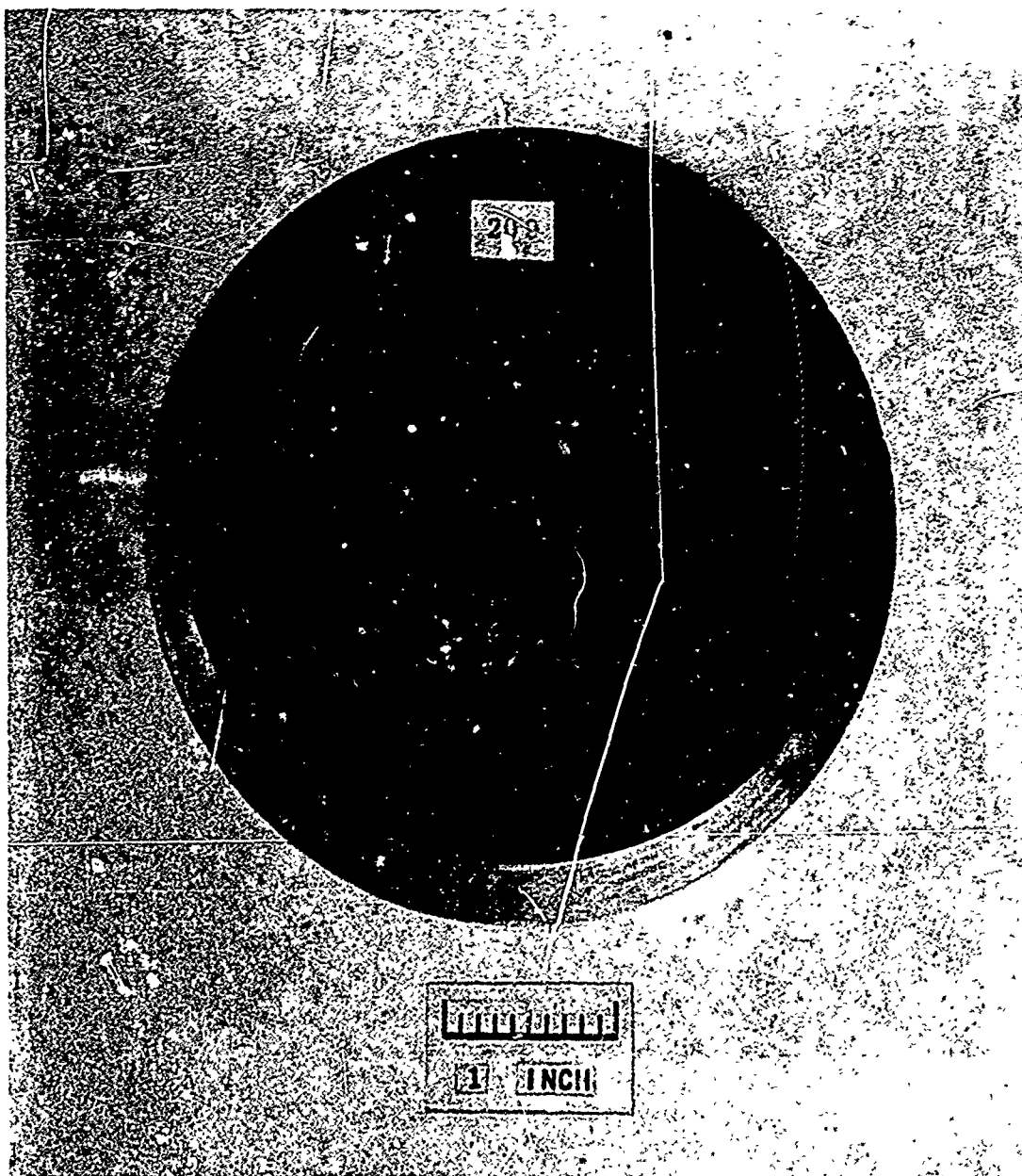
FIGURE 70

VIEW OF THE LEAD IMPACT PLATE FOLLOWING AN IMPACT WITH A
FRAGMENTED 5/16 INCH DIAMETER ONE CALIBER POLYETHYLENE
PROJECTILE (RUN NO. 209)
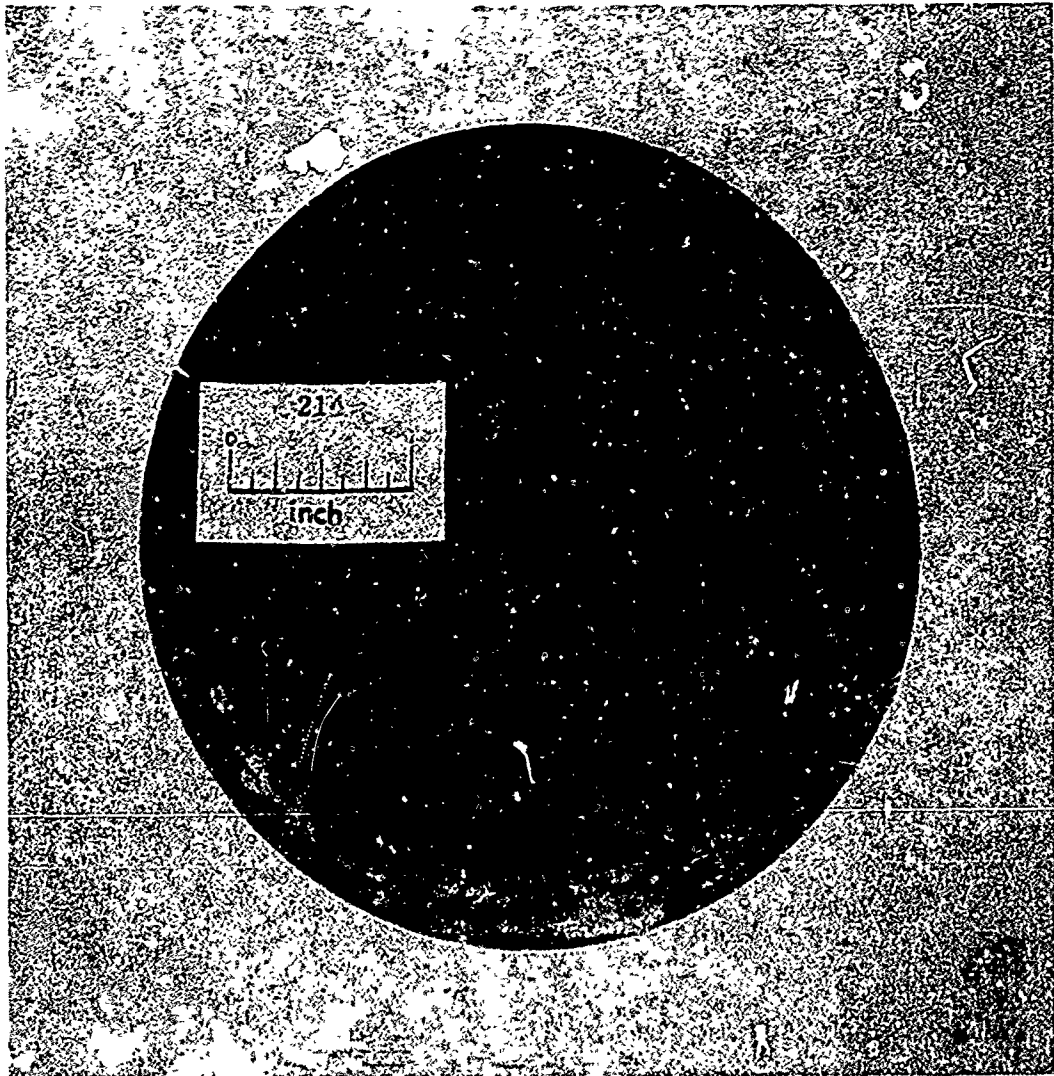
FIGURE 71

VIEW OF THE LEAD IMPACT PLATE FOLLOWING AN IMPACT WITH AN
INTACT 5/16 INCH DIAMETER, ONE CALIBER MAGNESIUM PROJECTILE
(V = 9100 FPS)
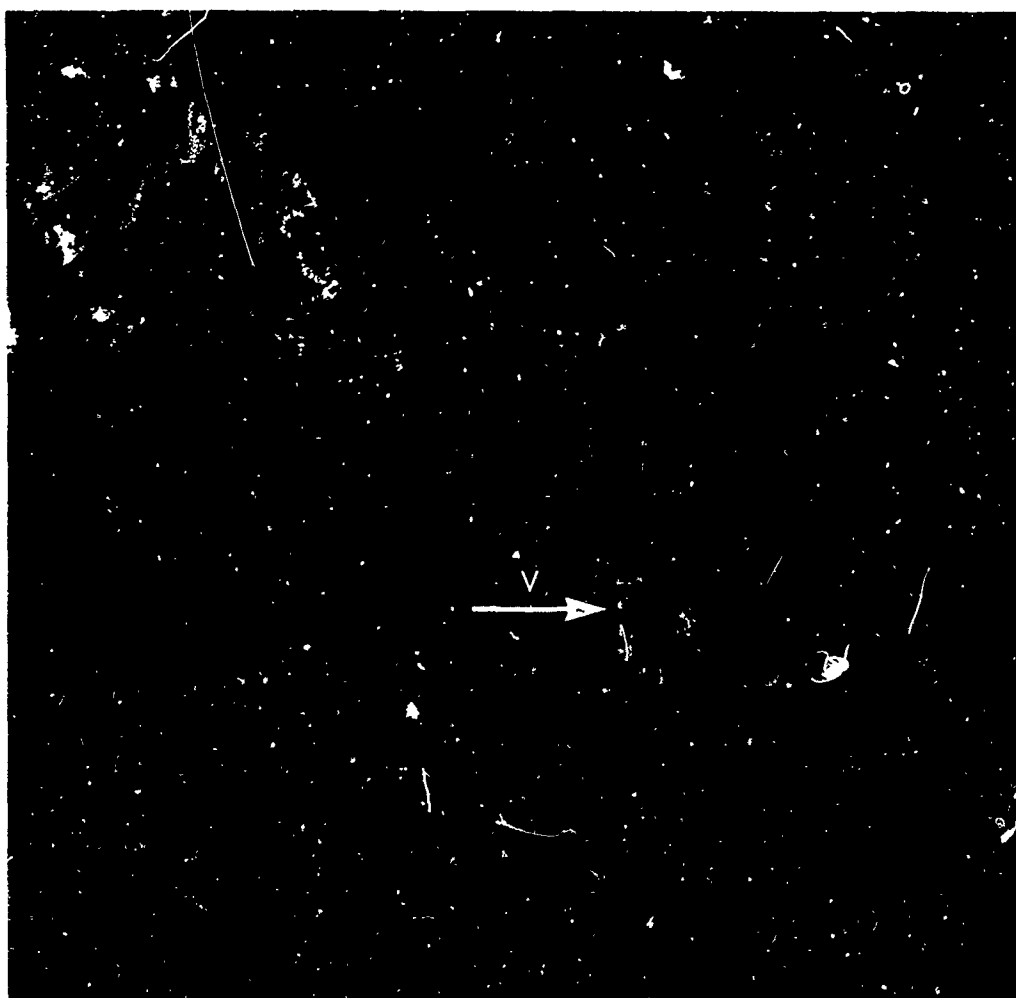
FIGURE 72

PHOTOGRAPH OF A FRAGMENTED 5/16 INCH DIAMETER ONE CALIBER
FIBERGLASS PROJECTILE AT A BULK VELOCITY OF 11100
AFTER A 90.8 GRAM PETN LAUNCH (RUN NO. 218)
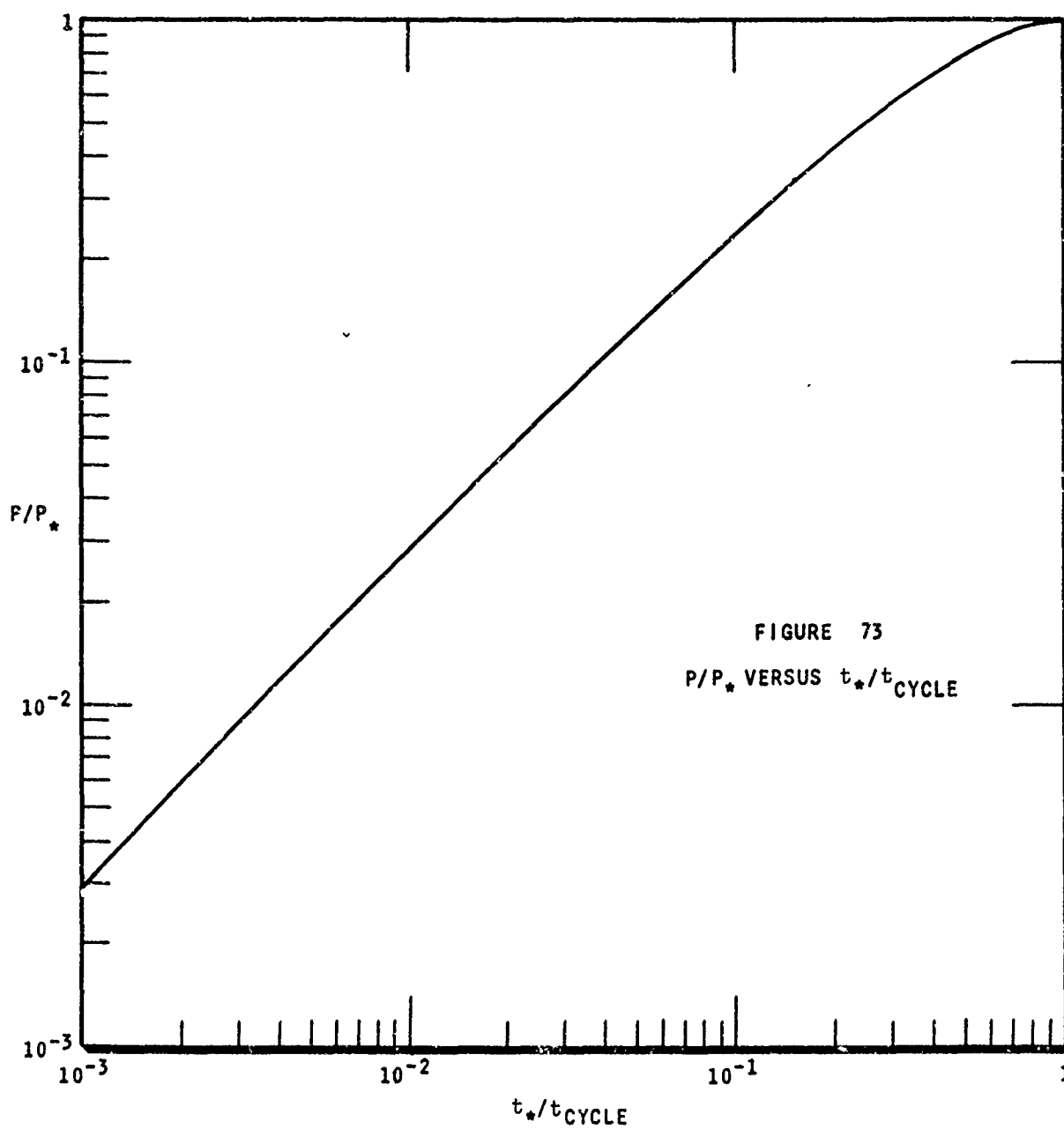
FIGURE 73

P/P_* VERSUS t_*/t_{CYCLE}
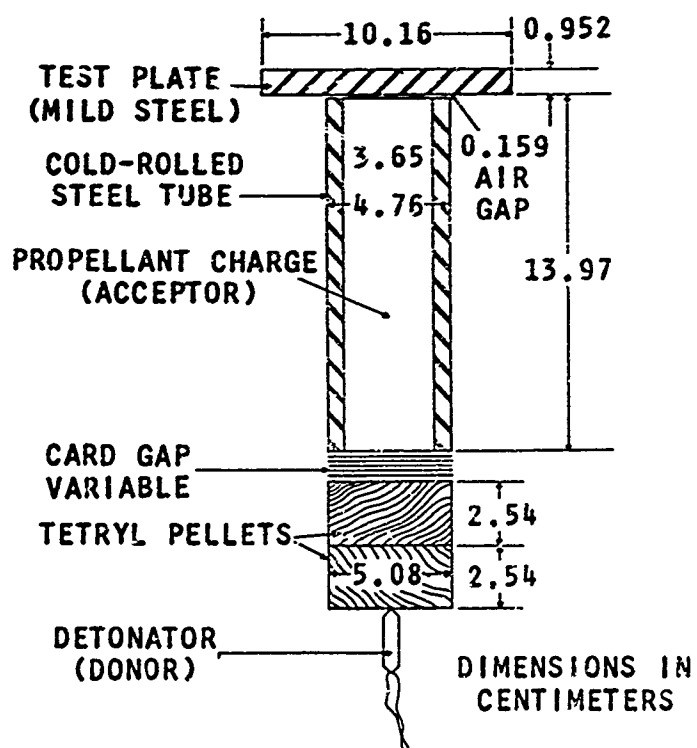
FIGURE   74

CHARGE ASSEMBLY AND DIMENSIONS FOR THE
STANDARDIZED NOL GAP TEST (REF 79)
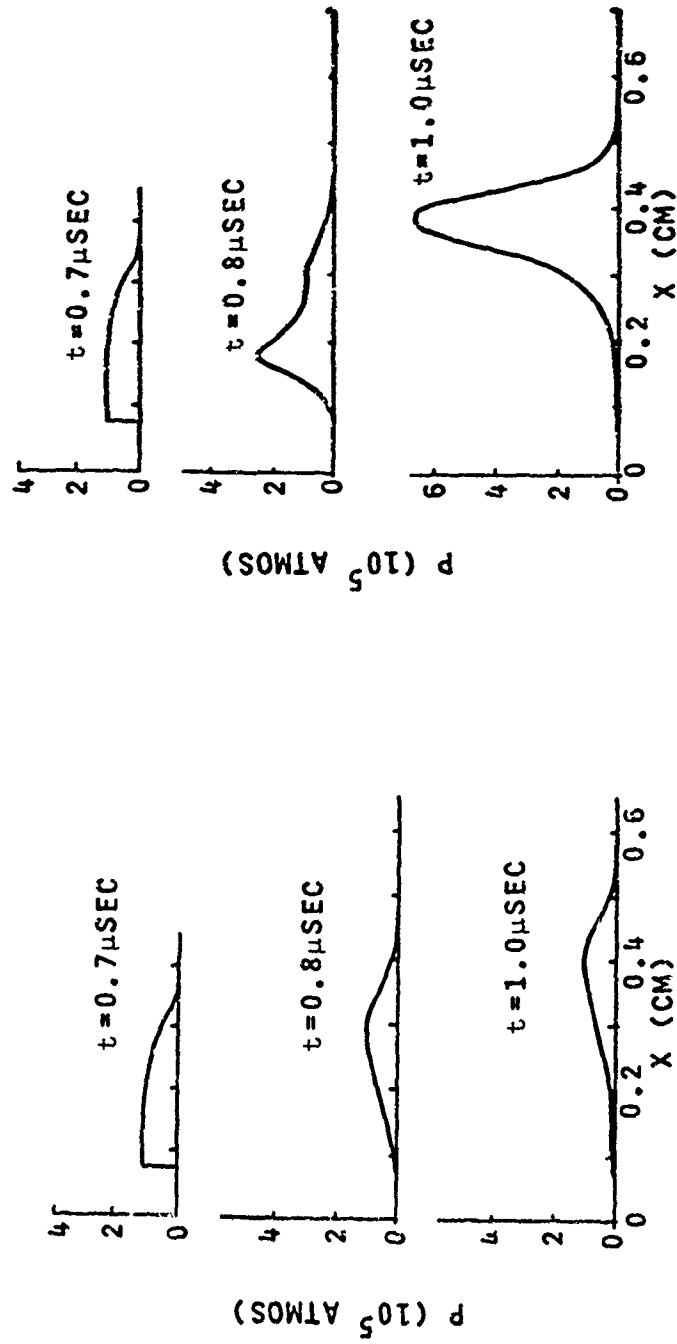
FIGURE 75

PRESSURE PROFILES IN A FICTICIOUS EXPLOSIVE AT SUCCESSIVE TIMES SHOWING

THE GROWTH TO DETONATION OR DECAY TO DEFLAGRATION AFTER SHOCK LOADING

(FROM REF 86)
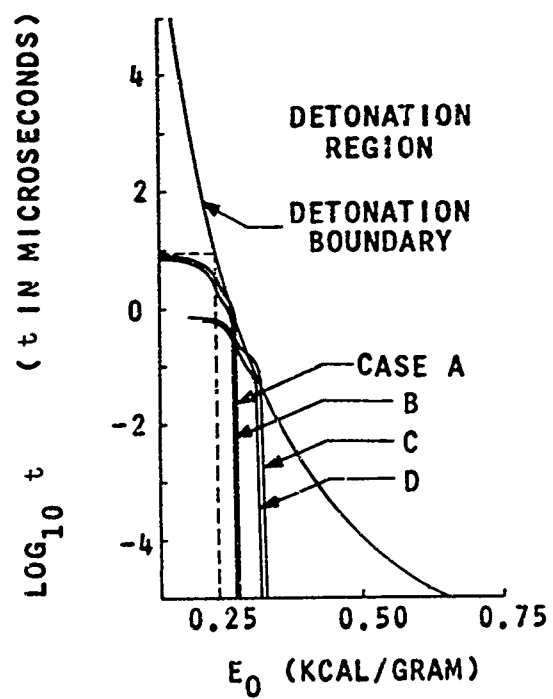
FIGURE 76

DETONATION - FAILURE DIAGRAM

FOR A FICTICIOUS EXPLOSIVE

(REF 86)
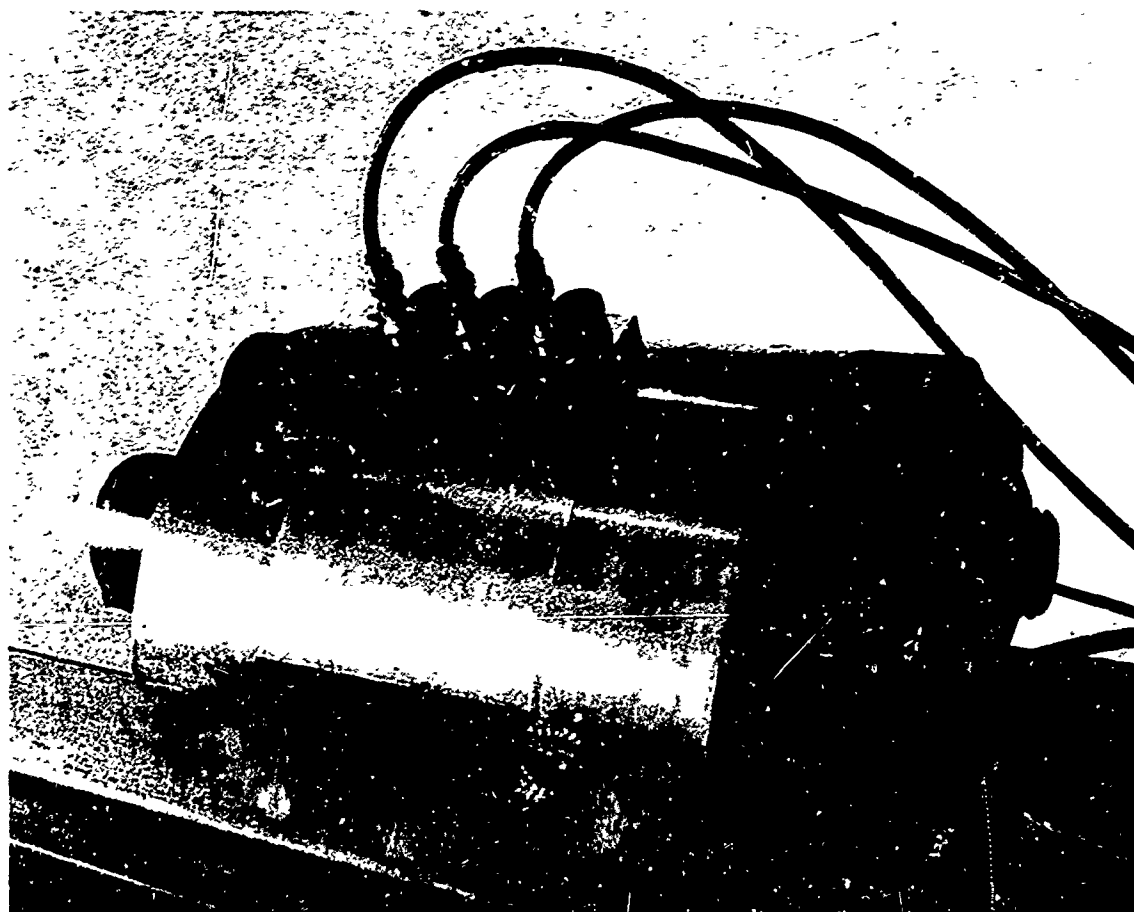
FIGURE 77

VIEW OF THE ONE-DIMENSIONAL CHAMBER USED FOR THE INVESTIGATION
OF THE INITIATION OF EXPLOSIVES BY GASEOUS DETONATION WAVES

IONIZATION PROBE LOCATIONS

WITNESS CUP

EXPLOSIVE

IGNITION CABLE CONNECTOR

EXPLODING WIRE

0   5   10
      CM
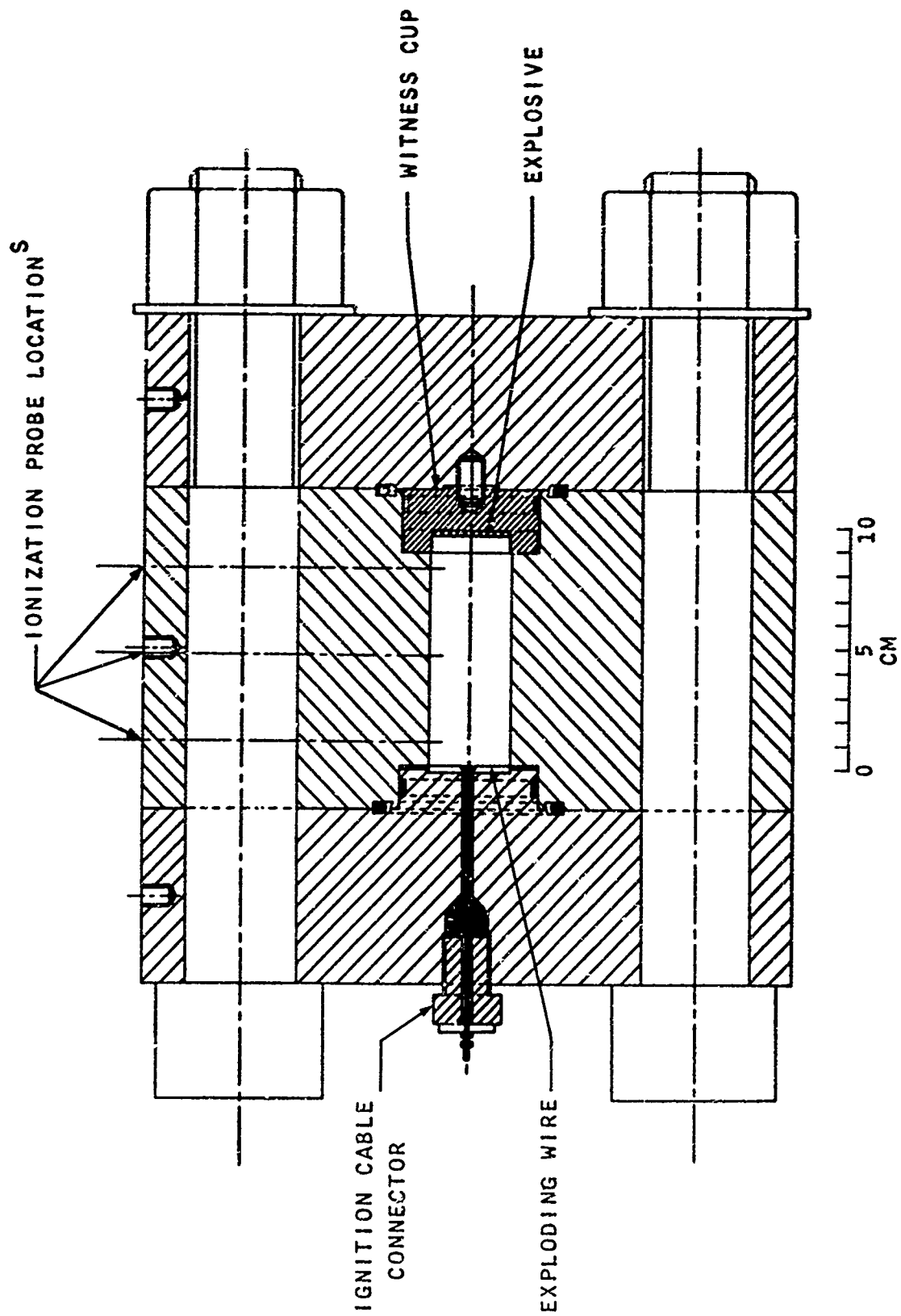
FIGURE 78   SECTION OF THE ONE-DIMENSIONAL CHAMBER

FIGURE 79 VIEW OF THE ASSEMBLED IONIZATION PROBE FOR WAVE-SPEED

MEASUREMENTS IN THE ONE-DIMENSIONAL CHAMBER

STANDARD BNC CONNECTOR

MOUNTING PLATE

HIGH STRENGTH STEEL CASE

EPOXY RESIN FILLED

ELECTRICAL LEAD

O-RING GROOVES

EPOXY SEAL

INSULATOR

STAINLESS STEEL TIP
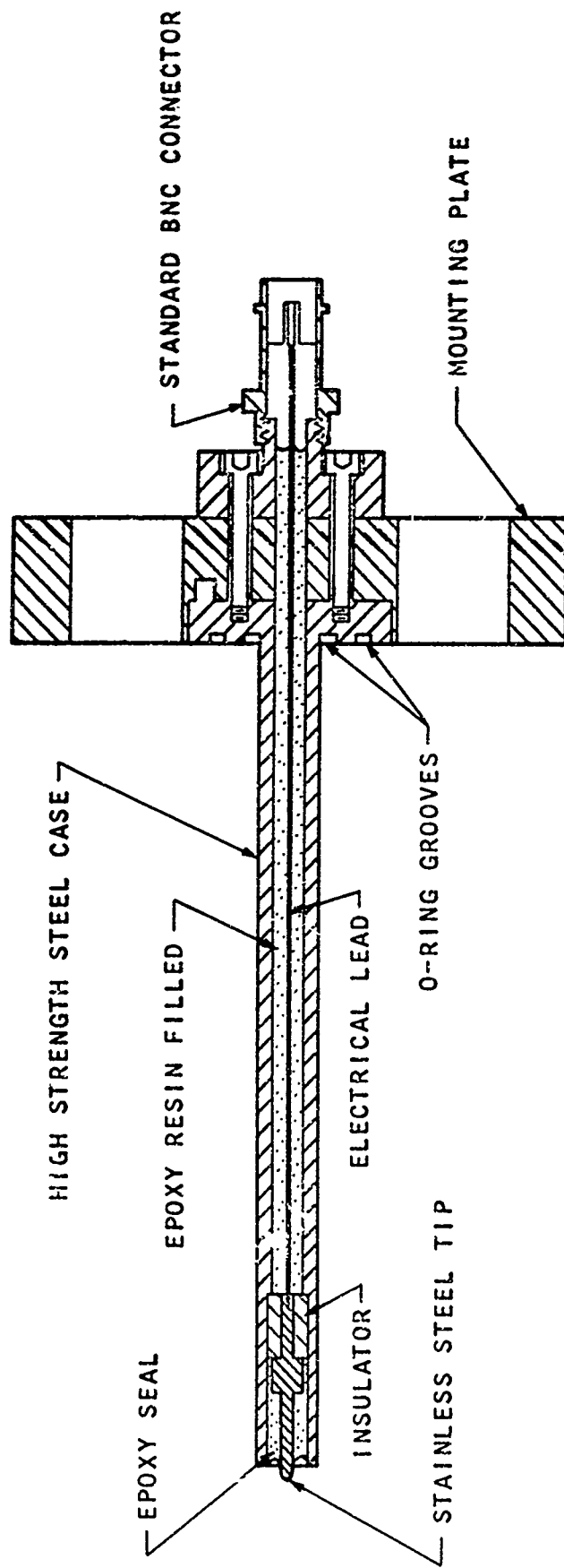
FIGURE 80   SECTION OF THE IONIZATION PROBE

-300 VDC

2.2 MEG   2.2 MEG   2.2 MEG

.001 MFD   .001 MFD   .001 MFD

30K   TO SCOPE

1N34   1N34   1N34
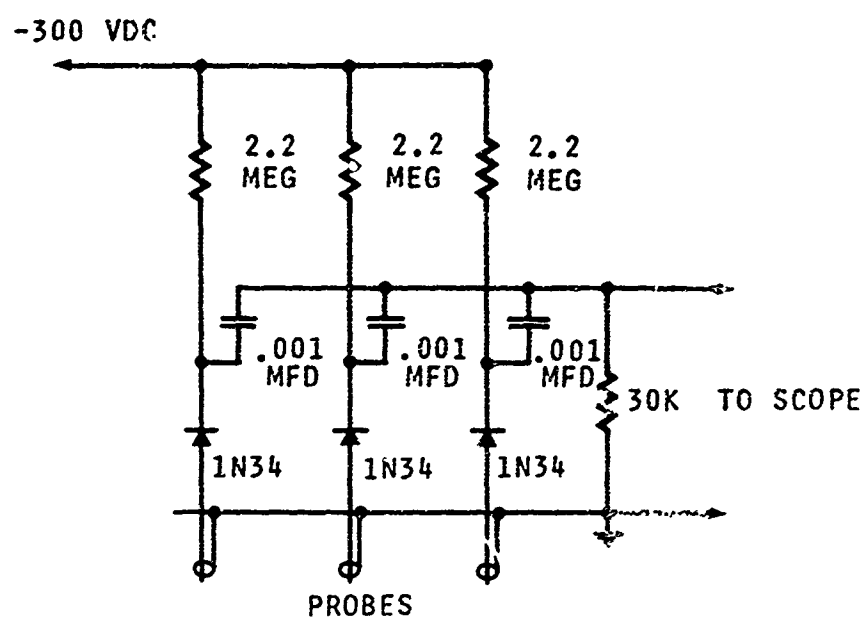
PROBES

A. CLASSICAL IONIZATION PROBE CIRCUIT
KNIGHT AND DUFF (REF 91)

-300 VDC

4.7K   4.7K   4.7K

1N39A   1N39A   1N39A

.001 MFD   .001 MFD   .001 MFD

200   TO   SCOPE

1N39A   1N39A   1N39A
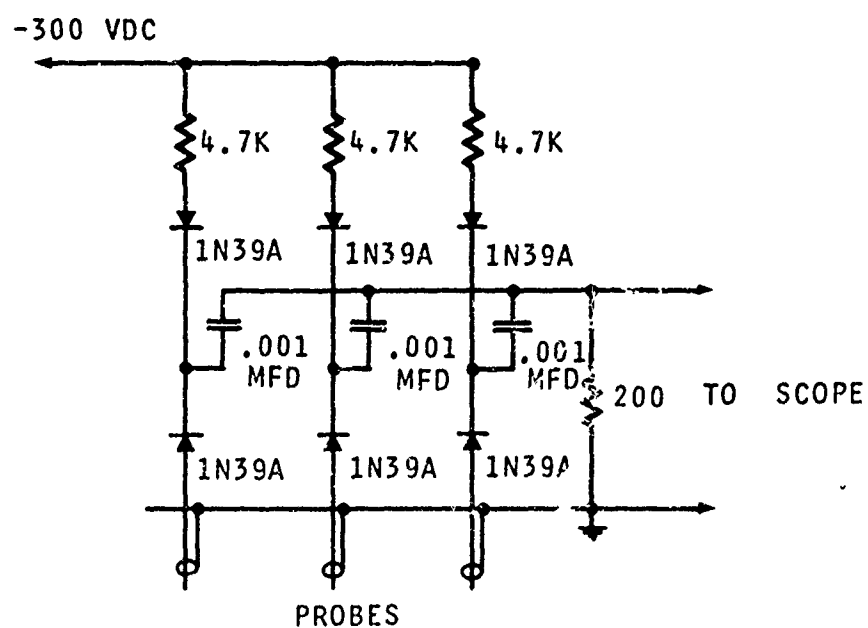
PROBES

B. IONIZATION PROBE CIRCUIT AS MODIFIED
TO DETECT REFLECTED WAVES

FIGURE   81   IONIZATION PROBE CIRCUITS
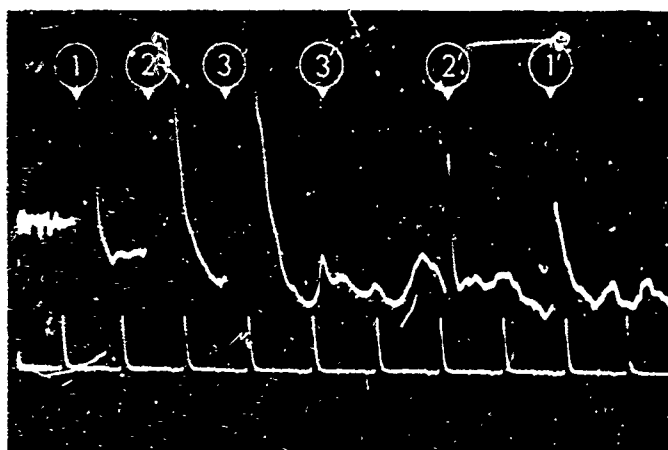
A. RESULT FROM A DEFLAGRATING RUN

P_1 = 200.5 PSIA $2H_2+O_2$

EXPLOSIVE = 1.3 GRAMS OF PETN
'CLOTH'
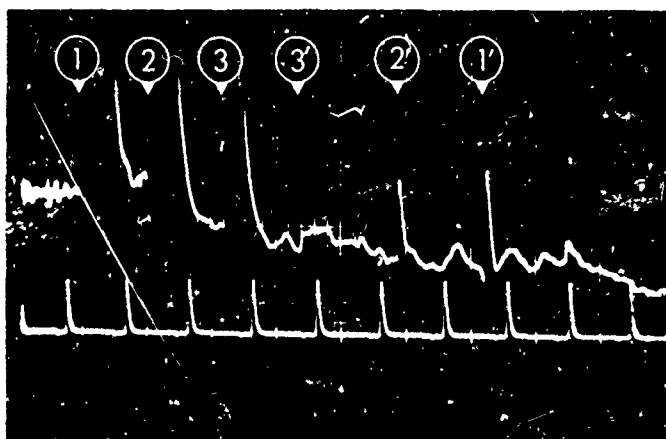
B. RESULT FROM A PARTIAL DETONATING RUN

P_1 = 201.0 PSIA $2H_2+O_2$

EXPLOSIVE PACKAGE = 1.3 GRAMS PETN 'CLOTH'
WITH A 0.4 GRAM PETN TOP LAYER
(ONLY THE TOP LAYER DETONATED)

FIGURE 82
TYPICAL OSCILLOGRAPH RECORDS OF WAVE-SPEED MEASUREMENTS IN
THE ONE-DIMENSIONAL CHAMBER OBTAINED USING THE MODIFIED CIRCUIT

TIME CALIBRATION
10 MICROSECONDS PER DIVISION

FIGURE 83

WAVE FRONT DIAGRAMS FOR $2H_2+O_2$
IN THE ONE-DIMENSIONAL CHAMBER FOR
SEVERAL VALUES OF INITIAL PRESSURE

$\overleftarrow{S}$

$\text{SLOPE}^{-1} =$
1.79 KM/SEC

SYMBOL	RUN NUMBER	INITIAL PRESSURE
□	42	270 PSIA
△	40	180 PSIA
○	32	90 PSIA

$\overrightarrow{D}$

TIME FROM REFLECTION t (MICROSECONDS)

DISTANCE x (CENTIMETERS)

FIGURE 84
WAVE FRONT DIAGRAMS FOR LEAD AZIDE
IN THE ONE-DIMENSIONAL CHAMBER FOR
SEVERAL VALUES OF INITIAL PRESSURE

FIGURE 85

WAVE DIAGRAMS FOR PETN PRESSINGS
IN THE ONE-DIMENSIONAL CHAMBER FOR
SEVERAL VALUES OF INITIAL PRESSURE

W = 4.229 GRAMS
DENSITY = 1.0 G/CC

REFLECTED SHOCK
TRAJECTORY FOR
NO EXPLOSIVE

SYMBOL	RUN NUMBER	INITIAL PRESSURE	$E_\square/P_1$
$\square$	18	160 PSIA	47.2
$\bigcirc$	43	180 PSIA	42.0
$\triangle$	38	270 PSIA	24.0

FIGURE 86

WAVE FRONT DIAGRAMS FOR NITROCELLULOSE
IN THE ONE-DIMENSIONAL CHAMBER FOR
SEVERAL VALUES OF INITIAL PRESSURE

FIGURE 87
WAVE FRONT DIAGRAMS FOR SUPERFINE PETN
IN THE ONE-DIMENSIONAL CHAMBER FOR
SEVERAL VALUES OF INITIAL PRESSURE

FIGURE 88

INCIDENT AND REFLECTED WAVE
VELOCITIES VERSUS DISTANCE

FIGURE 89

OVERDRIVING INCREMENT VERSUS DISTANCE
FOR DETONATION WAVES IN STOICHIOMETRIC
OXYGEN - HYDROGEN (REF 94)

FIGURE 90

STOICHIOMETRIC OXYGEN – HYDROGEN DETONATION
WAVE VELOCITY VERSUS INITIAL PRESSURE
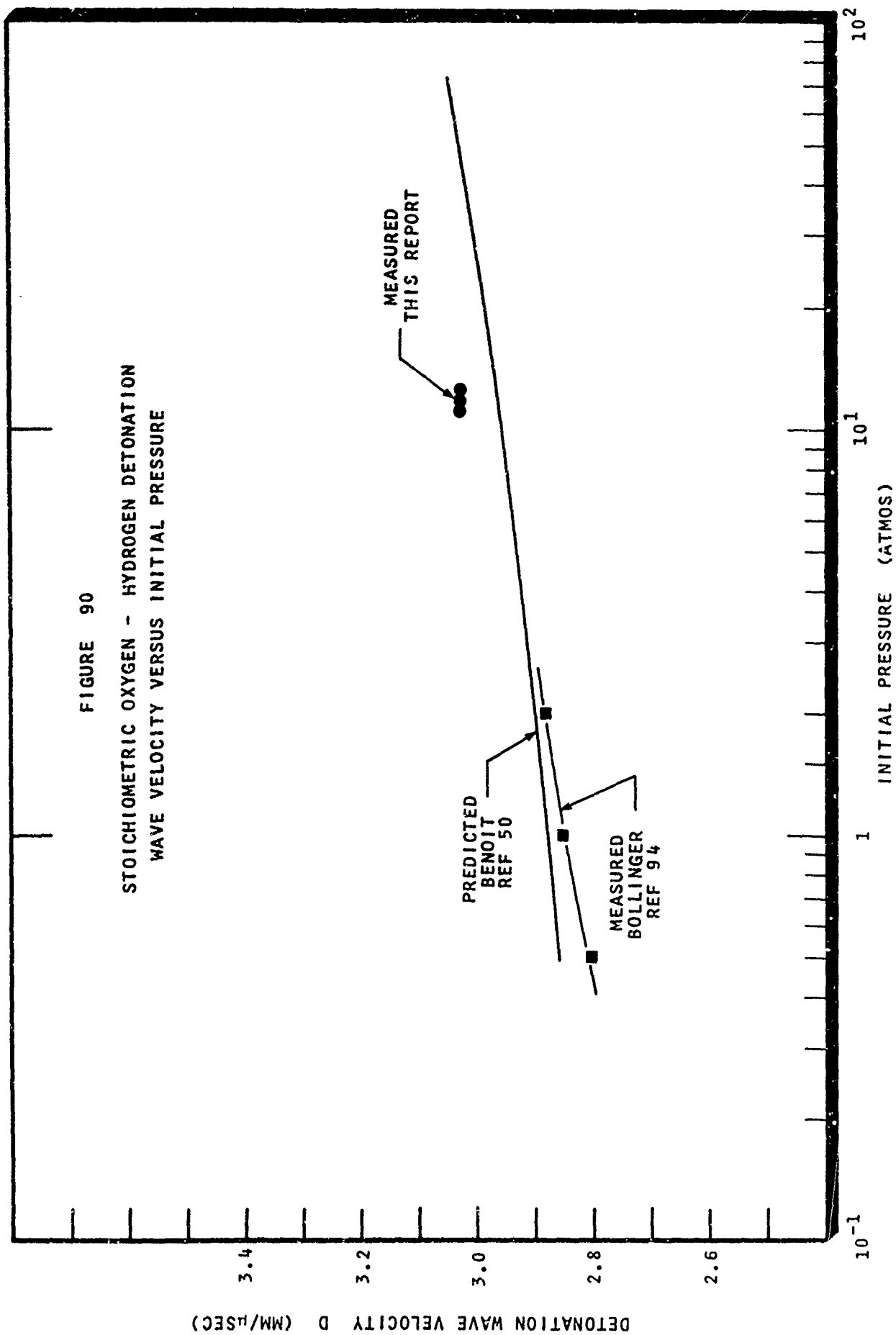
FIGURE 91

DETONATION, DEFLAGRATION AND NO COMBUSTION REGIONS OF SOME EXPLOSIVES USING
STOICHIOMETRIC OXYGEN – HYDROGEN DETONATION WAVES FOR INITIATION

FIGURE 92

DEPTH OF INITIATION VERSUS
SHOCK PRESSURE FOR PETN (REF 96)

FIGURE 93

INITIAL REFLECTED WAVE VELOCITY VERSUS $E_\square/P_1$ FOR VARIOUS DETONATING EXPLOSIVES INITIATED BY A DETONATION WAVE IN $2H_2 + O_2$

FIGURE 94

AVERAGE REFLECTED WAVE VELOCITY BETWEEN STATIONS 1 AND 2 VERSUS $E_\square/P_i$ FOR SEVERAL DETONATING EXPLOSIVES INITIATED BY A DETONATION WAVE IN $2H_2+O_2$

CH₃OH OMITTED
CH₂C₂ INCLUDED
IN PRODUCTS

BOTH INCLUDED

CH₃OH INCLUDED
CH₂O₂ OMITTED
IN PRODUCTS

O   EXPERIMENT ORNELLAS ET AL[101]

▲■● CALCULATED COOK[72]

FIGURE 95

HEAT OF DETONATION VERSUS DENSITY
FOR PETN

DENSITY ρ (GRAMS/CUBIC CENTIMETER)

HEAT OF DETONATION Q (KILOCALORIES/GRAM)

FIGURE 96

MEASURED DELAY TIMES FOR INITIATION OF
DETONATION VERSUS INITIAL PRESSURE
OF $2H_2+O_2$

SYMBOL	EXPLOSIVE
□	NITROCELLULOSE
◇	LEAD AZIDE
△	TETRAZENE
●	SUPERFINE PETN
○	PETN $\rho=1.0$ G/CC
▽	PETN $\rho=0.87$ G/CC
■	PETN PASTE/PETN (SF)

DELAY TIME (MICROSECONDS)

INITIAL PRESSURE (ATMOSPHERES)
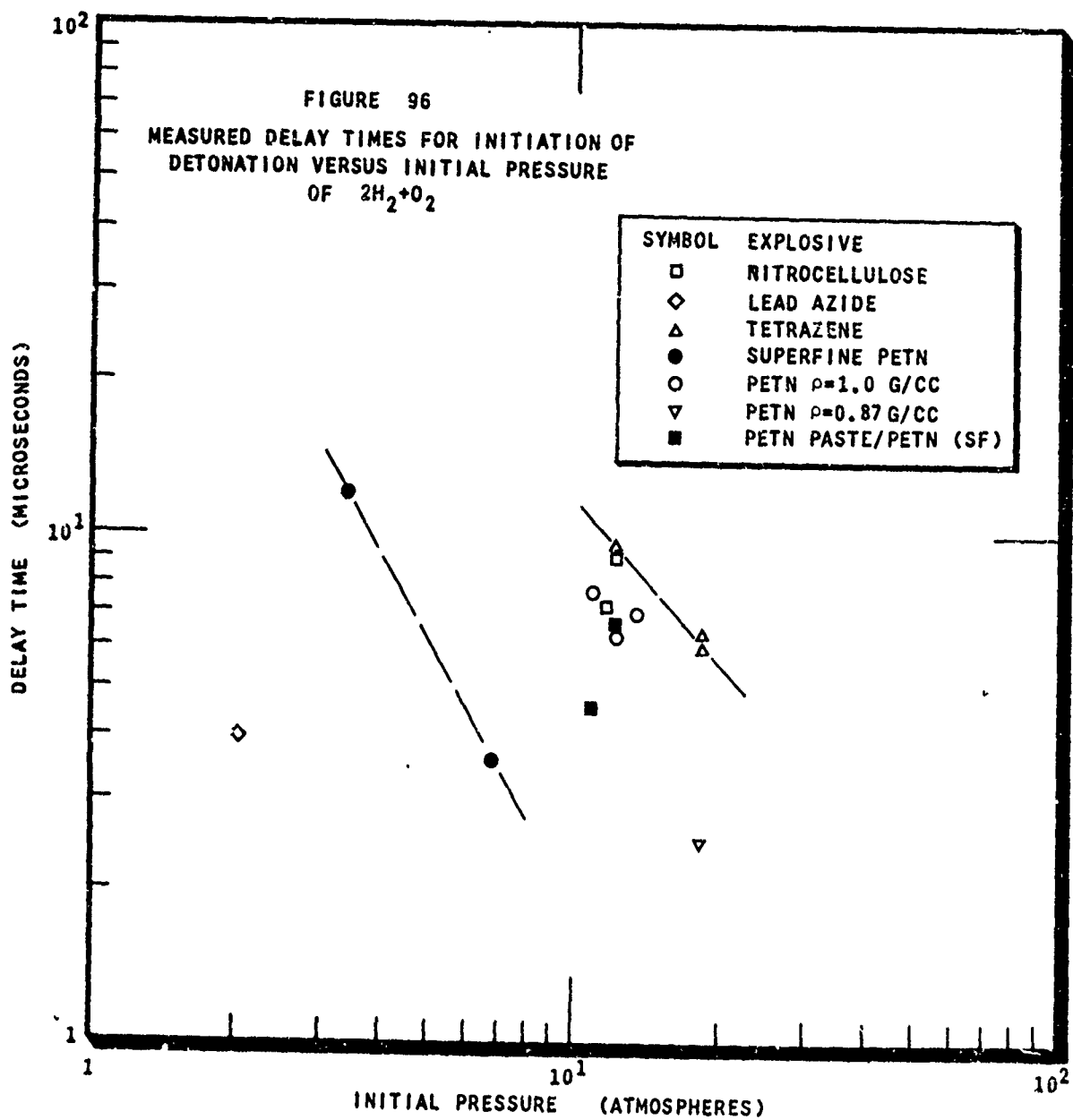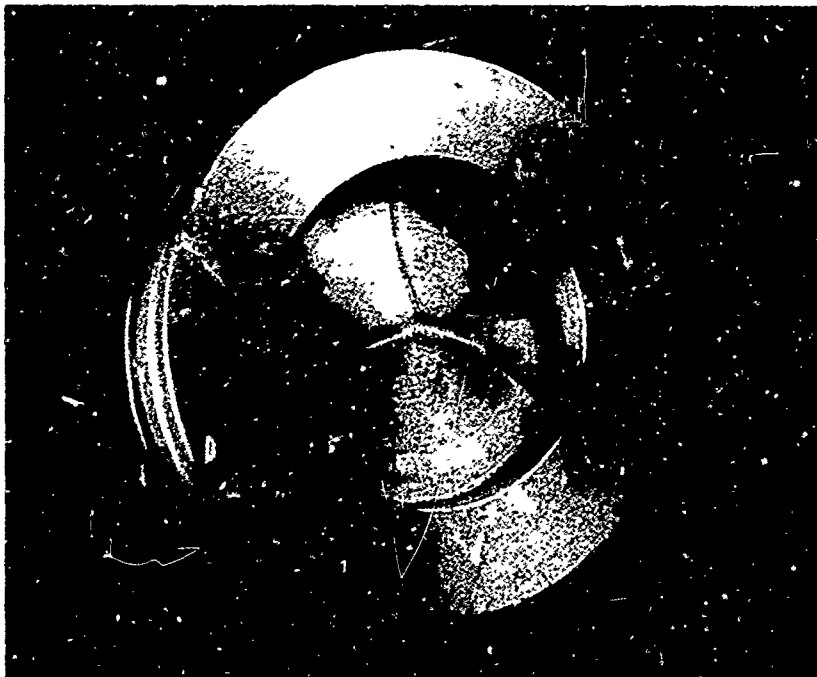
A. MARKINGS LEFT BY DETONATING PETN PRESSINGS AT AN
INITIAL GAS PRESSURE OF 160 PSIA OF $2H_2+O_2$. GROOVES
ARE THOUGHT TO BE LOCI OF COLLIDING DETONATION WAVES
IN THE EXPLOSIVE.
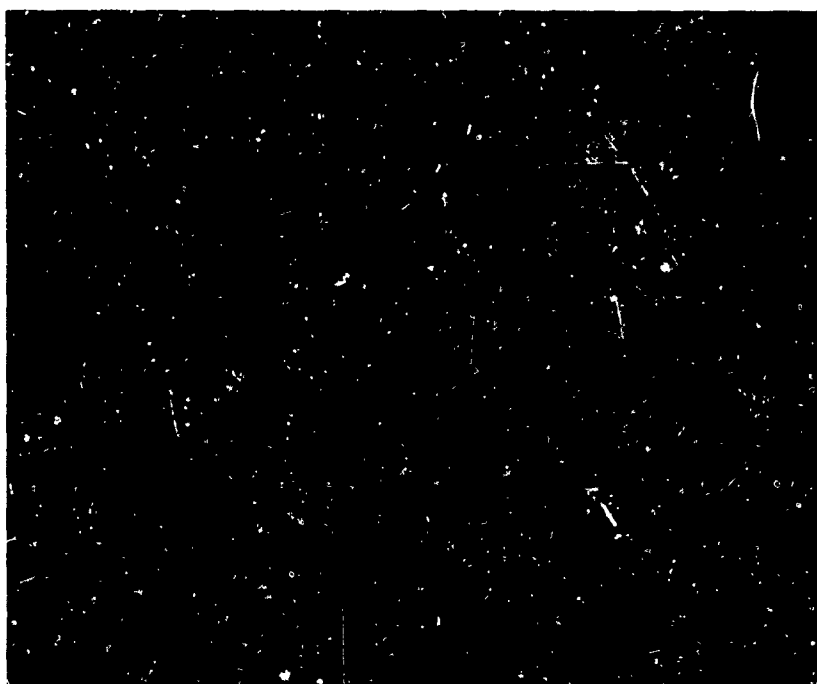
B. MARKINGS LEFT BY DETONATING SUPERFINE PETN AT AN
INITIAL GAS PRESSURE OF 50 PSIA OF $2H_2 + O_2$. HOMOGENEOUS
CHARACTER OF DAMAGE INDICATES NEARLY SIMULTANEOUS
INITIATION OF THE EXPLOSIVE.

FIGURE   97
MARKINGS LEFT ON WITNESS CUPS BY DETONATING EXPLOSIVES

FIGURE 98

DETONATION PRESSURE VERSUS PACKING DENSITY
FOR SEVERAL EXPLOSIVES (REF 71)
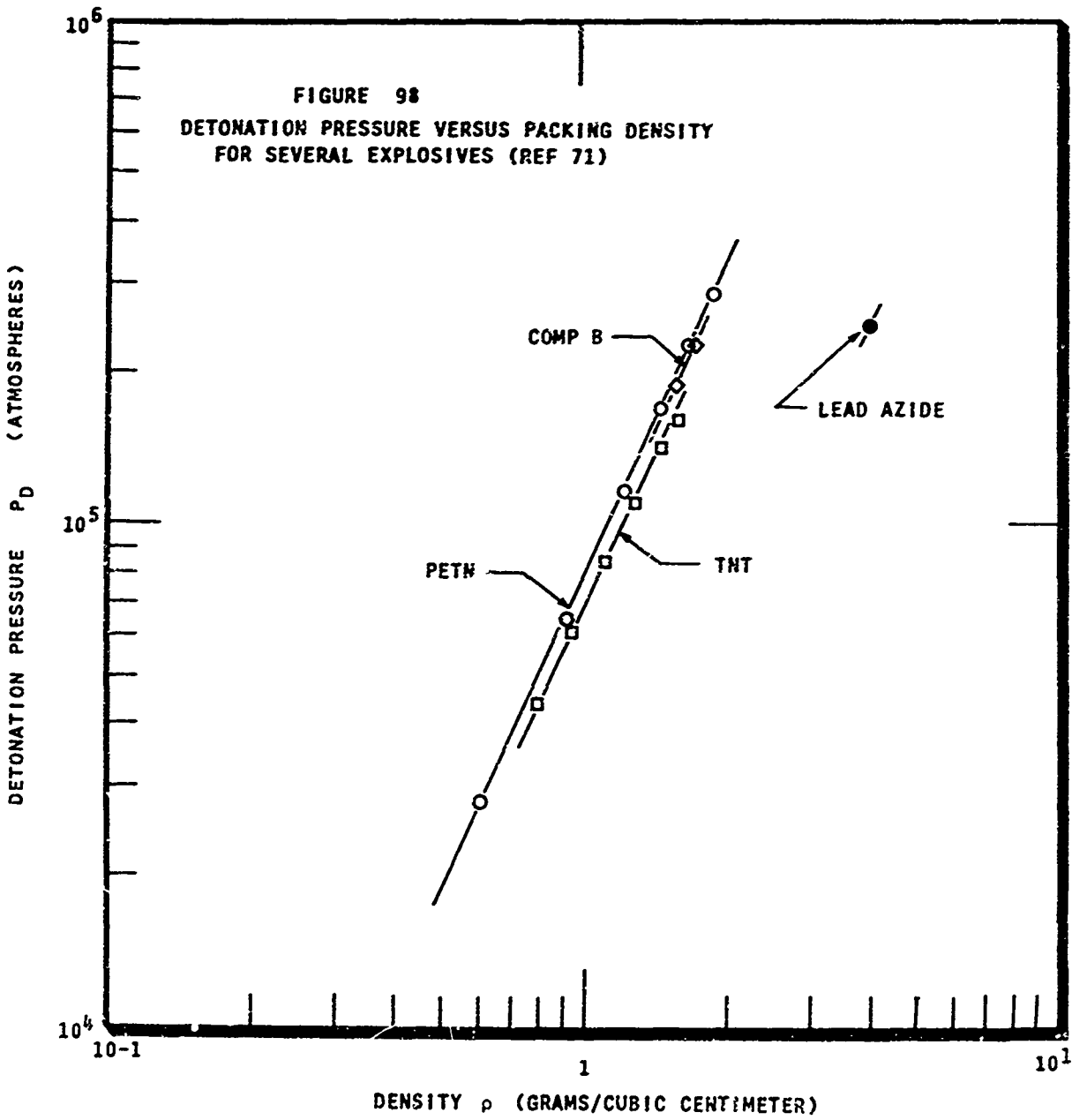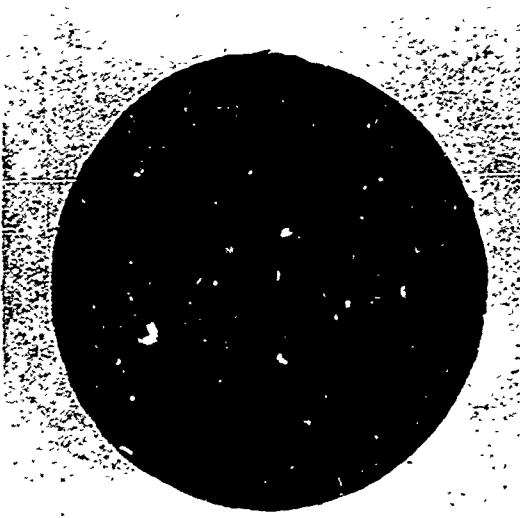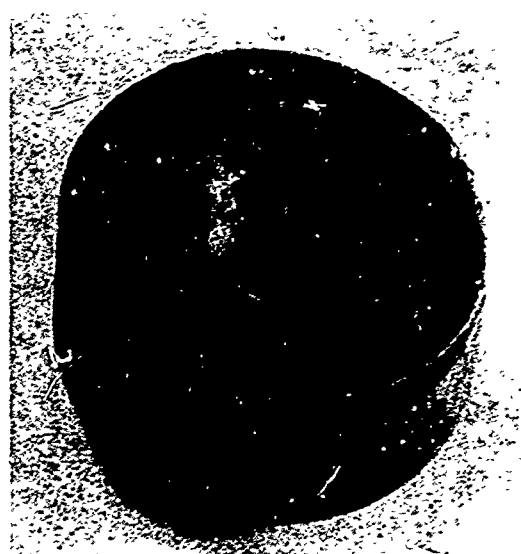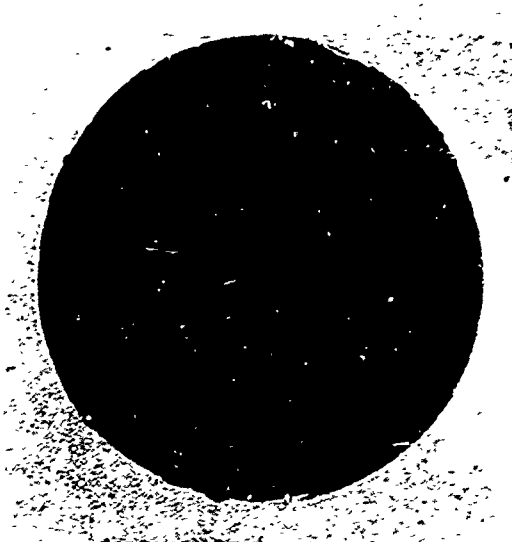
FIGURE 99 IMPRINTS LEFT IN COPPER WITNESS BLOCKS OF IMPLOSION RUNS.

ABOVE LEFT. IMPRINT LEFT BY 86.5 GRAM PETN - 200 PSIA STOICHIOMETRIC OXYGEN - HYDROGEN RUN. THE SUBSTANTIAL DEPRESSION IN THE CENTER IS CAUSED BY THE HIGH PRESSURES GENERATED BY THE IMPLOSION.

ABOVE. SIDE VIEW OF THE PETN RUN. THE ENTIRE WITNESS BLOCK HAS YIELDED.

LEFT. IMPRINT LEFT BY A 500 PSIA STOICHIOMETRIC OXYGEN - HYDROGEN RUN. THE DEPRESSION IN THE CENTER IS DUE TO THE FOCUSSED IMPLODING SHOCK WAVE.
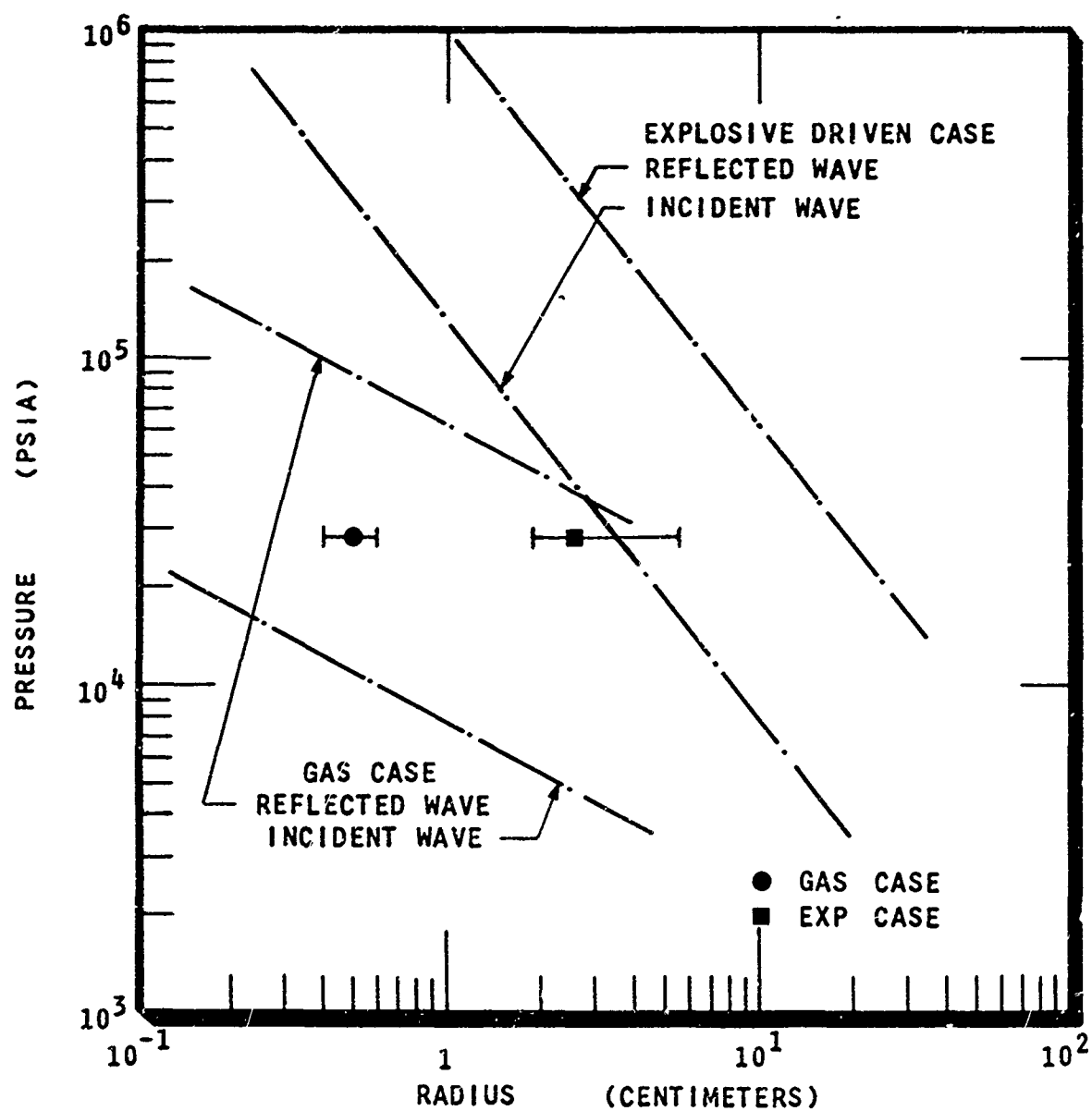
FIGURE 100

THEORETICAL PEAK PRESSURES VERSUS RADIUS FOR IMPLODING AND
REFLECTED WAVES USING THE IMPLOSION IN A SPHERE MODEL AND
THE EXTENT OF THE YIELDED REGIONS FROM THE COPPER WITNESS
BLOCKS
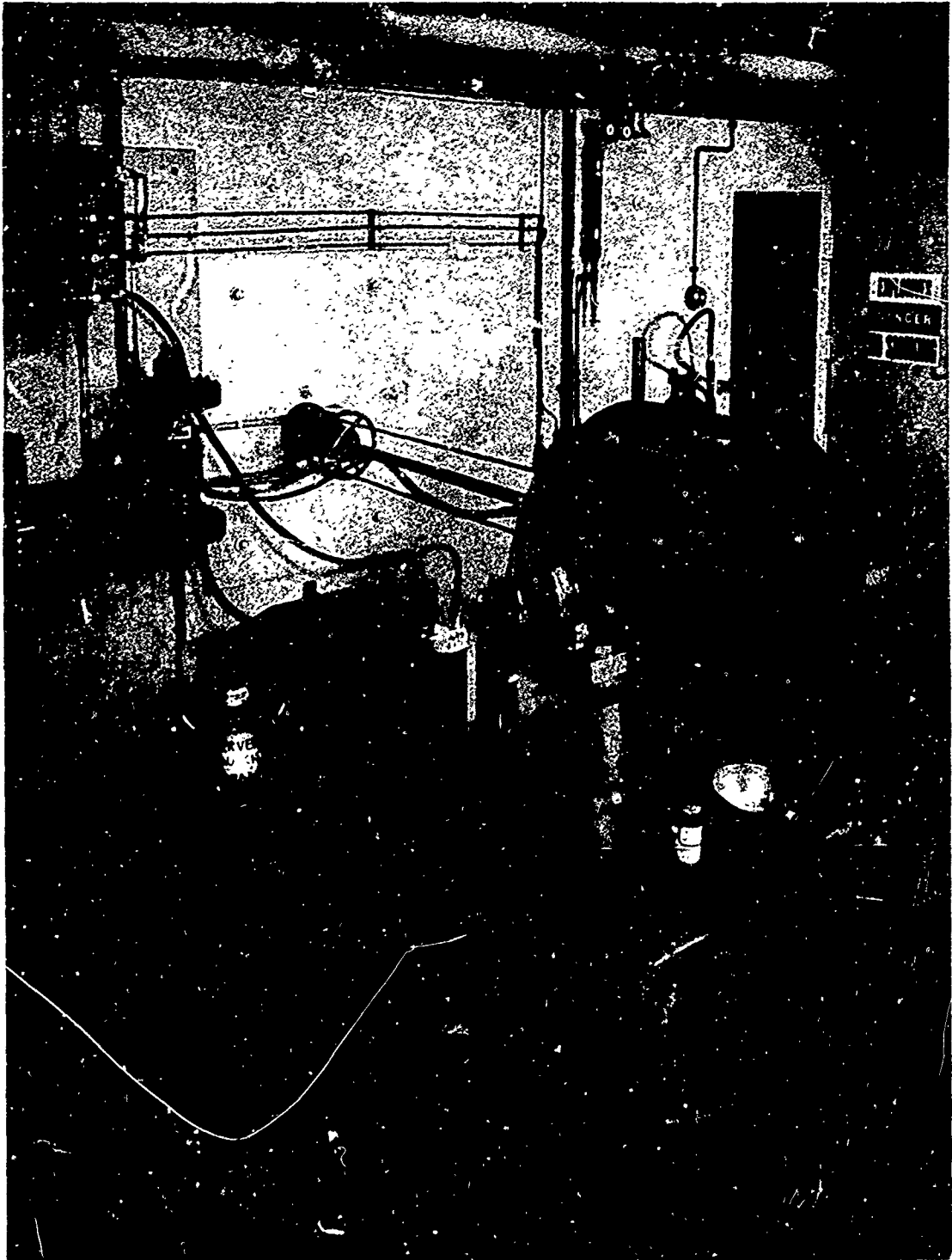
FIGURE 101
VIEW OF THE IMPLOSION DRIVEN LAUNCHER IN THE FIRING POSITION
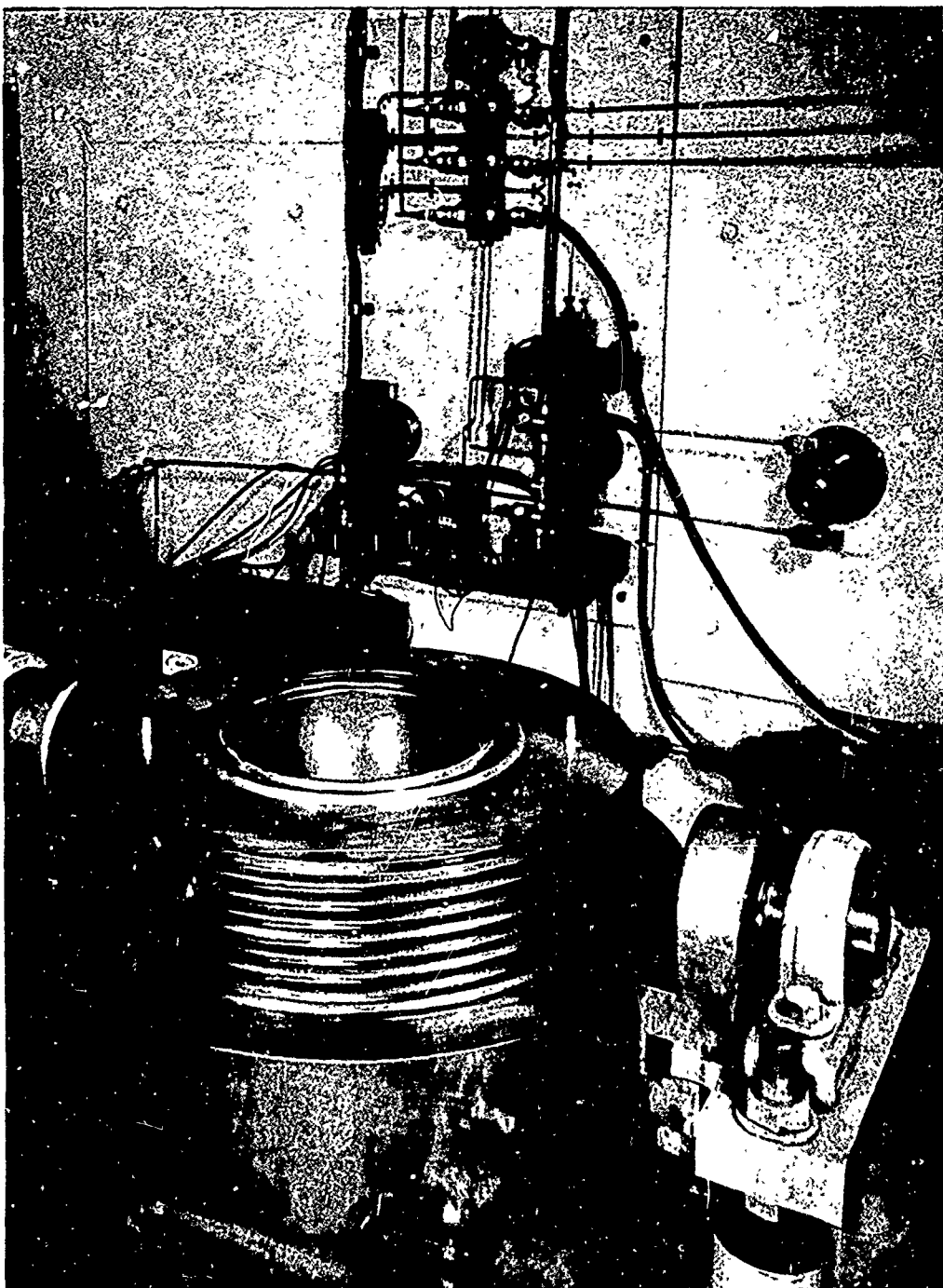
FIGURE 102

VIEW OF THE HEMISPHERICAL CHAMBER IN THE OPENED POSITION
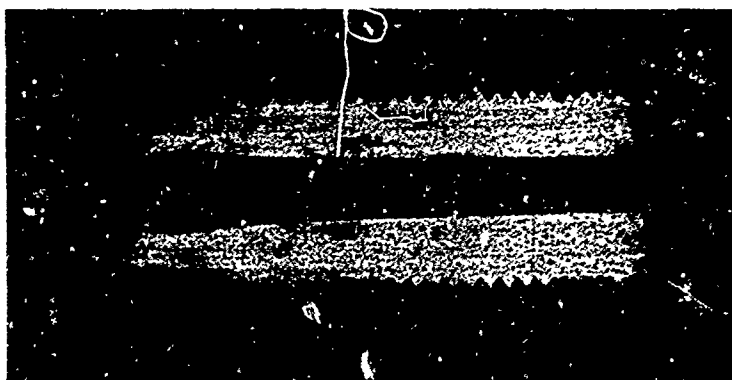
A. EROSION FROM SEVERAL CONSTANT VOLUME COMBUSTION RUNS
(V = 3000 - 5000 FT/SEC)

B. EROSION FROM A SINGLE GASEOUS DETONATION RUN USING 500
PSIA OF STOICHIOMETRIC OXYGEN - HYDROGEN (V = 7750 FT/SEC)

C. EROSION FROM A SINGLE EXPLOSIVE DRIVEN RUN USING 81 GRAMS
OF PETN (V = 17,650 FT/SEC)

FIGURE 103   EXAMPLES OF BARREL EROSION

MAXIMUM DEFLECTION

CASE   LOADING DIAGRAM   MAXIMUM STRESS

A UNIFORMLY DISTRIBUTED LOAD – FIXED EDGE

$$\sigma_{max} = \frac{0.5\, r^2 p}{t^2}$$

$$\delta = \frac{0.17\, r^4 p}{t^3\, E}$$

B UNIFORMLY DISTRIBUTED LOAD – FREELY SUPPORTED EDGE

$$\sigma_{max} = \frac{0.75\, r^2 p}{t^2}$$

$$\delta = \frac{0.60\, r^4 p}{t^3\, E}$$

C UNIFORMLY DISTRIBUTED LOCALIZED LOAD – FREELY SUPPORTED

$$\sigma_{max} = 4.5 \left(1 - \frac{2}{3}\frac{r_o}{r}\right)\frac{r_o^2 p}{t^2}$$

$$\delta = \frac{1.41\, r^2\, r_o\, p}{t^3\, E}$$

FIGURE 104   DEFLECTION AND STRESS RELATIONS FOR THIN CIRCULAR PLATES SUBJECTED TO VARIOUS EDGE CONSTRAINTS AND LOADINGS
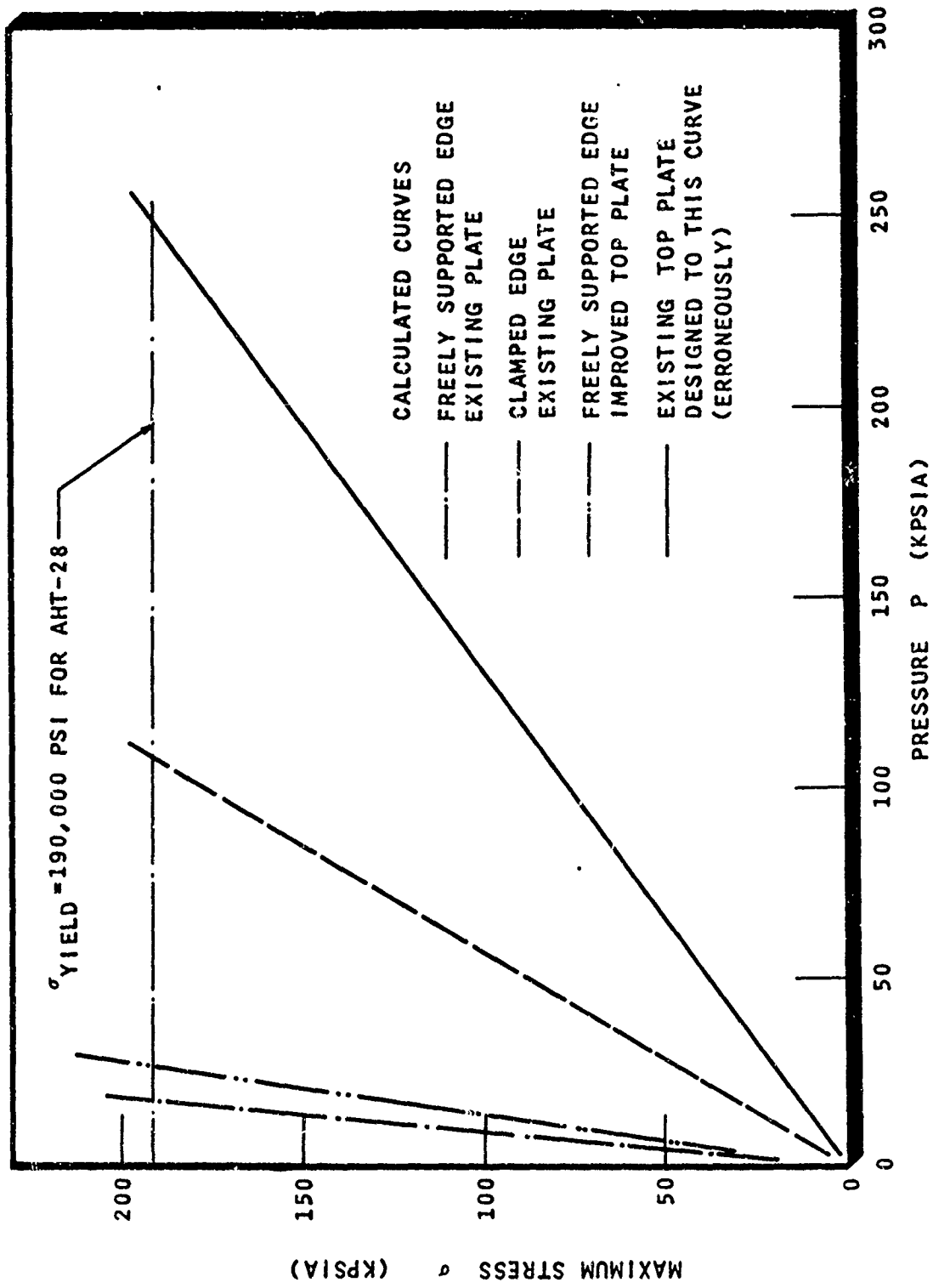
FIGURE 10°

MAXIMUM STRESS IN THE TOP PLATE VERSUS PRESSURE FOR SEVERAL EDGE CONSTRAINTS

FIGURE 106

MAXIMUM DEFLECTION AT THE CENTER
OF THE TOP PLATE VERSUS PRESSURE
FOR SEVERAL THEORETICAL MODFLS AND
MEASURED VALUES

EXISTING TOP PLATE
CALCULATED DEFLECTION
CLAMPED EDGE CASE
0.16 µIN/PSI

EXISTING TOP PLATE
MEASURED DEFLECTION
5.75 µIN/PSI

CALCULATED DEFLECTION
FREELY SUPPORTED EDGE
5.82 µIN/PSI

IMPROVED TOP PLATE
MEASURED DEFLECTION
2.93 µIN/PSI

FREELY SUPPORTED EDGE
3.00 µIN/PSI

PRESSURE P (KPSIA)

DEFLECTION AT CENTER δ (INCHES)

A ORIGINAL TOP PLATE DESIGN
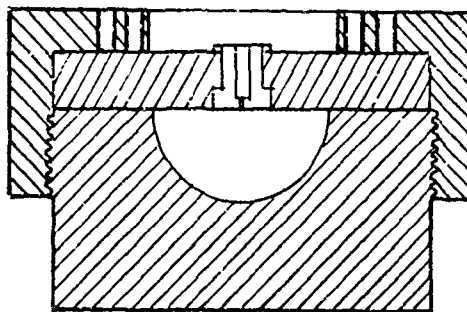
B EXISTING TOP PLATE DESIGN AS MODIFIED
BY THE ADDITION OF 24 SET SCREWS
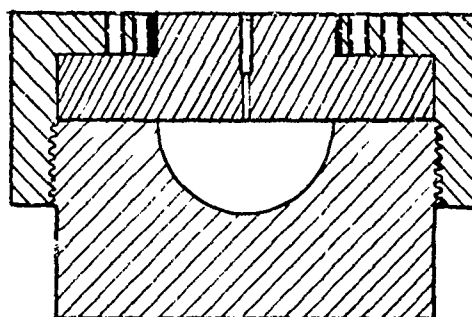
C IMPROVED TOP PLATE USING EXISTING NUT
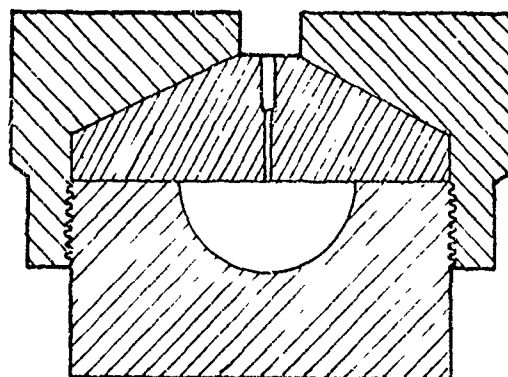
D PROPOSED HIGH PRESSURE TOP PLATE
DESIGN PRESSURE LIMIT 100,000 PSIA

FIGURE   107 TOP PLATES USED IN THIS STUDY
AND THE PROPOSED HIGH PRESSURE TOP PLATE
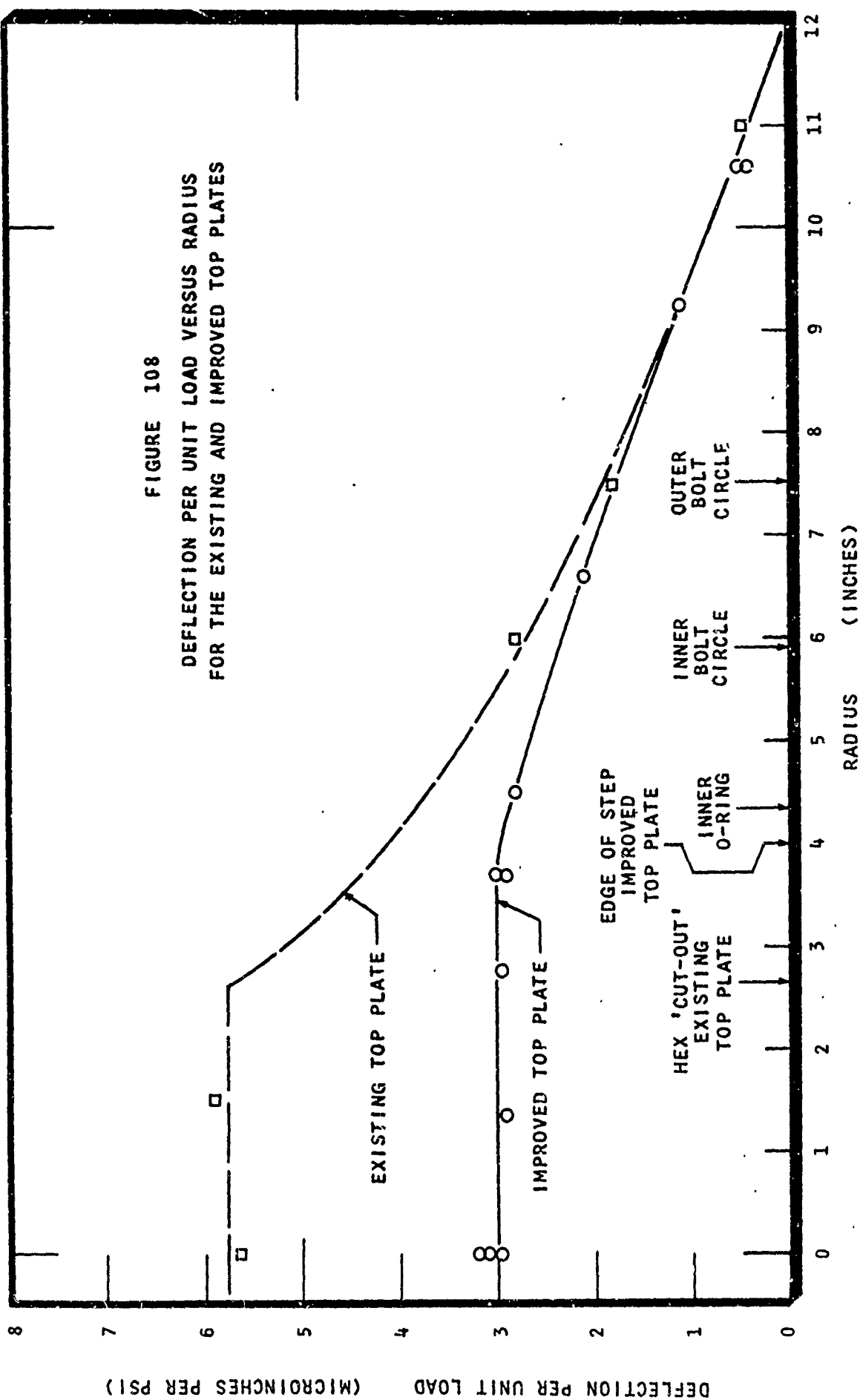
FIGURE 108

DEFLECTION PER UNIT LOAD VERSUS RADIUS
FOR THE EXISTING AND IMPROVED TOP PLATES
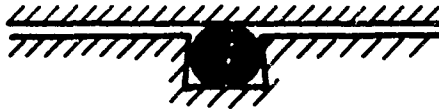
A ORIGINAL O-RING DESIGN.NO LOAD CONDITION
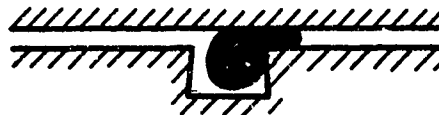
B ORIGINAL O-RING DESIGN . LOADED CONDITION
(EXTRUDES AND FAILS)

C PRESENT O-RING DESIGN . NO LOAD CONDITION
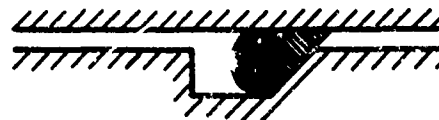
D PRESENT O-RING DESIGN.LOADED CONDITION
BACK-UP RING PREVENTS EXTRUSION

FIGURE 109
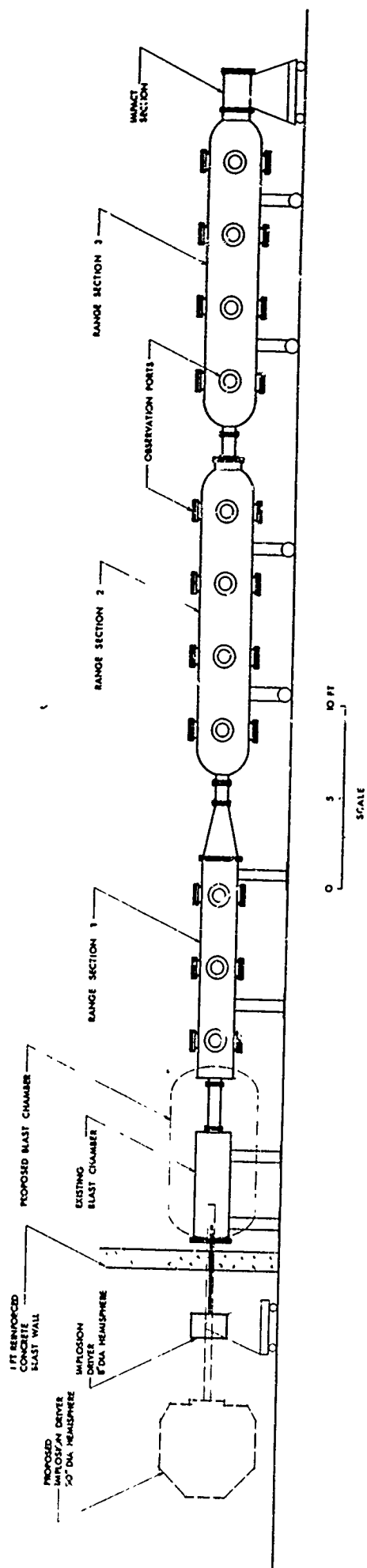O-RING EXTRUSION CHARACTERISTICS AND
AN EXTRUSION RESISTANT DESIGN
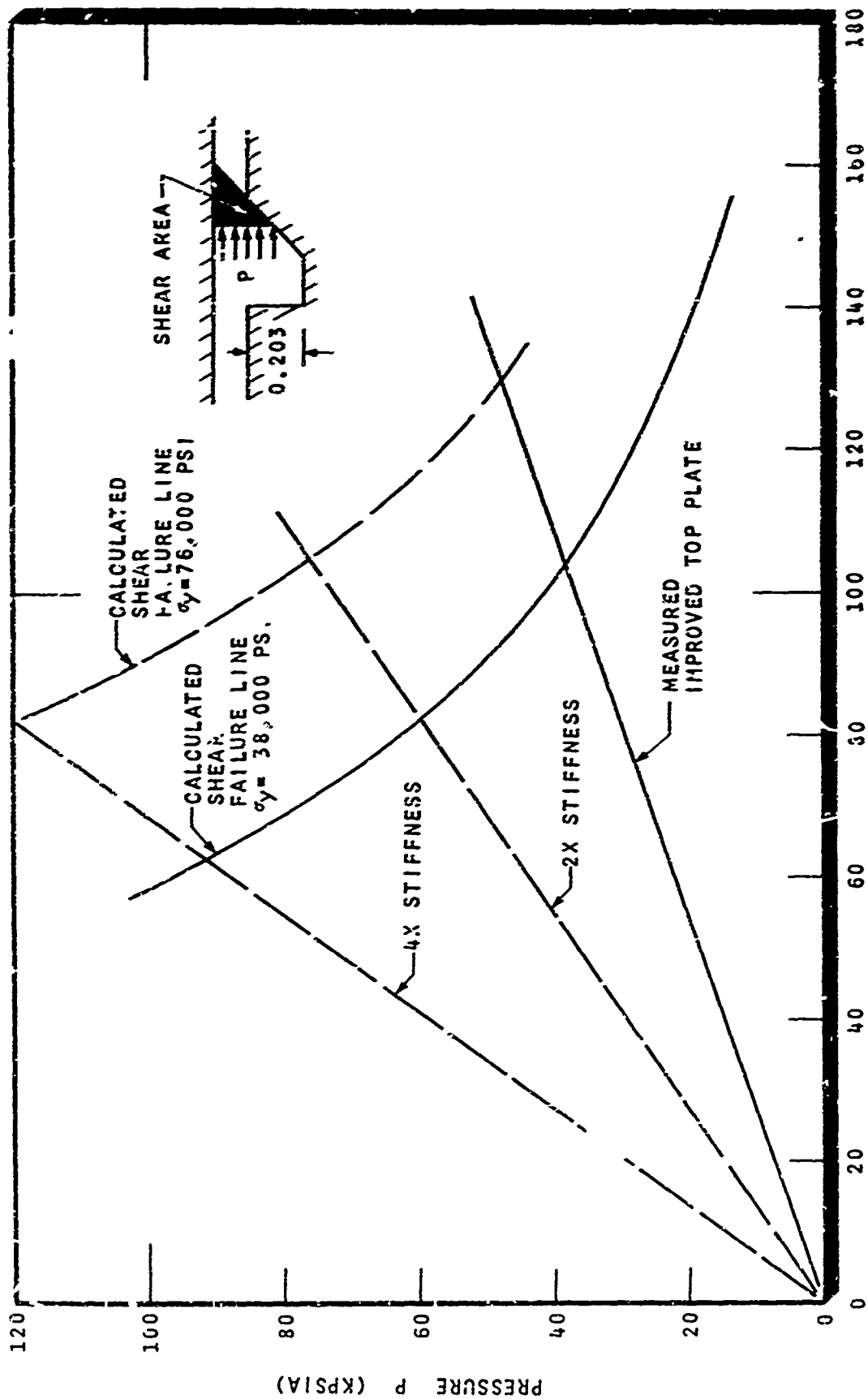
FIGURE 110 PRESSURE - DEFLECTION PLOT FOR IMPROVED TOP PLATE THE AND CALCULATED BACK-UP RING FAILURE LINES

FIGURE 111

DEFLECTION - LOAD CURVES FOR SEVERAL STATIONS
FOR THE IMPROVED TOP PLATE

R = 0.00 INCHES

R = 3.70 INCHES

R = 6.60 INCHES

DEFLECTION δ (0.001 INCHES)

PRESSURE P (KPSIA)

FIGURE 112

VARIATION OF THE SPHERICAL PLASTIC WAVE DEPTH
WITH PEAK PRESSURE RATIO AND β

$\beta = 0.151 \, \alpha n R_o / C_e$
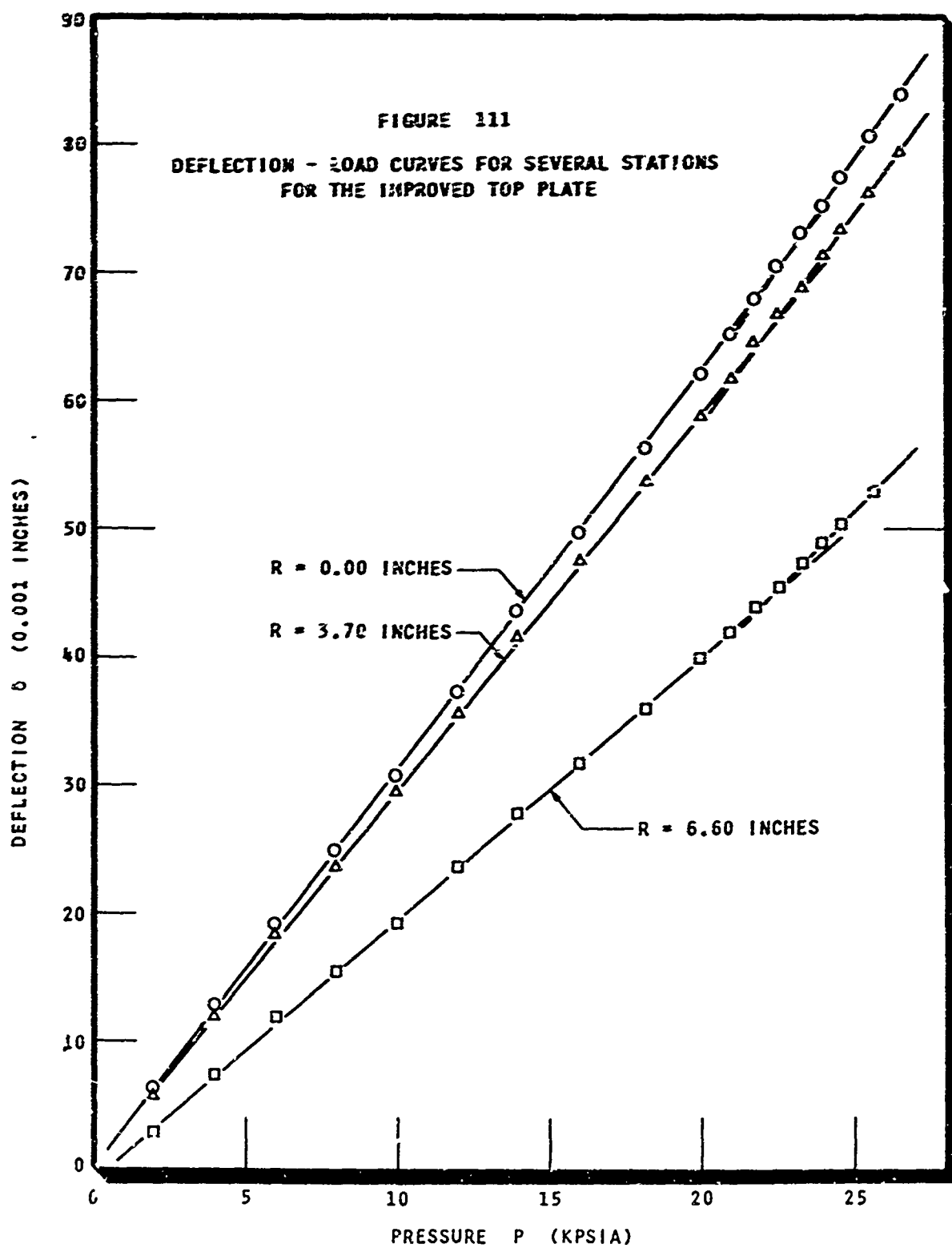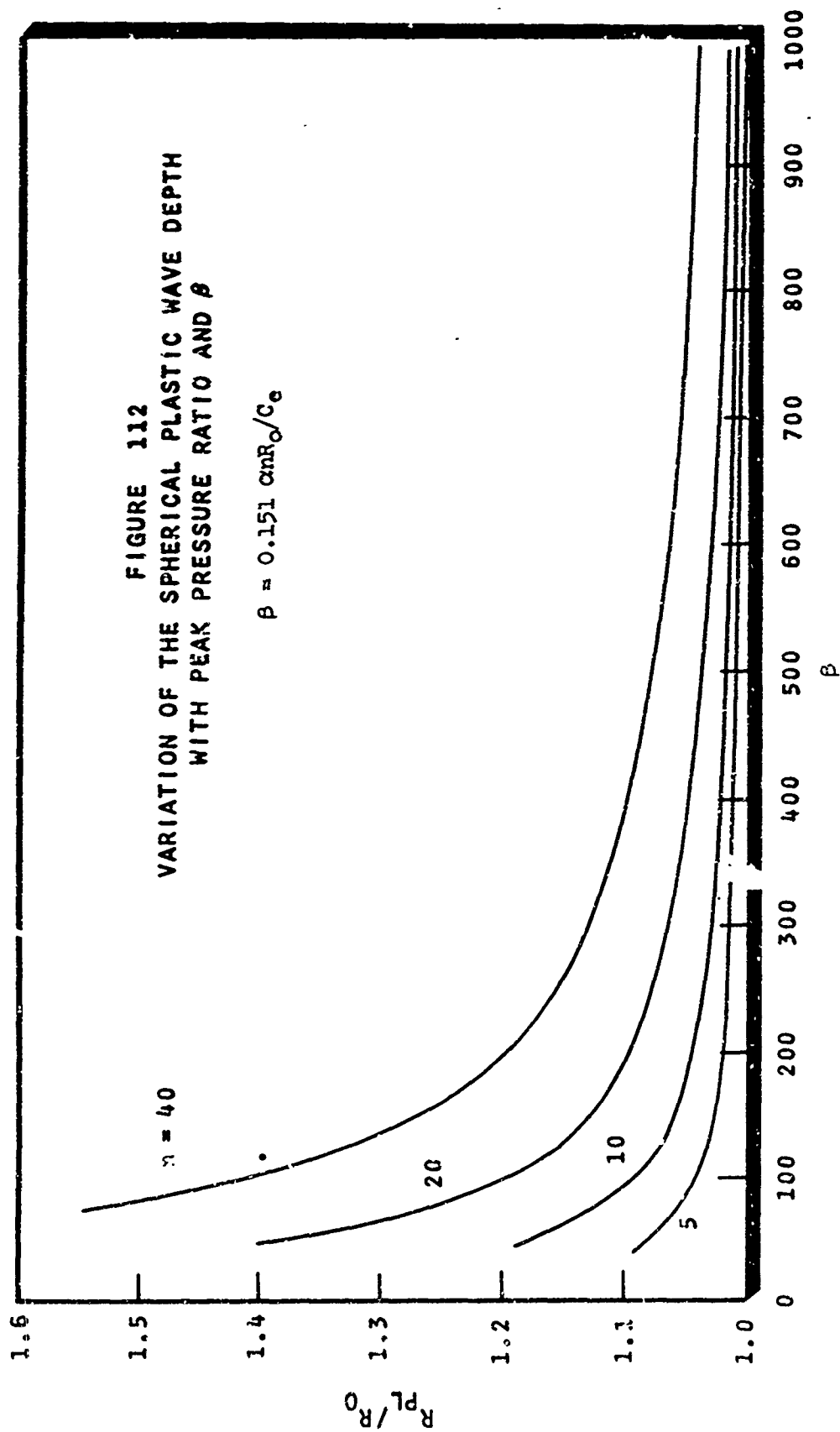
FIGURE 113

UTIAS   IMPLOSION   DRIVEN   HYPERVELOCITY   LAUNCHER   FACILITY

FIGURE   114

VIEW OF THE RAIGE SHOWING RANGE SECTION 1 AND THE BLAST CHAMBER
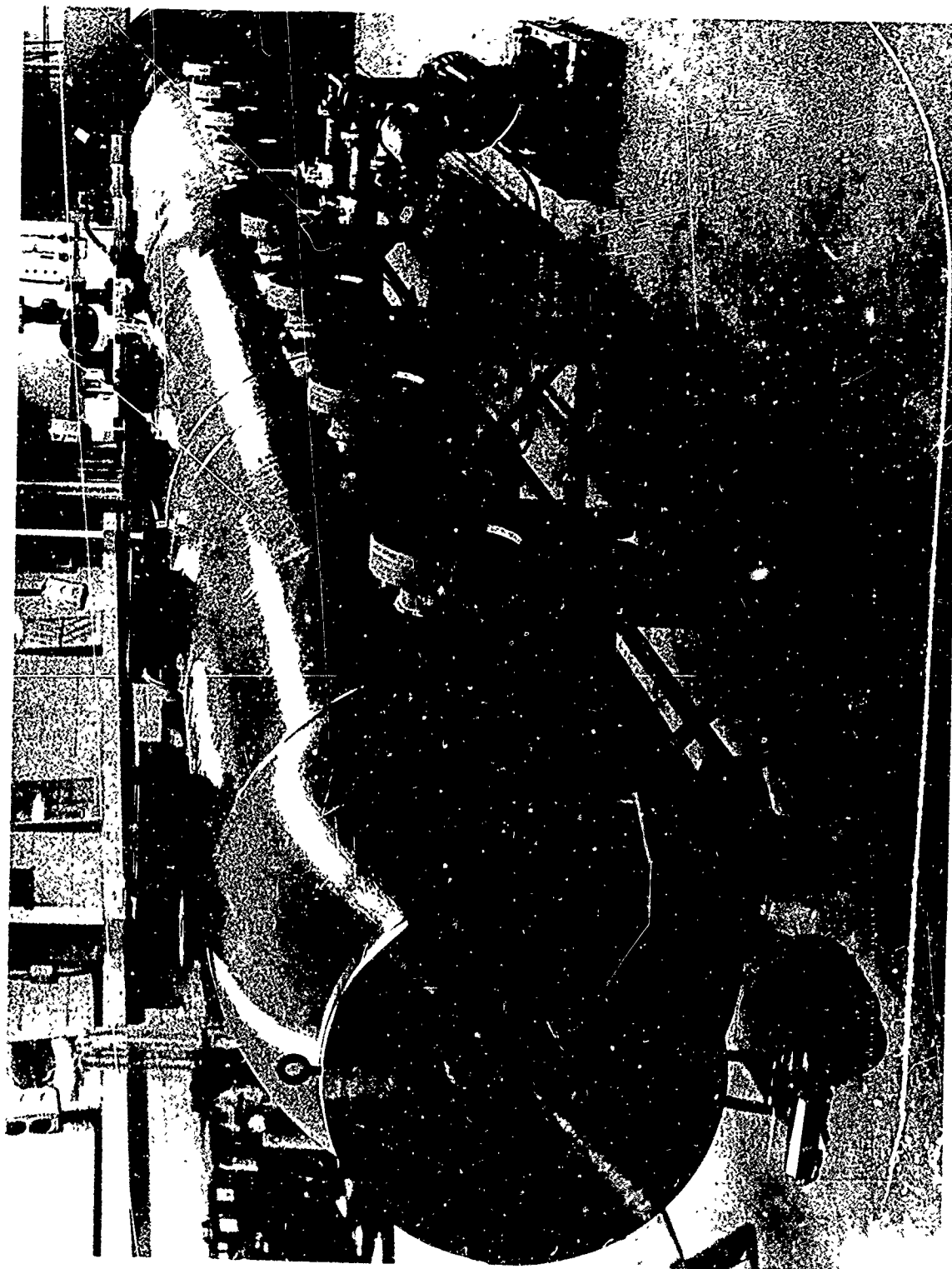
FIGURE 115 VIEW OF THE BALLISTICS RANGE — RANGE SECTIONS 2 AND 3
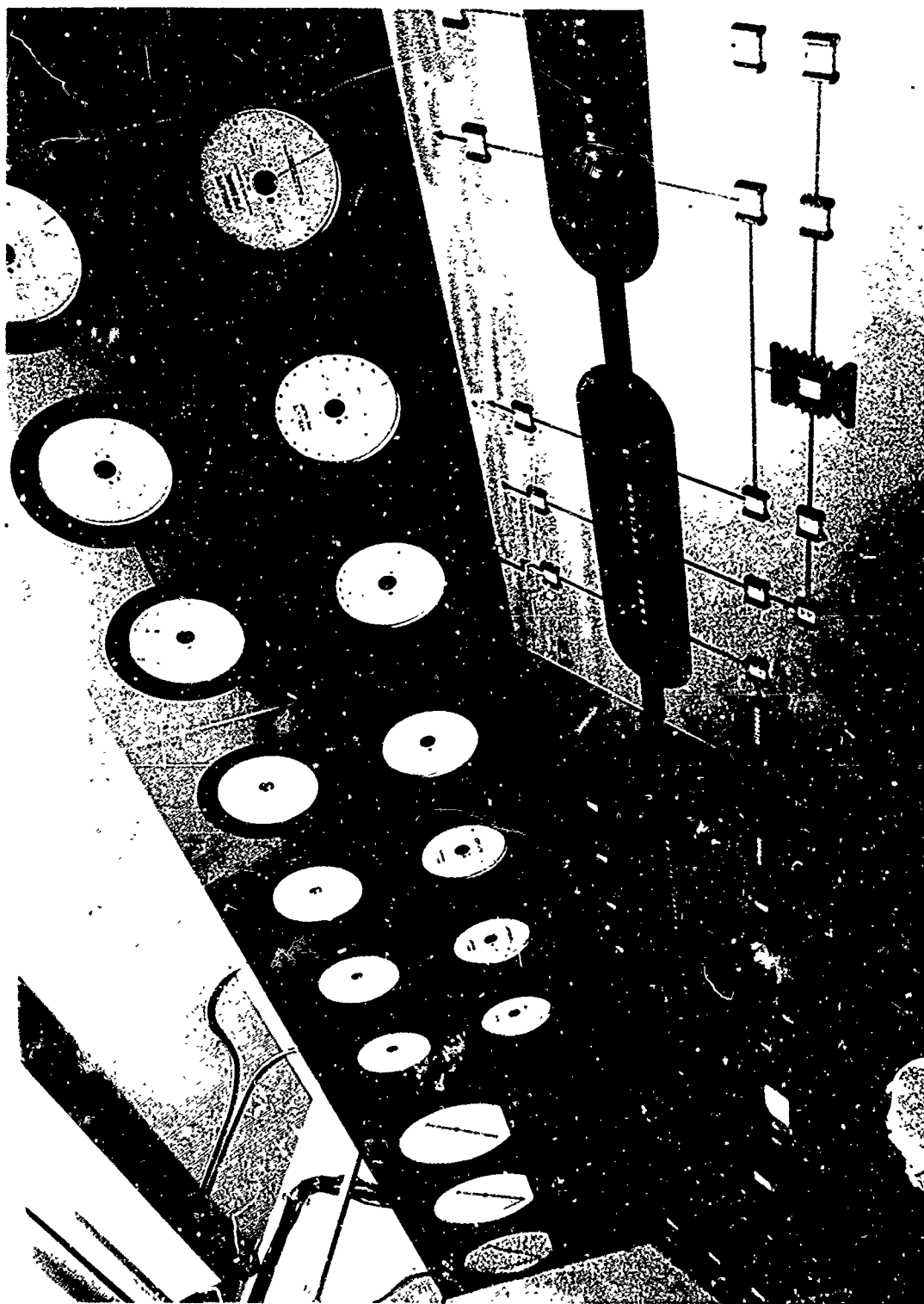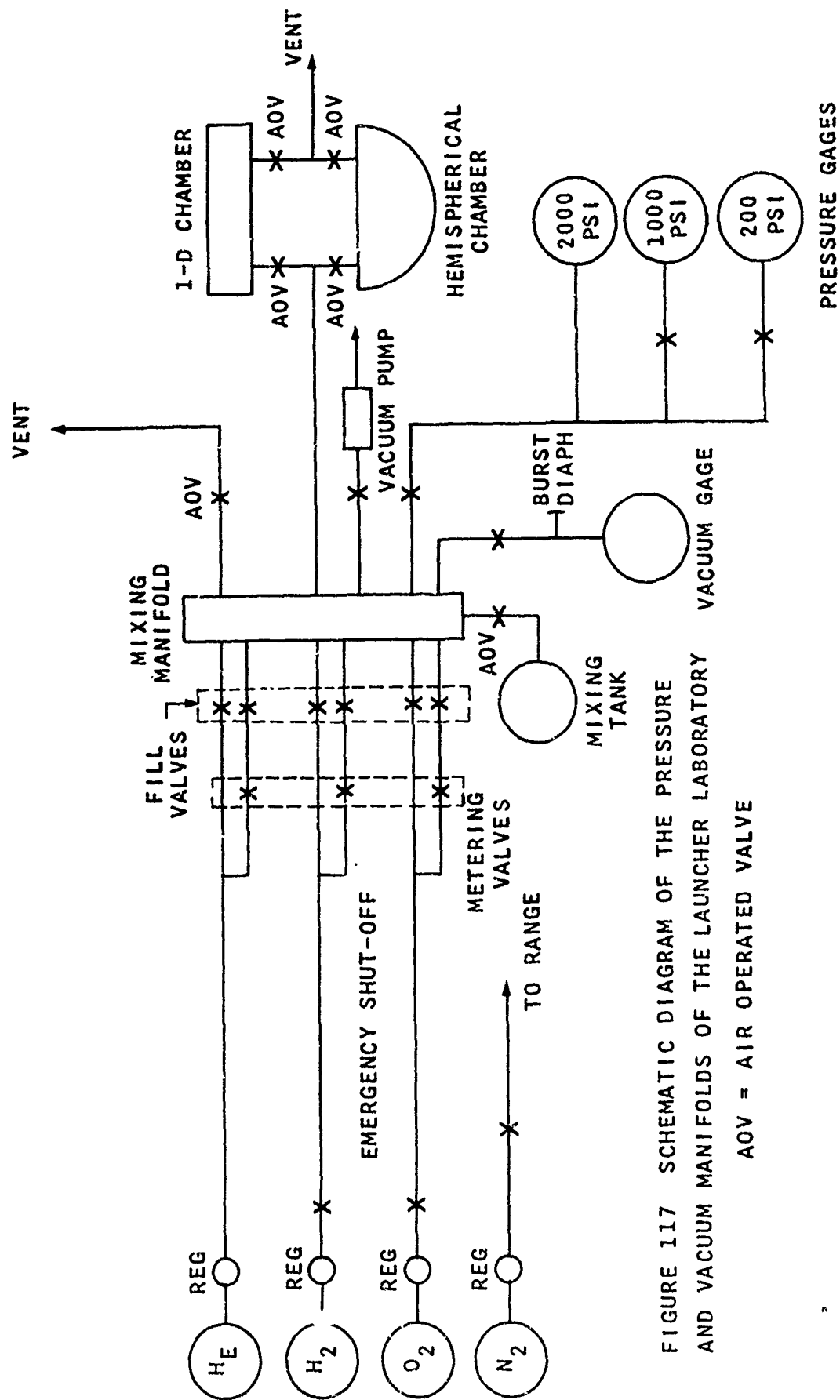
FIGURE 116   VIEW OF THE CONTROL CONSOLE

FIGURE 117 SCHEMATIC DIAGRAM OF THE PRESSURE
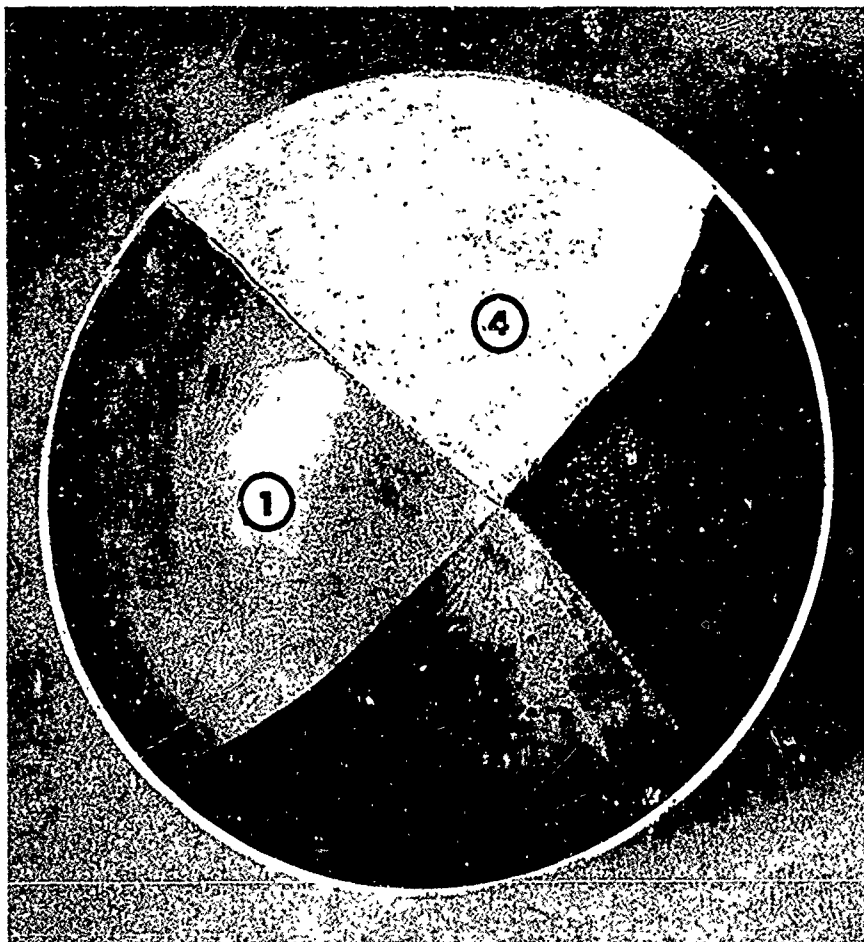AND VACUUM MANIFOLDS OF THE LAUNCHER LABORATORY

AOV = AIR OPERATED VALVE

FIGURE 118 FULL VIEW OF A MOCK-UP SHOWING THE
STEPS TAKEN IN THE MANUFACTURE OF THE EXPLOSIVE
LINER PACKAGE

1 SACRIFICIAL LEAD LINER

2 THIN COAT OF CEMENT

3 OPEN CORE FOAM PLASTIC MATRIX

4 PETN SLURRY FORCED INTO PLASTIC MATRIX

FIGURE 119
FULL VIEW OF THE REMAINS OF A 0.1 INCH LEAD
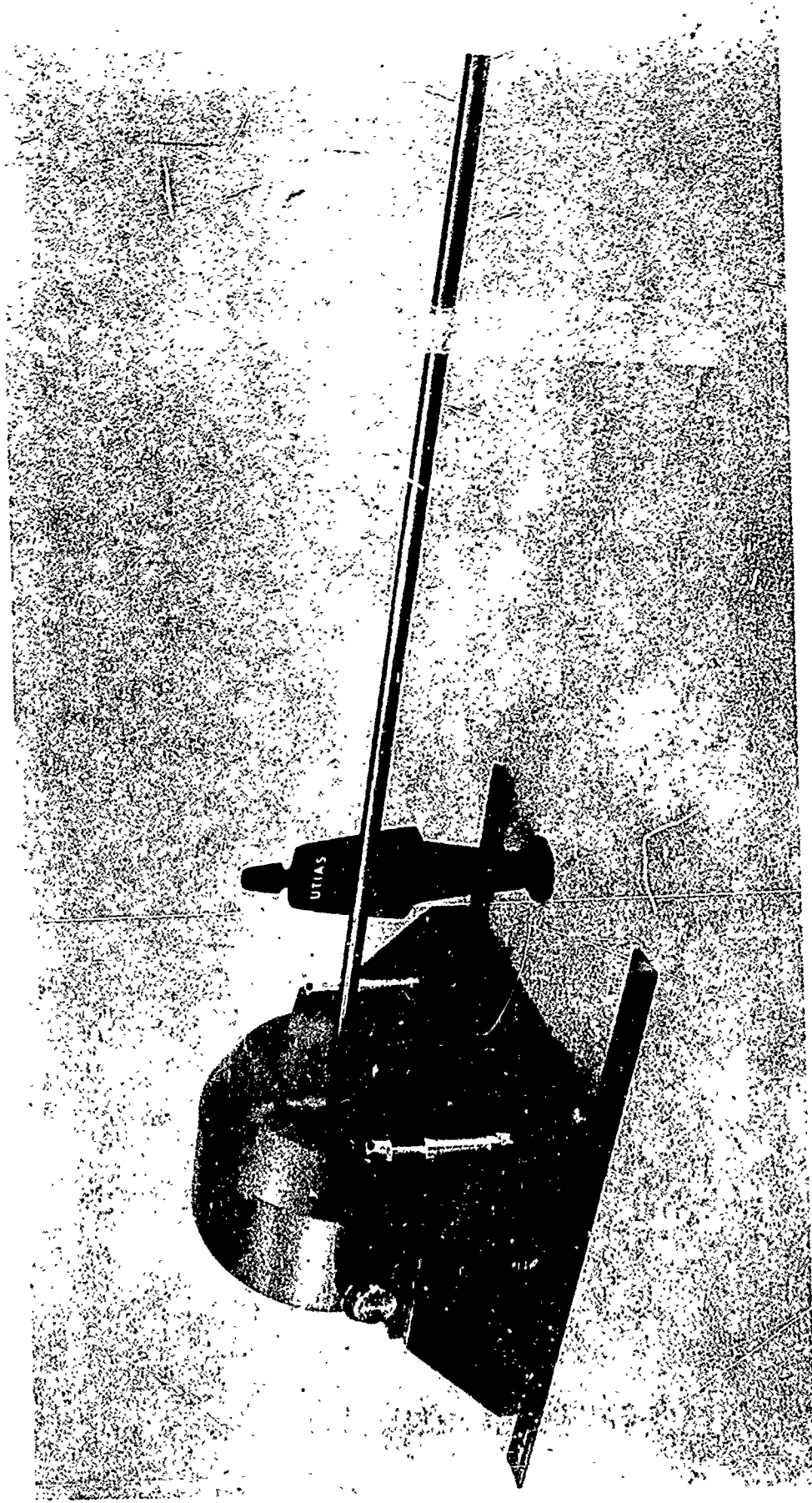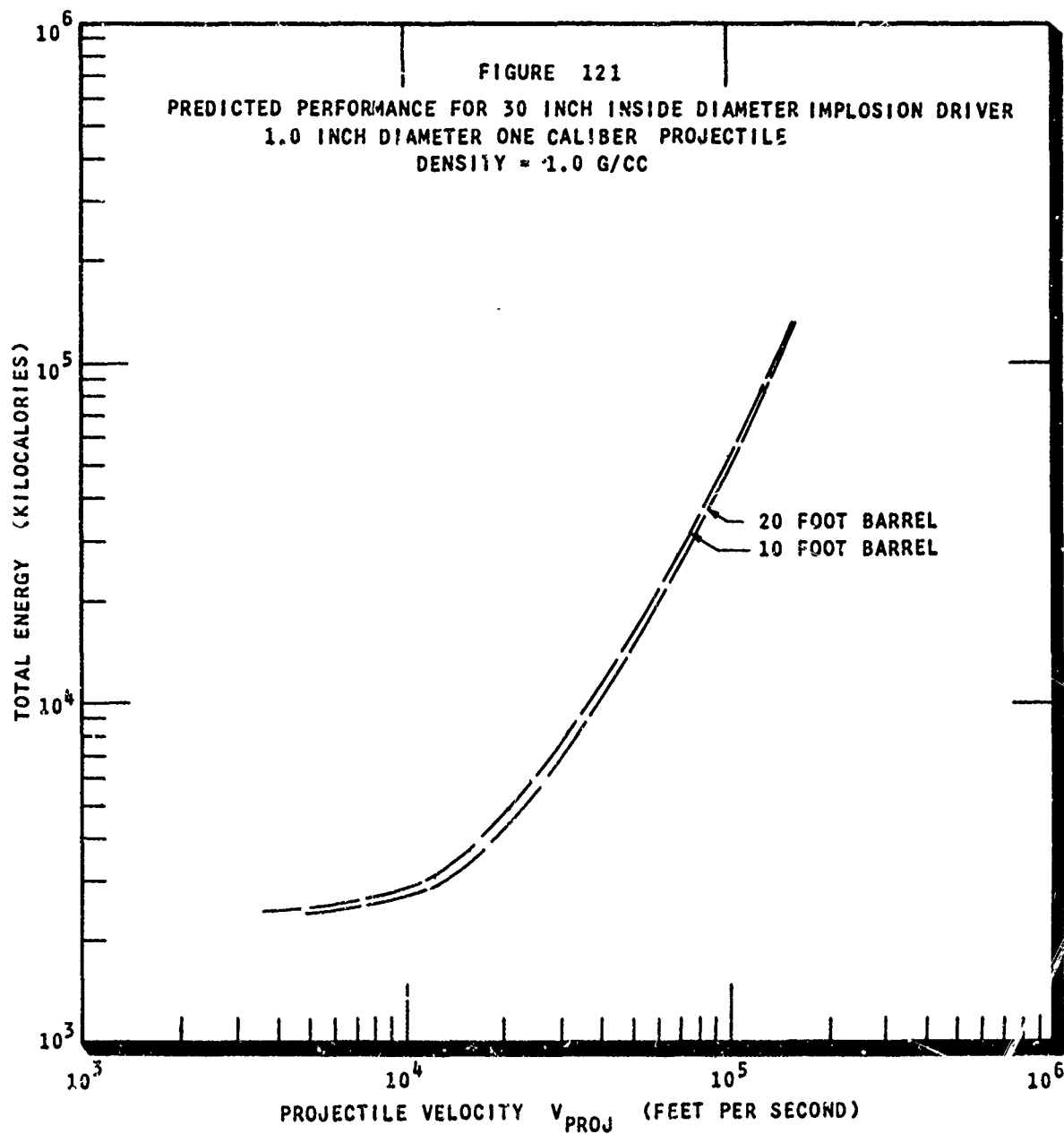LINER AFTER A NOMINAL 80 GRAM PETN RUN

FIGURE 120

STUDY MODEL OF A 30 INCH INSIDE DIAMETER IMPLOSION DRIVEN LAUNCHER
BARREL INSIDE DIAMETER 1.0 INCHES

FIGURE 121

PREDICTED PERFORMANCE FOR 30 INCH INSIDE DIAMETER IMPLOSION DRIVER
1.0 INCH DIAMETER ONE CALIBER PROJECTILE
DENSITY = 1.0 G/CC

END